

Electron Dynamics and Coherence Effects in Mesoscopic Hybrid
Normal Metal - Superconductor Devices

A Dissertation
Presented to the Faculty of the Graduate School
of
Yale University
in Candidacy for the Degree of
Doctor of Philosophy

By
Alexay Alexandrovich Kozhevnikov

Dissertation Director: Professor Daniel E. Prober

December, 2001

Acknowledgments

This dissertation is a result of collective effort of many people. First of all, I wish to thank my parents for giving me everything they could give and providing me with the best education they could provide. Whether at home or away from home, I always felt their continuous attention and support.

It was very important for me to receive the right guidance in my research. My advisor Daniel Prober has provided me with advice, support, and encouragement throughout my work at Yale. He has guided me through both good and bad times, and his confidence that it all was going to work out in the end made it possible for me to accomplish my work. I very much appreciate his patience in bearing with me and trying to make me more organized. I hope I have absorbed some of his advice. Dan, thank you very much for your support, wisdom, and patience.

I am grateful to my collaborators at different stages of my work at Yale - Peter Burke, Peter Wahlgren, Michael Rooks, Laurie Calvet, and especially Rob Schoelkopf. I got my first serious exposure to experimental physics at Yale, and Rob was a role model experimentalist for me. He taught me many things from making SMA connectors to running the dilution fridge and LabView programming. It was a great pleasure to work with him and to learn from him in the lab.

I am indebted to all of the current and a few of past members of ProberLab, namely, Peter Burke, Ifan Siddiqi, Ken Segall, Chris Wilson, Liqun Li, Luigi Frunzio, Stephan Friedrich, and Alexandr Verevkin for making ProberLab such a pleasant work environment. Thanks to my colleagues, it was a lot of fun to be at Yale. I wish to thank Michel Devoret for many enlightening discussions and helpful hints and comments.

I am thankful to Jayne Miller, Pam Patterson, Jean Belfonti and Jo-Ann Bonnett for helping

me to deal with Yale bureaucracy. Last, but not least, I express special thanks to my wife Ludmila and my daughter Elvira for bearing with my work schedule and for their love and support.

Contents

Acknowledgments	iii
List of figures	xiii
List of tables	xiv
List of symbols and abbreviations	xv
1 Introduction	1
1.1 Motivation	3
1.1.1 Studies of shot noise in mesoscopic systems	3
1.1.2 Using non-equilibrium noise to probe electron dynamics in mesoscopic superconductors	5
1.1.3 Possible applications: importance of understanding noise in N-S devices	6
1.2 Thesis overview	7
1.3 Definition of most frequently used terms	8
2 Theory	9
2.1 A brief historical note	10
2.2 Shot noise	14
2.2.1 Shot noise as a manifestation of granularity of electrical charge	14
2.2.2 Application of the scattering formalism to calculations of shot noise	15
2.2.3 Effects of the finite transmission probability	16

2.2.4	Crossover from thermal noise to shot noise	17
2.3	Non-equilibrium noise in diffusive conductors	17
2.3.1	Influence of electron-phonon interactions on shot noise	19
2.3.2	Shot noise in diffusive mesoscopic conductors in the regime $L \ll L_e$	20
2.3.3	Hot-electron noise in diffusive conductors in the regime $L \gg L_e$	21
2.3.4	Summary of non-equilibrium noise in diffusive conductors: dependence of noise on the device length	23
2.3.5	The role of non-ideal reservoirs and large bias voltages	23
2.4	Shot noise in the presence of high-frequency irradiation. Photon-assisted noise	28
2.5	Andreev reflection and proximity effect on mesoscopic scale	30
2.5.1	Andreev reflection	31
2.5.2	Propagation of the superconducting correlations into a diffusive normal wire. Usadel equation	33
2.5.3	Diffusive normal metal - superconductor junctions	37
2.5.4	Andreev interferometers	39
2.5.5	Definition of a "clean interface" applied to diffusive systems	42
2.6	Shot noise in hybrid normal metal - superconductor junctions	45
2.6.1	Ballistic case	45
2.6.2	Diffusive N-S junctions	47
2.6.3	Photon-assisted noise in normal metal - superconductor junctions	51
2.6.4	Comparison of non-equilibrium noise predictions for a normal diffusive con- ductor and for a diffusive N-S junction. Signatures of an effective charge $2e$	52
2.6.5	Shot noise and current-current correlations in multi-terminal devices with An- dreev reflection	56
3	Fabrication of Hybrid Normal Metal - Superconductor Devices	58
3.1	Physical parameters of devices	58
3.2	Fabrication Process	59
3.2.1	Resist spin-on	59
3.2.2	E-beam lithography for normal wire and contact pads	60

3.2.3	Resist development	65
3.2.4	Pattern evaluation	65
3.2.5	Deposition of Au	65
3.2.6	Au liftoff	66
3.2.7	Evaluation of the Au wires	66
3.2.8	Resist spin-on for the second step of E-beam lithography	66
3.2.9	Second step of E-beam lithography	68
3.2.10	Deposition of Nb	69
3.2.11	Nb liftoff	69
3.2.12	Evaluation of the devices	70
4	Experimental techniques	71
4.1	DC measurement setup	71
4.1.1	DC electronics	71
4.1.2	Shielding and filtering	75
4.2	RF measurement setup	76
4.3	Model of the measurement setup. Effects of the device impedance change	79
4.4	Calibration	87
5	Results of experiments	92
5.1	Devices measured	92
5.2	DC electrical characteristics of N-S devices	94
5.3	Shot noise measurements in diffusive N-S junctions	97
5.3.1	Dependence of noise on bias voltage	97
5.3.2	Correction for the change of the differential resistance of the device	100
5.3.3	Estimate of the errors of correction for reflected rf power	103
5.3.4	Comparison of shot noise between different N-S devices	107
5.3.5	Non-equilibrium noise of an N-S device driven normal	108
5.4	Photon-assisted noise in diffusive N-S junctions	111
5.5	Summary of experimental results for diffusive N-S junctions	121

5.6	Transport and noise measurements in Andreev interferometers	121
5.6.1	Transport and noise properties of a device of "cross" geometry	122
5.6.2	Transport and noise properties in device of "Y" geometry	135
6	Discussion	149
6.1	Summary of results presented in this thesis	149
6.2	Suggestions for future experiments	150
	Bibliography	160

List of Figures

2.1	Theoretically expected phase-breaking and electron-phonon length vs. temperature for quasi-1D diffusive wire with diffusion constant $D = 30 \text{ cm}^2/\text{sec}$	18
2.2	Dependence of Fano factor η on the length of a diffusive normal conductor (adapted from Steinbach et al 1996. Dashed lines are interpolations.	23
2.3	Predicted differential noise $(dS_I/dI)/(2e)$ vs. bias voltage for shot noise theory with ideal reservoirs, shot noise theory with finite thermal conductance of reservoirs and for hot-electron noise.	27
2.4	a. Single-particle tunneling in an opaque N-S junction and its I-V curve at zero temperature; b. Andreev reflection in transparent tunnel junction and an I-V curve in case of unity transparency (adapted from Blonder et al. 1982).	34
2.5	Energy dependence of normalized differential resistance of a diffusive N-S junction.	39
2.6	Schematic of device from (Petrashov et al. 1995) at integer and semiinteger external magnetic flux.	41
2.7	Comparison of shot noise of a diffusive N-S junction and of a normal diffusive conductor in the absence of high-frequency excitation.	54
2.8	Comparison of photon-assisted noise of a diffusive N-S junction and of a normal diffusive conductor.	55
3.1	The layout of the pattern for the first lithography step (not to scale). All dimensions are in μm . Dashed squares are alignment "windows".	61
3.2	Damage to deposited Au after 1 hr bake at 170°C	67

4.1	Schematic of DC measurement setup.	73
4.2	Simplified circuit diagram with the feedback circuit off and on.	76
4.3	Block diagram of the principal components of the measurement setup.	79
4.4	Schematic of the measurement setup.	80
4.5	Model of the device with rf amplifier.	83
4.6	Block diagram with the circulator between the device and the amplifier.	85
4.7	Dependence of output dc voltage of the crystal detector ($\times 1000$) vs. mixing chamber temperature. Device is biased at $V = 0$. Linear fit gives $\tilde{G} = 0.346 \pm 0.02$ V/K, $T_A = 9.3$ K.	89
5.1	SEM pictures and schematics of diffusive N-S junctions measured.	93
5.2	Dependence of differential resistance dV/dI of device 1 on bias voltage and temperature. Top: dV/dI vs. bias voltage at several mixing chamber temperatures. The inset shows wider range of bias voltages. Bottom: zero-bias differential resistance vs. temperature.	95
5.3	Dependence of differential resistance dV/dI of device 2 on bias voltage and temperature. Top: dV/dI vs. bias voltage at several mixing chamber temperatures. The inset shows wider range of bias voltages. Bottom: zero-bias differential resistance vs. temperature.	96
5.4	Top: dependence of differential non-equilibrium noise dT_N/dV and R_{diff} on bias voltage for device 1 at $T_{M/C} = 70$ mK; bottom: dependence of differential shot noise vs. bias voltage for device 1 at several mixing chamber temperatures.	99
5.5	Theoretical and experimental dependence of differential shot noise dT_N/dV of device 1 vs. bias voltage at $T_{MC} = 70$ mK and 200 mK.	100
5.6	Uncorrected differential noise $(dT_N^{out}/dV)/G$ and corrected differential noise dT_N/dV of device 1 at 70 mK.	102
5.7	Uncorrected differential noise $(dT_N^{out}/dV)/G$ and corrected differential noise dT_N/dV of device 2 at 50 mK.	102
5.8	Block diagram of the experiment testing the circulator.	104
5.9	Dependence on the ratio P_3/P_2 on the "load" resistance R	105

5.10	Uncorrected differential noise and corrected dT_N/dV for device 1 with error bars due to uncertainties in R_A and T_{iso} . The error bars are shown for "worst" combinations of $\pm 2 \Omega$ error in R_A and ± 1 K error in T_{iso}	106
5.11	Uncorrected differential noise and corrected dT_N/dV for device 2 with error bars due to uncertainties in R_A and T_{iso} . The error bars are shown for "worst" combinations of $\pm 2 \Omega$ error in R_A and ± 1 K error in T_{iso}	106
5.12	Comparison of bias voltage dependence of: (a) differential resistance, and (b) non-equilibrium noise $(R_N/e)(dS_I/dV)$ for devices 1 and 2.	109
5.13	Dependence of shot noise vs. bias voltage in device 1 driven normal by a magnetic field of 6T at several mixing chamber temperatures. Bottom panel presents data and theoretical predictions at $T = 70$ mK and 800 mK.	110
5.14	Comparison of measured shot noise with theoretical predictions for a diffusive N-S junction (device 1) and for the same device driven normal. Dashed line shows theoretical predictions for hot-electron noise - non-equilibrium noise in the regime $L_{ee} \ll L \ll L_{e-ph}$	111
5.15	Photon-assisted noise features for a diffusive N-S junction (device 1) under rf irradiation at $f = 33.6$ GHz.	113
5.16	Dependence of dT_N/dV on rf power for device 1 at bias voltage $V = 20 \mu\text{V}$	115
5.17	Dependence of d^2T_N/dV^2 on bias voltage for a diffusive N-S junction (device 1 at zero magnetic field) under 10 GHz irradiation.	118
5.18	Photon-assisted noise peaks location vs. frequency of rf excitation for device 1.	120
5.19	SEM picture and schematic of device of "cross" geometry. Nb loop extends beyond the area of the SEM picture.	123
5.20	Differential resistance vs. bias voltage for "cross" device for several values of magnetic flux at mixing chamber temperature $T_{M/C} = 50$ mK. AC voltage drive $\sim 8 \mu\text{V}$ p-p.	124
5.21	Zero bias differential resistance vs. magnetic field for "cross" device. AC bias voltage drive $\sim 4 \mu\text{V}$ p-p.	124
5.22	Zero bias differential resistance vs. temperature for integer and semi-integer magnetic flux. Bias voltage ac drive $\sim 2 \mu\text{V}$ p-p.	125

5.23	Differential resistance at bias voltage $V = 37 \mu\text{V}$ vs. temperature for integer and semi-integer magnetic flux.	126
5.24	a. Schematic of an N-S device with a dangling superconductor and equivalent circuit. Because of conversion of the quasiparticle current into the supercurrent the superconducting reservoirs are shorted together at small currents (adapted from (Gueron 1997)). b. Schematic of the "cross" device and the equivalent circuit.	128
5.25	(a) Oscillatory dependence of dI/dV on applied rf power at $\nu = 2.5 \text{ GHz}$ at bias voltages, corresponding to $n\hbar\nu/e$, for $n = 0, 1, 2, 3$; (b) Bias voltage dependence of the differential conductance dV/dI under RF excitation at 2.5 GHz showing PAT features at bias voltages $V = n\hbar\nu/e$	131
5.26	Schematic of the device with dc bias V_{dc} and rf excitation V_{ac} and equivalent circuit	132
5.27	Bias voltage dependence of differential noise temperature dT_N/dV for the "cross" device for an integer and semi-integer magnetic flux. Behavior at bias voltages $V \lesssim 20 \mu\text{V}$ is likely due to onset of Josephson coupling between superconducting terminals.	133
5.28	SEM picture and schematic of device of "Y" geometry.	135
5.29	Differential resistance vs. bias voltage at different values of magnetic flux and zero-bias differential resistance vs. magnetic field of a "Y" structure.	137
5.30	Model for calculation of conductance of "Y" structure.	138
5.31	Theoretical and experimental dependence of differential resistance of "Y" structure vs. bias voltage. Top panel: experimental data at integer and semi-integer flux and theoretical predictions at $T = 0$. Bottom panel: experimental data and theory for finite temperatures. The fit assuming $T = 100 \text{ mK}$ is in better agreement with experiment than the fit assuming $T = T_{M/C} = 50 \text{ mK}$	140
5.32	Differential noise of the rf chain referred to the input vs. bias voltage of the device at several values of magnetic flux.	143
5.33	Bias voltage dependence of dc differential resistance and reflected rf power at 1.5 GHz at integer and half-integer flux.	143

5.34	Corrected dT_N/dV for device "Y" at several different values of magnetic flux ($T_{M/C} = 50$ mK). Error bars are the worst error estimates due to $\pm 2 \Omega$ uncertainty for R_A and ± 1 K uncertainty for T_{iso}	145
5.35	(a) Noise temperature of the device at $I = 1.06 \mu\text{A}$ vs. magnetic field; (b) Effective charge calculated from data in (a).	147

List of Tables

5.1 Physical parameters of diffusive N-S junctions measured.	93
--	----

List of symbols and abbreviations

BCS Bardeen - Cooper - Schrieffer

rf Radio frequency

T Temperature

T_A Amplifier (input) noise temperature

T_{out} Output noise

T_e Electron temperature

T_{bath} Bath temperature

T_{John} Input noise due to Johnson noise

$T_{M/C}$ Mixing chamber temperature

T_n Transmission probability

η_{rf} rf coupling

Γ Voltage reflection coefficient

Z_L Load impedance

Z_0 Characteristic impedance (377 Ω in free space)

R_L Load resistance

D Diffusion constant

L_e Electron energy relaxation length $\equiv \sqrt{D\tau_e}$

L_{e-ph} Electron-phonon length $\equiv \sqrt{D\tau_{e-ph}}$

L_{ee} Electron-electron length $\equiv \sqrt{D\tau_{e-e}}$

l Elastic mean free path

τ_{th} Thermal time constant

τ_m Momentum relaxation time

τ_{e-ph} Electron-phonon interaction time

τ_{e-e} Electron-electron interaction time

τ_e Electron energy relaxation time

τ_D Diffusion transit time $\equiv L^2/D$

φ Phase of the order parameter in the superconductor

Φ_0 Magnetic flux quantum $\equiv h/(2e)$

e Absolute value of electron charge (e is considered positive)

E_C Thouless energy $\equiv \hbar D/L^2$

G Conductance

G_{diff} Differential conductance $\equiv dI/dV$

R Resistance

R_{\square} Sheet resistance

R_N Normal state resistance

R_{diff} Differential resistance $\equiv dV/dI$

I_{dc} dc current

V_{dc} dc voltage

S_I Current spectral density

$S_I^{Poisson}$ Poisson current spectral density $\equiv 2eI$

S_V Voltage spectral density

\mathcal{L} Lorenz number

K Thermal conductivity

G Thermal conductance

c Specific heat

C Heat capacity

η Shot noise suppression factor (Fano factor)

ξ Coherence length in normal metal (thermal length)

φ Phase of the superconductor

θ Pairing angle

PMMA Poly(methyl methacrylate)

PAT Photon-assisted tunneling

MIBK Methyl isobutyl ketone

N-S Normal metal - superconductor

S-N-S Superconductor - normal metal - superconductor

NPGS Nanometer Pattern Generation System

FDT Fluctuation-dissipation theorem

FQHE Fractional Quantum Hall effect

SEM Scanning electron microscope

MRF Multiple run file

SIS Superconductor - insulator - superconductor

GL Ginzburg - Landau

CL Condenser lens

OL Objective lens

Chapter 1

Introduction

Advances in nanotechnology made it possible to fabricate submicron-sized solid-state devices with great flexibility and control. This sparked a great interest in the investigation of these "mesoscopic" devices, both theoretical and experimental, which resulted in the emergence of a new area of solid-state physics - mesoscopic physics. The term "mesoscopic device" is usually referred to a structure, which consists of a very large number of atoms, but which is small enough so that quantum coherence effects become important. This corresponds to the physical regime when the dimensions of the device become comparable to the electron phase-breaking length.

Electron dc transport properties in mesoscopic devices have been studied most extensively. A variety of novel phenomena was discovered. Quantization of conductance in nanoconstrictions, weak localization and conductance fluctuations in mesoscopic diffusive conductors, charging effects and Coulomb blockade of transport in small conductors, and Fractional Quantum Hall effect are just a few of the novel phenomena which are peculiar to mesoscopic devices and are not present on a macroscopic scale. There are recent reviews of several areas of electron transport in mesoscopic structures (Sohn et al. 1997).

DC electron transport measurements are the easiest measurements to perform experimentally on a solid-state device, even though they can be quite challenging for mesoscopic devices because of low temperatures: one must carefully filter the leads to get rid of rf leakage. DC transport properties are also easier than dynamic properties to treat theoretically. However, measuring dc conductance

yields only information about time-averaged transport properties and does not give insight into the dynamics of electron transport in the system.

The situation started to change about ten years ago, when several theoretical works predicted unexpected properties of non-equilibrium current fluctuations in mesoscopic regime. Since then, more and more attention has been given to studies of dynamic properties of mesoscopic structures, in particular, to the investigation of non-equilibrium current fluctuations (noise) and current-current cross-correlations.

Electrical noise is one of the most common frustrations for experimental physicists. Noise is also of major importance for a wide range of areas of knowledge ranging from telecommunications and electronics to biology and environmental safety. Besides being a hassle, noise can be used as an instrument to study the dynamical behavior of a physical system. Noise may be used as a probe that yields information about a physical system which is difficult to obtain otherwise. Probing current fluctuations (noise) yields information about dynamical properties of the system, whereas dc conductance measurement can yield only time-averaged properties of the physical system.

Some of the most common types of electrical noise are thermal (Johnson-Nyquist) noise, $1/f$ -noise, generation-recombination noise (particularly important for semiconductors) and shot noise. A comprehensive review of various mechanisms of noise in solid state systems is available (Kogan 1996).

In the work described below, an experimental investigation of shot noise is used to probe the nature of current carriers in mesoscopic hybrid normal metal - superconductor (N-S) devices. The shot noise is found to bear clear signatures of the effective charge being $2e$, due to Andreev reflection at the N-S boundary.

In the next section of this chapter, we discuss the motivations for investigation of shot noise in mesoscopic devices in general and, in particular, in hybrid N-S systems. In the third section, we give the thesis overview. In the fourth section, brief definitions of the most commonly used terms are given.

1.1 Motivation

1.1.1 Studies of shot noise in mesoscopic systems

The study of electrical fluctuations in mesoscopic systems has become an exciting area in both experimental and theoretical physics in recent years. Special attention is given to shot noise, which is a term for non-equilibrium electrical fluctuations due to discreteness of the electrical charge.

There are several reasons for such intense interest in the subject of shot noise in mesoscopic systems. Shot noise can serve as a very sensitive instrument for probing temporal correlations of electrical current carriers. In a conventional transport measurement, the I-V curve (or conductance) of the device is measured. Such experiments measure average current, but not the current fluctuations, *i.e.*, a conductance measurement does not allow one to probe correlations of a current. In mesoscopic devices, there are physical regimes where current fluctuations and current-current correlations become very important.

Classical Poisson shot noise corresponds to the fluctuations of a current due to single-electron pulses which are completely uncorrelated with each other. A stationary random process can be characterized in terms of its spectral density. The spectral density of a random signal is the rms of the signal per unit bandwidth (a more rigorous definition will be given below). Poisson shot noise is "white" (frequency-independent) and has current spectral density

$$S_I = 2eI. \tag{1.1}$$

In degenerate Fermi systems correlations arise due to the quantum statistics of the current carriers - for fermions, non-equilibrium fluctuations decrease compared to the uncorrelated case. The fluctuations of number of particles Δn is given by (Landau and Lifshitz 1980):

$$\Delta n = \bar{n}(1 \pm \bar{n}), \tag{1.2}$$

where \bar{n} is the average occupation number, and the plus sign corresponds to bosons, while the minus sign corresponds to fermions. In a solid-state device, shot noise is present if electron transport is elastic, that is, if electrons traverse the device without exchanging energy with phonons or other elec-

trons. Therefore, mesoscopic solid-state systems are well-suited for realizing a "clean" experimental situation where one can observe the effects of shot noise suppression due to Fermi statistics of electrons. These experiments are complimentary to optics experiments with photons which obey Bose statistics and usually display fluctuations larger than Poisson (bosons display "bunching" whereas fermions display "antibunching").

Another major source of electron correlations are interactions. Coulomb interactions are known to decrease shot noise in vacuum diodes. Strongly correlated mesoscopic systems provide a variety of novel physical phenomena. In these systems, shot noise is frequently an instrument of choice to probe the electron correlations. A classical example is Fractional Quantum Hall Effect. At certain filling factors, due to interactions of electrons with the external magnetic field and due to electron-electron interactions, current is effectively carried by Laughlin quasiparticles which carry fractional charge. The existence of Laughlin quasiparticles carrying fractional charge was experimentally confirmed by measurements of shot noise in devices in FQHE regime (De-Picciotto et al. 1997), (Saminadayar et al. 1997). FQHE is not the only example when shot noise is used to probe correlation in a mesoscopic system; we will discuss several others in the next chapter. In short, one of the main sources of motivation for this work is that measurements of shot noise can be an important experimental tool to probe correlations in mesoscopic systems.

Several important contributions to the field of shot noise in mesoscopic systems were made at Yale. The spectrum of the shot noise in a diffusive mesoscopic conductors was measured (Schoelkopf et al. 1997). In this work the influence of zero-point fluctuation on the spectrum of the non-equilibrium noise was directly observed in the experiment. The work (Schoelkopf et al. 1997) is one of the very few experiments in mesoscopic physics where the observed finite-frequency behavior of the system is fundamentally different from the dc behavior. Following this work, photon-assisted noise in a normal diffusive conductor was observed (Schoelkopf et al. 1998). The first experimental observation of the shot noise doubling in a diffusive N-S junction as compared to a normal diffusive conductor was done in our recent work (Kozhevnikov et al. 2000a). Our measurements of photon-assisted noise in a diffusive N-S junction (Kozhevnikov et al. 2000) provide the signatures of the effective charge $2e$ which are more uniquely indicative than the shot noise doubling alone.

From a more practical point of view, studies of shot noise in mesoscopic systems are important

for understanding fundamental limitations of device performance. Shot noise limits the sensitivity of a variety of electronic devices, including FET transistors and several types of radiation detectors. Rapid progress in nanofabrication technology and minituarization of devices may eventually make the transistors mesoscopic at room temperatures. Understanding noise properties of devices in mesoscopic regime may become an area of importance for mass production technology in the foreseeable future.

1.1.2 Using non-equilibrium noise to probe electron dynamics in mesoscopic superconductors

As mentioned before, shot noise measurements can be a sensitive tool for probing current fluctuations and correlations. In this work, shot noise is used to obtain information about electron dynamics in mesoscopic hybrid normal metal - superconductor systems.

Mesoscopic superconductivity and mesoscopic proximity effect (penetration of superconducting correlations into a normal metal) is currently an area of active research. The basic notions of the theory of mesoscopic superconductivity - Andreev reflection (Andreev 1964), Ginzburg-Landau description of proximity effect in diffusive samples (Deutscher and de Gennes 1969) and Usadel equation (Usadel 1970) have been worked out in the late 60's and early 70's. However, a detailed experimental investigation of mesoscopic N-S structures was difficult before a substantial progress in microfabrication was made. Only after a wide introduction of electron beam lithography has it become possible to routinely fabricate a variety of mesoscopic N-S devices having well-controlled geometries and to study their properties. Experiments with hybrid N-S devices revealed a number of interesting and unexpected results. Based on Usadel theory, a modern Green function-based description of mesoscopic proximity effect was introduced (Nazarov and Stoof 1996), which was able to explain many of observed effects in transport of mesoscopic N-S samples. Until very recently, however, both theoretical predictions and experiments dealt almost exclusively with the dc transport properties of mesoscopic N-S structures. Very little was known about non-equilibrium noise in mesoscopic N-S structures and, more generally, about time-dependent processes in these devices.

One of the first theoretical predictions regarding current fluctuations in N-S systems was made by de Jong and Beenakker (de Jong and Beenakker 1994). Although a complete theory for arbitrary

energies has not been worked out yet, theory predicts a number of interesting signatures of proximity effect and correlations due to Andreev processes in N-S structures. One of the most dramatic effects is *doubling* of shot noise in a mesoscopic normal metal wire which is attached to one normal and one superconducting reservoir, as compared to a normal metal wire with normal reservoirs. This doubling of shot noise is predicted to occur in a system where conductance is modified only slightly by the presence of the superconducting reservoir. This is one example where the electron correlations which are induced by interaction have small effect (maximum $\approx 15\%$) on conductance of the system, but large effect (a factor of 2) on shot noise. The origin of doubling of shot noise is the Andreev process, which is a correlated transfer of 2 electrons from a normal metal into a superconductor. Because of this correlated transfer of 2 electrons, the effective charge of current carriers is $2e$, and shot noise is doubled compared to a normal conductor. As discussed below, of special interest are measurements of shot noise in N-S devices in the presence of high-frequency rf excitation which also provides unambiguous signatures of the effective charge being $2e$.

In this work, one of the first experimental investigations of shot noise in mesoscopic N-S devices was performed. Doubling of shot noise due to Andreev reflection was experimentally observed. Our measurements of shot noise in the presence of rf excitation revealed signatures of the Josephson frequency in a normal wire with only one superconducting reservoir. In this system a true Josephson effect cannot take place. This is the first experimental observation where the Josephson frequency manifests itself in a system with only one superconducting reservoir and no weak links.

1.1.3 Possible applications: importance of understanding noise in N-S devices

At present, the subject of non-equilibrium noise in N-S devices and in superconducting devices with weak links is very important for various applications of superconducting devices, in particular, to superconducting detectors. Ideally, a detector should be shot noise limited. However, in some instances shot noise is much larger than Poisson noise due to the peculiar nature of correlations. An example is non-equilibrium noise much larger than Poisson noise in NbN superconductor - insulator - superconductor (SIS) tunnel junctions which are used as microwave detectors (Dieleman and Klapwijk 1998). This increased noise is believed to be due to multiple Andreev reflection process

which leads to a correlated transfer of a charge much larger than the electron charge e . The shot noise due to these "clusters" of charge largely exceeds Poisson noise: $S_I = 2q_{eff}I \gg 2eI$.

Other examples illustrating the importance of non-equilibrium noise in superconducting systems with weak links are partition noise (Segall and Prober 2001) and generation-recombination noise (Wilson et al. 2001). Understanding the physical mechanisms of these noise sources is an important design factor for single-photon tunnel junction detectors for X-ray and visible photons.

Investigation of noise mechanisms in mesoscopic superconductors may also have applications for detectors. Diffusive S-N-S junctions have been proposed as sensitive direct detectors of microwave radiation (Karasik et al. 1999), (Chouvaev et al. 1999). One of the important sources of noise in such a device at non-zero bias voltages may be shot noise. Due to multiple Andreev reflections, it may be much larger than Poisson noise and may limit the sensitivity of this type of detectors.

1.2 Thesis overview

The composition of this thesis is as follows. In chapter 2, we discuss the theory of shot noise, the theory of Andreev reflection, and the proximity effect. We focus on discussion of shot noise theory in diffusive normal and normal metal - superconducting devices. There are two main predictions of the theory. First, the shot noise in a diffusive N-S junction is predicted to be *doubled* as compared to a normal diffusive conductor. Second, under high-frequency excitation of frequency ν , photon-assisted noise features are predicted to occur at bias voltages $V_{NS} = nh\nu/(2e)$ for a diffusive N-S junction, whereas for a normal diffusive conductor these features occur at $V_N = nh\nu/e$. Both effects constitute signature of effective charge $2e$ due to Andreev reflection. In chapter 3, a detailed description of device design and fabrication is presented. Chapter 3 is not meant to be a microfabrication manual, but contains all the information peculiar to the fabrication process used at Yale to make N-S junctions. Chapter 4 describes measurement techniques, in particular, high-frequency noise measurement methods. The measurement apparatus setup, filtering and shielding, and calibration procedures are discussed. In chapter 5, the results of low-temperature transport and noise measurements are presented and compared to theoretical predictions. Shot noise magnitude for a diffusive N-S junction is found to be doubled compared to a normal mesoscopic conductor, in good agreement with theory. We also observe photon-assisted noise features occur at bias voltages $nh\nu/(2e)$ for an

N-S junction. For the same device driven normal by a magnetic field, photon-assisted features occur at bias voltages $nh\nu/e$, as predicted by theory. The results of shot noise measurements in Andreev interferometers will also be discussed. In chapter 6, conclusions are drawn.

1.3 Definition of most frequently used terms

Below we give brief definitions and explanations of several terms that are frequently used in this thesis. Some of these terms will be explained in more detail in subsequent chapters.

Andreev interferometer - an N-S device (containing superconducting loop) in which transport is sensitive to the phase difference between superconducting terminals, which can be tuned by external magnetic flux. Andreev interferometers will be discussed in some detail in chapter 2.

Ballistic N-S junction - a tunnel junction between a normal metal lead and a superconductor. The leads are assumed to have negligible resistance and to be disorder-free (ballistic). All the resistance of the device is due to a tunnel barrier between a normal metal and a superconductor.

Diffusive N-S junction - a mesoscopic diffusive normal metal wire between one normal reservoir and one superconducting reservoir.

Mesoscopic device - a device containing macroscopically large number of atoms, but having dimensions such that phase coherence and quantum interference effects become important.

Normal metal tunnel junction - a tunnel junction between two normal metal leads. Unless otherwise noted, leads are supposed to have resistance negligible compared to the resistance of a tunnel barrier. Below, unless otherwise noted, the term **tunnel junction** means normal metal tunnel junction.

Normal diffusive conductor - a mesoscopic diffusive normal metal wire between 2 normal metal reservoirs.

Chapter 2

Theory

The emphasis of this thesis is performing precise measurements of shot noise and extracting physical quantities of interest, e.g., the effective charge of current carriers, from the results of these measurements.

In the first section, we discuss the theory of shot noise. After a historical note which briefly summarizes the most significant theoretical and experimental results in the field of shot noise, we discuss the application of scattering formalism to the calculations of shot noise. Some of the theoretical results were first derived without the explicit use of scattering formalism. However, the use of the scattering formalism and the second quantization provides a unified framework for calculating shot noise in the case of phase-coherent transport and makes many derivations simpler and more understandable. In the end of this section, we discuss non-equilibrium noise in diffusive normal metal wires.

In the second section, we discuss shot noise in mesoscopic systems in the presence of high-frequency irradiation. If transport in the device is elastic, in the presence of high-frequency irradiation of frequency ν , the noise develops features at bias voltages $V = nh\nu/e$. The underlying mechanism is similar to photon-assisted tunneling (Tien and Gordon 1963), and the dependence of these photon-assisted noise features on the frequency and power of the rf excitation is similar to the features in photon-assisted tunneling.

In the third section, we discuss Andreev reflection and the proximity effect on a mesoscopic

scale. Throughout this thesis, we call "mesoscopic" a system which consists of a very large number of atoms, but which has small enough dimensions such that phase-coherence effects are important. The literature on the mesoscopic proximity effect, both theoretical and experimental, is vast. In this thesis, we do not go deeply into the advanced theory of the proximity effect, but rather we will state the most important theoretical results that we need to understand and to model the behavior of our devices. We also review the main experimental results for diffusive systems.

In the fourth section, we discuss the theoretical predictions of shot noise in mesoscopic hybrid normal metal - superconductor (N-S) systems. We pay particular attention to diffusive N-S junctions; for this case theory has been largely worked out. We also discuss theoretical predictions regarding shot noise in Andreev interferometers.

2.1 A brief historical note

Before laying out the fundamentals of the modern scattering approach to mesoscopic noise problems, let us give a brief historical note regarding theoretical and experimental advances in the field of shot noise and noise in general. This note briefly summarizes the results which turned out to be important for modern understanding of non-equilibrium mesoscopic noise. There are several recent reviews of work on shot noise in mesoscopic systems (de Jong and Beenakker 1997), (Blanter and Büttiker 2000).

The fluctuations of electrical current due to the discrete nature of electron charge are referred to as shot noise. Shot noise was first reported by Schottky (Schottky 1918) for ideal vacuum diodes. For such a vacuum diode, the current spectral density is frequency-independent and proportional to the mean current:

$$S_I = 2eI. \quad (2.1)$$

Nyquist (Nyquist 1928) has derived the expression for thermal noise, *i.e.*, electrical noise in a circuit due to thermal fluctuations. In its simplest form, Nyquist's theorem states, that a resistor R at temperature T , will have voltage fluctuations across it with a voltage spectral density

$$S_V = 4h\nu R \left[\exp\left(\frac{h\nu}{k_B T}\right) - 1 \right]^{-1}, \quad (2.2)$$

At small frequencies ($h\nu \ll k_B T$) equation 2.2 becomes:

$$S_V = 4k_B T R. \quad (2.3)$$

In 1928, the low-frequency thermal noise described by equation 2.3 was observed experimentally by Johnson (Johnson 1928).

In 1951, Callen and Welton derived a general relation relating fluctuations in equilibrium to the real part of the generalized impedance (Callen and Welton 1951). This relation, known as the fluctuation-dissipation theorem, states that in equilibrium, under fairly general assumptions, the noise power spectral density is given by a modified Johnson-Nyquist relation. Voltage spectral density S_V in equilibrium is going to be directly proportional to the real part of the impedance. Therefore, noise in equilibrium does not yield any new information compared to the conductance. The importance of the fluctuation-dissipation theorem (FDT) is that it does not make any assumptions on what the system under consideration is, as long as it can be regarded as a linear system with the impedance $Z(\omega)$. The equilibrium voltage fluctuations of such a system are given by:

$$S_V(\nu, T) = 4Re [Z(\omega)] \left[\frac{1}{2} h\nu + \frac{h\nu}{\exp\left(\frac{h\nu}{k_B T}\right) - 1} \right]. \quad (2.4)$$

Note that equation 2.4 differs from equation 2.2 by an extra term $h\nu/2$. This term represents vacuum fluctuations - ground-state fluctuations due to zero-point energy $h\nu/2$. The effects of quantum noise due to zero-point fluctuations were experimentally observed in resistively shunted Josephson junctions (Koch et al. 1982). The "coloredness" of high-frequency noise due to zero-point fluctuations was directly observed in a mesoscopic normal conductor (Schoelkopf et al. 1997).

Rogovin and Scalapino (Rogovin and Scalapino 1974) have considered theoretically both equilibrium and non-equilibrium noise in tunnel junctions. Using a tunneling Hamiltonian approach and effectively a perturbation theory, they derived relations allowing one to express the noise in a tunnel junction based on the I-V curve of the tunnel junction. These relations were applicable both in equilibrium (at $V = 0$) and out of equilibrium, and also both for zero frequency and for finite frequencies (but at frequencies smaller than the inverse tunneling time: $\nu \ll \tau_{tunnel}^{-1}$). For a noise

due to quasiparticle current of a tunnel junction, they derived the following expression:

$$S_I(V, \nu, T) = e \left[I_{qp}(V + h\nu/e) \coth \left[\frac{eV + h\nu}{2k_B T} \right] + I_{qp}(V - h\nu/e) \coth \left[\frac{eV - h\nu}{2k_B T} \right] \right] \quad (2.5)$$

Note that for $\nu = 0$ and $T = 0$ the Poisson shot noise result is recovered: $S_I = 2eI$. For the case $eV, h\nu \ll k_B T$ equation 2.5 reduces to Johnson thermal noise: $S_I = 4k_B T/R(V = 0)$. For $V = 0$ and $T, \nu \neq 0$, equation 2.5 reduces to the fluctuation-dissipation theorem. Equation 2.5 shows that Johnson-Nyquist noise and shot noise are special cases of a more general expression, and that, in general, noise cannot be represented as a simple superposition of thermal and shot noise. Noise power, in general, is a non-linear superposition of thermal and non-thermal noise sources.

In 1957, Landauer (Landauer 1957) discussed the problem of electrical transport as a scattering problem. If transport is phase-coherent, a mesoscopic device can be modeled as a disordered region connected to the reservoirs. Conductance is determined by the scattering matrix of the disordered region. The idea proved to be of great significance for mesoscopic physics because it allowed a very convenient description of phase-coherent electron transport. Between 1989 and 1992, the Landauer-Büttiker formalism was successfully applied to the calculations of shot noise in mesoscopic devices (Martin and Landauer 1992), (Beenakker and Buttiker 1992), (Lesovik 1989), (Büttiker 1992). In the paper by Büttiker (Büttiker 1992) a detailed derivation was given relating noise to the scattering matrix of the disordered region and to the distribution functions in the reservoirs. Application of the scattering formalism led to predictions of several interesting and unexpected effects. First, shot noise current spectral density is expected to be suppressed compared to Poisson noise $S_I = 2eI$ when the transmission probability through the disordered region is close to 1. For a tunnel junction with transmission probability T_n , shot noise is:

$$S_I = 2eI(1 - T_n). \quad (2.6)$$

This suppression is a manifestation of quantum statistics of current carriers - shot noise is suppressed for Fermions (they exhibit antibunching), while shot noise is enhanced for Bosons (they exhibit bunching). These effects are appreciable only when the occupation number $f \gtrsim 1$. If $f \ll 1$, both Bosons and Fermions exhibit Poisson noise. The effects of shot noise suppression may be significant

in quantum point contacts where T_n can be varied in wide range between $T_n \ll 1$ and $T_n \approx 1$. Suppression of shot noise in quantum point contacts was observed experimentally (Reznikov et al. 1995), (Kumar et al. 1996). The results were in good agreement with theoretical predictions once finite temperature was accounted for.

Application of the scattering formalism not only allowed calculation of the current fluctuations (shot noise), but also of the cross-correlations between currents through different leads in multiterminal geometries. The sign of the correlations depends on the quantum statistics of the current carriers.

In 1956, R. Hanbury Brown and R.Q. Twiss reported correlations in the intensities of two coherent beams of light (Hanbury Brown and Twiss 1956). The result was strange and unexpected; the existence of the effect was debated at the time. Analogous experiments were recently done with electrons (Liu et al. 1998), (Henny et al. 1999). As expected, because of the quantum statistics of electrons, the current-current cross-correlations in experiments with electrons were negative.

In physical systems with strong electron correlations, the effective charge of current carriers may be different from the charge of electron e . An example of such a system is a device in the fractional Hall quantum effect (FQHE) regime. At fractional filling factors $\nu = 1/(2m + 1)$ the current is carried by Laughlin quasiparticles, which have fractional charge $q_m = e/(2m + 1)$. If the tunneling is weak in the FQHE regime, the shot noise is expected to be equal to $S_I = 2q_m I$ (Kane and Fisher 1994). Experiments were performed at $\nu = 2/3, 1/3$ and $1/5$ (Saminadayar et al. 1997), (De-Picciotto et al. 1997), (Reznikov et al. 1999). The results of the experiments were in agreement with theory: shot noise was smaller than Poisson noise and was consistent with the expected fractional charge of Laughlin quasiparticles.

Another example of a system with the effective charge of current carriers different from e is a mesoscopic normal metal - superconductor (N-S) junction. At subgap energies, transport through such an N-S junction occurs via Andreev reflection, which is a correlated transfer of two electrons from a normal metal into a superconductor. Because of Andreev reflection, the effective charge of current carriers is expected to be $q_{eff} = 2e$. Theoretically, shot noise is expected to display a signature of effective charge $2e$. Experimentally, shot noise in N-S junctions was recently studied (Kozhevnikov et al. 2000b; Kozhevnikov et al. 2000; Jehl et al. 2000) and was found to

bear signatures of effective charge $2e$. In short S-N-S junctions multiple Andreev reflections are possible, and the effective charge may be even larger: $q_{eff} \approx 2Ne$, where N is the number of Andreev reflections. Increased noise in leaky S-N-S junctions with multiple Andreev reflections was observed (Dieleman et al. 1997). Measurements of shot noise in superconducting atomic-scale point contacts (Cron et al. 2001) show an increase of shot noise due to multiple Andreev reflections. In the following sections, shot noise in systems with Andreev reflection will be discussed in detail.

2.2 Shot noise

2.2.1 Shot noise as a manifestation of granularity of electrical charge

The fluctuations of an electrical current due to the discrete nature of the electron charge are referred to as shot noise. Shot noise was first reported by Schottky (Schottky 1918) for ideal vacuum diodes. Consider an electrical current consisting of a series of infinitely short pulses, completely uncorrelated with each other and each carrying a charge q , i.e.:

$$I(t) = q \sum_i \delta(t - t_i), \quad (2.7)$$

where t_i are randomly distributed and not correlated with each other. The power spectral density of such process, defined as:

$$S_I(\omega) = 2 \int_{-\infty}^{+\infty} \langle \Delta I(t) \Delta I(t + \tau) \rangle e^{i\omega\tau} d\tau \quad (2.8)$$

is frequency-independent and is directly proportional to the average current $\langle I(t) \rangle = I$ and the charge carried by each current pulse q :

$$S_I(\omega) = 2qI \quad (2.9)$$

In equation 2.8, $\Delta I(t) = I(t) - \langle I \rangle$ is a deviation of current from its expectation value ($\langle \dots \rangle$ denotes expectation value). For pulses of finite time duration, shot noise is frequency-independent up to the frequencies corresponding to the duration of a pulse and vanishes at much higher frequencies.

In devices exhibiting shot noise, measurement of shot noise can yield information about the

charge of current carriers q . The magnitude of the electron charge was measured using shot noise in a considerable number of experiments starting back from about 1925. The magnitude of the electron charge that was inferred from shot noise measurements was close to the value of e obtained by other methods. An undergraduate experiment is described which allows measurement of the electron charge by doing a shot noise measurement (Spiegel and Helmer 1995).

Under most circumstances measuring noise is not the best way to measure the charge of current carriers because measurements of noise are notoriously difficult. However, there are situations where shot noise is the instrument of choice for the measurements of q_{eff} .

2.2.2 Application of the scattering formalism to calculations of shot noise

Many theoretical results for shot noise can be very conveniently derived using the scattering formalism, also commonly referred to as Landauer - Büttiker formalism. The most commonly used model consists of two reservoirs either separated by a tunnel junction or by a disordered region having a transmission probability T_n . A particle impinging on a barrier from a reservoir has a probability T_n to tunnel into the other reservoir, and a probability of $1 - T_n$ to be reflected back. The average current through a tunnel junction between two normal metal reservoirs can be expressed through the electron distribution functions in the reservoirs:

$$\langle I(t) \rangle = \frac{2e}{h} T_n \int_{-\infty}^{+\infty} (f_L(E) - f_R(E)) dE, \quad (2.10)$$

where $f_L(E)$ and $f_R(E)$ are occupation numbers of quasiparticles as functions of energy in the left and right reservoirs, and transmission probability T_n is assumed to be independent of energy E . The factor of 2 arises from spin degeneracy. Note that the average current is related to the first moment of the distribution functions in the leads.

The fluctuations of current are related to the second moment of distribution functions. The general formula was derived by Büttiker (Büttiker 1992). For the case of zero frequency, the noise

current spectral density can be written as:

$$S_I = \frac{2e^2}{h} \int_{-\infty}^{+\infty} dE \{T_n [f_L(E)(1 - f_L(E)) + f_R(E)(1 - f_R(E))] + T_n(1 - T_n)(f_L(E) - f_R(E))^2\}. \quad (2.11)$$

This general formula is applicable both in equilibrium and in non-equilibrium situations. By taking appropriate limits, both equilibrium (Johnson-Nyquist) noise and non-equilibrium (shot) noise can be derived from 2.11. Equation 2.11 also describes the crossover between Johnson-Nyquist and shot noise.

Let us note the physical assumptions under which equation 2.11 is derived. The passage of electrons through the device has to be phase-coherent, and the electrons are assumed to be non-interacting, i.e., they must behave as independent quasiparticles. Interactions (for example, Coulomb interactions in devices with few quantum channels) may affect the non-equilibrium noise.

2.2.3 Effects of the finite transmission probability

Shot noise corresponds to the regime $eV \gg k_B T$. That is equivalent to assuming that the distribution functions are the step functions in equation 2.11. In this case, taking the Fermi level in the left reservoir to be zero, $f_L(E) = \theta(-E)$, $f_R(E) = \theta(-E - eV)$, where $\theta(x)$ is the Heavyside step function, and at all energies $f_L(1 - f_L) = f_R(1 - f_R) = 0$, so we get:

$$S_I = 2eI(1 - T_n). \quad (2.12)$$

In case of a small transmission probability, $T_n \ll 1$, equation 2.12 gives Poisson shot noise: $S_I = 2eI$. However, shot noise is always expected to be smaller than Poisson shot noise by a factor of $(1 - T_n)$. In case of very transparent interface, $T_n \approx 1$, shot noise vanishes. The suppression of shot noise as compared with full Poisson noise due to finite transmission probability was predicted before the general equation 2.11 was derived (Khlus 1987; Lesovik 1989).

2.2.4 Crossover from thermal noise to shot noise

Consider first the case of an opaque normal metal tunnel junction having $T_n \ll 1$. Neglecting the terms proportional to T_n^2 in equation 2.11, and taking $f_L(E) = f(E)$ and $f_R(E) = f(E - eV)$ where $f(x)$ is Fermi function and integrating, one obtains:

$$S_I = 2eV \frac{2e^2}{h} T_n \coth\left(\frac{eV}{2k_B T}\right) \quad (2.13)$$

Taking into account that the current is:

$$I = \frac{2e^2}{h} T_n V, \quad (2.14)$$

we can write noise current spectral density as

$$S_I = 2eVG \coth\left(\frac{eV}{2k_B T}\right) = S_I^{\text{Poisson}} \coth\left(\frac{eV}{2k_B T}\right), \quad (2.15)$$

where G is conductance (Pucel 1961).

For arbitrary transmission probability T_n and temperature T , the noise of a tunnel junction at low frequencies is given by the following expression (Büttiker 1992), (Martin and Landauer 1992):

$$S_I = 2 \frac{e^2}{h} \left[2k_B T T_n^2 + T_n(1 - T_n) eV \coth\left(\frac{eV}{2k_B T}\right) \right] \quad (2.16)$$

2.3 Non-equilibrium noise in diffusive conductors

In this section, we discuss in some detail theoretical results concerning non-equilibrium noise in diffusive conductors. By "non-equilibrium noise" we mean noise that occurs out of thermodynamic equilibrium, *i.e.*, at finite bias voltages. By "diffusive" we denote a device with elastic mean free path much smaller than the sample length, *i.e.* $\ell \ll L$. Non-equilibrium noise of a diffusive device depends on the ratio of sample length L to phase coherence length L_φ , to electron-electron energy relaxation length L_{ee} and electron-photon scattering length L_{e-ph} . In disordered metal films at low temperatures, typically $\ell \ll L_\varphi \lesssim L_{ee} \ll L_{e-ph}$.

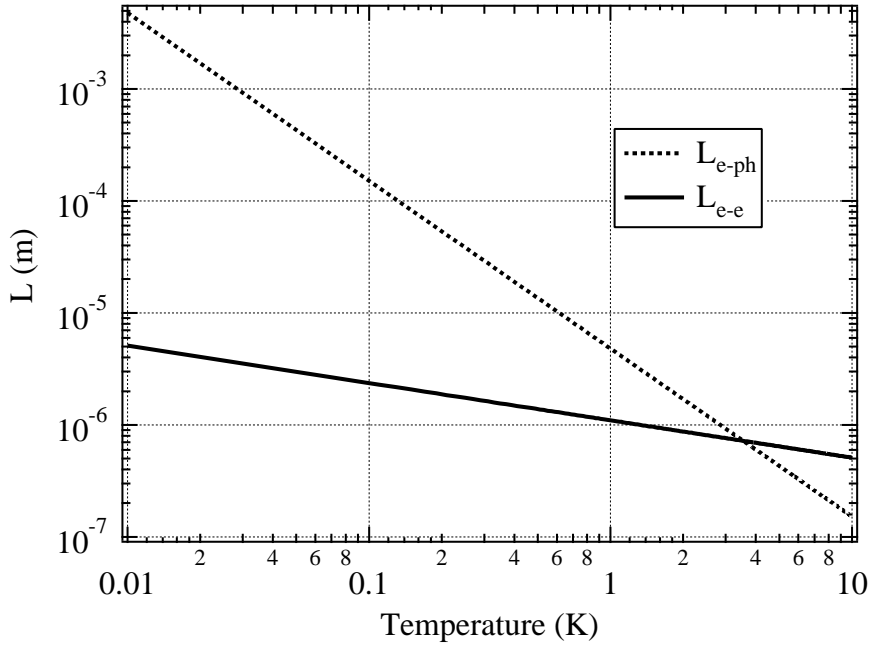


Figure 2.1: Theoretically expected phase-breaking and electron-phonon length vs. temperature for quasi-1D diffusive wire with diffusion constant $D = 30 \text{ cm}^2/\text{sec}$.

To illustrate typical length scales in disordered metal films, in figure 2.1 we plot the theoretically expected temperature dependence of electron-electron inelastic scattering length L_{ee} and electron-phonon length L_{e-ph} for disordered quasi-1D diffusive wire with diffusion constant $D = 30 \text{ cm}^2/\text{sec}$ and sheet resistance $R_{\square} \approx 10 \text{ } \Omega$. The electron-phonon length $L_{e-ph} = \sqrt{D\tau_{e-ph}}$. For Au thin films with $R_{\square} \sim 10 \text{ } \Omega$, the dependence of electron-phonon time on temperature is (Echternach et al. 1993): $\tau_{e-ph}^{-1} \approx 1.3 \times 10^8 T^3 \text{ s}^{-1}$. The quasi-1D electron-electron inelastic rate for disordered wire is shown to be (Altshuler et al. 1982), (Wind et al. 1986)

$$\tau_{ee}^{-1} = \left[\frac{R_{\square}}{\sqrt{2}(\hbar/e^2)} \left(\frac{k_B}{\hbar} \right) \frac{\sqrt{D}}{W} \right]^{2/3} T^{2/3}, \quad (2.17)$$

where D is diffusion constant, R_{\square} is sheet resistance, and W is the width of wire. For curves in figure 2.1, the width of the wire is assumed to be 100 nm. The film parameters (sheet resistance, diffusion constant and the width) correspond to the devices that we have studied experimentally.

If $L \ll L_\varphi$, electrons traverse the sample without losing phase coherence. This situation is similar to the tunneling of an electron across a barrier, and in this regime diffusive conductors exhibit shot noise. If $L_{ee} \ll L \ll L_{e-ph}$, there is a well-developed temperature profile in a sample. Energy can get out of the wire only by outdiffusion of hot electrons. In this regime, noise is determined by Johnson-Nyquist noise of the temperature profile developed in a wire. This is so-called "hot electron noise". If $L \ll L_{e-ph}$, electrons thermalize, and the energy is transferred from electron system to phonon system. Non-equilibrium noise is going to be determined by Johnson-Nyquist noise of the resulting temperature profile. The three cases: $L \ll L_\varphi$, $L_{ee} \ll L \ll L_{e-ph}$ and $L \gg L_{e-ph}$ are discussed in more detail in the next subsections.

From figure 2.1, we see that below $T \sim 4$ K the inelastic scattering is dominated by electron-electron interactions. At $T = 0.1$ K, the electron-electron inelastic length $L_{ee} \approx 2 \mu\text{m}$, so it is possible to fabricate a device with $L \ll L_{ee}$ using standard electron beam lithography techniques.

2.3.1 Influence of electron-phonon interactions on shot noise

The influence of electron-phonon scattering on shot noise was considered theoretically (Nagaev 1992), (Nagaev 1995). If $L \gg L_{e-ph}$, non-equilibrium noise is expected to be much smaller than shot noise. The temperature in the device will be determined by the balance of Joule power and the power transferred from electron system to phonons (except regions of length $\sim L_{e-ph}$ close to the reservoirs, where electron outdiffusion will be important). In disordered metal films, electron-phonon time τ_{e-ph} is difficult to calculate from first principles. Empirically, the electron-phonon time constant frequently has a power-law dependence on temperature (Belevtsev et al. 1998):

$$\tau_{e-ph}^{-1} = \alpha T^p, \quad (2.18)$$

where p depends on material, film resistivity and temperature range and is usually between 2 and 3. For example, in disordered Au films with sheet resistance $R_\square \approx 10 \Omega$, it was found (Echternach et al. 1993) that $\tau_{e-ph}^{-1} \approx 1.3 \times 10^8 T^3 \text{ s}^{-1}$. Assuming that phonons are at bath temperature, the heat balance equation will be:

$$\frac{V^2}{R} = \frac{\alpha \gamma N}{p+2} (T_e^{p+2} - T_{bath}^{p+2}), \quad (2.19)$$

where V is bias voltage, R is resistance, $\gamma = 0.73 \text{ mJ}/(\text{mol}\cdot\text{K}^2)$ is the proportionality constant between electron heat capacitance and temperature, and N is the number of moles in the sample. Solving for $T_e(V)$, we get:

$$T_e(V) = \left(T_{bath}^{p+2} + \frac{(p+2)V^2}{\alpha\gamma RN} \right)^{\frac{1}{p+2}}. \quad (2.20)$$

At large bias voltages the asymptotic behavior of $T_e(V)$ is sublinear:

$$T_e(V) \sim V^{\frac{2}{p+2}}. \quad (2.21)$$

Therefore, $S_I = 4k_B T_e(V)/R \ll 2eI$ - Johnson-Nyquist noise of a phonon-cooled device is going to be much smaller than shot noise. For $p = 3$ one will get: $S_I \sim V^{2/5}$ (Nagaev 1992). To summarize, if the length of a normal diffusive conductor is much smaller than electron-phonon length, the non-equilibrium noise is much smaller than shot noise.

2.3.2 Shot noise in diffusive mesoscopic conductors in the regime $L \ll L_e$

If the length of a diffusive metal wire is much smaller than the electron energy relaxation length, *i.e.* $L \ll L_e$, a diffusive metal wire can be thought of as a disordered electron waveguide. This "electron waveguide" has transmission modes with different transmission probabilities. For the purposes of calculation of conductance and noise, each transmitting mode can be considered as a tunnel junction with certain transmission probability. A diffusive normal wire can be thought as a parallel combination of tunnel junctions having different transmission probabilities. The distribution of transmission probabilities for a diffusive normal metal wire was calculated (Dorokhov 1984). For a wire of length L and total number of channels N the probability density for a channel to have a transmission probability T_n is:

$$\rho(T_n) = \frac{N\ell}{2L} \frac{1}{T_n \sqrt{1-T_n}}, \quad (2.22)$$

where ℓ is electron mean free path. It is assumed that the wire is not localized, *i.e.* $\ell \ll L \ll N\ell$. The distribution 2.22 has nonintegrable divergence near $T_n = 0$. Equation 2.22 is valid for $T_n \in [4e^{-2L/\ell}, 1]$. The distribution 2.22 has peaks near $T_n \sim 1$ and near $T_n \sim 0$. Channels having $T_n \approx 1$ will be noiseless. The noise is going to be due to channels having a transmission probability not too

close to 1. Summing the noise contributions of all channels gives:

$$S_I = 2eI \frac{\sum_n T_n(1 - T_n)}{\sum_n T_n} = 2eI \frac{\int_0^1 T_n(1 - T_n)\rho(T_n)dT_n}{\int_0^1 T_n\rho(T_n)dT_n} = \left(\frac{1}{3}\right) 2eI. \quad (2.23)$$

The integration in equation 2.23 can be taken from 0 to 1 because the integrand is nonsingular as $T_n \rightarrow 0$. The shot noise of a metallic diffusive wire with elastic transport is suppressed by a factor of 3 as compared to Poisson shot noise. Expression 2.23 for the shot noise in a diffusive metallic wire was derived by Beenakker and Büttiker (Beenakker and Buttiker 1992).

For finite temperatures the noise of a normal diffusive conductor can be obtained by summing equation 2.16 over transmission probability distribution. The result is

$$S_I = \frac{8}{3} k_B T G + \frac{2}{3} eV G \coth\left(\frac{eV}{2k_B T}\right). \quad (2.24)$$

Equation 2.24 reduces to Johnson-Nyquist noise at $eV \ll k_B T$ and becomes equation 2.23 for suppressed shot noise at $eV \gg k_B T$. The crossover from Johnson to shot noise is determined by the ratio $eV/(2k_B T)$.

The suppression factor of 3 for shot noise in a diffusive metallic wire was also derived by using the Boltzmann - Langevin approach (Nagaev 1992). The Boltzmann-Langevin approach can be used when phase coherence is not essential. It allows calculations of shot noise in multiterminal diffusive conductors, and it also allows taking inelastic (electron-electron and electron-phonon) scattering into account.

2.3.3 Hot-electron noise in diffusive conductors in the regime $L \gg L_e$

The problem of non-equilibrium noise in a diffusive wire longer than electron-electron inelastic length was considered theoretically (de Jong 1995; Nagaev 1995). If the length of the wire is much larger than the electron-electron relaxation length L_{ee} , but, at the same time, much smaller than the electron-phonon length L_{e-ph} , *i.e.* $L_{ee} \ll L \ll L_{e-ph}$, electrons exchange energy with each other and effectively thermalize. In this regime there is well-defined electron temperature profile $T_e(x)$ along the wire, but there is no energy exchange between the electron system and the photon bath. The only way for the energy to get out of the wire is by diffusion of hot electrons from the wire into

reservoirs. The noise of a diffusive wire in this physical regime will be due to Johnson noise of the wire with the temperature profile $T_e(x)$:

$$S_I = \frac{4k_B}{RL} \int_0^L T_e(x) dx = \frac{4k_B}{R} \langle T_e \rangle, \quad (2.25)$$

where $\langle T_e \rangle$ is the mean electron temperature in the wire. If a voltage V is applied across a wire of length L and with resistance R , the temperature profile in the wire in the absence of electron-phonon interactions can be shown to be (de Jong 1995):

$$T_e(x) = T_{bath} \sqrt{1 + \frac{x}{L} \left(1 - \frac{x}{L}\right) \frac{V^2}{T_{bath}^2 \mathcal{L}}}, \quad (2.26)$$

where T_{bath} is bath temperature. Using equations 2.25 and 2.26, the non-equilibrium noise due to the hot electrons can be calculated (de Jong 1995):

$$S_I(V) = \frac{2k_B T_{bath}}{R} + 2eI \left[\frac{2\pi}{\sqrt{3}} \left(\frac{k_B T_{bath}}{eV} \right)^2 + \frac{\sqrt{3}}{2\pi} \right] \arctan \left(\frac{\sqrt{3}}{2\pi} \frac{eV}{k_B T_{bath}} \right). \quad (2.27)$$

At large bias voltages ($eV \gg k_B T_{bath}$) the hot electron noise will increase linearly with bias current:

$$S_I \approx \frac{\sqrt{3}}{4} 2eI. \quad (2.28)$$

The dependence of the hot-electron noise on bias voltage is qualitatively similar to the suppressed shot noise in a diffusive mesoscopic conductor, but the Fano factor (defined as the ratio of observed noise to full Poisson shot noise $2eI$) is different. The Fano factor is 1/3 for "true" shot noise in a diffusive wire (*i.e.* when $L \ll L_e$), whereas for the "hot-electron noise" the Fano factor is $\sqrt{3}/4 = 0.43$. The experimental observations of hot-electron noise in diffusive metallic wires were reported (Steinbach et al. 1996). The results for wires longer than electron-electron length were in good agreement with theoretical predictions. Surprisingly, non-equilibrium noise in shorter wires, which were expected to be much shorter than L_{ee} , was observed to be intermediate between suppressed shot noise $(2/3)eI$ and hot-electron noise $(\sqrt{3}/4)eI$ (Steinbach et al. 1996).

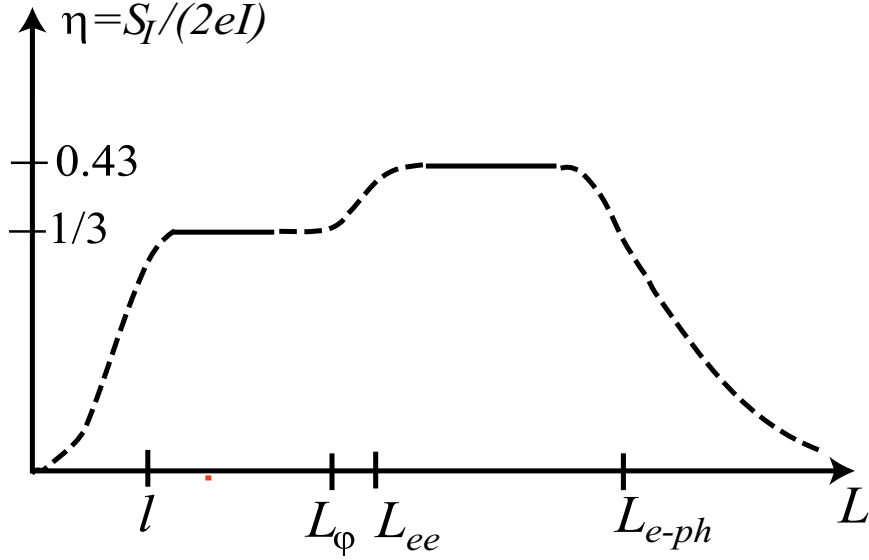


Figure 2.2: Dependence of Fano factor η on the length of a diffusive normal conductor (adapted from Steinbach et al 1996. Dashed lines are interpolations.

2.3.4 Summary of non-equilibrium noise in diffusive conductors: dependence of noise on the device length

To briefly summarize the theoretical predictions for non-equilibrium noise in normal diffusive conductors, in figure 2.2 the Fano factor η , defined as the ratio of current spectral density S_I to Poisson noise $2eI$, is plotted vs. wire length (figure 2.2 is adapted from the paper by Steinbach *et al.* (Steinbach et al. 1996)). For $L \lesssim \ell$, the sample is ballistic and shot noise is strongly suppressed as for a transparent quantum point contact. For the case $\ell \ll L \ll L_\phi$, shot noise is suppressed with $\eta = 1/3$. $L_{ee} \ll L \ll L_{e-ph}$ is the regime of hot-electron noise with $\eta = \sqrt{3}/4$. For $L \gg L_{e-ph}$, the noise is much smaller than Poisson (strictly speaking, in this case noise current spectral density is a sublinear function of voltage, so the Fano factor will be a function of bias voltage).

2.3.5 The role of non-ideal reservoirs and large bias voltages

Both the "true" shot noise result $S_I = (2/3)eI$ and the hot-electron noise $S_I^{h.el.} = (\sqrt{3}/4)eI$ are derived assuming ideal reservoirs, i.e., reservoirs with infinite electrical and thermal conductance. This assumption is implicit in the derivation of shot noise, because as the bias voltage across the

device is increased, the distribution function in the reservoirs is assumed to not be modified by heating of the reservoirs and by influx of "hot" electrons from the mesoscopic wire. The ideality of reservoirs is also important for the hot-electron noise because the boundary conditions for the distribution function are assumed to be a Fermi distribution with the base temperature. Heating of the reservoirs is also not taken into account.

In practice, however, all reservoirs have some finite electrical and thermal conductance. In a paper by Henny et al. (Henny et al. 1999), the possible influence of non-ideal reservoirs on $1/3$ shot noise suppression factor is investigated, both theoretically and experimentally. Most theoretical results of Henny et al. are rough estimates. A complete model should involve solving for the electron distribution function in the reservoirs, taking into account both inelastic electron-electron and electron-phonon scattering and would have to be solved numerically. Their simplified model predicts that the finite electrical conductance of the reservoirs can significantly affect the dependence of current spectral density on bias voltage $S_I(V)$. The main features of their model can be reproduced by the following argument. The model assuming ideal reservoirs predicts the following dependence of current spectral density on bias voltage:

$$S_I(V) = \frac{8}{3} k_B T_e G + \frac{2}{3} e V G \coth\left(\frac{eV}{2k_B T_e}\right), \quad (2.29)$$

where G is the conductance of the sample and $T_e = T_{bath}$ is electron temperature in the leads, which is equal to the bath temperature. The main effect of finite thermal conductance of the leads is that the electrons in the leads are heated up as the bias voltage is increased, so T_e is not a constant, but a function of V : $T_e = T_e(V)$.

For macroscopically large leads, the dependence of temperature on bias voltage can be approximated by the following expression:

$$T_e(V) = \sqrt{T_{bath}^2 + \beta^2 V^2}, \quad (2.30)$$

where β is a measure of thermal coupling between metallic leads and the thermal bath and is related to the geometry and to the thermal conductance of the leads. Equation 2.30 predicts quadratic dependence of temperature on bias voltage in the case of weak heating (i.e. when $\beta V \ll T_{bath}$),

and linear dependence in the case of strong heating (when $\beta V \gg T_{bath}$). Both types of behavior are easy to understand qualitatively. The thermal conductance of electron gas is a linear function of temperature. In the case of weak heating, the electron temperature change is small, so the thermal conductance is constant, and $\Delta T \approx V^2/(RG) \sim V^2$. If the heating is strong, the change in temperature is approximately equal to the temperature - $\Delta T \approx T$, and the thermal conductance is proportional to ΔT : $G \sim \Delta T$, so $\Delta T \sim V^2/G \sim V^2/\Delta T$. This yields $T \sim V$.

The estimate of β is made (Henny et al. 1999):

$$\beta = \sqrt{\frac{1}{\pi \mathcal{L}} \frac{R_{\square}}{R} \ln \frac{L_{e-ph}}{L_{ee}}}, \quad (2.31)$$

where \mathcal{L} is Lorenz number, R_{\square} is the sheet resistance of the leads, R is the resistance of the device, and L_{e-ph} and L_{ee} are electron-phonon and electron-electron inelastic lengths, respectively.

If $\beta V \gg k_B T_{bath}$, $T(V) \approx \beta V$. The measured shot noise, described by equation 2.29, except with T_{bath} replaced by the expression 2.30, will be given by:

$$S_I(V) = \frac{8}{3} k_B \beta V G + \frac{2}{3} e V G \coth \left(\frac{e}{2k_B \beta} \right). \quad (2.32)$$

In this case, the measured suppression factor will not be 1/3, as in the case of ideal reservoirs, but will be given by:

$$\frac{1}{2e} \frac{dS_I}{dI} = \frac{4}{3} \frac{k_B}{e} \beta + \frac{1}{3} \coth \left(\frac{e}{2k_B \beta} \right). \quad (2.33)$$

We can make an estimate of β for our devices. We have $R \approx 50 \Omega$, $R_{\square} \approx 0.5-1 \Omega$, and $\ln(l_{e-ph}/l_{e-e}) \sim 1$, so we can make an estimate of $\beta \approx 400$ K/V. The slope corresponding to this value of β is about 0.41. This lies between the shot noise value of 1/3 and the hot-electron noise value of $\sqrt{3}/4 = 0.43$, and it is closer to the slope corresponding to hot-electron noise.

The above estimate is done based on a naive model and should be regarded only as an "order of magnitude" estimate. However, it is sufficient to illustrate a very important point: non-ideal reservoirs may substantially affect the dependence of non-equilibrium noise vs. bias voltage.

Another important issue is the role of finite bias voltages. "True" shot noise is present when transport is elastic, i.e., when $L \ll L_e \approx \min[L_{ee}, L_{e-ph}]$. The theoretical expressions for L_{ee} and L_{e-ph} are derived for equilibrium distribution of quasiparticles at temperature T . In order to observe

shot noise, a bias voltage $V \gg k_B T$ has to be applied, and the distribution of quasiparticles is non-thermal. Application of large (compared to $k_B T/e$) bias voltages may reduce the electron energy relaxation length compared to the equilibrium distribution. Due to reduction of L_e , the device may not be in the regime of elastic transport when $eV \gg k_B T$.

Let us make a rough estimate of inelastic length reduction for our devices due to finite voltages. From equation 2.24, it can be shown, that in order for thermal effects to contribute less than 1 % to the slope of S_I vs. I , the ratio of voltage to temperature has to be: $eV/(2k_B T) > 4$. For a bath temperature of 0.1 K the voltage has to satisfy: $V > 8k_B T/e \approx 70 \mu\text{V}$. We assume that the inelastic length at $V = 70 \mu\text{V}$ is approximately equal to inelastic length at temperature $T = eV/k_B = 0.8 \text{ K}$. From figure 2.1 we get $L_e \approx 1.2 \mu\text{m}$. This is a factor of 4-5 larger than the length of our devices.

Using equation 2.30 and the estimate of β for our devices, we can estimate the temperature in the leads at bias voltage $V = 70 \mu\text{V}$. The estimate gives $T \approx 105 \text{ mK}$, so at this bias voltage an increase of lead temperature due to Joule heating is not appreciable. This means that bias voltages $\sim 70\text{-}100 \text{ m}\mu\text{V}$ should be appropriate for shot noise measurement, i.e., that at these voltages the device is substantially shorter than energy relaxation length and heating of the reservoirs is unimportant.

We also have to consider how much will the slope of S_I vs I change due to heating of the reservoirs. This is determined from the derivative dT_e/dV where $T_e(V)$ is given by equation 2.30. Using our estimate $\beta \approx 400 \text{ K/V}$, we get:

$$\left(\frac{dS_I}{dV}\right)_{leads} = \frac{4k_B}{R} \frac{dT_e}{dV} = \frac{\beta^2 V}{\sqrt{T_{bath}^2 + \beta^2 V^2}} \approx \frac{4k_B}{R} 100\text{K/V} \quad (2.34)$$

The ratio of this additional slope of S_I vs I to the "pure" shot noise $S_I = (2/3)eI$ is:

$$\left(\frac{\frac{dS_I}{dV}_{leads}}{\frac{dS_I}{dV}_{shotnoise}}\right) \approx \frac{10^2\text{K/V}}{1.9 \times 10^3\text{K/V}} \approx 0.05 \quad (2.35)$$

At these parameters, if our estimate is correct, the change in heating of the reservoirs contributes only 5 % of the contribution of "true" shot noise. Instead of "ideal" suppression factor of 1/3, one would measure the Fano factor of ~ 0.35 , and it should be possible to distinguish shot noise from hot electron noise by the slope of S_I vs V . This is a consequence of heating being "weak" in a sense that if β is small, there exists a range of bias voltages V such that $eV > 8k_B T_{bath}$ (thermal noise

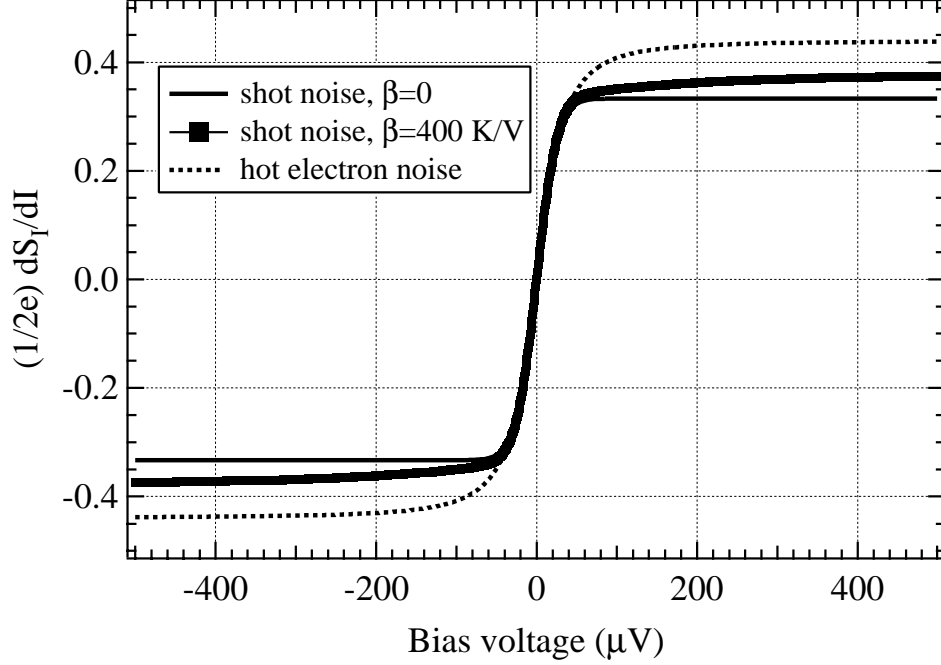


Figure 2.3: Predicted differential noise $(dS_I/dI)/(2e)$ vs. bias voltage for shot noise theory with ideal reservoirs, shot noise theory with finite thermal conductance of reservoirs and for hot-electron noise.

is unimportant, and shot noise can be measured accurately), and, at the same time, βV is small enough compared to T_{bath} so that heating of electrons in the leads is insignificant. One has to keep in mind that the above estimate is based on phenomenological equation 2.30 and on rough estimate of β .

To illustrate our analysis, in figure 2.3 we plot the predictions for differential noise $(dS_I/dI)/(2e)$ vs. bias voltage for 3 different cases. For $eV \gg k_B T$, the quantity $(dS_I/dI)/(2e)$ is equal to Fano factor. The solid line is a predictions of suppressed shot noise theory assuming ideal reservoirs. The dotted line is hot-electron noise. The markers are theoretical predictions for shot noise with $\beta = 400$ K/V. We see that with estimated value of β , the predicted shot noise should be closer to shot noise than to hot-electron noise.

2.4 Shot noise in the presence of high-frequency irradiation. Photon-assisted noise

In papers (Lesovik and Levitov 1994; Lesovik et al. 2000) the effect of the high-frequency radiation on shot noise of a tunnel junction was considered. The main result is that, in the presence of high-frequency irradiation of frequency ν , shot noise exhibits features at bias voltages $V = nh\nu/e$, where n is an integer number. The phenomenon is similar to photon-assisted tunneling (PAT) (Tien and Gordon 1963). The main effect of photon-assisted tunneling is that, in the presence of elastic transport, the non-linearities in the I-V curve are replicated at bias voltages offset by $nh\nu/e$ for irradiation of frequency ν . The magnitude of these features displays oscillatory behavior vs. rf power. In the presence of high-frequency ac bias voltage $V(t) = V_{ac}\cos(2\pi\nu t)$, the dependence of current on bias voltage $\tilde{I}(V)$ is:

$$\tilde{I}(V) = \sum_{n=-\infty}^{+\infty} J_n^2\left(\frac{eV_{ac}}{h\nu}\right) I\left(V + \frac{nh\nu}{e}\right), \quad (2.36)$$

where $I(V)$ is the I-V curve in the absence of ac excitation, and J_n is the n-th order Bessel function. A simplified explanation of equation 2.36 can be given. Suppose, an electron has energy E , so the time dependence of its state (in Schrödinger representation) is $|E(t)\rangle = |E_0\rangle e^{iEt/\hbar}$. In the presence of adiabatic time-varying potential $V(t) = V_{ac}\cos\omega t$ the time dependence of the wave function becomes (Tien and Gordon 1963):

$$|E(t)\rangle = |E_0\rangle e^{i(E_0t + \int eV_{ac}\cos\omega t dt)/\hbar} = \sum_{-\infty}^{+\infty} J_n\left(\frac{eV_{ac}}{\hbar\omega}\right) |E_0 + n\hbar\omega\rangle e^{i(E_0 + n\hbar\omega)t/\hbar}. \quad (2.37)$$

Due to the interaction with time-varying potential state $|E_0\rangle$, which had a well-defined energy it acquires additional "components" at energies $|E + n\hbar\omega\rangle$. These components are due to coherent absorption and reemission of photons from external field $V_0\cos\omega t$. If, in the absence of rf irradiation, the distribution function of electrons is a step function: $f(E) = \Theta(E_F - E)$, in the presence of

irradiation the distribution function will have "side-steps" offset from E_F by $n\hbar\omega$:

$$f(E) = \sum_{n=-\infty}^{+\infty} J_n^2 \left(\frac{eV_{ac}}{\hbar\omega} \right) \Theta(E_F - E - n\hbar\omega). \quad (2.38)$$

If the device has a non-linearity in the I-V curve, additional steps in the distribution function will lead to a replication of the non-linearity at energies offset by $n\hbar\omega$. Note the similarity between equation 2.38 and equation 2.36: the modification of the distribution function translates directly into modification of I-V curve. Note that the effect is crucially dependent on elastic transport in the device; the only allowed inelastic process is photon absorption from the external ac field and photon reemission. If other inelastic processes (electron-electron or electron-phonon scattering) are significant, the steps in the distribution function will be rounded, and no photon-assisted features will be observed.

For a normal tunnel junction or a mesoscopic diffusive conductor, the I-V curve is linear, so rf irradiation doesn't affect the I-V curve. However, while I-V curve is linear, shot noise has a non-linearity; at zero temperature it has a "corner" at $V = 0$. At finite temperature this "corner" is rounded on a voltage scale of a few $k_B T/e$. Under rf irradiation of frequency $\nu \gg k_B T/h$, this "corner" at zero bias voltage is expected to be replicated at bias voltages $V_n = nh\nu/e$. The result of work (Lesovik and Levitov 1994) can be written in a form, which resembles the result of PAT theory. In the presence of external high-frequency ac excitation, current spectral density $\tilde{S}_I(V)$ can be expressed as:

$$\tilde{S}_I(V) = \sum_{n=-\infty}^{+\infty} J_n^2 \left(\frac{eV_{ac}}{h\nu} \right) S_I \left(V + \frac{nh\nu}{e} \right), \quad (2.39)$$

where $S_I(V)$ is the current spectral density without rf applied. More explicitly, for a single-mode normal metal tunnel junction with transparency T_n , the shot noise in the presence of high-frequency excitation is:

$$\tilde{S}_I(V) = 4k_B T \frac{2e^2}{h} T_n^2 + \frac{2e^2}{h} T_n (1 - T_n) \sum_{n=-\infty}^{+\infty} J_n^2 \left(\frac{eV_{ac}}{h\nu} \right) 2(eV + nh\nu) \coth \left(\frac{eV + nh\nu}{2k_B T} \right) \quad (2.40)$$

For a diffusive normal metal wire, after summing over the transmission channels, the noise

becomes:

$$\tilde{S}_I(V) = \frac{8}{3}k_B T G + \frac{1}{3} \sum_{n=-\infty}^{+\infty} J_n^2 \left(\frac{eV_{ac}}{h\nu} \right) 2(eV + nh\nu) \coth \left(\frac{eV + nh\nu}{2k_B T} \right) \quad (2.41)$$

Equations 2.40 and 2.41 predict several features of shot noise under high-frequency rf excitation. The first and most important one is that the non-linearity in noise at $V = 0$ is expected to be replicated at bias voltages $V_n = nh\nu/e$. At zero temperature, the locations of these features are independent of the magnitude of ac bias V_{ac} . The features should be visible only if $h\nu \gg k_B T$. Otherwise, no features should be observed. Second, the magnitude of the feature at $V_n = nh\nu/e$ is expected to exhibit oscillatory behavior vs. rf power ($\sim J_n^2(\alpha)$, where $\alpha = eV_{ac}/(h\nu)$). An important property of these "photon-assisted" noise features is that they are visible only if the energy exchange with external high-frequency field $V(t) = V_{ac} \cos(\omega t)$ is the dominant inelastic mechanism. If other inelastic processes (i.e., electron-electron inelastic scattering or electron-phonon scattering) contribute significantly, there will be no well-defined steps in the quasiparticle distribution function, and the photon-assisted features will be "washed out". Photon-assisted noise features can be used as signatures of elastic transport in the device. Experimentally, photon-assisted noise was first observed in a normal diffusive conductor (Schoelkopf et al. 1998).

Let us summarize the theoretical predictions of photon-assisted noise in normal conductors. In the presence of high-frequency excitation, photon-assisted noise features are observed at characteristic voltages $nh\nu/e$; their magnitude displays oscillatory behavior vs. rf power. Observation of the effect can be used as a clear evidence of elastic transport in the device.

2.5 Andreev reflection and proximity effect on mesoscopic scale

In this section, we give a brief introduction in the theory of Andreev reflection and the proximity effect. By the term "proximity effect" we denote propagation of superconducting correlations into the normal metal (and vice versa). Andreev reflection is the process of conversion of quasiparticles in a normal metal into Cooper pairs in a superconductor across the N-S boundary. The time-reversed process describes the propagation of superconducting correlations into a normal metal.

Microscopically, Andreev reflection is the process that couples quasiparticles in normal metal and Cooper pairs in the superconductor and thus realizes the proximity effect. In the literature, the term "Andreev reflection" is more commonly applied to describe propagation of superconducting correlations into a normal metal for ballistic devices, whereas the term "proximity effect" is more commonly applied to diffusive systems. In this section the basic mechanism of Andreev reflection is illustrated in case of a ballistic N-S junction. After that we discuss a theoretical description of the proximity effect in diffusive N-S devices. In the case of weak superconductivity ($T \approx T_C$), the proximity effect in a diffusive system can be described using Ginzburg-Landau (GL) theory. At $T \ll T_C$, GL description is not accurate, and more elaborate formalism which is based on Green functions must be applied.

2.5.1 Andreev reflection

Tunneling in normal metal - insulator - superconductor (NIS) tunnel junctions has been used as an instrument to probe the density of states in the superconductor. The current can be expressed as the first moment of the quasiparticle distribution functions in the leads convolved with the product of densities of states in the normal metal and in the superconductor:

$$I_{NS}(V) = A \int_{-\infty}^{+\infty} N_1(E)N_2(E)[f(E) - f(e + eV)]dE, \quad (2.42)$$

where A is a constant proportional to the area of the junction and the transparency of the N-S interface, $f(E)$ is the Fermi function, $N_1(E)$ is the density of states in normal metal, and $N_2(E)$ is density of states in a superconductor. Zero energy is considered to coincide with the chemical potential in a superconductor. Equation 2.42 is effectively a result of application of the scattering approach, although it was used earlier by Giavar for the description of tunneling in N-I-S junctions. At energies $E - E_F \ll E_F$ the density of states in normal metal is constant: $N_1(E) \approx \text{const}$. The density of states in the superconductor is given by the BCS expression (Tinkham 1995):

$$N_2(E) = \text{Re} \left[\frac{N_n}{\sqrt{E^2 - \Delta^2}} \right], \quad (2.43)$$

where N_n is the density of states in the normal state of superconductor, and Δ is the superconducting energy gap. It follows from equations 2.42 and 2.43 that at $T = 0$ there is no current at bias voltages $V < \Delta/e$. At finite temperatures the conductance of an N-S tunnel junction is exponentially suppressed at bias voltages $eV \ll \Delta$ as compared to the normal state conductance of the tunnel junction.

N-S junctions exhibit the behavior described above if the N-S interface is opaque, *i.e.*, if the transparency of the N-I-S interface is much smaller than unity: $T_n \ll 1$. In this regime, the only allowed transport process is single quasiparticle tunneling. If the interface is transparent, *i.e.* $T_n \sim 1$, a different process becomes possible. This process is Andreev reflection. It is a correlated transfer of 2 electrons from the normal metal into the superconductor, where they form a Cooper pair. Andreev reflection was first discussed in relation with heat conductance of a mixed state of the superconductor (Andreev 1964). Andreev reflection is a 2-particle process, so its contribution to the conductance is appreciable only for transparent N-S interfaces.

A process of Andreev reflection can be regarded as electron being "reflected" off an N-S boundary as a hole. When two electrons enter a superconductor and form a Cooper pair, the energy of one of them is above the chemical potential of the superconductor, and the energy of the other electron is below the chemical potential in the superconductor. When the electrons enter the superconductor, the electron with lower initial energy leaves an unoccupied state (hole) behind.

The first systematic theoretical description of Andreev reflection in ballistic N-S junctions was done in 1982 (Blonder et al. 1982). Using Bogolubov - de Gennes equations, the dependence of the probability of Andreev reflection on energy and disorder at the N-S boundary was calculated. From the probability of Andreev reflection, the I-V curves of N-S junctions were calculated. BTK theory predicted that, for a very transparent interface, the conductance is doubled compared to the normal state conductance of the tunnel junction. This conductance doubling is due to the fact that 2 electrons are transferred from the normal metal into the superconductor per each attempt. This behavior is in sharp contrast with "conventional" opaque N-S tunnel junctions where the conductance at $eV < \Delta$ is exponentially suppressed at $k_B T \ll \Delta$. An increased subgap conductance due to Andreev reflection leads to excess current - the I-V curve at high bias voltages does not extrapolate back to zero. Figure 2.4 schematically illustrates the difference in transport mechanisms

for opaque and transparent N-S junctions and the difference in the I-V curves for opaque and transparent N-S junctions. The dashed lines passing through the origin are the normal state I-V curves of the junctions.

Increased subgap conductance and excess currents were reported experimentally for transparent N-S junctions. Increased subgap conductance was observed in a nanosized contact between a normal metal and a superconductor (nanopore) (Upadhyay et al. 1998). Doubled subgap conductance, which corresponds to a very transparent N-S interface ($T_n \approx 1$), was observed in a Nb-Cu point contact (Soulen et al. 1999), (Strijkers et al. 2001).

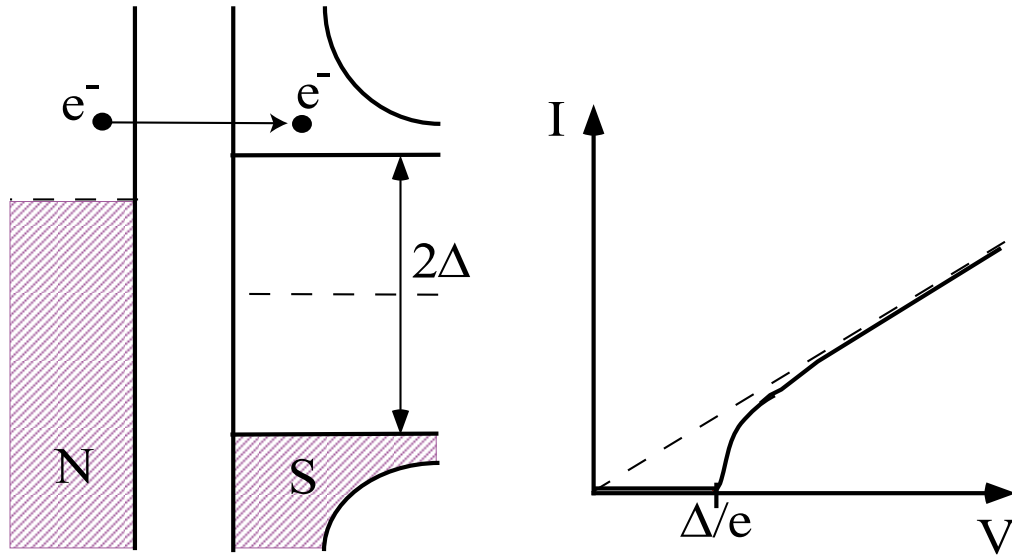
The BTK description of the process of Andreev reflection which is based on Bogolubov - de Gennes (de Gennes 1966) equations is natural to use when there is no disorder in the leads. In the presence of disorder (for example, when either the normal metal lead or the superconductor is diffusive) the application of Bogolubov - de Gennes equations becomes difficult. If the leads are diffusive, one cannot use plane waves as in- and outgoing states. Also, a quasiparticle can undergo a process of multiple Andreev reflections, because it can "hit" the N-S boundary many times during its diffusive motion in a normal metal. In the following subsection, we discuss Andreev reflection and proximity effect in diffusive systems.

The description of proximity effect on mesoscopic scale is based on Green's functions in Nambu space. The mathematical formalism of Green function is cumbersome. Therefore, in this thesis, a bare minimum of mesoscopic proximity effect theory is given, only that which is necessary to understand the behavior of our devices. A detailed and understandable description of theory of mesoscopic proximity effect can be found in S. Gueron's thesis (Gueron 1997). There is also a recent review of theoretical and experimental work (Esteve et al. 1997).

2.5.2 Propagation of the superconducting correlations into a diffusive normal wire. Usadel equation

A simple treatment of the proximity effect in a diffusive system when superconductivity is weak can be done using Ginzburg - Landau (GL) theory. It has been shown (Deutscher and de Gennes 1969), that if a normal metal is in contact with a superconductor, the order parameter $\varphi(x)$ in normal

(a) $T_n \ll 1$ - single-particle tunneling



(b) $T_n \sim 1$ - Andreev reflection

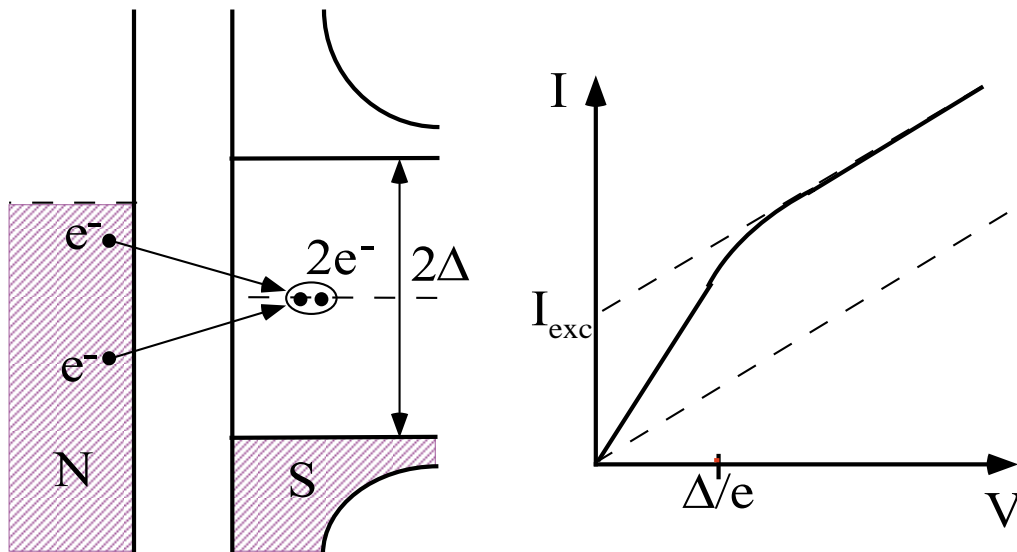


Figure 2.4: a. Single-particle tunneling in an opaque N-S junction and its I-V curve at zero temperature; b. Andreev reflection in transparent tunnel junction and an I-V curve in case of unity transparency (adapted from Blonder et al. 1982).

metal will decay with the distance from the superconductor:

$$\varphi(x) \sim \exp(-x/\xi) \quad (2.44)$$

where $\xi = \sqrt{\hbar D / (2\pi k_B T)}$ is the coherence length in the normal metal (also called thermal length). A simple way to illustrate that $\xi \sim \sqrt{D/T}$ is to consider a time-reversed Andreev process, where a Cooper pair "splits" into 2 electrons which enter the normal metal. The relative phase difference of the wave functions of these 2 electrons will not change appreciably over time $\tau \sim \hbar/\Delta E$, where ΔE is the energy difference of 2 electrons. At temperature T : $\Delta E \sim k_B T$, so $\tau \sim \hbar/(k_B T)$. In the diffusive regime during time τ the electrons will travel a characteristic distance $L_0 \sim \sqrt{D\tau} \sim \sqrt{\hbar D / (k_B T)}$. This distance L_0 gives a characteristic length over which 2 electrons retain coherence relative to each other, *i.e.* the length scale for propagation of superconducting correlations into a diffusive normal metal. The thermal length ξ sets a length scale over which electrons retain *relative phase coherence*. This is different from the phase-breaking length L_φ which sets a length scale over which an electron has definite phase relation with itself.

The GL description of the proximity effect by a single order parameter is simplified and cannot be applied if superconductivity is strong. It can be illustrated by noting that the decay length is a function of the energy difference of electrons ΔE , and so the propagation of superconducting correlations into a normal metal is energy-dependent. An equation describing the propagation of superconducting correlations in a diffusive normal metal was derived by Usadel (Usadel 1970). The Usadel equation describes the propagation of superconducting correlations in terms of 2 energy-dependent parameters. One parameter φ is similar to the phase of the GL order parameter. The other parameter - the so-called pairing angle θ is, in general, a complex quantity characterizing the strength of the superconductivity. For a normal metal reservoir, $\theta = 0$, while for a superconducting reservoir at energies $E \ll \Delta$, $\theta = \pi/2$.

The cosine and sine of the pairing angle θ can be loosely interpreted as being related to the densities of "unpaired" and "paired" electrons, respectively, at least at small energies. One could think of "unpaired" electron density $\rho_N \sim \cos^2\theta$ and the "paired" electron density $\rho_S \sim \sin^2\theta$. For a BCS superconductor, that will give $\rho_N = 0$, as expected. In case of weak superconductivity ($\theta \ll 1$), one would get $\rho_S \sim \theta^2$. This will correspond to GL regime, and in this case θ will be equal to the

magnitude of GL order parameter.

Both quantities - θ and φ are parametrizations of the advanced and retarded Green's functions in Nambu space. Once the energy and spatial dependence of $\theta(x, E)$ and $\varphi(x, E)$ are known, the advanced and retarded Green's functions and, hence, the equilibrium properties of the system can be determined.

In a diffusive system, the advanced and retarded Green functions obey diffusion-like equations. Consider a simple case of a normal wire of constant cross-section in contact with one superconducting reservoir. In this case, there is no gradient of the superconducting phase φ , (φ is indetermined in a normal reservoir), and we can take $\varphi = 0$. The Usadel equation in this case becomes:

$$\frac{\hbar D}{2} \frac{\partial^2 \theta(x, E)}{\partial x^2} + \left[iE - \frac{\hbar}{\tau_{sf}} \cos \theta(x, E) \right] \sin \theta(x, E) + \Delta(x) \cos \theta(x, E) = 0. \quad (2.45)$$

E is the energy with respect to the chemical potential in a superconductor, D is the quasiparticle diffusion constant, τ_{sf} is a spin-flip time, and $\Delta(x)$ is a gap parameter.

The first term in equation 2.45 describes a diffusive propagation of the superconducting correlations. The term, containing the spin-flip time τ_{sf} , describes the decay of superconducting correlations due to spin-flip processes and will tend to decrease $|\theta(x, E)|$. The third term describes the pairing of electrons in a superconductor, and $\theta(x, E)$ will tend to approach $\pi/2$ due to this term.

In the normal metal, $\Delta(x) = 0$, while in the superconductor $\Delta(x)$ has to be found self-consistently. The condition $\Delta(x) = 0$ greatly simplifies the solution of the Usadel equation in the normal metal. We are primarily interested in the conductance. Once $\theta(x, E)$ is obtained by solving Usadel equation, the differential resistance of the normal wire is calculated according to the formula:

$$R_{diff}(E) = \frac{dV}{dI}(E) = \frac{R_N}{L} \int_0^L \frac{dx}{\cosh^2 [\text{Im } \theta(x, E)]} \quad (2.46)$$

The problem of describing of transport in diffusive N-S devices is solved using the Usadel equation to find the pairing angle and then using the solution of the Usadel equation to determine the differential conductance.

2.5.3 Diffusive normal metal - superconductor junctions

As an example of the application of the Usadel equation, we consider transport in a diffusive N-S junction - a normal metal wire of length L in contact with normal reservoir on one end and a superconducting reservoir on the other end. We assume that the N-S boundary is at $x = 0$. We consider the boundary condition on the N-S boundary to be given by a BCS pairing angle at energies much smaller than the gap of the superconductor Δ : $\theta(x = 0) = \pi/2$.

First, consider the case $L \rightarrow \infty$, $\tau_{sf} \rightarrow \infty$. In this case equation 2.46 can be solved analytically (Volkov et al. 1993):

$$\theta(x, E) = 4\arctan \left[\left(\sqrt{2} - 1 \right) \exp \left((i - 1) \sqrt{\frac{Ex^2}{\hbar D}} \right) \right]. \quad (2.47)$$

At large distances from N-S boundary, *i.e.* when $x \gg \sqrt{\hbar D/E}$ the pairing angle is small and decays exponentially: $|\theta(x, E)| \sim \exp(-x/\sqrt{\hbar D/E})$ - that is the GL regime. At energy E , superconductivity penetrates a distance $L \sim \sqrt{\hbar D/E}$ into diffusive normal metal. Of course, at small energies the penetration of superconductivity is limited by spin-flip processes.

For the normal wire of finite length L in contact with a superconducting reservoir, the Usadel equation has to be solved numerically. The boundary conditions are $\theta(0, E) = \pi/2$ (superconducting reservoir) and $\theta(L, E) = 0$ (normal reservoir). It is easier to use a variational method than to solve a boundary value problem of a non-linear differential equation directly. The Usadel equation is a Lagrange-Euler equation of an effective action functional given by (Gueron 1997):

$$U[\theta(x, E)] = n_0 \int \left[\frac{\hbar D}{4} \left(\frac{\partial \theta}{\partial x} \right)^2 + iE \cos \theta + \frac{\hbar}{\tau_{sf}} \frac{\sin^2 \theta}{2} - \Delta(x) \sin \theta \right] dV \quad (2.48)$$

The integration in equation 2.48 is over the volume of the sample. In our numerical solution, we neglect spin-flip scattering. At zero energy the solution is a straight line: $\theta(x) = (\pi/2)(1 - x/L)$. At finite energies the solution is obtained numerically by a gradient method. The iterative procedure converges to a function $\theta(x, E)$, for which $\delta U[\theta(x, E)] = 0$. After finding the solution of the Usadel equation, differential resistance is calculated using equation 2.46. The results of our calculation for a diffusive N-S junction are presented in figure 2.5.

The Usadel equation was numerically solved for a diffusive N-S junction (Stoof and Nazarov 1996), (Nazarov and Stoof 1996). It was predicted, that the conductance of a diffusive N-S junction would exhibit reentrant behavior vs. bias voltage, and zero-bias conductance would display reentrant behavior vs. temperature. Reentrant behavior of zero-bias conductance vs. temperature is, of course, a consequence of reentrant behavior of conductance vs. energy. At finite temperatures, a window of energies of order $k_B T$ is "sampled" by the device, and the conductance is given by a convolution of zero-energy conductance with the thermal kernel:

$$G(V, T) = e \int_{-\infty}^{+\infty} G(V + V') \frac{1}{4k_B T \cosh^2(eV'/2k_B T)} dV' \quad (2.49)$$

Equation 2.49 can be derived by differentiating equation 2.42, and the thermal kernel is just a derivative of the Fermi function. Surprisingly, the differential resistance of a diffusive N-S junction at zero energy is exactly equal to the normal state resistance of the wire.

Figure 2.5 presents the energy dependence of the differential resistance of a diffusive N-S junction. The differential resistance is normalized by the normal-state resistance R_N . The energy is in units of the Thouless energy $E_C = \hbar D/L^2$. At small energies ($E \ll E_C$) the differential resistance is equal to the normal state resistance of the wire. This is a numerical coincidence. The density of states is suppressed in a normal wire at $E \lesssim E_C$, but the effective diffusion constant is enhanced (loosely speaking, "paired" electrons diffuse faster). These two effects turn out to exactly cancel each other at $E = 0$. At high energies the normal-state resistance is recovered. This can be understood by noting that at $E \gg E_C$ only a small fraction of wire's length is going to be proximitized. This small fraction $\Delta L \sim \sqrt{\hbar D/E}$ is going to be superconducting, so the change in resistance is going to be $\Delta R \sim 1/\sqrt{E}$ at $E \gg E_C$. The differential resistance exhibits a minimum at $E \approx 5E_C$. The maximal change of resistance is about $0.12R_N$. This result is obtained assuming a perfect interface between a diffusive normal wire and a superconducting reservoir.

The reentrant behavior of resistance of a diffusive N-S junction vs. bias voltage and temperature has been experimentally observed (Charlat et al. 1996), although the magnitude of the effect was much smaller than what would be expected from an "ideal" N-S junction. Subsequently, reentrant behavior was observed both in metallic diffusive N-S structures (Courtois et al. 1999), (Petrashov

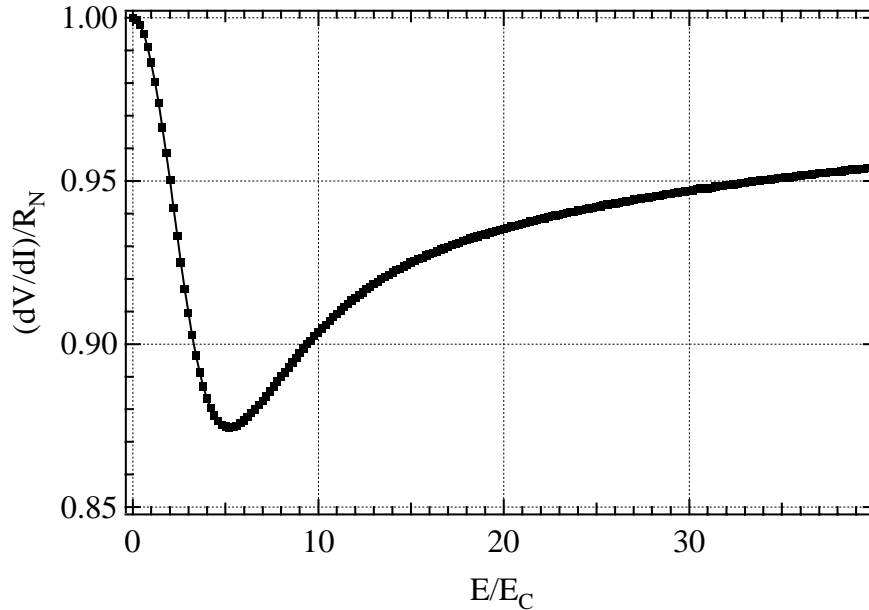


Figure 2.5: Energy dependence of normalized differential resistance of a diffusive N-S junction.

et al. 1998) and in disordered semiconductor - superconductor junctions (den Hartog et al. 1997). The agreement between the theory and the experiment is usually semiquantitative, likely due to heating of the reservoirs.

The density of states in a normal metal wire in contact with a superconducting reservoir was experimentally investigated using tunnel spectroscopy (Gueron et al. 1996). The results were in quantitative agreement with the predictions of the Usadel equation. The work (Gueron et al. 1996) is one of the few experiments in mesoscopic superconductivity where quantitative agreement between theory and experiment is achieved for a diffusive device.

2.5.4 Andreev interferometers

We have seen that the propagation of superconducting correlations into the normal metal can be described by two parameters - pairing angle $\theta(x, E)$, which is, in general, a function of energy and position and the phase of the superconductor $\varphi(x)$. If there is only one superconducting reservoir and no magnetic field, $\varphi = \text{const.}$ the Usadel equations are invariant with respect to change of $\varphi(x)$ by a constant. This means that, without loss of generality, we can assume $\varphi = 0$. However, if

there is more than one superconducting reservoir with a definite phase relation between them, the physical properties of the system may depend on the phase differences between the superconducting reservoirs. These phase differences may be tuned by application of a weak external magnetic field or by changing the current through an array of Josephson junctions.

There is a class of geometries of hybrid N-S devices in which the conductance of the structure is phase-sensitive. They are generically called "Andreev interferometers", because the origin of this phase sensitivity is phase-conjugation of an electron and an Andreev-reflected hole, by means of which information about the phase of the superconductor is conveyed in the normal metal.

One of the first observations was a dramatic increase of the magnitude of Aharonov-Bohm oscillations in metal rings connected to superconducting "mirror" reservoirs (Petrashov et al. 1993). In several works published shortly thereafter, phase-sensitive transport was studied in true "interferometer" geometries where phase difference between superconducting reservoirs was modulated by either external magnetic flux (Pothier et al. 1994), (Dimoulas et al. 1995), (Petrashov et al. 1995) or by changing the current through the array of Josephson junctions (de Vegvar et al. 1994).

In diffusive Andreev interferometers studied experimentally (Petrashov et al. 1995), the magnitude of conductance oscillations was $\sim 100 e^2/h$, two orders of magnitude larger than the expected Aharonov-Bohm oscillations amplitude for a normal diffusive ring. The period of the oscillations corresponded to a changing magnetic flux through the superconducting ring by a flux quantum $h/(2e)$. At first, it was thought that such a large conductance modulation could not be explained within conventional theory of the mesoscopic proximity effect.

The nature of this large, phase-sensitive modulation of conductance of diffusive Andreev interferometer was studied theoretically (Nazarov and Stoof 1996). The equation for energy dependence of Green functions was solved and the conductance of the structure was calculated. Theory predicted $h/(2e)$ -periodic conductance modulation of the structure with magnitude $\Delta G \approx 0.1G$, which was in good agreement with experiments (Petrashov et al. 1995).

The nature of the effect can be understood qualitatively. For example, consider a device measured in the work of Petrashov *et al.* (Petrashov et al. 1995) - see figure 2.6. The conductance is measured between normal reservoirs (denoted as "N" in figure 2.6). The superconducting loop contacts the ends of a normal "cross". The section of superconductor on top of normal reservoirs

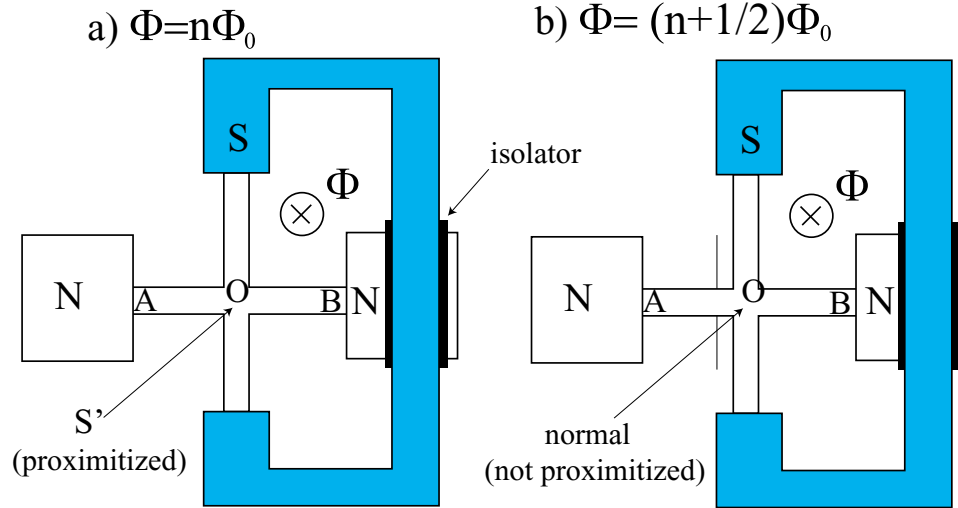


Figure 2.6: Schematic of device from (Petrashov et al. 1995) at integer and semiinteger external magnetic flux.

is isolated from the normal reservoir wire. When the external magnetic flux satisfies the condition $\Phi = n\Phi_0$, the phases of two superconducting terminals differ by $2n\pi$, and superconducting correlations induced in the center of the normal wire (point O) by each of the superconducting terminals interfere constructively. In this case point O is going to be proximitized most, and the conductance of the normal wire measured from A to B will be enhanced.

On the other hand, when $\Phi = (n + 1/2)\Phi_0$, the superconducting correlations induced by two superconducting terminals interfere destructively, and the resulting order parameter in the center of the cross is zero - the wire across the measurement path is not proximitized, and the conductance should be equal to the conductance of the normal wire. By changing the external magnetic field, the phase difference between the ends of superconducting loop may be continuously tuned. The conductance of the structure will be periodically modulated by the external magnetic field.

The conductance of a diffusive Andreev interferometer can be calculated from a numerical solution of the Usadel equation, but the necessity of dealing with 2 variables - ϑ and φ , as well as having multiple segments and having to solve the Usadel equation in each of them separately and then matching the solutions makes numerical modeling of these structures complicated. The phase

modulation of the conductance of an Andreev interferometer was numerically calculated using a linearized Usadel equation and a model of a normal metal ring in series with the normal wire as two independent N-S circuits in series (Charlat et al. 1996). The linearized Usadel equation is applicable when superconductivity is weak, i.e., either when there is a tunnel barrier between a normal metal and a superconductor or when the distance to the superconductor exceeds ξ .

Transport in diffusive Andreev interferometers using the complete Usadel equation was studied theoretically (Nazarov and Stoof 1996), (Stoof and Nazarov 1996), (Golubov et al. 1997). Experimental studies of reentrant behavior and thermopower in Andreev interferometers were recently reported (Eom et al. 1998), (Eom et al. 1999).

2.5.5 Definition of a "clean interface" applied to diffusive systems

Many of the above results for diffusive N-S junctions (reentrant behavior of differential resistance, for example) are derived under two assumptions. First, the contact between normal metal and superconductor is assumed to be perfectly transparent, i.e., there is no tunnel barrier between normal wire and superconducting reservoir. Second, the solution of the Usadel equation is greatly simplified if one assumes BCS boundary conditions on the boundary between a normal metal wire and a superconducting contact. This way the Usadel equation has to be solved only in the normal wire, and the superconducting contact is assumed to be a BCS superconductor, i.e., reverse proximity of the superconductor by a normal metal is neglected. We need to discuss whether these approximations are applicable to our devices.

The assumption that the interface between the normal metal and the superconductor is clean means that the pairing angle is continuous across the N-S boundary. We assume that there is only one superconducting reservoir so that the phase of the superconductor φ can be taken equal to 0. It was derived in (Yip 1995), that in the presence of a tunnel barrier the boundary condition for the pairing angle θ on the N-S boundary (at $x = 0$) becomes:

$$\sigma_{N,S} \left(\frac{d\theta_{N,S}}{dx} \right)_{x=0} = (AR_T)^{-1} \sin(\theta_S(0, E) - \theta_N(0, E)). \quad (2.50)$$

In equation 2.50, σ_N and σ_S are the normal-state conductivities of a normal metal and of a super-

conductor, and $\theta_S(0, E)$ and $\theta_N(0, E)$ are pairing angles at the N-S boundary in the superconductor and normal metal, respectively. R_T is the normal-state resistance of the tunnel junction at the N-S boundary and A is the area of the junction.

If $R_T \rightarrow 0$, the pairing angle is continuous across N-S boundary: $\theta_S(0, E) = \theta_N(0, E)$. If the jump of the pairing angle across the boundary is not too large, we can make an estimate $d\theta_N/dx \sim \theta_S(x=0)/L \sim \pi/(2L)$, where L is the length of the normal wire. The above estimate merely states that the gradient of the pairing angle at the boundary is roughly equal to the maximal angle divided by the length of the wire. Substituting this into equation 2.50, we get:

$$\frac{\sigma_{N,S} A R_T \pi}{2L} = \frac{\pi R_T}{2R_N} \sim \sin(\theta_S(0, E) - \theta_N(0, E)), \quad (2.51)$$

where R_N is the resistance of the normal wire. From the estimate 2.51, it is evident that as long as the resistance of the tunnel junction is much smaller than the resistance of the normal wire, i.e., $R_T \ll R_N$, the drop of the pairing angle across the N-S boundary is small, and a perfectly transparent interface theory can be used to good accuracy. Thus, for a diffusive N-S junction, it is only the ratio of the tunnel junction and the normal metal wire resistances that determines whether the N-S interface is transparent. The absolute value of the transmission probability from N into S is not important, so even when the tunnel junction is "opaque", i.e. $T_n \ll 1$, the diffusive N-S junction will still be in the regime of a transparent interface if the condition $R_T \ll R_N$ is satisfied. This influence of barrier transparency on the conductance of the N-S structure was studied numerically (Courtois et al. 1999). If the ratio $R_T/R_N < 0.1$, the dependence of differential resistance vs. bias voltage is in good agreement with the model assuming a perfect interface ($R_T = 0$). For $R_T/R_N \sim 0.2$, the reentrant behavior is still preserved, although the minimum of R_{diff} is shifted to lower energies. For high values of R_T/R_N , the minimum in differential resistance is shifted to zero energy - in this regime the reentrant behavior is not observed, but zero-bias anomalies are observed.

We cannot directly measure the resistance of the interface between the normal metal and the superconductor. We try to make the interface as transparent as possible - we clean the surface of Au with an Ar ion bombardment just prior to a Nb deposition to get rid of possible remnants of resist processing. We can make an estimate of the interface resistance by comparing the resistance of the Au wire before and after the Nb deposition. Before the Nb deposition, the resistance of the device

is dominated by a $1\mu\text{m}$ - long Au wire. After the deposition, the resistance decreases due to the wider and thicker Nb film covering part of the wire. Knowing the Au wire resistivity and Nb film resistivity, we can estimate the resistance of the interface. We estimate the interface resistance not to exceed $5\ \Omega$, which is small compared to the typical resistance of the devices ($\sim 40 - 50\ \Omega$), so our devices are expected to be close to the physical regime of a transparent N-S interface. Observation of reentrant behavior at cryogenic temperatures supports the claim that our devices are in the regime of a transparent N-S interface.

Let us discuss the second approximation - a BCS pairing angle on the N-S boundary. Consider two quasi-1D diffusive wires, a normal metal wire with a cross-sectional area A_N and a superconducting wire with a cross-sectional area A_S , that are in contact with each other. For a transparent N-S interface, the boundary condition for the pairing angle at the interface becomes (Yip 1995):

$$\sigma_N A_N \frac{\partial \theta_N}{\partial x} = \sigma_S A_S \frac{\partial \theta_S}{\partial x}. \quad (2.52)$$

The problem of calculating the pairing angle at the N-S boundary was considered in (Gueron 1997). For a transparent N-S interface and for $A_N = A_S$, it has been shown that at energies $E \ll \Delta$, the pairing angle at an N-S boundary is close to a BCS value $\pi/2$. The analysis (Gueron 1997) did not take into account the spatial dependence of the superconducting gap $\Delta(x)$ near the N-S boundary. It is applicable in a normal metal and in a superconductor at a distance larger than certain distance L_Δ over which the BCS gap is recovered. It has been shown (Belzig and Bruder 1996) that the BCS gap is recovered at distances about $L_\Delta = \sqrt{\hbar D / \Delta}$ from the N-S interface. For our devices, $D_{Nb} \approx 15\ \text{cm}^2/\text{sec}$ and $L_\Delta \approx 25\ \text{nm}$. Moreover, the Nb film is much thicker than the Au wire, and the cross-sectional area of the Nb contact increases with the distance from the N-S boundary. This will make the superconductor become BCS-like over even a shorter distance from the N-S boundary.

Let us assume that the BCS behavior is recovered in Nb at a distance $L_\Delta \approx 25\ \text{nm}$ from the N-S boundary. The superconductor within $\sim 25\ \text{nm}$ from the N-S boundary can be regarded as a "tunnel barrier" where the pairing angle undergoes a transition from its value in the normal metal near N-S boundary to its BCS value in the superconductor. Since L_Δ is smaller than the width of

a normal metal wire d , the resistance of this fictitious "tunnel junction" is:

$$R_T \sim R_{\square}^{Nb} \frac{L\Delta}{d}, \quad (2.53)$$

where R_{\square}^{Nb} is the normal state sheet resistance of Nb. For our films $R_{\square}^{Nb} \approx 4 \Omega$, and the width of the normal wires is 50-100 nm, so $R_T \sim 1-2 \Omega$. This value is much smaller than the resistance of a normal diffusive wire: $R_T \ll R_N \sim 50 \Omega$. Hence, from equation 2.51, the drop of the pairing angle across this region of superconductor is going to be small. This estimate shows that, for our device parameters, the value of the pairing angle in the normal metal at the N-S boundary θ_{NS}^N is going to be close to the BCS value: $\theta_{NS}^N \approx \theta_{BCS} = \pi/2$ at $E \ll \Delta$.

2.6 Shot noise in hybrid normal metal - superconductor junctions

Since Andreev reflection is a correlated process of the transfer of 2 electrons, one might expect the effective charge $2e$ of the current carriers to affect shot noise of the N-S junction. This simple expectation is what rigorous theory predicts in case of opaque ballistic N-S junction. For a diffusive N-S junction, the shot noise is predicted to be *doubled* compared to a normal diffusive conductor. In this section, we discuss the theory of shot noise in hybrid normal metal - superconductor systems.

2.6.1 Ballistic case

For an N-S tunnel junction with low transmission probability ($T_n \ll 1$) the shot noise was predicted to be doubled compared to an N-N tunnel junction. Intuitively, this is easily understood considering Andreev reflection as a correlated transfer of two electrons. If a current I flows in an N-S junction due to the Andreev process, one may expect the shot noise to be $S_I = 2q_{eff}I = 4eI$.

For an N-S tunnel junction of transparency T_n , an expression for shot noise at zero temperature (i.e., with no thermally excited quasiparticles) was obtained (de Jong and Beenakker 1994):

$$S_I = 2eI \frac{8(1 - T_n)}{(2 - T_n)^2}. \quad (2.54)$$

If $T_n = 1$, shot noise vanishes. If $T_n \ll 1$, shot noise is twice the Poisson noise. This doubling of shot noise compared to that of a normal tunnel junction is indeed due to the effective charge being $2e$.

Practical issues of ballistic N-S junctions

In practice, it is not easy to realize a measurement of shot noise in a ballistic N-S junction. The junction must have a small transmission probability $T_n \ll 1$, otherwise the shot noise will be suppressed due to the effects of large T_n . However, the transmission probability cannot be too small, otherwise the current will have a substantial contribution from thermally-activated quasiparticles. Criteria for a "good" ballistic N-S junction for observation of doubled shot noise would be: $G_A \gg G_{qp}$ and $T_n \ll 1$, where G_A is the Andreev conductance and G_{qp} is the conductance due to the thermally-excited quasiparticles.

In practice, Al is usually a material of choice for superconducting tunnel junctions because of good isolating properties of its oxide. The zero-bias quasiparticle conductance of N-S tunnel junction is (Tinkham 1995):

$$G_{qp} = G_N \left(\frac{2\pi\Delta}{k_B T} \right)^{\frac{1}{2}} \exp \left(-\frac{\Delta}{k_B T} \right) \quad (2.55)$$

Using equation 2.55 we can write the criteria for a "good" N-S junction as:

$$1 \gg T_n \gg \frac{1}{2} \left(\frac{2\pi\Delta}{k_B T} \right)^{\frac{1}{2}} \exp \left(-\frac{\Delta}{k_B T} \right) \quad (2.56)$$

If we take $T_n < 0.1$ (at this transmission probability the effects due to finite T_n cause suppression of shot noise by less than 1 %) and assume the gap equal to the gap of Al: $\Delta = 170 \mu\text{eV}$, the condition 2.56 will be satisfied at temperatures below ~ 300 mK.

However, shot noise cannot be measured at zero bias voltage. To measure the slope of S_I vs. I one needs to be in shot noise regime ($eV \gg k_B T$). In practice, for an N-S junction, to measure the slope so that the error due to thermal noise contribution does not exceed 1 %, one needs to have $eV \gtrsim 4k_B T$. This makes the constraint on temperature more stringent: the condition becomes:

$$1 \gg T_n \gg \frac{1}{4} \left(\frac{2\pi(\Delta - 4k_B T)}{k_B T} \right)^{\frac{1}{2}} \exp \left(-\frac{(\Delta - 4k_B T)}{k_B T} \right) \quad (2.57)$$

Condition 2.57 will be satisfied for an N-S junction with Al as a superconductor having a transmission probability $T_n = 0.1$ and at a temperature $T < 200$ mK. These requirements should in principle be realizable experimentally, but it is very difficult to achieve uniform transparency $T_n \sim 0.1$ of an Al tunnel junction (such a transmission probability would correspond to only a few atomic layers of oxide) - any regions with high transparency (pinholes) will act like noiseless shunts and will obscure the measurement.

At temperatures below 100 mK, the condition 2.57 will be satisfied for tunnel junction transparencies $T_n > 5 \times 10^{-6}$. A tunnel junction with $T_n \sim 10^{-3} - 10^{-4}$ and with an area of 100×100 nm² will have a resistance of ~ 10 -100 Ω . Fabrication of such junctions could be done using a double-angle evaporation technique.

There are several other N-S systems in which doubled shot noise, $S_I = 4eI$, could be observed. One could use a relatively high-transparency tunnel junction between Nb (S) and a normal metal. Nb oxide tunnel junctions usually have "pinholes" - regions with higher transparency. If one has a device with pinholes having $T_n \sim 0.1$ and with the current dominated by the conductance of the pinholes, the shot noise should be doubled as compared to that of a normal tunnel junction. It is not clear how to estimate the transparency of the pinholes in such a Nb tunnel junction. Yet another possibility would be to use an N-S point contact with a tunnel barrier. This could be either touching normal metal and superconductor wires or an N-S nanopore. Both for N-S point contacts and for nanopores, large transparencies of N-S interfaces are achievable (Soulen et al. 1999), (Upadhyay et al. 1998), although for each type of device obtaining the suitable transparency of the interface is not easy. Another candidate might be superconductor - semiconductor (S-Sm) junctions. For these devices, one can use Nb as a superconductor, and in this case current is going to be dominated by the Andreev processes for a much wider range of transmission probabilities T_n . Likely due to difficulties in the fabrication of suitable ballistic N-S junctions, doubled shot noise in a ballistic N-S tunnel junction has not yet been observed experimentally.

2.6.2 Diffusive N-S junctions

The situation is different for diffusive N-S junctions. The expression for shot noise in a diffusive N-S junction is derived for the case $2eV \ll E_C = \hbar D/L^2$ (de Jong and Beenakker 1994). In this case,

an electron and an Andreev-reflected hole see the same scattering matrix in the normal region. A normal wire, with normal reservoirs, having a set of channels with transmission probabilities T_n has a conductance of

$$G_N = \frac{2e^2}{h} \sum_n T_n. \quad (2.58)$$

If one reservoir is made superconducting, the conductance becomes (Beenakker 1992):

$$G_{NS} = \frac{4e^2}{h} \sum_n \frac{T_n^2}{(2 - T_n)^2}. \quad (2.59)$$

The factor $4e^2$ in equation 2.59 is due to the fact that in each event charge $2e$ is transferred, but the spin degeneracy is lifted. The diffusive N-S junction can be regarded as having transmissive "channels" with transmission probabilities R_n which can be expressed through the transmission probabilities T_n of normal region (Beenakker 1992):

$$R_n = \frac{2T_n^2}{(2 - T_n)^2} \quad (2.60)$$

The shot noise of a diffusive mesoscopic wire with normal reservoirs is:

$$S_I^N = 2eV \frac{2e^2}{h} \sum_n T_n (1 - T_n) \quad (2.61)$$

Analogously, for a diffusive N-S junction (de Jong and Beenakker 1994):

$$S_I^{NS} = 4eV \frac{4e^2}{h} \sum_n R_n (1 - R_n) \quad (2.62)$$

with R_n given by equation 2.60. The factor $4eV$ in equation 2.62 instead of $2eV$ in equation 2.61 is due to the fact that a charge of $q_{eff} = 2e$ is transferred in the Andreev reflection process, so for each mode with conductance $G_n^{NS} = (4e^2/h)R_n$ the shot noise spectral density is

$$S_{I_n}^{NS} = 2q_{eff}V G_n^{NS} (1 - R_n) = 4eV G_n^{NS} (1 - R_n). \quad (2.63)$$

Using Dorokhov's distribution (equation 2.22) of transmission probabilities $\rho(T_n)$, it is straight-

forward to calculate the conductance of a diffusive N-S junction:

$$G_{NS} = G_N. \quad (2.64)$$

At energies much smaller than the Thouless energy, the conductance of a diffusive N-S junction is exactly the same as the conductance of a normal diffusive conductor. This result can also be obtained by solving the Usadel equation as discussed in the previous section. The Usadel equation can be applied at finite energies as well, while a scattering formalism cannot be applied at energies $eV \gtrsim E_C$. The shot noise calculation yields (de Jong and Beenakker 1994):

$$S_I^{NS} = \frac{4}{3}eI = \frac{2}{3}q_{eff}I \quad (2.65)$$

with $q_{eff} = 2e$. The shot noise of a diffusive N-S junction is expected to be *doubled* compared to a normal diffusive conductor. Doubling of the shot noise in a diffusive N-S junction was also predicted by using Boltzmann-Langevin approach (Nagaev and Büttiker 2001). For arbitrary bias voltages and temperatures, the result can be obtained by using equation 2.16. One needs to replace T_n by R_A and replace e by $2e$. After summing over transmission channels, the noise of a diffusive N-S junction becomes:

$$S_I^{NS} = \frac{8}{3}k_B T G_{NS} + \frac{4}{3}eV G_{NS} \coth\left(\frac{eV}{k_B T}\right). \quad (2.66)$$

The above derivation assumes that the energy is much smaller than the Thouless energy and the superconducting gap, *i.e.* $eV \ll E_C$ $eV \ll \Delta$. It is possible to perform the calculation in the case when eV is comparable to Δ , but one still needs to have $eV \ll E_C$ in order to apply scattering formalism. In the case $eV \ll E_C$, the coherence length in the normal metal is much larger than the length of the sample, $\xi \gg L$. In this case electrons and Andreev-reflected holes retain coherence over the whole length of the sample. This physical regime is called the coherent regime.

The other limiting case is $eV \gg E_C$. This is the incoherent regime. In this case, the coherence length in the normal metal is much shorter than the normal wire length: $\xi \ll L$. To our knowledge, the derivation of shot noise for the incoherent case ($2eV \gg E_C$) was first done by D.Ivanov (Ivanov 1998). When $eV \gg E_C$, electrons and holes can be regarded as completely incoherent.

The incoherent case, where the diffusive N-S junction is of length L and a bias voltage V is applied across it, is equivalent to the normal diffusive conductor of length $2L$ and with bias voltage $2V$ applied. The shot noise for this case is obtained by replacing V by $2V$ everywhere in the formula for the shot noise of a normal diffusive conductor. Graphically, this is equivalent to shrinking the voltage scale by a factor of 2. Doubling the voltage leads to a doubling of the shot noise, so the shot noise of a diffusive N-S junction in the incoherent regime is $S_I = (4/3)eI$ - it is also doubled as compared to that of a normal diffusive conductor.

In the regime $eV \sim E_C$, the calculation of shot noise becomes difficult. One cannot apply scattering formalism, and one cannot regard electrons and holes as being completely incoherent. The shot noise in a diffusive N-S junction was calculated at arbitrary energies by numerically solving the matrix equation leading to a calculation of full counting statistics of the transmitted charge (Belzig and Nazarov 2001). It was predicted (Belzig and Nazarov 2001) that the differential current spectral density dS_I/dV should exhibit a small broad peak (about 7 % above the "naively" expected noise corresponding to $(4/3)eI$) at bias voltage, corresponding to a few E_C .

It is interesting to consider the problem of non-equilibrium noise in a diffusive N-S junction in the "hot-electron" regime, i.e., when $L_{ee} \ll L \ll L_{e-ph}$. This problem is similar to the case of a normal diffusive conductor, except that heat can diffuse out of one end of the wire. This leads to different boundary conditions. If a wire of length L is in contact with ideal normal reservoir at $x = 0$ and with superconducting reservoir at $x = L$, the boundary conditions for the electron temperature are: $T_e(x = 0) = T_{bath}$ and $dT_e/dx(x = L) = 0$. The solution for the profile of the electron temperature $T_e(x)$ can be obtained from 2.26 by replacing V by $2V$ and L by $2L$. The resulting dependence of current spectral density vs. bias voltage can be obtained by replacing V by $2V$ (and I by $2I$, since $I = V/R$) in equation 2.27:

$$S_I(V) = \frac{2k_B T_{bath}}{R} + 4eI \left[\frac{2\pi}{\sqrt{3}} \left(\frac{k_B T_{bath}}{2eV} \right)^2 + \frac{\sqrt{3}}{2\pi} \right] \arctan \left(\frac{\sqrt{3}}{\pi} \frac{eV}{k_B T_{bath}} \right). \quad (2.67)$$

At large bias voltages, $eV \gg k_B T$, the hot-electron noise of a diffusive N-S junction will be *doubled* compared to the hot-electron noise in a normal diffusive conductor and will correspond to Fano

factor of $\sqrt{3}/2$ (Kozhevnikov et al. 2000):

$$S_{I \text{ hot el.}}^{NS} = \frac{2\sqrt{3}}{4}eI = 2S_{I \text{ hot el.}}^N. \quad (2.68)$$

This doubling has nothing to do with effective charge being $2e$. Rather, it is a consequence of the decrease of heat conductance by a factor of 2 due to one reservoir being superconducting. It is sometimes difficult in experiments to distinguish shot noise from hot electron noise for a normal diffusive conductors. We see that this may also be an issue for diffusive N-S junctions.

2.6.3 Photon-assisted noise in normal metal - superconductor junctions

For a normal mesoscopic conductor in the presence of high-frequency excitation, photon-assisted features are observed at bias voltages $h\nu/e$. Shot noise in an N-S junction in the presence of high-frequency irradiation was considered by Lesovik *et al.* (Lesovik et al. 1999). It is predicted that for a ballistic N-S junction in the presence of ac excitation of frequency ν and far below the gap, the shot noise is given by (Lesovik et al. 1999):

$$S_I = \frac{4e^2}{h}R_A(1 - R_A) \sum_{n=-\infty}^{+\infty} J_n^2\left(\frac{2eV_{ac}}{h\nu}\right) 2(2eV + nh\nu) \coth\left(\frac{2eV + nh\nu}{2k_B T}\right) + \frac{8e^2}{h}R_A^2 k_B T. \quad (2.69)$$

Here, R_A is the probability of Andreev reflection, V_{ac} is the amplitude of ac voltage, and T is the temperature.

Equation 2.69 is remarkably similar to the equation for normal tunnel junction 2.40, except tunneling probability T_n is replaced by the Andreev reflection probability R_A and the charge e is replaced by $2e$ everywhere.

Generalization for a diffusive N-S junction in the case $eV, h\nu \ll E_C$ is straightforward - one needs to average expression 2.69 over the distribution of R_A . The result is:

$$S_I = 4k_B T G_{NS}(1 - \eta) + 2\eta G_{NS} \sum_{n=-\infty}^{+\infty} J_n^2(\alpha) (2eV + nh\nu) \coth\left(\frac{2eV + nh\nu}{2k_B T}\right). \quad (2.70)$$

Here, $\eta = 1/3$ is the shot noise suppression factor for a normal diffusive conductor and the dimensionless parameter $\alpha = 2eV_{ac}/(h\nu)$ characterizes the strength of ac excitation. G_{NS} is the conductance

of a diffusive N-S junction at bias voltages $eV \ll E_C$. Equation 2.70 is expected to be valid in the incoherent regime $eV \gg E_C$ as well, but only in the low-frequency regime $h\nu \ll E_C$. All of the theoretical results considering photon-assisted tunneling discussed above were derived assuming that the tunneling time (or diffusive traversal time across the sample in case of a diffusive conductor) is much smaller than the period of the ac excitation. When the frequency of the ac excitation, ν , becomes larger than the inverse traversal time $\tau^{-1} \sim D/L^2$, the quasiparticle "sees" a time-varying field while traversing the diffusive wire. The simple "replicas" picture doesn't take this into account. To our knowledge, no complete theory of photon-assisted noise exists for the regime $h/\nu \gtrsim E_C$.

Equations 2.69 and 2.70 predict that for an N-S junction in the presence of rf excitation of frequency ν , photon-assisted noise features will occur at bias voltages $V = h\nu/(2e)$. The locations of these photon-assisted features constitute evidence of the effective charge being $2e$. They also satisfy the Josephson relation, even though an N-S junction has only one superconducting reservoir, and a true Josephson effect cannot take place.

2.6.4 Comparison of non-equilibrium noise predictions for a normal diffusive conductor and for a diffusive N-S junction. Signatures of an effective charge $2e$

In this section, we summarize the main differences in the expected shot noise of a diffusive N-S junction and of a normal diffusive conductor. Comparing theoretical predictions for shot noise and for photon-assisted noise in a normal diffusive conductor and in a diffusive N-S junction (equations 2.24, 2.66, 2.41 and 2.70), we can see that there are *four* places where a factor of 2 due to effective charge $2e$ enters the equation for a diffusive N-S junction.

First, consider the case with no rf power. Theoretical predictions of equations 2.24 and 2.66 for temperature $T = 100$ mK are plotted in figure 2.7. Noise power is expressed in the units of effective noise temperature $T_N = S_I R_{diff}/(4k_B)$, where R_{diff} is the differential resistance of the device. It is assumed that the differential resistance of a diffusive N-S junction is constant and equal to normal-state resistance. The top panel of figure 2.7 displays the bias voltage dependence of effective noise temperature. The bottom panel displays the bias voltage dependence of the derivative of the noise temperature with respect to the bias voltage, dT_N/dV .

Two distinctions between the cases of a normal conductor and of a diffusive N-S junction can be noted. First, at bias voltages $eV \gg k_B T$, the overall slope of T_N vs. bias voltage V is doubled for an N-S junction (doubled shot noise). Second, the crossover from Johnson-Nyquist to shot noise is determined by the ratio $eV/(2k_B T)$ for a normal diffusive conductor, whereas for a diffusive N-S junction it is determined by the ratio $eV/(k_B T)$. This means that the crossover from Johnson to shot noise occurs at bias voltages that are two times smaller for a diffusive N-S junction than for a normal mesoscopic conductor.

In the presence of high-frequency ac excitation of frequency ν , the step in dT_N/dV is replicated at bias voltages $V = nh\nu/e$ for a normal conductor. For an N-S junction, the photon-assisted noise features occur at bias voltages satisfying the Josephson relation $V = nh\nu/(2e)$. The top panel of figure 2.8 presents the theoretically expected bias voltage dependence of dT_N/dV for a normal diffusive conductor and for a diffusive N-S junction under 30 GHz rf excitation corresponding to $\alpha = 1.5$ (note that α is defined differently for a normal conductor than for an N-S junction: $\alpha_N = eV_{ac}/(h\nu)$ whereas $\alpha_{NS} = 2eV_{ac}/(h\nu)$). The temperature is assumed to be 100 mK. The steps occur at bias voltage of about $h\nu/e \approx 130 \mu\text{V}$ for a normal device and at bias voltage of about $h\nu/(2e) \approx 65 \mu\text{V}$ for an N-S junction. This factor of two is another signature of the effective charge $2e$.

Finally, the dependence of the magnitude of the photon-assisted noise features corresponding to an integer n (n -photon process) exhibits oscillatory behavior vs. rf power and is proportional to $J_n^2(\alpha)$ where $\alpha = eV_{ac}/(h\nu)$ for a normal conductor. For a diffusive N-S junction, the oscillatory behavior is similar, but the argument of the Bessel function is different: $\alpha_{NS} = 2eV_{ac}/(h\nu)$. The bottom panel presents the ac voltage dependence of the derivative dT_N/dV at a bias voltage satisfying the condition $k_B T \ll eV \ll h\nu/2$. The ac voltage is plotted in dimensionless units $2eV_{ac}/h\nu$. dT_N/dV for both N-S junction and for normal conductor display oscillatory ($\sim J_0^2(\alpha)$) behavior vs. ac voltage. Because of the difference between α_N and α_{NS} , the minima occur at ac voltages which differ by a factor of two.

Mathematically, the formulas for a diffusive N-S junction are obtained by replacing electron charge e by $2e$ everywhere in formulas for a normal conductor (replacing voltage V by $2V$ gives the same result). All four signatures of effective charge $2e$ are easy to picture by taking the noise curves

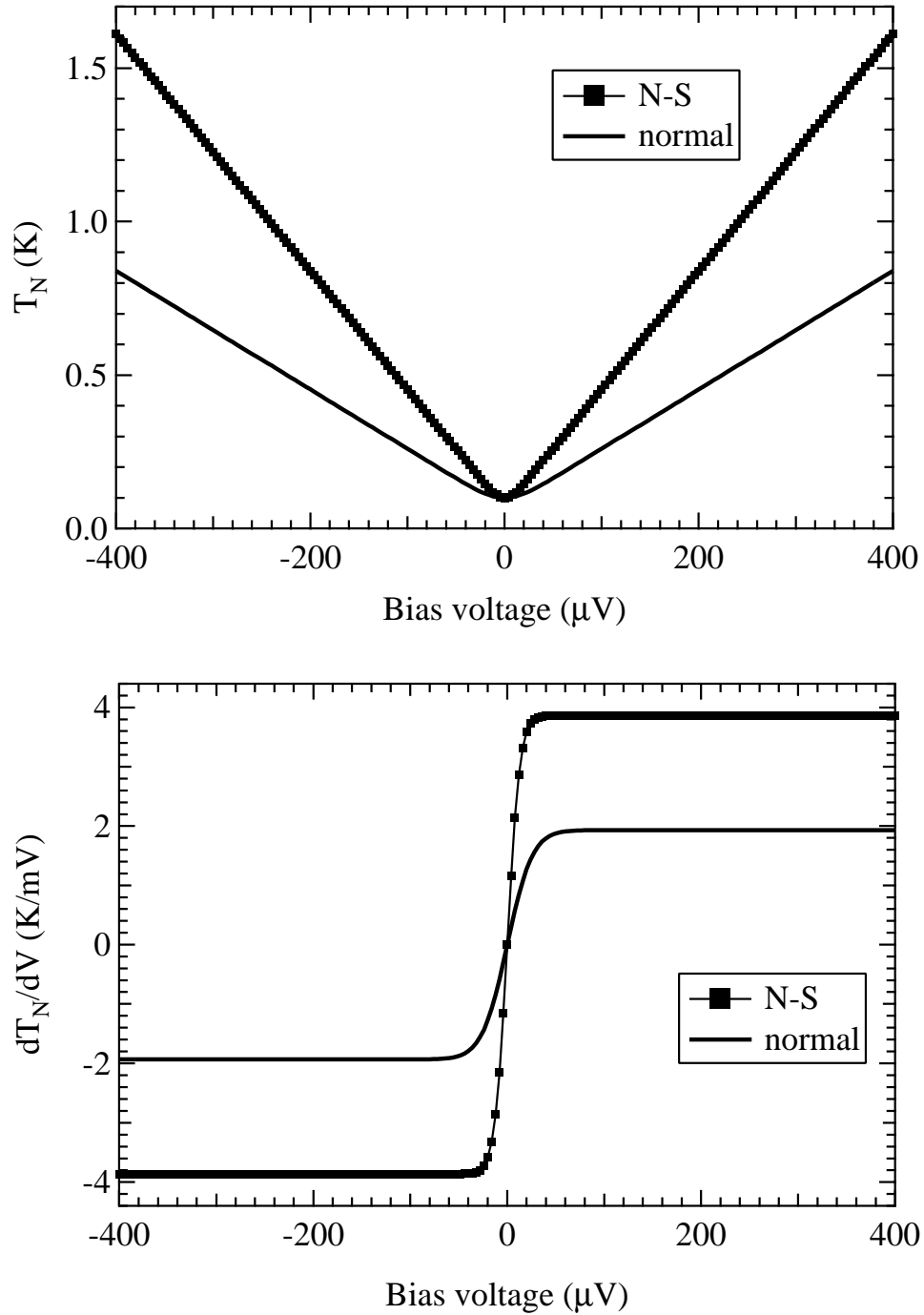


Figure 2.7: Comparison of shot noise of a diffusive N-S junction and of a normal diffusive conductor in the absence of high-frequency excitation.

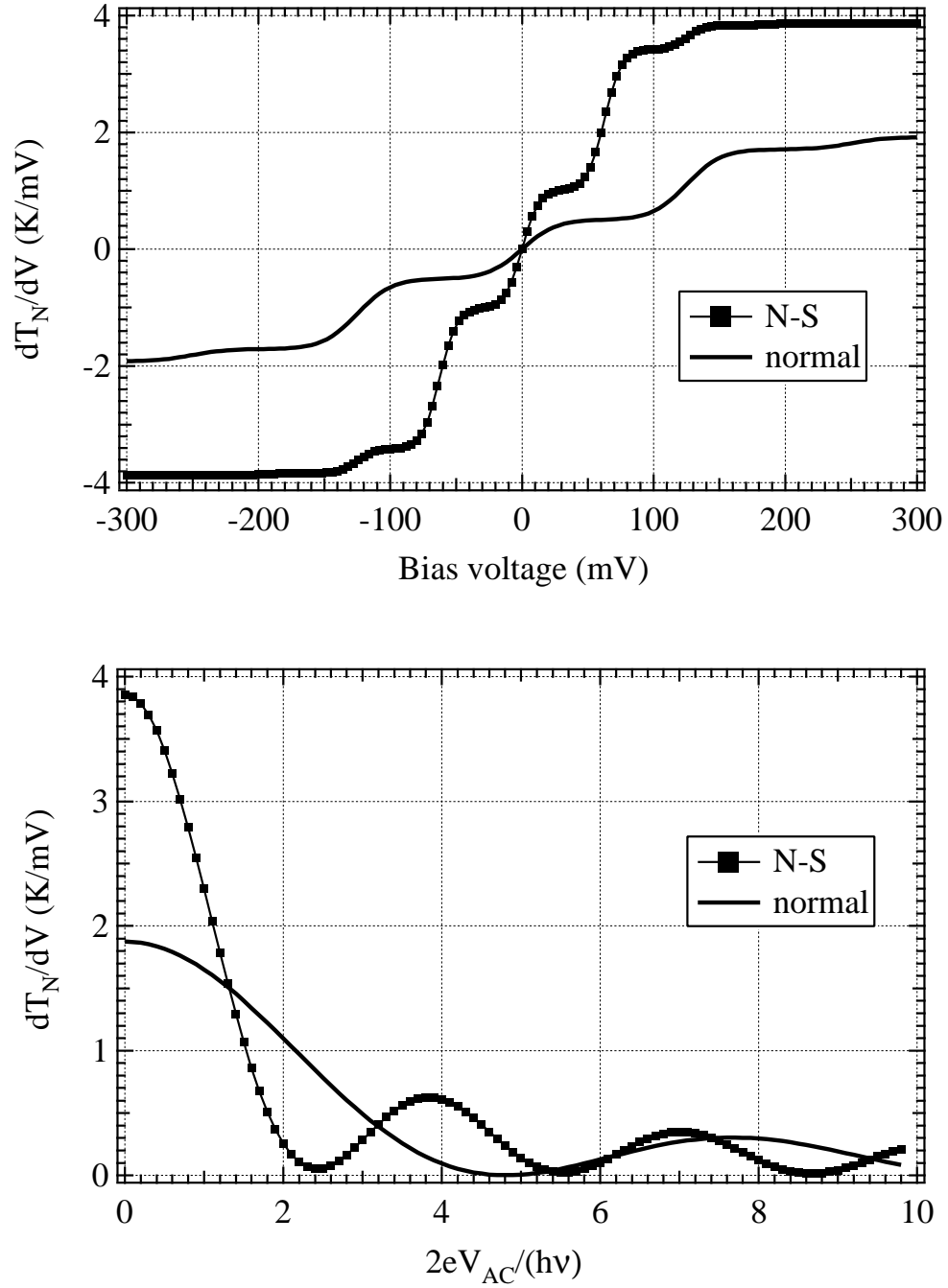


Figure 2.8: Comparison of photon-assisted noise of a diffusive N-S junction and of a normal diffusive conductor.

for a normal diffusive conductor and shrinking both dc and ac voltages scale by a factor of two.

2.6.5 Shot noise and current-current correlations in multi-terminal devices with Andreev reflection

Shot noise and current-current correlations in several Andreev interferometer geometries were considered theoretically (Anantram and Datta 1996). The calculation is based on a scattering approach and is valid for the energies $eV \ll E_C$. It was predicted that the shot noise of Andreev interferometer exhibits strong modulation with phase difference between superconducting terminals. For a multiterminal Andreev interferometer, current-current self-correlations were also phase sensitive. Current-current cross-correlations between different contacts are expected to be phase sensitive and can be *both positive and negative*. The results were derived for a ballistic device and for a single-channel case.

Predictions that the sign of the current-current cross-correlations may be changed by tuning the superconducting phase difference are interesting. For non-interacting current carriers, the sign of current-current cross-correlations depends on quantum statistics of current carriers (Büttiker 1992). Current-current correlations can be either positive or negative for bosons and are always negative for fermions. In a normal (non-superconducting) device an electron entering a terminal i will always leave some other terminal j as an electron. This will lead to a negative current-current cross-correlation: $\langle \Delta I_i \Delta I_j \rangle < 0$. In a multiterminal device with Andreev reflection, however, an electron entering a normal terminal i may be Andreev reflected and leave the other terminal j as a hole. For such a process, $\langle \Delta I_i \Delta I_j \rangle > 0$. Depending on the superconducting phase difference, either "normal" processes or Andreev reflection will dominate, and the sign of current-current correlations will change as a function of superconducting phase difference.

The problem of current-current correlations in multiterminal N-S structures was also considered in a more recent work (Torres and Martin 1999). The authors considered a three-terminal device with two normal contacts and one superconducting contact. The superconducting lead was coupled to the two normal leads via a beam splitter. It was shown that the current-current cross-correlations in the normal contacts may be either positive or negative, depending on the transparency of the beam-splitter.

Both works (Anantram and Datta 1996; Torres and Martin 1999) considered single-channel cases. The possibility of positive cross-correlations in the two above devices in a multi-channel case was recently considered (Gramespacher and Büttiker 2000). It was shown that both for Andreev interferometers and for the beam splitter geometry the processes that lead to positive current-current cross-correlations are purely mesoscopic, *i.e.* of order 1, whereas the "normal" processes that lead to negative cross-correlations are of order N (number of channels). This means that both for the Andreev interferometer (Anantram and Datta 1996) and for the beamsplitter (Torres and Martin 1999) the effect of positive correlations disappears as the number of channels increases. It was proposed (Gramespacher and Büttiker 2000), that positive cross-correlations could be observed only in a device with only a few open channels.

It is worth noting, though, that all of the above theoretical calculations of current-current cross-correlations are based on scattering formalism. These results are applicable for diffusive N-S devices only at $eV \ll E_C$. This zero-energy scattering approach is limited. Using a scattering approach would predict that the modulation of the conductance of an Andreev interferometer also disappears as one increases the number of channels (Belzig and Nazarov 2001). That is not true; at finite energies the modulation of the conductance of a diffusive Andreev interferometer is non-zero and is independent of the number of channels if $N \gg 1$. This follows from the Usadel equation - in a multi-channel diffusive device, modulation of the conductance is due to the change of the pairing angle *at finite energies* as a function of the superconducting phase difference. This effect is independent of the number of channels as long as $N \gg 1$. To our knowledge, there has not been a theoretical treatment of current-current cross-correlations at finite ($\sim E_C$) energies yet.

Chapter 3

Fabrication of Hybrid Normal Metal - Superconductor Devices

In this chapter the techniques used for fabrication of the normal metal - superconductor (N-S) devices are described. In the first section, the physical parameters of our devices are considered. These parameters impose certain requirements on fabrication techniques. In the second section, we describe in detail the sequence of the fabrication steps.

3.1 Physical parameters of devices

Our devices are diffusive normal metal wires in contact with a normal reservoir on one side and in contact with a superconducting loop on the other (Andreev interferometers). In order for the length of the devices to be smaller than the energy relaxation length at a temperature of ~ 100 mK, the wire has to be shorter than ~ 1 μm . To perform the noise measurements at GHz frequencies, the device has to be well-matched to the RF amplifier, i.e., the device resistance has to be close to 50 Ω . Thin Au films (of ~ 10 nm thickness) have a sheet resistance of ~ 10 Ω/square . That means the wire has to have ~ 5 squares, i.e. have a width of about 100 nm for 0.5 μm long wire. The contact pads have to be large enough to conveniently make contact to them using a wire-bonder (that is, at least about 100×100 μm^2). We used electron beam lithography to write both wires and contact

pads - this way the alignment of wire patterns to the contact pad patterns was trivial.

3.2 Fabrication Process

The fabrication process consists of the following steps: spin-on of resist, E-beam exposure, resist development, double angle Au deposition, Au liftoff, second resist spin-on, second E-beam exposure, resist development, Nb deposition, and Nb liftoff. The following subsections describe these steps in excruciating detail. This section is not meant to be an electron beam lithography manual. An excellent introduction is available (McCord and Rooks 1989). Also, the NPGS manual (Nabity 1998) is very well-written and contains virtually all of the information necessary to get started with E-beam lithography.

3.2.1 Resist spin-on

A double-layer poly(methyl methacrylate) (PMMA) was used as a resist. The top (imaging) layer had a molecular weight of 950,000 (950 k). The bottom (buffer) layer has a molecular weight of 100 k. For the top layer we used a 2% solution of 950 k PMMA in methyl isobutyl ketone (MIBK). For the bottom layer a 5% solution of 100 k PMMA in MIBK was used. PMMA for both layers was premixed by a manufacturer and stored in a refrigerator at about 4°C. The solutions were purchased from Microlithography Chemical Corp., Newton, MA. Resist was spun on an oxidized Si substrate. Si oxide was thermally grown by wet oxidation and had a thickness of about 400 nm, as determined by the color of the wafer after oxidation. Before the spin-on, a piece of the oxidized Si wafer was cleaned in acetone for 30 sec with ultrasound excitation then in methanol for 30 sec with ultrasound excitation. After cleaning, the piece of Si was blown dry with nitrogen gas, then spun dry for 60 sec at 3000 rpm. The bottom (100 k) PMMA layer was spun on a piece of Si having an area of ~ 1 cm², at 3000 rpm for 60 seconds, and then baked at a temperature of 170°C for at least 1 hour. After that the upper (950 k) layer was spun on. In order to speed up the evaporation of MIBK and minimize intermixing between 2 layers of resist, the speed of the spinner was ramped from 3000 rpm to 8000 rpm during the spin-on. The spin-on time for the second layer was 60 sec. After spin-on, the Si chip with resist was baked for at least 1 hour at 170°C. The Si pieces with resist were stored

in darkness at room temperature. Usually the resolution and sensitivity of the resist were stable for several months after spin-on and baking. In some cases, however, the sensitivity had increased and the resolution decreased over the time of about a month. The reason may have been absorption of water from the atmosphere. If a Si chip with resist was to be used for lithography more than 2-3 weeks after the spin-on, the chip was baked prior to exposure at 170°C for 15-20 minutes to get rid of water.

3.2.2 E-beam lithography for normal wire and contact pads

In this section I focus on the details of the e-beam lithography process relevant to the fabrication of the N-S devices. A lot of information provided below is process- and equipment-specific and is likely to be of interest only to a narrow circle of readers.

Design of the pattern was done using DesignCAD software. DesignCAD was purchased with NPGS and additional graphical macros, which were compatible with NPGS were installed in DesignCAD during the NPGS installation. DesignCAD allowed entities to be drawn in different layers. Within each layer, graphical objects could be drawn in different colors. The pattern was saved in internal DesignCAD format. After pattern design the multiple run file (MRF file) was created by NPGS. The MRF file contains information necessary for the writing of the pattern. In particular, the user specifies which layers were to be written and which layers were to be skipped. The beam current, distance between points and SEM magnification were assigned separately for each layer. Within each layer, graphical entities drawn in different colors could be assigned individual doses. All these options allowed for great flexibility during e-beam writing. A well-written description of DesignCAD commands which are compatible with NPGS and of MRF settings can be found in NPGS manual (Nabity 1998).

The layout of the pattern for the first e-beam lithography step is presented in figure 3.1. The bottom part is a zoom-in of the central part of the pattern. The layout consists of 3 layers. Layer 1 is the wire 1 μm long and two small pads (shown in gray on the inset to fig. 3.1) Layer 2 is a set of 6 alignment marks. The large contact pads are in Layer 3. The layout of Layer 1 in figure 3.1 is the pattern that was used for fabrication of diffusive N-S junctions. Layer 1 has different patterns for Andreev interferometers (they are discussed in chapter 5). Layers 2 and 3 are the same for all

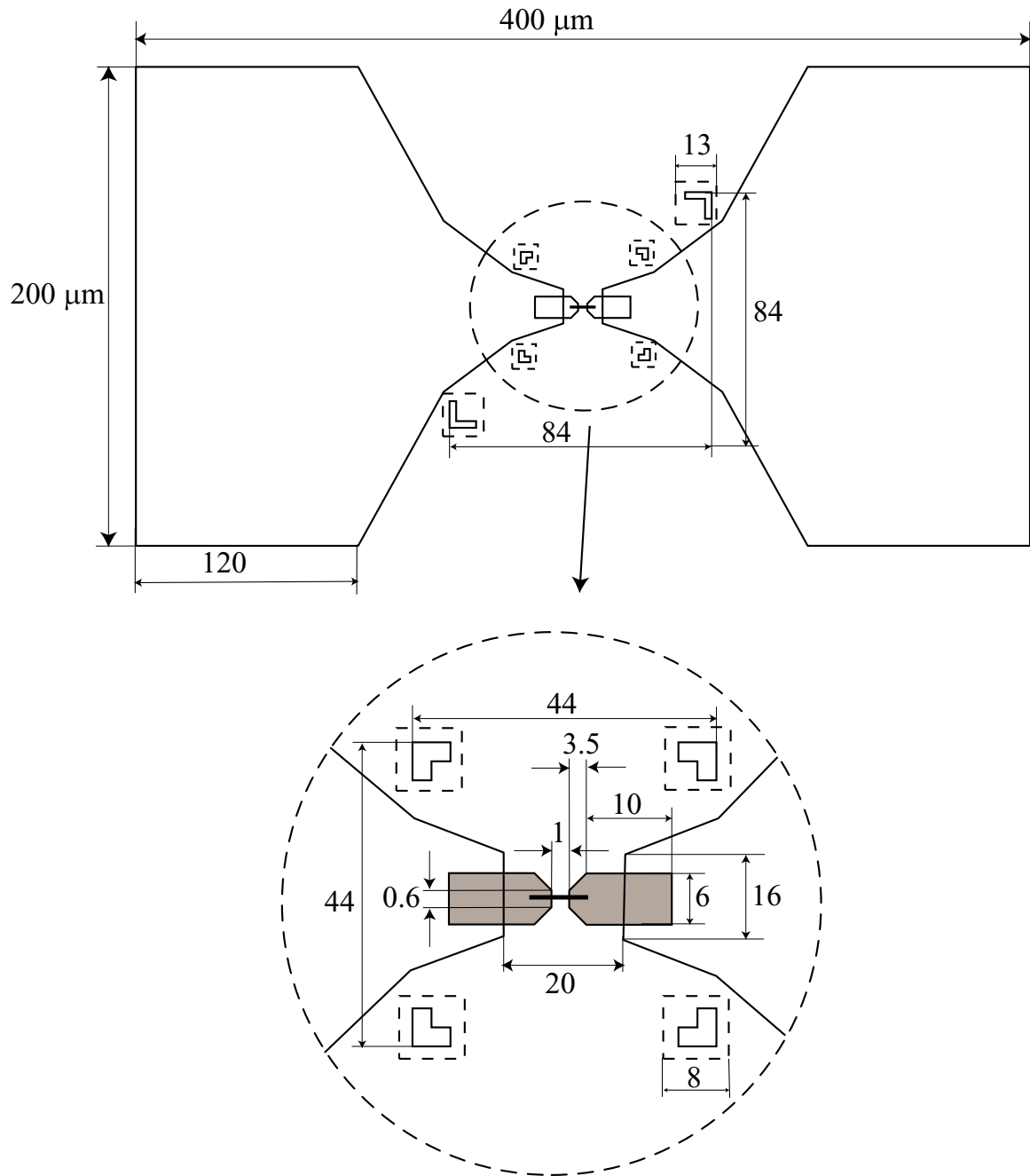


Figure 3.1: The layout of the pattern for the first lithography step (not to scale). All dimensions are in μm . Dashed squares are alignment "windows".

devices that were fabricated. There is no resist processing between exposures of Layers 1, 2 and 3. NPGS allows to select different layers in the pattern to be written. For each layer, the point-to-point distance, distance between the lines (these two quantities determine the "pixel size"), SEM magnification (which determines the field size) and beam current can be set independently. Within each layer, entities of the pattern drawn with different colors can be assigned different exposure doses. This flexibility of settings allows fine tuning of the writing process to be done at any time and is very convenient.

It is desirable that the wire be narrow (under 100 nm wide), so the wire is written as a single-pass line. The exposure dose of a single-pass line must be larger than area dose exposure. Typically, the line exposure dose for the wire was 1.8 nC/cm with point-to-point distance of 10 nm. For the small pads and alignment marks an area dose of 350 $\mu\text{C}/\text{cm}^2$ typically yielded good results. The point-to-point spacing was 10 nm, the distance between the lines was 10 nm (the effective "pixel size" is 10nm \times 10nm). The exposure doses varied slightly among the fabrication runs. In most cases, I performed a test exposure right before the e-beam lithography run to determine the best dose. Test exposure was performed either on a test chip with resist which was spun on at the same time as the resist for the "real" chip, or on the same chip where the devices would be written. After development the best exposure dose for the pads and alignment marks was determined by evaluating lithography results under optical microscope. The correct exposure dose for the fine wires was determined by viewing the test pattern in developed resist in the SEM. The "bare" oxidized Si substrate (areas where resist dissolved away during development) and Si covered with PMMA charged differently, and it was possible to get an image of developed resist. I did not sputter Au to visualize the results of test exposure - contrast between Si and PMMA is sufficiently high to allow SEM imaging even at small (~ 3 pA) beam currents.

All e-beam exposures were done at SEM high voltage 40 keV (maximal voltage for JOEL6400 SEM that was used). For writing fine features a small beam current was needed. Both Layer 1 and Layer 2 were written in a single exposure at a $\times 1000$ magnification (100 $\mu\text{m}\times$ 100 μm field of view) with a beam current of $I_{beam} = 3.6$ pA. The stage of the SEM was not moved between writing of Layers 1 and 2, so Layers 1 and 2 were aligned to each other. The process of writing Layers 1 and 2 takes about 5 minutes per pattern.

Layer 3 had features larger than the size of the field at $\times 1000$ magnification, so it was written at a $\times 100$ magnification (1mm \times 1mm field of view). Because of the large area of the contact pads, it was desirable to write large pads at larger beam current to speed up writing (it would have taken more than 1 hr to write large pads at a beam current of 3.6 pA). I wrote Layer 3 of the pattern at a beam current of 10 nA. The point-to-point distance was 250 nm, the distance between the lines was 250 nm, so the "pixel size" was 250nm \times 250 nm. Because of the large point-to-point distance the beam was defocused by 50 on fine objective lens (OL) setting to ensure more uniform exposure of the large pads area. The process of writing Layer 3 took about 1 minute.

In most fabrication runs I created arrays of patterns (typically 15 to 25 patterns). NPGS allowed the user to define the location and dimensions of the array, after that the array of patterns can be written automatically - NPGS can control the SEM stage and move it to the location of the next pattern in the array. It was not desirable to have to switch the beam current between 3.6 pA for the small features in Layers 1 and 2 and 10 nA for the large pads in Layer 3 for each pattern. Switching the beam current has to be done manually and can spoil the fine focus of the SEM. Fine focus is absolutely crucial for small features.

To avoid switching the beam current many times, I first wrote an array of patterns consisting only of Layers 1 and 2. After that, the beam current was changed, the beam was defocused, and an array of Layer 3 patterns (large pads) was written at the same locations where previously Layers 1 and 2 had been written. The stage position proved to be reproducible enough for the errors in the stage position to be unimportant. These errors typically did not exceed a few μm if, after each stage move, the stage was given a command to move by a few tens of microns both in X and Y directions and then back. If such command is given, the stage always approaches the target location from the same directions, and the effects of backlash are minimized. The pattern was designed having in mind a few μm irreproducibility of stage location, so the design is robust against few μm misalignment of large pads to the Layers 1 and 2.

Focusing of the SEM was performed by viewing Au clusters about 100 nm in diameter. These clusters provide high contrast and are usually spherical which allows easy stigmatism of the SEM. A small droplet with colloid solution of Au clusters (100 nm gold colloid EM.GC100, Ted Pella, Inc., Redding, CA) was placed on the chip, usually about 1 mm from the edge. In earlier fabrication runs

SEM focus (determined mainly by objective lens settings of the SEM) was not changed after the focusing on Au clusters was performed. In some instances, because the surface of the chip was not horizontal, this led to systematic variations of the fine wire width across the sample. Occasionally, these variations made devices from certain areas of the chip unusable because the width of the wires was too large. In subsequent runs, the situation was remedied by using focus correction feature of NPGS. Several (typically 5-7) droplets of Au colloid were placed along the edges of the chip. At each location of the droplet, SEM was focused on Au clusters, and the SEM objective lens (OL) fine setting was recorded by NPGS. NPGS performed interpolation of the acquired OL setting and the coordinates of the stage:

$$OL = A + BX + CY \quad (3.1)$$

where OL is objective lens fine setting, X and Y are stage coordinates, and A , B and C are fit parameters. When writing the array of patterns, NPGS sets the focus according to 3.1. This procedure corrects for the surface of a chip not being flat. NPGS stores parameters A , B , C in file PG_FOCUS.SYS in the directory where NPGS is installed. *WARNING: It is important to delete this file after the exposure is done, preferably before Layer 3 is written, and definitely before next fabrication run.* If NPGS finds this file (no matter how old), it will use the settings from it and change OL fine focus according to equation 3.1 without prompting the user. This will have dire consequences for lithography results, as fine OL settings are not reproducible between the fabrication runs. In the focus correction mode, one also has to make sure that OL rough setting is the same for all the locations of Au clusters where focusing is performed. NPGS records and corrects only the fine OL setting, ignoring the rough OL setting. Having a rough OL setting offset by 1 from the correct value will result in strongly defocused beam. In spite of the features of the focus correction mode described above, the results were worth the effort. Using the focus correction feature allowed to make the width of the wires substantially more uniform across the chip and allowed to write larger arrays of devices with better yields. The focus correction mode was not used for writing Layer 3 (large pads).

A change of the beam current and a change of the SEM magnification lead to a systematic shift of field. To compensate for that, after some experimenting, Layer 3 was shifted electronically by 5 μm in the X direction (parallel to the wire), and by 2 μm in the Y direction (perpendicular to the

wire). This resulted in an almost perfect cancellation of the systematic shift of Layer 3 with respect to Layers 1 and 2. These values seem to be a reproducible feature of the SEM that was used - they stayed the same throughout several filament replacements.

3.2.3 Resist development

The chip with exposed resist was soaked in a mixture of MIBK and isopropanol (IPA) (1:3 by volume) for 30 sec at room temperature, then in IPA for 30 sec at room temperature (the SEM room has no temperature control). After that, the chip was blown dry with nitrogen.

3.2.4 Pattern evaluation

After development, the large features were examined using an optical microscope. The width of the wires can be evaluated using the SEM - the PMMA charges differently from oxidized Si, and that creates contrast for SEM viewing. Large overexposure and underexposure are straightforward to see under the optical microscope. Small underexposure can be seen under the SEM as dark "islands" (regions of resist that has not been dissolved during development) on light background (regions where resist has been dissolved). Monitoring the width of narrow wires with an SEM has to be done quickly and at a small beam current. If the current is too large, the resist is destroyed due to electron beam exposure during the SEM examination and the lines become wider. A typical current used for examination was ~ 3 pA.

3.2.5 Deposition of Au

First, 1 nm of Ti was deposited at a rate of 0.1 nm/sec. Ti serves as an adhesion layer for Au, because Au atoms don't stick well to Si or SiO₂. After that, 10 nm of Au was deposited at normal incidence to the substrate at a rate of 0.1 nm/sec. At such a low evaporation rate, the deposited metal may contain a lot of impurities, which should increase the sheet resistance of the film. The stage with the sample was tilted by about 60°, and 110 nm of Au was evaporated at this angle at a rate of 0.3-0.5 nm/sec. The sample stage rotation was performed without breaking the vacuum in the evaporator chamber. After the deposition, the sample cooled down for about 40 minutes before it was exposed to the atmosphere.

3.2.6 Au liftoff

After the Au deposition, the Au film covering unexposed resist was lifted off. The liftoff was performed in acetone. A beaker with acetone was warmed up in a hot water bath to induce convection and facilitate liftoff. The water bath was warmed by a hot plate set at a temperature of 80-90°C. Typically, the sample was left soaking in warm acetone for 2 hours. The beaker with acetone was covered with a Petri dish cover to minimize the acetone evaporation. Overheating of the acetone was undesirable; if acetone started boiling, the hot plate temperature was slightly decreased so the boiling would stop. After soaking in warm acetone, a syringe was used to direct a jet of acetone to the chip surface and facilitate liftoff. In most fabrication runs small pieces of thick Au film remained near the very fine features of the pattern. We used ultrasound excitation (30 sec., the beaker with acetone was immersed in water in the ultrasound cleaner but did not touch the bottom of the ultrasound cleaner) to help get rid of these features. In all fabrication runs there were some devices which still had the remnants of the thick Au film in the vicinity of the thin Au wires. In some devices these remnants were shorting the thin wires and making the devices unusable. Attempts to get rid of these thick Au film flakes by prolonged ultrasound excitation in some cases resulted in damage to the Au wires.

3.2.7 Evaluation of the Au wires

After the Au liftoff, the samples were evaluated, first, by optical microscopy, then by scanning electron microscopy. Optical microscopy lets us evaluate the large-scale structure of the sample, down to a few μm . The continuity and the width of the wire is easy to monitor using the SEM. The DC resistance of several wires in each batch was measured using a DC bias electronics set and a probe station. Using a probe station and a low-noise bias electronics setup proved to be safe and usually did not destroy the devices. In more than 10 batches of devices there were only 2 devices which seemed to become open circuits during dc measurement with the probe station.

3.2.8 Resist spin-on for the second step of E-beam lithography

The second layer of E-beam lithography had to be performed on a chip with a deposited Au wire and with Au contact pads. Baking of the resist helped to get rid of the water and increased the resolution

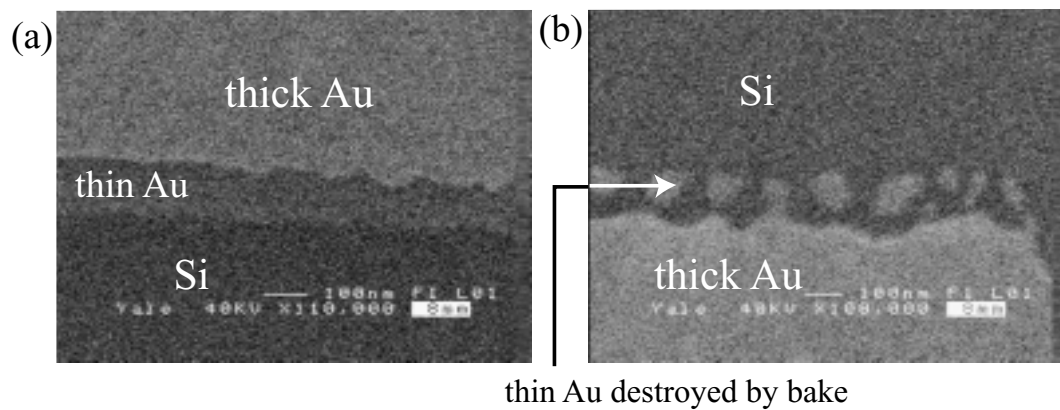


Figure 3.2: Damage to deposited Au after 1 hr bake at 170°C.

of the resist. However, thin Au wires get easily damaged by baking at 170°C. SEM pictures taken before and after baking of a chip with Au wires revealed that thin Au films and wires got damaged by baking at 170°C; Au tends to "ball up" and the continuity of the wire is destroyed. Figure 3.2(a) shows the thin Au "shadow" near the edge of a thick Au pad. The top section of figure 3.2(a) is covered with thick Au, the bottom section has no metal on it, the thin Au "shadow" is in the middle. This shadow occurs due to double-angle evaporation.

Figure 3.2(b) shows what becomes of such a "shadow" after baking the chip for 1 hour at 170°C. The edge of the Au film in 3.2(b) has a different orientation than in figure 3.2(a) - it is rotated 180°, so the bottom section is covered with thick Au and the top section has no metal on it. Figure 3.2(b) shows no "shadow" of the thin Au film - after baking, thin Au film "balls up" and the continuity of the thin Au film is destroyed. This leads to destruction of the continuity of Au wires. A resist spin-on process was developed in which baking was performed at a substantially lower temperature and for a much shorter time, described below. The baking process did not damage Au wires. At the same time, the resolution of the resulting resist was sufficient for our purposes (to write Nb contacts which are about 250 nm wide).

A double-layer PMMA was used with a molecular weight of the bottom layer of 100 k and a molecular weight of the top layer of 950 k. The baking time and temperature were decreased compared to the resist for the first e-beam lithography step. The first layer was spun on at 3000 rpm for 60 sec and then baked for 6 minutes at a temperature of 90°C. After that, the second layer

was spun on at an initial spinner speed of 3000 rpm, which was ramped to 8000 rpm during the spin-on. The resist was then baked for 5 minutes at a temperature of 90°C.

3.2.9 Second step of E-beam lithography

The patterns for Nb contacts or rings were done using e-beam lithography. The general procedure was similar to writing Au wires. The exposure doses were similar to the doses in the first step and were between 250-330 $\mu\text{C}/\text{cm}^2$. A crucial difference was the necessity to precisely align the Nb pad or ring to the Au wire. For diffusive N-S junctions, the length of the wire was determined by the distance at which Nb pad was deposited from one of Au contact pads, so a pattern for Nb pad had to be aligned to within ~ 200 nm in the direction along the wire. For Andreev interferometers the alignment requirements were even more stringent - misplacement of Nb ring by ~ 150 nm in either direction may have led to the wrong topology of the device.

Preliminary alignment was performed by using an optical microscope, which was coaxial with the SEM. The coordinates (X,Y) of the stage when a device was in the center of the optical microscope field were stored by the computer controlling the SEM stage. During the writing, the stage was moved to the stored location (X,Y) of the pattern. This rough alignment put the stage within about 10 μm of the desired location. Further alignment was performed using the alignment procedure described below.

During the alignment procedure a set of 6 square regions ("windows") in the places of the pattern where alignment marks were expected to be was scanned. We used 2 larger windows for rough alignment and a set of 4 smaller windows for fine alignment. Alignment windows are shown as dashed squares around alignment marks in figure 3.1. During the rough alignment the 2 windows surrounding larger alignment marks were continuously scanned in the SEM-like mode (without averaging), and the position of the SEM stage was adjusted by hand to get the alignment marks within the windows. After this rough alignment, a fine alignment was performed electronically. A set of 4 smaller alignment windows was scanned. The software calculated the positions of 4 alignment marks and, based on them, calculated the offset (X,Y) by which the pattern needed to be displaced and rotation angle θ , by which the pattern had to be rotated. The pattern was then written with the calculated offset and rotation.

NPGS allows use of either the manual or the semi-automatic mode for alignment. For devices with intact alignment marks the semi-automatic procedure usually gave good results. For partially damaged marks or for marks with incomplete liftoff the semi-automatic alignment procedure sometimes failed to identify the alignment mark location, so manual alignment was necessary. During fine alignment some amount of averaging was necessary in order to facilitate the alignment mark recognition. The procedure worked better if, before automatic alignment, the alignment marks were roughly placed on the right positions by hand. The spacing of the points during the scan was 50 nm in the X direction and 50 nm in the Y direction in order to achieve the desired accuracy of alignment of about 100 nm.

While fabricating Andreev interferometers, an additional issue was the necessity of very fine alignment in both the X and the Y directions. The Nb pattern had to be aligned to the thin Au wire, while the alignment marks were made of the thick Au film. Because of the double angle evaporation, the thick metal patterns were displaced with respect to the thin metal pattern by about 200 nm in the Y direction. This was unimportant for diffusive N-S junctions, because the tolerance to alignment in the Y direction was about $0.5 \mu\text{m}$, but it proved to be important for the Andreev interferometers. After a few trials, an additional offset of -200 nm in the Y direction was introduced for the Nb pattern to compensate for the displacement due to the double angle evaporation. This additional offset improved the quality of the alignment.

3.2.10 Deposition of Nb

Nb films 70-80 nm thick were sputtered in a Lesker sputtering system at a rate of about 1 nm/sec. To ensure good contact between the Nb and the previously deposited Au, the chip was cleaned by an Ar ion beam for 7 sec right before the Nb deposition. The ion beam current during cleaning was 4.7 mA, and the voltage was 500 V. The Ar pressure in the deposition chamber during Nb sputtering was 11 mtorr, and the power supplied to the Ar plasma was 500 W (500 V, 1 A).

3.2.11 Nb liftoff

Hot acetone was used for the liftoff of Nb. Nb films deposited at our parameters of deposition had some tensile stress and that made liftoff easy. Nb liftoff usually took about 15-30 minutes to

complete. A syringe was used to direct a flow of acetone toward the surface of the chip. In most fabrication runs no ultrasound excitation was necessary for the Nb liftoff.

3.2.12 Evaluation of the devices

After the fabrication the devices were tested both electrically at room temperature (using a probe station) and with an SEM. An SEM examination was necessary to test whether the alignment procedure was successful and to determine the actual dimensions of the devices.

Chapter 4

Experimental techniques

In this thesis, high-sensitivity transport and noise measurements of the mesoscopic normal metal - superconductor devices were performed. A variety of experimental techniques was used to make these dc and rf measurements.

In this chapter, I describe the experimental setup and calibration procedure used to perform the measurements. In the first section, the dc electronics setup is described. In the second section, the rf setup is described. In the third section, the model of the measurement setup is presented and explained. In particular, how to calculate the noise of the device from the output noise of the system in case the differential resistance of the device is not constant is explained. In the fourth section, I describe a calibration procedure used to determine the gain and the noise temperature of the measurement setup and to convert measured noise to absolute units.

4.1 DC measurement setup

4.1.1 DC electronics

The devices that were tested were metal structures of sub- μm length. They were extremely sensitive to electrostatic discharge. The electronic setup had to be electrostatically safe in order not to destroy them. In order to measure thermal noise, the voltage noise introduced by the electronics across the device and the "read-out noise" had to be smaller than $k_B T/e \sim 4\mu\text{V}$ at 50 mK, so the setup had

to be fairly low-noise. The schematic of the DC measurement setup is presented in figure 4.1.

The setup consists of three main components - a bias box, an isolator box and an adder box. The bias box contains electronics for applying bias voltage to the device and for low-noise measurements of the dc voltage across the device and the current through the device. We use a three-wire measurement scheme, because the wires going to the device in the dilution refrigerator have fairly high resistance ($\sim 100 \Omega$). The current lead and the voltage measuring lead are joined together at the dc input of a bias tee, which is bolted to the mixing chamber of the dilution refrigerator. The current through the device is measured by measuring a voltage drop across a resistor connected in series with the device. The isolation box breaks the ground loop so that the "device ground" (which is the case of the cryostat which, in turn, is connected to the water pipe) is not connected to the "measurement ground" (shared by oscilloscopes and lock-ins) through the DC electronics setup. The adder box allows manipulations and generation of the voltage signal which determines bias voltage or bias current through the device. There are 3 signal lines which need to go from the measurement electronics and signal generators to the device and back. One is the drive voltage which determines bias voltage on the device (or bias current through the device). Two other lines are voltages proportional to the bias voltage across the device and the current through the device. Below, the main components of each of the three boxes are described.

The bias box takes "drive" voltage which is generated in the adder box, buffers this signal and then biases the device through a selectable bias resistor. In our experiments the device has a differential resistance of under 100Ω . Bias resistors are much larger than that, so it is effectively a current bias. There are 2 low-noise instrumentation amplifiers AD624 (Analog Devices) that are used to measure bias voltage and bias current. Current is measured by measuring a voltage drop that develops across a known bias resistor. The amplified signals are buffered and then, through the isolation box, go to the measurement electronics. There is a feedback loop which can be turned on or off. With feedback off the device is current biased. With feedback on, the device is voltage biased.

The isolation box has three opto-isolation instrumentation amplifiers 3652MG (Burr Brown) which break the ground loop and isolate the "device ground" from the "measurement ground". Each amplifier is configured to have a gain $G = 1$, so it effectively serves as a buffer that has different

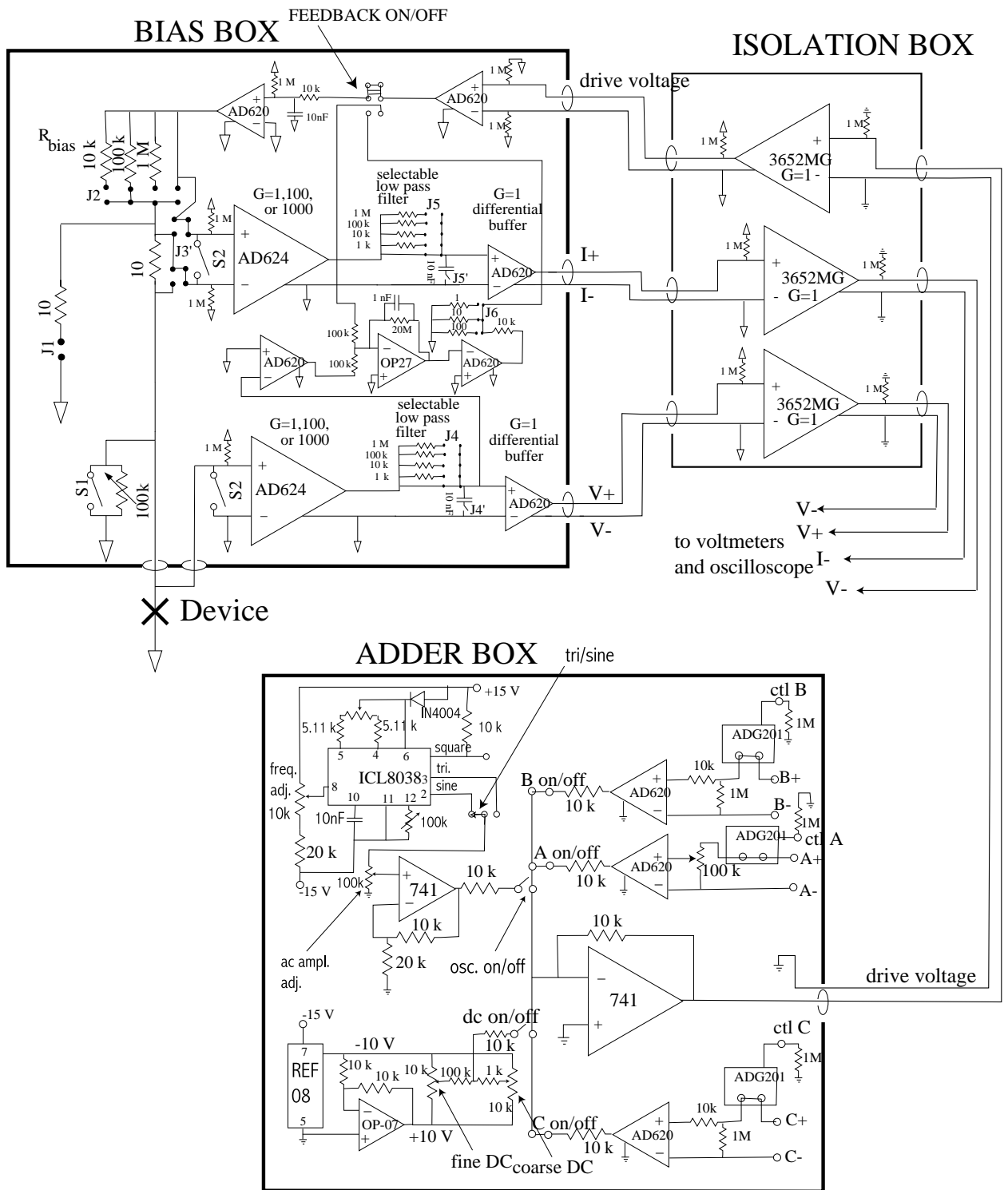


Figure 4.1: Schematic of DC measurement setup.

input and output grounds.

The adder box has 3 inputs for applying external voltages and can add them to form a voltage signal which "drives" the device. It also has internal dc and ac voltage sources. In our experiments, we typically apply a sum of dc voltage and a small ac voltage. Both dc and ac voltages are generated externally. These voltages are fed into the adder box and added there. The internal dc and ac sources are convenient to use for debugging the experiment. DC bias electronics were powered by 2 floating output bench power supplies (HP E3630A) - one power supply was needed for the bias box and the side of the optoisolation box sharing ground with the bias box, while the other supply was used for the adder box and the part of the isolation box sharing ground with the adder box.

All of the switches and jumpers in figure 4.1 are drawn in the positions which were used for our measurements. Below, we describe the purposes of the switches and jumpers. We start from the bias box. Switch S1 and a 100 k potentiometer in parallel are used for shorting the device for protection. Switch S2 is used for shorting the inputs of the instrumentation amplifiers. J1 allows changes in the way device is biased; if the device is current biased and J1 is shorted, bias conditions become closer to voltage bias. Jumper J2 allows selection of the bias resistor. Jumper J3' allows a choice of the resistor across which the voltage drop is measured. This is proportional to the dc current through the device. One can choose either a bias resistor or a 10 Ω resistor. J4, J4', J5 and J5' allow introduction of low-pass RC filters on the voltage and current signal lines. The "FEEDBACK ON/OFF" switch is used to turn on and off the feedback loop and switch between voltage and current bias of the device. Jumper J6 allows a choice of the voltage division ratio for the feedback loop. In our experiments, the feedback loop was not used.

The adder box has a number of switches for connecting internal ac and dc sources and external inputs to form a voltage signal and also several potentiometers for tuning dc and ac voltages produced by internal ac and dc sources. An ac voltage frequency is tuned by a variable resistor labeled as "FREQ. ADJ.", and the ac voltage amplitude is tuned by the potentiometer "AC AMPL. ADJ." The output of the ac voltage source can be connected to the summing junction of the operational amplifier forming the "drive voltage" or disconnected from it by an "OSC. ON/OFF" switch. The "tri/sin" jumper allows a choice between a sinusoidal or a triangular waveform for ac voltage. The magnitude of internal dc voltage is tuned by 2 potentiometers - "fine DC" and "coarse DC". The

output of the dc voltage source is connected to the summing junction of the op.amp. via "DC on/off" switch. Both dc and ac internal voltage sources are used for debugging of the experiment, and their outputs are normally disconnected from the 741 operational amplifier that forms the drive voltage. There are also 3 external differential inputs - A, B, and C. The inputs can be electronically enabled or disabled by an analog solid-state switch ADG201 (ADG201 is a quadruple switch, 3 switches on the same ADG201 chip are used for inputs A, B, and C). Three control voltages - one for each external input, can be used to disable the external inputs. These control voltage inputs are labeled as "ctl A", "ctl B", and "ctl C". Each of the inputs is connected to the summing junction of the 741, which forms the "drive voltage" signal by a switch (switches "A on/off", "B on/off", and "C on/off").

Let us briefly explain the difference in circuit operation with and without feedback. In figure 4.2(a) the drive voltage, after passing through an op-amp buffer, is applied to the series combination of a bias resistor and a device under test. The resistance of a bias resistor (usually 100 k Ω in our experiments) is much larger than the differential resistance of the device ($\sim 100 \Omega$), so the current through the device is: $I_{dc} \approx V_{drive}/R_{bias}$, and the device is current biased.

Figure 4.2(b) shows the essential parts of the circuit when the feedback is on. At equilibrium, $V_A = V_{drive} - G_V V_{device} = 0$, and the voltage across the device is proportional to drive voltage: $V_{device} = V_{drive}/G_V$. Suppose, there is a small deviation from equilibrium, e.g., the voltage across the device decreases. Then $V_A > 0$, the output of AMP1 goes negative, which, in turn, makes the output of AMP2 positive. The positive output of AMP2, after being divided by 100, is applied to AMP3, and AMP3 increases its output. Hence, it increases the bias voltage across the device, bringing it to an equilibrium value V_{drive}/G_V . We see that the system is in a stable equilibrium and the device is voltage biased.

4.1.2 Shielding and filtering

In these experiments it is important to minimize rf leakage from room temperature to the device. The DC signal passes through a bias tee before reaching the device. The bias tee (Model K250, Wiltron - Anritsu) effectively blocks rf leakage along DC lines above ~ 30 MHz and up to at least 30 GHz. To further prevent rf leakage along dc lines, all of the dc lines are filtered. Three sets of cryogenic powder filters are installed in the dilution refrigerator - one set is thermally anchored to

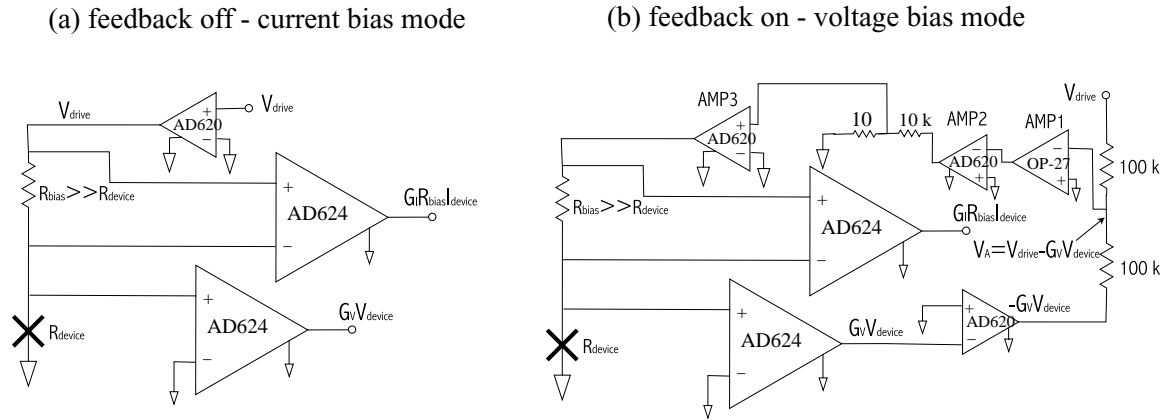


Figure 4.2: Simplified circuit diagram with the feedback circuit off and on.

a 1K plate, another one is anchored to the still (which is at a temperature of 600-700 mK), and the third set of filters is thermally anchored to the mixing chamber. The fabrication procedure of these powder filters and their characteristics are described in detail elsewhere (Wahlgren 1998). Also, room temperature pi filters (Model 56-735-005, Spectrum Control Inc.) are installed between the bias box and the isolator box and on top of the dilution refrigerator. Pi filters have a 3 dB cutoff frequency of 0.8 MHz and better than 13 dB attenuation at frequencies above 10 MHz. Each cryogenic powder filter typically has attenuation better than 20 dB at above $f \approx 300$ MHz. However, below $f \sim 10$ MHz, neither the bias tee, nor the cryogenic and room-temperature filters have large attenuation. To improve rf shielding at lower frequencies, 1.9 MHz coaxial low-pass filters (model BLP-1.9, Mini-Circuits) were installed on DC lines on top of the dilution fridge.

4.2 RF measurement setup

The simplified block diagram of the principal components of the rf setup is presented in figure 4.3. The device is biased by dc current, and ac current fluctuations across the device pass are capacitively coupled to the cryogenic rf amplifier with a frequency band between 1 and 2 GHz. There are two other rf components installed between the device and the amplifier. These are a broadband directional coupler and a circulator. The directional coupler passes through the rf signal from the device to the amplifier with a very small insertion loss and also allows application of rf bias to the device in

the frequency window between 0.1 and 40 GHz. The circulator is a 3-port non-reciprocal device with "cyclic" coupling between the ports (i.e. port 1 is coupled to port 2, but not to port 3; port 2 is coupled to port 3, but not to port 1, and port 3 is coupled to port 1, but not to port 2). The rf signal from the device passes through the circulator to the input of the rf amplifier, and the current noise emitted by the amplifier is "directed" toward the termination on the circulator. The circulator works in a frequency band between 1.25 and 1.75 GHz. The purpose of the circulator is to prevent noise radiated by the amplifier from reaching the device and to make sure the amplifier effectively "sees" a $50\ \Omega$ termination at its input regardless of what the impedance of the device is. In our setup, the noise of the amplifier is comparable to the Johnson noise of a $50\ \Omega$ termination at 4 K. However, the pass band of the circulator is narrower than the noise band of the amplifier. Therefore, the circulator should reduce the rf power reaching the device. The amplified rf signal is passed through a 1.25 to 1.75 GHz bandpass filter. The pass band of the filter matches the pass band of the circulator, so that the ratio of noise power coming from the device to the noise power due to the noise of the amplifiers is maximized. Eventually, the amplified and filtered signal is fed into a crystal detector. A crystal detector is a diode that has a $50\ \Omega$ rf input impedance. The output dc voltage of the diode is directly proportional to the input rf power. Typical sensitivities of commercial crystal detectors are around $1\ \text{mV}/\mu\text{W}$. The dc voltage on the diode is the measure of the power of the signal amplified by the rf chain.

A more detailed schematic of the experimental setup is shown in figure 4.4 The rf current fluctuations in the device pass through a bias tee (model K250, Wiltron - Anritsu), through the directional coupler (model C4238-20, MAC), then through the cryogenic isolator (PAMTECH, frequency band 1.25-1.75 GHz). The rf signal is amplified by a cryogenic amplifier (manufactured by NRAO, frequency band 1-2 GHz). There is a 3dB attenuator on the output of the amplifier to minimize standing waves on the line. The signal then passes through an inside-outside DC block (Narda, cut-off frequency of about 10 MHz), which is installed to break the observed ground loop. The signal is then filtered and further amplified by 2 room-temperature amplifiers (MITEQ, both amplifiers have frequency bands of 1-2 GHz and gains of about 45 dB and 35 dB, respectively). The signal is then branched by a directional coupler (model C4238-10, MAC). The "through" (practically unattenuated) component is applied to a crystal detector (model DHMA18AB, Herotek, frequency band

0.1-19 GHz, sensitivity $\sim 1 \text{ mV}/\mu\text{W}$). The "coupled" (attenuated by 10 dB) component is fed into the spectrum analyzer. Using the spectrum analyzer allows convenient debugging and fast analysis; it also allows monitoring of the output rf signal for the presence of unwanted peaks due to cell phones (signals due to cell phones were seen once due to a loose connector between the circulator and the amplifier). The dc voltage on the output of the crystal detector gives a measure of the total output power of the rf chain.

Performing noise measurements at GHz frequencies has two important advantages as compared to more common low-frequency noise measurements. Performing noise measurements at GHz frequency makes it possible to use large ($\sim\text{GHz}$) bandwidths. Measuring noise power is effectively obtaining a good measure of rms of a fluctuating signal. The ratio of an rms to the error on the rms can be called a "signal-to-noise" ratio for a noise power measurement. This signal-to-noise ratio depends on the bandwidth and the integration time (Dicke 1946):

$$\frac{S}{N} \approx \frac{T_{\text{signal}}}{T_{\text{noise}}} (B\tau)^{\frac{1}{2}}, \quad (4.1)$$

where B is bandwidth and τ is integration time. In our case, noise is the signal so the statistical accuracy of the measured output noise power is $S/N \approx \sqrt{B\tau}$. Using a bandwidth of 0.5 GHz allows us to achieve a very high "signal-to-noise" ratio on noise in our measurements in a short integration time. Most low-frequency noise measurement setups have a bandwidth of ~ 1 MHz or less. Another important advantage of performing noise measurements at higher frequencies is the availability of very low-noise cryogenic rf amplifiers which do not have appreciable $1/f$ -noise.

In the experiments we use a bias modulation scheme (Reznikov et al. 1995), (Schoelkopf et al. 1997), in which a small ac current is applied to the device and the output voltage of the crystal detector is amplified by 10^3 and fed into the lock-in amplifier. The output of the lock-in is proportional to the differential noise - the change of output power of the rf chain as the bias voltage is "dithered" by an ac current. This bias modulation scheme has several advantages. First, the noise of the amplifiers is effectively subtracted because it does not depend on the bias current of the device, assuming that the differential resistance of the device is constant. Moreover, using bias modulation technique enables us to average noise power for a long time and get a good signal-to-noise ratio in our noise measurement. The noise temperature of the device is small (~ 0.4 K at $V = 100\mu\text{V}$). The

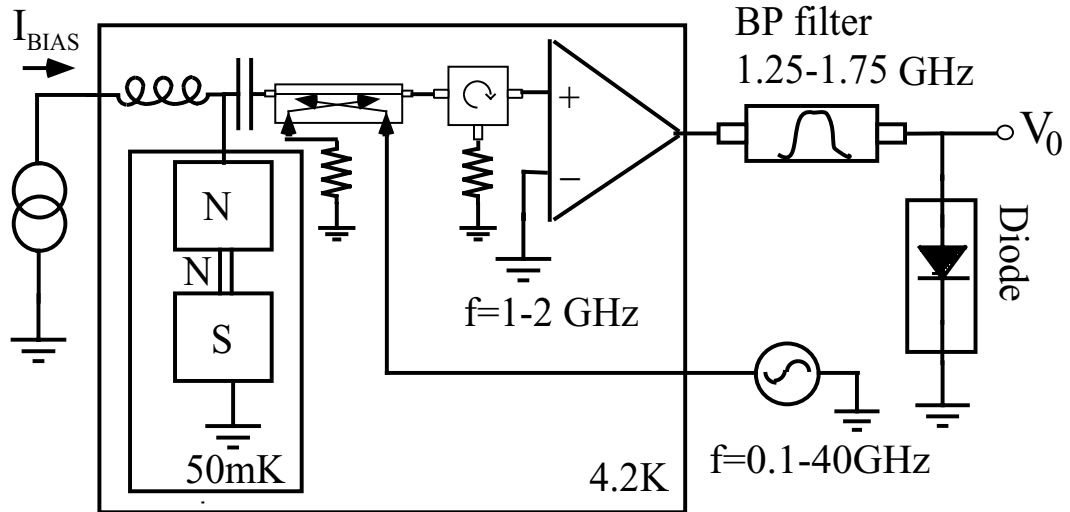


Figure 4.3: Block diagram of the principal components of the measurement setup.

noise temperature of the rf chain is dominated by the noise temperature of the NRAO cryogenic amplifier and is $T_A \approx 5$ K. The noise temperature of the amplifier has a slow drift (probably related to the change of the temperature of the amplifier as the level of He in the He bath changes). If we average noise temperature for a long time, the signal is going to be "washed away" by this drift in the amplifier's noise temperature. The differential noise signal is not affected by the drift of the noise temperature of the amplifier, so by doing a lock-in measurement we can average for a long time and get very good "signal-to-noise ratio" in our noise measurements.

4.3 Model of the measurement setup. Effects of the device impedance change

The raw data that we record from the experiment are five dc voltage signals. Three dc voltage signals are proportional to dc voltage across the device V , dc current through the device I , and the total output noise power of the rf chain P_{out} . A small ac current with amplitude $\Delta I_{ac} \approx (400 \text{ nA}) \cos \omega_{ac} t$ is superimposed on a dc bias current through the device at a frequency $f_{ac} = \omega_{ac}/(2\pi) \approx 460$ Hz. This ac current corresponds to a bias voltage "dither" of about $\pm 2 \mu\text{V}$. This ac voltage is small as

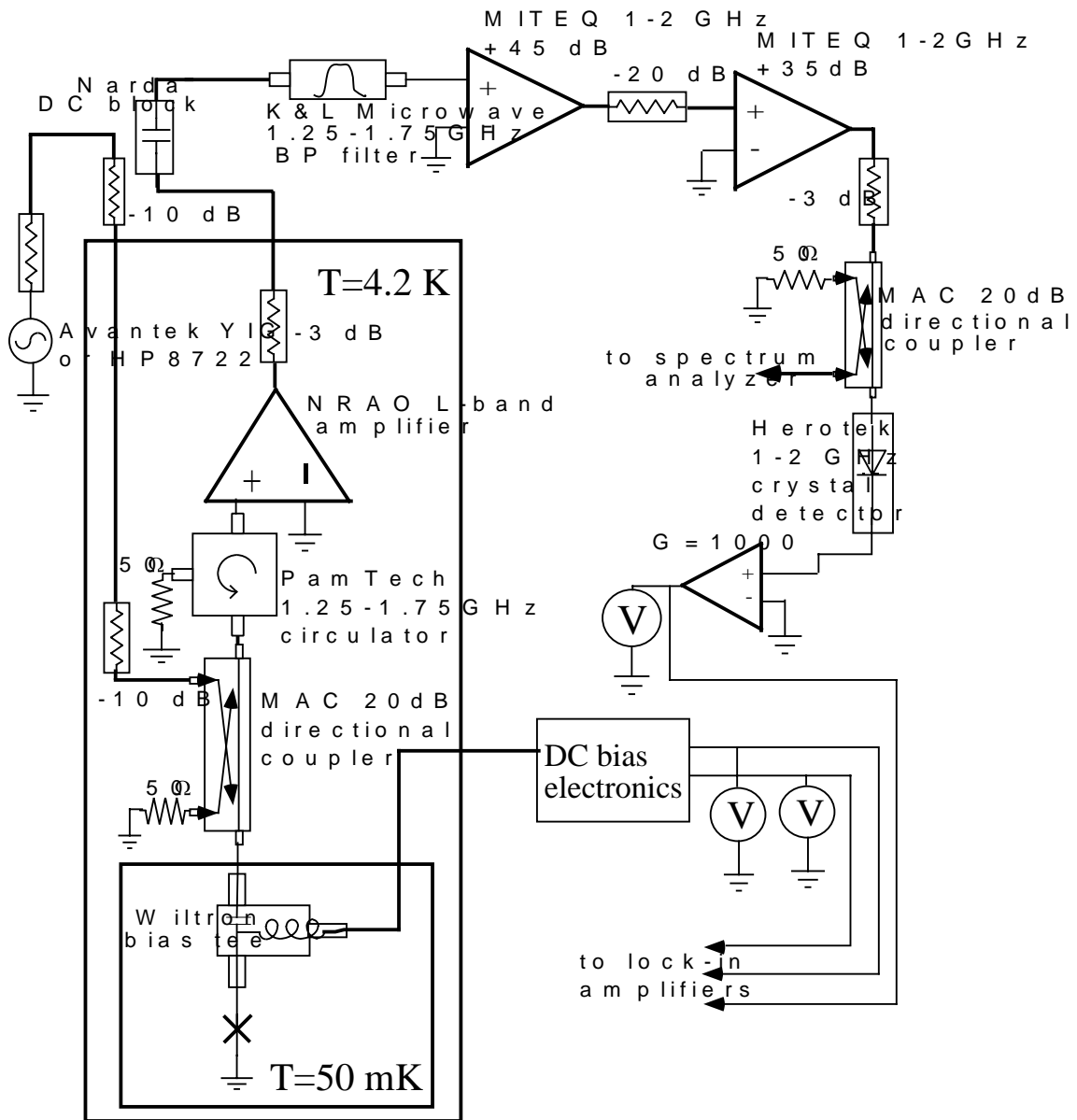


Figure 4.4: Schematic of the measurement setup.

compared to the voltage range of nonlinearities in the conductance and in the noise of the device. The corresponding ac components of the bias voltage ΔV and the change in the total output noise power ΔP_{out} are measured with lock-in amplifiers. The ratio of ΔV to ΔI_{ac} gives the differential resistance of the device:

$$R_{diff} = \frac{dV}{dI} = \frac{\Delta V}{\Delta I_{ac}} \quad (4.2)$$

The ratio of ΔP_{out} to ΔV gives the differential output noise power:

$$\frac{dP_{out}}{dV} = \frac{\Delta P_{out}}{\Delta V} \quad (4.3)$$

We need to convert the recorded dc voltages into physical quantities of interest. Knowing voltage and current gains of our dc measurement setup, it is straightforward to calculate the dc voltage, the current and the differential resistance of the device. It is much more difficult to relate voltages corresponding to P_{out} and ΔP_{out} to noise of the device. In this section we model the noise measurement setup and derive quantitative relations between raw data and the physical quantities of interest.

An important issue for high-frequency noise measurements is rf coupling between the device and the amplifier. To make precise high-frequency noise measurements, it is important to have good coupling (otherwise the signal is lost and the sensitivity degrades). It is also important that coupling stays constant, otherwise a change in coupling may be perceived as a change in the noise. The coupling between a device having an impedance Z and an amplifier with an input impedance Z_A is (Pozar 1993):

$$C = 1 - |\Gamma|^2 = 1 - \frac{|Z - Z_A|^2}{|Z + Z_A|^2} \quad (4.4)$$

The rf amplifiers typically have $Z = R_A = 50\Omega$. Ideally, the impedance of the device is the differential resistance of the device R_{diff} . In practice, however, the parasitic inductances (for example, inductance of wirebonds) and capacitances (capacitance of the contact pads) contribute to the rf impedance of the device. In order to minimize the parasitic reactances the wirebonds were kept short (the length of a wirebond did not exceed ≈ 1 mm) and 2 or 3 wirebonds in parallel were used. The inductance of one wirebond is $L_{wirebond} \sim \mu_0 \times 10^{-3} \text{m} \approx 10^{-9}$ H. There are two sets of wirebonds, each consisting of 2-3 wirebonds in parallel (one set attached to each contact pad), so the total inductance would be $\approx 10^{-9}$ H. At a frequency of 1.5 GHz the inductive impedance is $|X_L| \approx 6 \Omega$.

The size of the contact pads is about $200 \times 250 \mu\text{m}^2$, and the thickness of Si wafer is 12.5 mil (0.32 mm). The capacitance of the pads to the ground plane is $\lesssim 1.6$ fF, which at $f \lesssim 2$ GHz results in capacitive impedance of $|X_C| \gtrsim 5$ k Ω in *parallel* with the device.

A device having a resistance $R = 50 \Omega$ and having $X_L = 6j \Omega$ in series and $X_C = -5000j \Omega$ in parallel will look like having an impedance of $Z = (R + X_L)X_C / (R + X_L + X_C) = (50.1 + 5.5j) \Omega$.

As we will show below, for our noise measurements the important factors are the rf power coupling coefficient given by equation 4.4 and the derivative of the rf coupling with respect to the resistance of the device R . The derivative of the coupling coefficient is needed for correcting for the noise of the circulator that is reflected off of the device. When the resistance of the device is between 39 Ω and 60 Ω , having 6 Ω of parasitic reactance does not change the rf coupling between the device and the amplifier ($Z_A = R_A = 50 \Omega$) by more than 0.4%. Therefore, the inductance of the wirebonds is not significant for the calculation of C . To estimate the importance of the parasitic reactance on the derivative dC/dR we need to compare the following expressions:

$$\frac{dC_1}{dR} = \frac{d}{dR} \left(1 - \frac{(R - R_A)^2}{(R + R_A)^2} \right) \quad (4.5)$$

which neglects the parasitic reactance of the wirebonds and

$$\frac{dC_2}{dR} = \frac{d}{dR} \left(1 - \frac{(R - R_A)^2 + X_L^2}{(R + R_A)^2 + X_L^2} \right), \quad (4.6)$$

which takes into account parasitic reactance $X_L \approx 6 \Omega$. Maximal value of $|dC_1/dR|$ in the region $40 \Omega < R < 60 \Omega$ is $\approx 3 \times 10^{-3} 1/\Omega$, whereas the maximal value of $|dC_1/dR - dC_2/dR|$ in the same resistance interval is $\approx 8 \times 10^{-5} 1/\Omega$. That means that neglecting the parasitic inductance will typically lead to a few percent error in the derivative of coupling dC/dR . An exception is in a narrow interval near $R = 50 \Omega$ where the derivative of rf coupling becomes very small. In this interval, since dC/dR is small, the change of the noise of the circulator reflected off the device is small, and the correction term proportional to dC/dR also becomes negligibly small. As will be shown below, $dC/dR \approx 3 \times 10^{-3} 1/\Omega$ translates into the correction of about 10% to the measured differential noise. The error due to neglecting the parasitic inductance will lead to $\approx 3\%$ error *on the correction term*, i.e., it will introduce $\approx 0.3\%$ error in the noise measurement. This error is

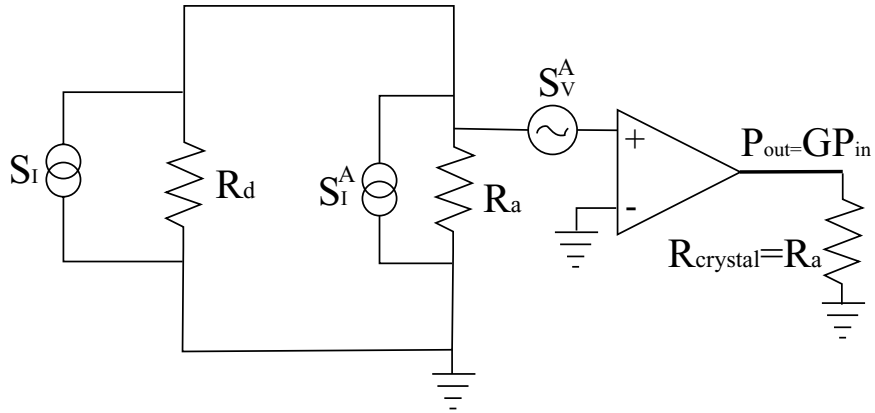


Figure 4.5: Model of the device with rf amplifier.

negligible. Therefore, neglecting X_L in the calculation of dC/dR is justified.

We see that at measurement frequencies (1.25 - 1.75 GHz) the parasitic reactances shouldn't appreciably change C and dC/dR . Therefore, parasitic capacitive and inductive impedances are not important for our experiments. In the following discussion, we neglect parasitic reactances and assume that the rf impedance of the device is equal to its dc differential resistance $Z = R_{diff} = dV/dI$.

The model of a device having differential resistance R_{diff} connected to an amplifier with input impedance R_A is presented in figure 4.5 (Horowitz and Hill 1989). The device is represented as a resistor having a resistance $R_{diff} = dV/dI$ and a current noise source with a current spectral density S_I in parallel with the resistor. The amplifier can be modeled as an ideal voltage amplifier with voltage gain \sqrt{G} connected to a resistor R_A , voltage noise source and a current noise source as shown in figure 4.5. The value of R_A is the input resistance of the amplifier: $R_A = 50 \Omega$. The voltage and current noise sources are used to model the noise of the amplifier. The noise of the amplifier has a component that is independent of the device impedance (voltage noise) and a component that depends on the impedance of the device (current noise). The voltage and the current noise of the amplifier, referred to the input, can be characterized in terms of their spectral voltage and current spectral densities S_V^A and S_I^A , respectively. The output of the amplifier goes to the crystal detector which has an impedance of $R_{crystal} = 50 \Omega$. Since $V_{out} = \sqrt{G}V_{in}$, the output power (power dissipated in the crystal detector) is proportional to the input power, i.e., power dissipated in resistor

R_A . Using the model shown in figure 4.5 and taking into account that $R_A = R_{crystal}$, we can write the output power per bandwidth dP_{out}/df as:

$$\frac{dP_{out}}{df} = G \left(\frac{S_V^A}{R_A} + S_I^A \frac{R_A^2 R_{diff}}{(R_{diff} + R_A)^2} + S_I \frac{R_{diff}^2 R_A}{(R_{diff} + R_A)^2} \right). \quad (4.7)$$

Note that dP_{out}/df is, in general, frequency-dependent because the gain of the amplifier G and the parameters of the noise sources S_I^A and S_V^A are frequency-dependent. Both in equilibrium and out of equilibrium the noise of our devices, S_I , is frequency-independent between 1.25-1.75 GHz. $1/f$ -noise is insignificant at these frequencies, and even at the lowest temperature achieved (≈ 50 mK) the frequency $f_{max} = 1.75$ GHz corresponds to the low-frequency regime of both Johnson-Nyquist noise and shot noise. For mesoscopic conductors, the frequency dependence of the impedance is determined by the energy dependence of the scattering matrices (Büttiker et al. 1993). For a diffusive conductor, the scattering matrices vary with energy over an energy scale of order Thouless energy E_C . It follows that at frequencies, corresponding to energies smaller than E_C , the impedance of a diffusive mesoscopic device should be frequency-independent and equal to its dc impedance. For N-S junctions that we studied, the diffusive transit time $\tau_D \sim L^2/D \ll 1/f_{max} \approx 0.6$ ns, so the impedance at frequencies $f \lesssim f_{max} = 1.75$ GHz is independent of frequency.

In our experiments the output dc voltage of the crystal detector is proportional to the total power output power of the rf chain between 1.25 and 1.75 GHz, so the quantity measured is the total integrated power in the band P_{out} :

$$P_{out} = \int_{f_{min}}^{f_{max}} \frac{dP_{out}(f)}{df} df \quad (4.8)$$

From equations 4.7 and 4.8 it follows that the output power is a linear function of the current spectral density S_I and a complicated function of differential resistance R_{diff} of the device. The output power P_{out} and differential resistance of the device R_{diff} are measured directly in the experiment whereas the physical quantity of interest is S_I . It is desirable to relate P_{out} and R_{diff} to non-equilibrium noise of the device S_I .

First, consider the situation when the differential resistance of the device is not changing, i.e.

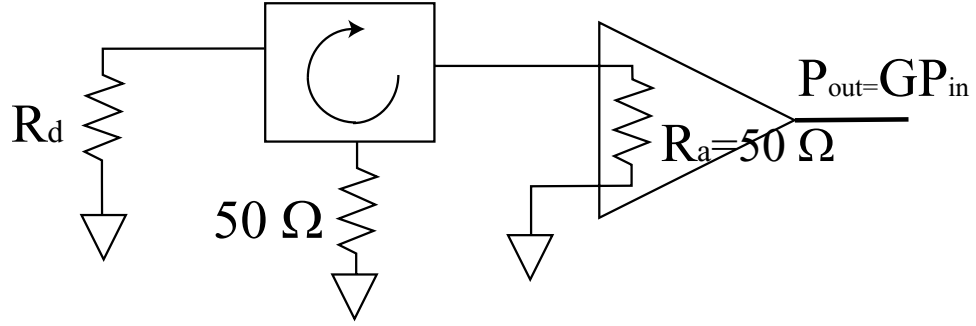


Figure 4.6: Block diagram with the circulator between the device and the amplifier.

$R_{diff} = const$. In this case, S_I is the only variable and the output power is a linear function of S_I : $P_{out} = P_0 + AS_I$, where P_0 and A are constants. If we measure P_{out} for 2 known values of S_I , we can determine P_0 and A . Knowing P_0 and A , we are able to calculate S_I for any output power P_{out} . A convenient way of applying known S_I to the input of the amplifier is to use Johnson-Nyquist noise of the device itself as a calibration signal.

The situation is more complicated when R_{diff} is changing. The main difficulty is that S_V^A and S_I^A are usually not known *a priori* for an rf amplifier. In our measurement setup, we have a 20 dB cryogenic circulator between the device and the rf amplifier. The block-diagram of the essential parts of the setup is presented in figure 4.6. With the circulator placed between the device and the amplifier, the amplifier "sees" a $50\ \Omega$ termination on the circulator, and the contribution of the current noise of the amplifier doesn't change when the impedance of the device changes. The Johnson noise of the $50\ \Omega$ termination gets reflected from the device, and the reflected termination noise gets amplified by the rf amplifier. The main advantage of having an circulator for our experiments is a simpler noise model of experimental setup - instead of having to deal with unknown current noise of the amplifier we need to deal with Johnson current noise of a $50\ \Omega$ termination. Let us introduce effective noise temperature, which is a quantity directly proportional to S_I :

$$T_N = \frac{S_I R_{diff}}{4k_B}. \quad (4.9)$$

For now, we assume the circulator to have zero insertion loss. We can express the output power in temperature units: $T_{out} = (dP_{out}/df)/k_B$. With the circulator between the device and the amplifier,

the output power can be written as:

$$T_N^{out} = G \left(T_A + T_N \frac{4R_A R_{diff}}{(R_A + R_{diff})^2} + T_{iso} \left(1 - \frac{4R_A R_{diff}}{(R_A + R_{diff})^2} \right) \right). \quad (4.10)$$

Here T_A is the noise temperature of the amplifier, T_{iso} is the physical temperature of the 50 Ω termination and T_N is the effective noise temperature of the device. The first term describes the noise of the amplifier (both the contributions due to voltage and current noise; with the circulator in place, neither of them depends on the impedance of the device). The second term describes the noise of the device coupled into the amplifier. The third term describes the 50 Ω termination noise that is partially reflected off of the device and coupled into the amplifier (Dubash et al. 1994). Note that the expression $4R_{diff}R_A/(R_{diff} + R_A)^2$ is exactly the rf coupling between a device having an impedance R_{diff} and an amplifier having an impedance R_A . Knowing R_{diff} , R_A , and T_{iso} , we can determine G and T_A by measuring T_{out} for 2 different known noise temperatures T_N . If the device is well-matched to the amplifier, i.e. if $|R_A - R_{diff}| \ll R_A$, the rf coupling is approximately unity: $C \approx 1$, and equation 4.10 can be simplified:

$$T_N^{out} = G (T_A + T_N). \quad (4.11)$$

Our devices are well-matched to the amplifier. However, the differential resistance of the device changes as a function of the bias voltage. Below, we define the rf coupling between the device and a 50 Ω amplifier as:

$$C(V) = \frac{4R_{diff}(V)R_A}{(R_{diff}(V) + R_A)^2} \quad (4.12)$$

From equation 4.10 we get:

$$\frac{dT_N^{out}}{dV} = G \left(\frac{dT_N}{dV} C(V) + (T_N - T_{iso}) \frac{dC}{dV}(V) \right). \quad (4.13)$$

Note that we have to use equation 4.13 for the calculation of dT_{out}/dV . We cannot use the simplified equation 4.11, because even though $C(V) \approx 1$, we cannot *a priori* say that the contribution of the term proportional to dC/dV is going to be negligible. In fact, for the devices measured, this term cannot be neglected and needs to be taken into account to calculate the differential noise of the

device dT_N/dV from the measured differential output noise dT_{out}/dV .

Equations 4.13 and 4.10 are the main result of this discussion. Knowing gain G of the rf chain and the differential resistance of the device $R_{diff}(V)$, it is possible to calculate differential noise of the device dT_N/dV .

In our experiments, a magnetic field is applied to drive the device normal and to tune magnetic flux through the superconducting loop of Andreev interferometers. The circulator has a permanent magnet and may be affected by the external magnetic field. For the noise measurements in the device driven normal, the circulator is not necessary because the resistance of the device does not change when the Nb is driven normal. For the measurements of the Andreev interferometer, the magnetic field in the center of the magnet does not exceed a few mT. The circulator is physically located about 3 ft from the center of the magnet. In addition, the magnet has compensation coils that reduce the field outside the magnet so that the external magnetic field at the location of the isolator is substantially smaller than 1 mT. This field is much smaller than the magnetic field due to the permanent magnets inside the circulator and will not change the properties of the circulator.

4.4 Calibration

In this section, we describe the calibration procedure which allows us to determine the gain and the noise temperature of the rf chain. The total output noise of the rf system has contributions from the noise of the device and from the noise of the measurement system itself. The noise of the measurement system is dominated by the noise of the cryogenic rf amplifier. We need to subtract the amplifier's noise contribution to access the "pure" noise of the device.

Experimentally, the output noise power of the rf measurement system is measured by measuring a dc voltage across a diode crystal detector. Using 4.11, we can express the dc voltage on the output of the crystal detector V_{out} as:

$$V_{out} = \alpha P_{out} = \alpha G k_B (T_N + T_A) B. \quad (4.14)$$

In equation 4.14, α is the sensitivity of the crystal detector, G is the power gain of the rf chain, T_N is the effective noise temperature of the device, T_A is the average noise temperature of the amplifier

in the band, and B ($= 0.5$ GHz) is the bandwidth (determined by the bandwidth of the isolator and of the bandpass filter). Equation 4.14 can be rewritten as:

$$V_{out} = \tilde{G}(T_{dev} + T_A), \quad (4.15)$$

where \tilde{G} is the "gain" of the measurement setup measured in Volts/Kelvin.

In order to perform an absolute noise measurement, i.e., to obtain an absolute noise temperature of the device T_N from measurement of V_{out} , one needs to know the gain \tilde{G} and the noise temperature T_A of the measurement setup. In order to calculate gain and noise temperature (2 unknown parameters), the output of the measurement system in response to at least 2 signals with different known effective noise temperatures T_N is needed.

We perform the calibration by using Johnson-Nyquist noise of the device itself as a known calibration signal. If we set a bias voltage across the device to zero, the noise temperature of the device is equal to its physical temperature. By changing the mixing chamber temperature of the dilution refrigerator, the intensity of the input noise is varied. Typically, a sweep of the mixing chamber temperature is performed from below 100 mK to 300-600 mK and back down to below 200 mK. The sweep takes about 5 minutes to perform. The device is biased at $V_{dc} = 0$, and the mixing chamber temperature T_{MC} and the output noise V_{out} are recorded. A straight line is fitted for the dependence of $V_{out}(T_{MC})$. The slope of the straight line is equal to the gain of the system G . The intercept of the straight line with the V-axis divided by the gain determines the noise temperature of the measurement system T_A . Using the device itself as a calibration source has several advantages. The rf coupling between the device and the amplifier and the loss in the cables is automatically taken into account by this calibration procedure, because the imperfect coupling and the rf loss affect the calibration signal and the measured signal in the same way, i.e., these factors get absorbed in the calculated gain and noise temperature of the measurement setup.

In figure 4.7 an example of the data obtained in a calibration sweep is presented. A linear fit in the temperature region above 100 mK gives $\tilde{G} = 0.346 \pm 0.02$ V/K and $T_A = 9.3$ K. Data obtained below 100 mK were not included for two reasons. First, at $T < 100$ mK, electrons may be hotter than the mixing chamber temperature because of imperfect coupling to the thermal bath or because of a small rf leak. Second, after the heater is turned on, the temperature of the mixing chamber

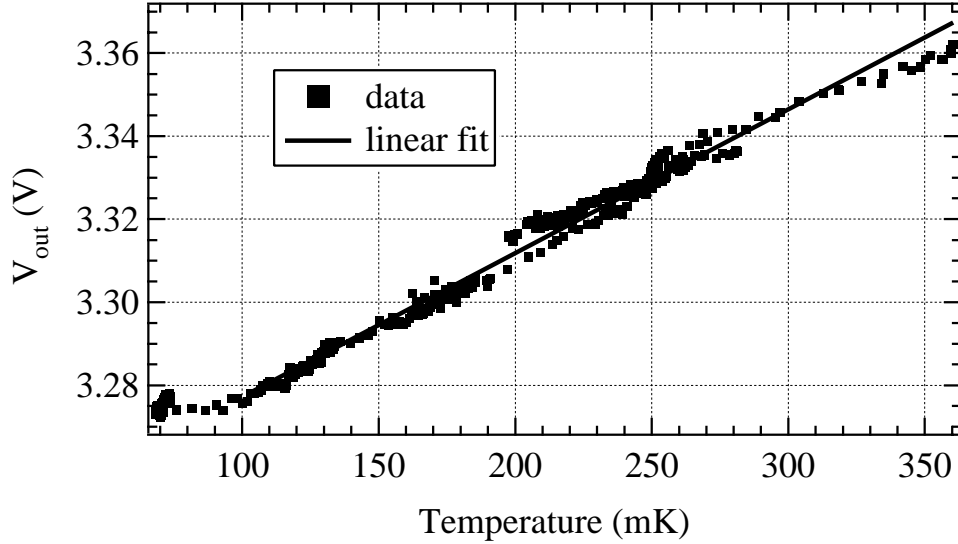


Figure 4.7: Dependence of output dc voltage of the crystal detector ($\times 1000$) vs. mixing chamber temperature. Device is biased at $V = 0$. Linear fit gives $\tilde{G} = 0.346 \pm 0.02$ V/K, $T_A = 9.3$ K.

rises quickly and there is an observable delay between the turning on of the heater and the increase of the Johnson noise of the device - this delay is at least in part responsible for a flat region in the dependence of $V_{out}(T_{M/C})$ at temperatures below 100 mK.

Since the noise temperature of the amplifier may drift over a time course of a few minutes, it is important to make sure that T_A does not change during the calibration. The gain of the rf chain proved to be much more stable than the amplifier noise temperature, but a drift of T_A during the calibration may be perceived as a change in gain. Sweeping the mixing chamber temperature up and down helps detect this - if there is appreciable drift of T_A , it will show as a "hysteresis" in the dependence of $V_{out}(T_{M/C})$. In addition, when the He level in the dewar is low, the gain of the cryogenic amplifier changes, too. To make sure that \tilde{G} and T_A did not drift during the calibration procedure, we performed a sequence of 2 temperature sweeps and used the mean inferred value of \tilde{G} only if the values of \tilde{G} determined in two sweeps separately were consistent to better than 5-6 %. Measuring the gain of the rf chain twice also provides a way to estimate the statistical error of the calculated \tilde{G} : if the values of gain obtained in 2 different temperature sweeps differ by 6 %, the statistical error of the average gain is about 3 %.

It is preferable to be able to perform the calibration sequence once and then to be able to convert the noise data from different data series into absolute units, possibly, from data series taken on different days. One way to do that is to use the high bias voltage dependence of the non-equilibrium noise vs bias voltage in order to convert noise into absolute units. For a given device, the slope of $V_{out}(V)$ at high bias voltages $V \gtrsim 2$ mV does not depend on mixing chamber temperature, at least up to 800 mK. We performed a sweep of bias voltage and measured output noise power (given by V_{out}) and the derivative of output noise power with respect to bias voltage (given by dV_{out}/dV) between the 2 temperature calibration sweeps. Using the dependence of total noise power vs bias voltage, we determined the average slope of $(dV_{out}/dV)_{av.}$ in the bias voltage range between 2.5 and 3 mV. We also calculated average differential noise (measured by lock-ins) in the same voltage interval $(dV_{out}/dV)_{lock-in\ av.}$. Using \tilde{G} determined from temperature sweeps, we can relate $(dV_{out}/dV)_{av.}$ to the average derivative of effective noise temperature of the device with respect to bias voltage $(dT_N/dV)_{av.}$:

$$\left(\frac{dT_N}{dV}\right)_{av.} = \frac{1}{\tilde{G}} \left(\frac{dV_{out}}{dV}\right)_{av.} \quad (4.16)$$

Then we can perform the conversion of lock-in noise data dV_{out}/dV into absolute units:

$$\frac{dT_N}{dV} = \left(\frac{dT_N}{dV}\right)_{av.} \left(\frac{dV_{out}}{dV}\right)_{lockin\ av.}^{-1} \frac{dV_{out}}{dV} \quad (4.17)$$

Equation 4.17 relates the lock-in differential data dV_{out}/dV to the differential effective noise temperature of the device dT_N/dV . Using equation 4.17, one can convert the voltages measured at the output of the rf chain into the characteristics of the non-equilibrium noise of the device.

Moreover, if the calibration sequence, consisting of temperature sweeps and a voltage sweep inbetween, is performed once, conversion of the other noise data for the same device (for example, noise data taken at different mixing chamber temperatures) is possible. As mentioned above, the average slope $(dT_N/dV)_{av.}$ at voltages larger than 2 mV was found to be independent of the mixing chamber temperature. The quantity $(dT_N/dV)_{av.}$ is a property of the device under test alone and does not depend on the amplifier noise temperature or the gain. If we know $(dT_N/dV)_{av.}$ for certain region of high bias voltages for a particular device, we can calculate $(dV_{out}/dV)_{av.}$ and $(dV_{out}/dV)_{lockin\ av.}$ for the same bias voltage range and then perform conversion of differential noise

data into absolute units by using equation 4.17. The amplifier noise temperature T_A and gain \tilde{G} may be different, but if $(dT_N/dV)_{av.}$ is determined previously for this device, it is possible to convert differential noise data to absolute units. The only necessary condition is that the values of \tilde{G} and of T_A do not change appreciably during the sweep. This can be checked by calculating $(dV_{out}/dV)_{av.}$ and $(dV_{out}/dV)_{lockin\ av.}$ for symmetrical ranges of bias voltages and checking that these values are the same.

In the end of the chapter, let us discuss peculiarities of the Johnson noise calibration if a diffusive N-S junction is driven normal by a magnetic field. In this case, the resistance of the device increases by about $10\ \Omega$ due to the series resistance of Nb contact. The question is, whether we should consider the Nb reservoir to be a separate resistor in series with a mesoscopic Au wire. The size of the Nb contact is about $700\ \text{nm} \times 700\ \text{nm}$. We can estimate the electron-electron inelastic length in the Nb film using the theory for 2D films (a film is 2D when its thickness is smaller than the thermal length $\xi = \sqrt{\hbar D / (2\pi k_B T)}$) (Abrahams et al. 1981):

$$\tau_{ee}^{-1} = \frac{e^2 R_{\square}}{2\pi\hbar^2} k_B T \ln \frac{T_1}{T}, \quad (4.18)$$

where T is temperature and $T_1 = 9 \times 10^5 (k_F \ell)^3$, k_F is Fermi wave vector and ℓ is electron mean free path. For $T \approx 0.1\ \text{K}$, we get: $L_{ee}^{Nb} = \sqrt{D\tau_{ee}} \approx 4\ \mu\text{m}$. That means that we cannot consider the Nb contact pad as a reservoir where thermalization of electrons occurs. Rather, it has to be regarded together with the Au wire as a single phase-coherent region. For an N-S device driven normal, both the Johnson noise at zero bias voltage and shot noise at larger bias voltages will be due to a "composite" mesoscopic conductor consisting of a mesoscopic Au in series with a mesoscopic Nb wire. From a technical point of view, this makes the calibration process easier, since one does not have to consider the effects of the extra resistance of the contact pad in series.

Chapter 5

Results of experiments

5.1 Devices measured

Electrical measurements of transport and noise were performed on 2 diffusive N-S junctions. Device 1 had a length of about $0.3 \mu\text{m}$ and width of about 100 nm , device 2 was about 200 nm long and 60 nm wide (as inferred from SEM examination). Device 1 was examined in a much greater detail than device 2. The measurements yielded similar results for both devices. Unless noted otherwise, the results presented in subsequent sections are for device 1. The SEM picture and schematics of both devices is presented in figure 5.1. The parameters of the devices (length of the Au wire L , width of the wire W , thickness of the Au wire d^{Auwire}) and the thickness (d^{Aupad} and d^{Nb}) and sheet resistances (R_{\square}^{Aupad} and R_{\square}^{Nb}) of Au and Nb contact pads are presented in table 5.1. The sheet resistance of the wires was calculated from the measurements of dc resistance of the wires before Nb deposition. The thickness and sheet resistances of contact pads were measured on the films which have the same thickness as contact pads and were deposited at the same deposition parameters as contact pads of the devices.

Device	L (μm)	W (nm)	d^{Auwire} (nm)	D^{wire} (cm^2/sec)	$R_{\square}^{\text{wire}}$ (Ω)	$R_{\square}^{\text{Aupad}}$ (Ω)	d^{Aupad} (nm)	R_{\square}^{Nb} (Ω)	d^{Nb} (nm)
1	0.28	100	10	≈ 30	$\approx 15^{\dagger}$	0.5^{\P}	600	4^{\S}	800
2	0.22	60	10	≈ 30	$\approx 15^{\dagger}$	0.5^{\P}	600	4^{\S}	800

Table 5.1: Physical parameters of diffusive N-S junctions measured.

\dagger - at room temperature, $R_{\square}^{\text{wire}}$ changes only slightly when cooled down.

\P - at $T = 4$ K.

\S - at room temperature.

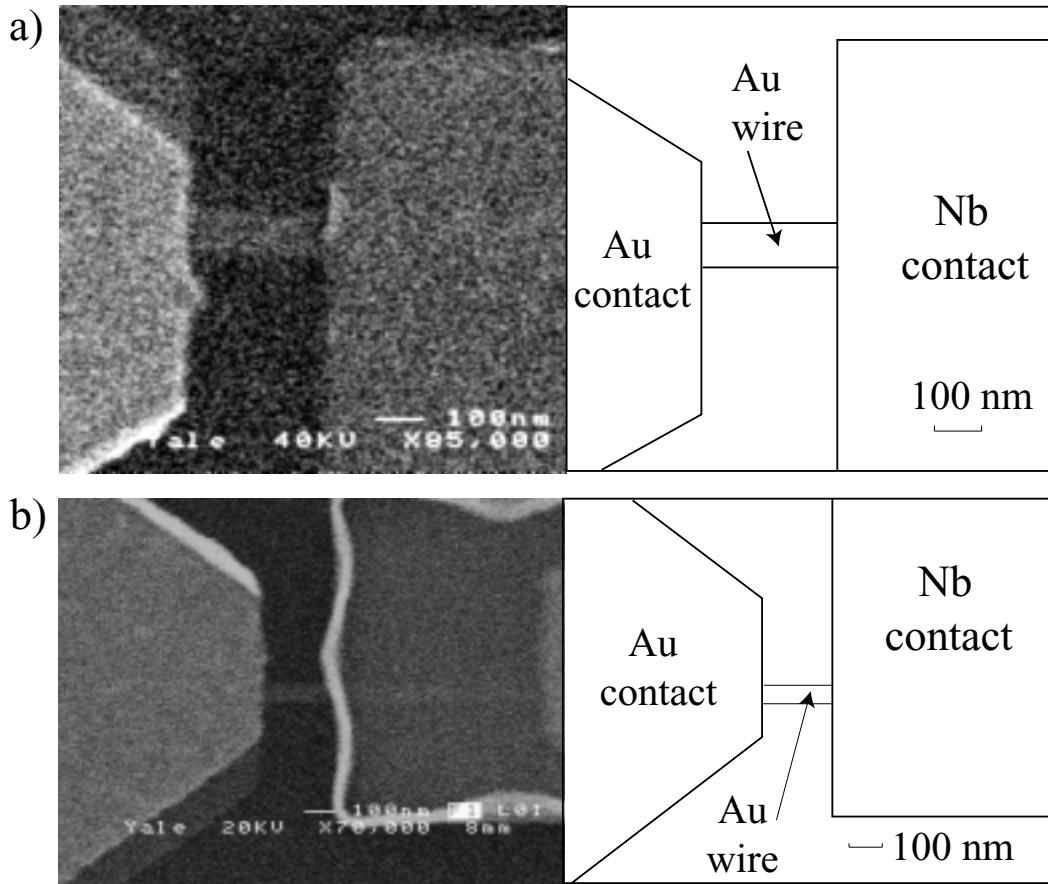


Figure 5.1: a. SEM picture and schematic of device 1; b. SEM picture and schematic of device 2.

5.2 DC electrical characteristics of N-S devices

At temperatures corresponding to energy smaller than Thouless energy a diffusive N-S junction is expected to display reentrant behavior vs. bias voltage. The zero-bias resistance of a diffusive N-S junction is expected to display reentrant behavior vs. temperature. DC conductance measurements were performed on both devices 1 and 2 at mixing chamber temperatures down to 50 mK. Both devices display reentrant behavior vs. bias voltage and temperature. Figure 5.2 presents the dependence of differential resistance of device 1 vs. bias voltage and temperature. Figure 5.3 presents these dependences for device 2.

As seen in figures 5.2 and 5.3, both N-S devices display reentrant behavior vs. both bias voltage and temperature. This behavior is qualitatively consistent with theoretical predictions. Theoretically, the maximal resistance change should be about $0.13R_N$ where R_N is the normal-state resistance of the normal metal wire (Stoof and Nazarov 1996). For our devices, the normal-state resistance of Au wire is not directly accessible for measurement, because the Au wire is in series with Nb contact, which above T_C of Nb adds an additional series resistance of about 10Ω .

At high bias voltages $|V| \gtrsim 600 \mu\text{V}$, the resistance of the devices further increases, as shown in the insets of figures 5.2 and 5.3. This increase is probably due to heating of Nb contact pad and driving parts of Nb contact normal. At bias voltages $\gtrsim 2 \text{ mV}$, most of Nb contact is driven normal. We assume the zero-bias differential resistance of the device $R_{diff}(V = 0)$ to be the normal-state resistance of the normal wire. This assumption is consistent with the estimate of the resistance of the wire inferred from the film sheet resistance measurements.

The magnitude of maximal resistance change is about 6% for device 1 and about 9% for device 2. For both devices, this is smaller than theoretically predicted value of 13%. The difference may be attributed to non-ideal reservoirs (Courtois et al. 1999) and the effects heating by high bias voltages. Also, a bias voltage of $100 \mu\text{V}$ corresponds to $T \sim eV/k_B \sim 1 \text{ K}$, and at 1 K the electron-electron inelastic length L_{ee} should be about $1 \mu\text{m}$. Reentrance effect depends on phase coherence of electrons in normal metal wire L_φ , which is usually smaller than L_{ee} (Altshuler et al. 1982). Reduction of L_φ due to finite bias voltages could cause the maximal resistance change become smaller than expected for the case $L_\varphi = \infty$. The magnitude of the maximal correction can also be reduced below 13% due to disorder at the N-S interface. According to the numerical predictions (Courtois et al. 1999), for

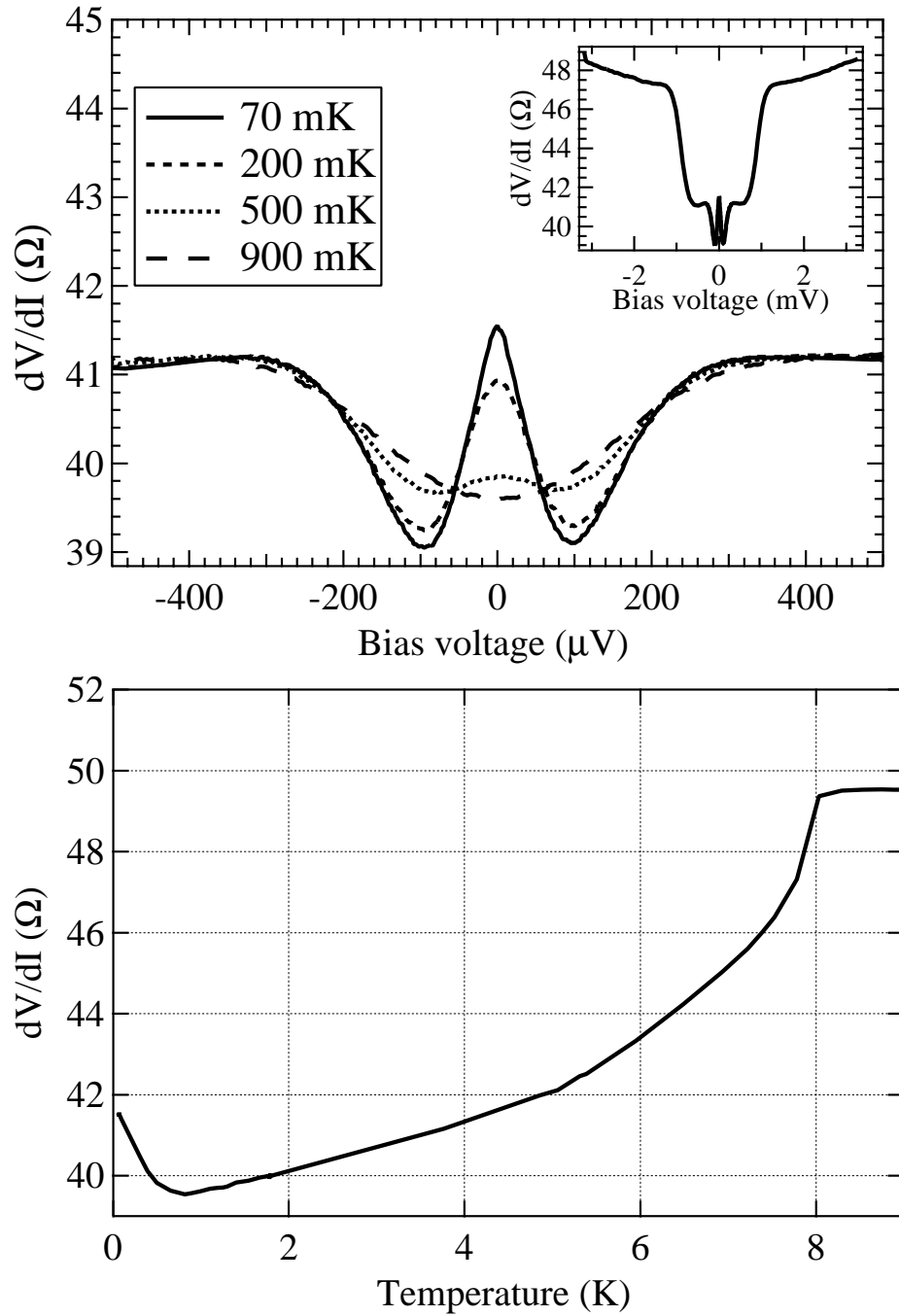


Figure 5.2: Dependence of differential resistance dV/dI of device 1 on bias voltage and temperature. Top: dV/dI vs. bias voltage at several mixing chamber temperatures. The inset shows wider range of bias voltages. Bottom: zero-bias differential resistance vs. temperature.

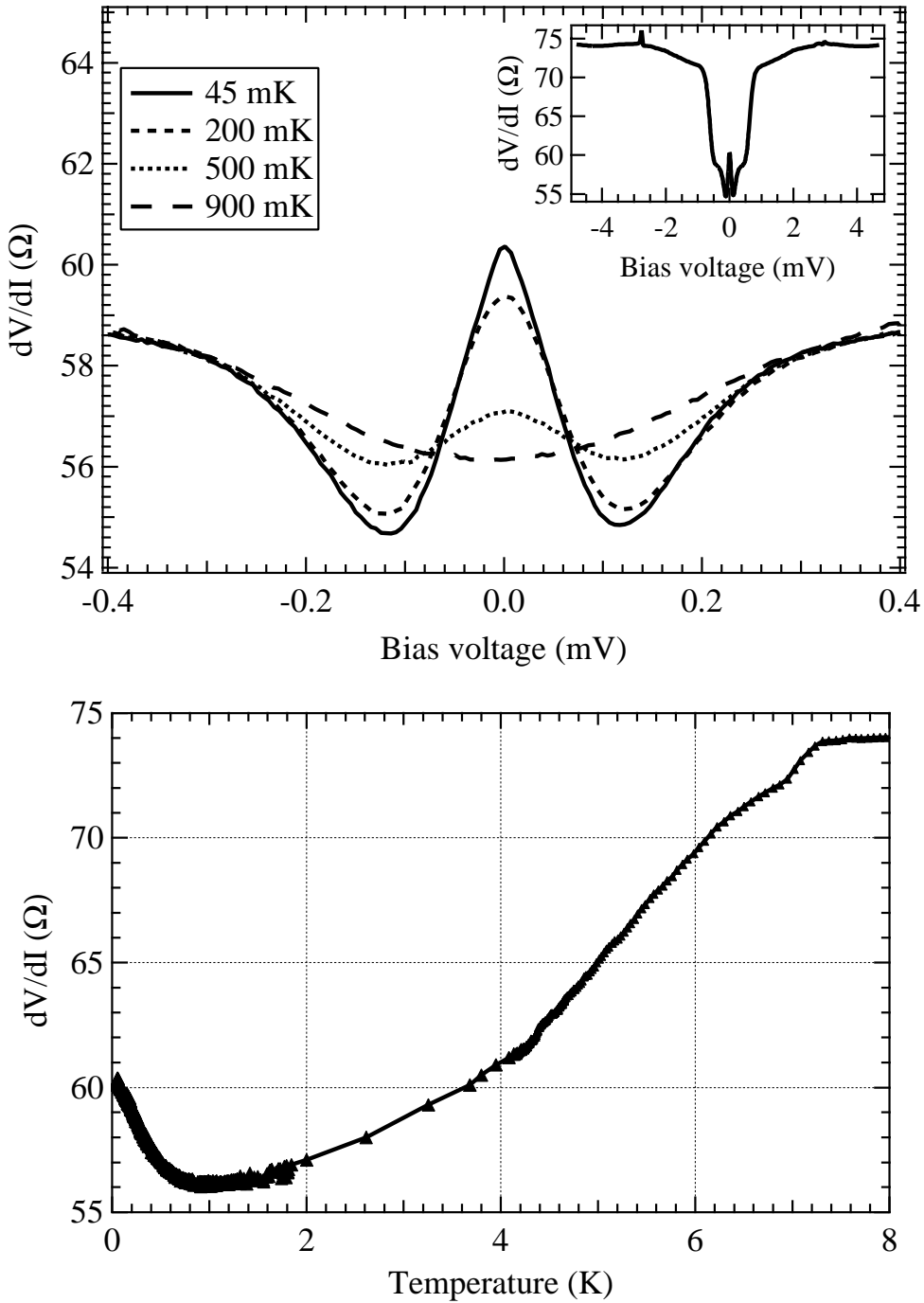


Figure 5.3: Dependence of differential resistance dV/dI of device 2 on bias voltage and temperature. Top: dV/dI vs. bias voltage at several mixing chamber temperatures. The inset shows wider range of bias voltages. Bottom: zero-bias differential resistance vs. temperature.

the ratio of an N-S interface resistance to the diffusive wire resistance $R_T/R_N = 0.2$, the magnitude of resistance change is reduced from 13% to about 9-10%. All the described effects will tend to decrease maximal correction to the resistance, and we cannot distinguish individual contributions of each mechanism. However, our observation of reentrant behavior is qualitatively consistent with theoretical predictions for a diffusive N-S junction with a transparent interface between a normal metal and a superconductor.

5.3 Shot noise measurements in diffusive N-S junctions

5.3.1 Dependence of noise on bias voltage

The top panel of figure 5.4 presents the bias voltage dependence of the derivative of effective noise temperature vs. bias voltage dT_N/dV (further referred to as "differential noise") and differential resistance of the device at mixing chamber temperature 70 mK. As bias voltage is increased, the derivative of noise temperature increases to about 4 K/mV and then decreases at bias voltages above 200 μV . A bias voltage of 200 μeV corresponds to temperature $T \sim eV/k_B = 2.5$ K. At such energies the electron energy relaxation length L_e may be comparable to the length of the device. We cannot calculate L_e for strongly non-equilibrium distribution, we will have to make a rough estimate: $L_e(V) \sim L_e(T = eV/k_B)$. From figure 2.1, at $T \approx 2.5$ K, the electron-electron inelastic length is $L_{ee} \approx 0.8 \mu m$ and the electron-phonon inelastic length is $L_{e-ph} \approx 1.2 \mu m$. Assuming that the electron-phonon and electron-electron scattering rates add independently, the energy relaxation length would be $L_e = (L_{ee}^{-2} + L_{e-ph}^{-2})^{-1/2} \approx 0.7 \mu m$. This estimate indicates that at $V \sim (k_B/e) \times 2.5 K \approx 200 \mu V$ transport in the device should still be elastic. A potential caveat of this argument is that we took energy relaxation length at equilibrium, whereas the quasiparticle distribution in the device can be strongly non-equilibrium.

Another, more abrupt decrease of differential noise occurs at bias voltages $V \gtrsim 800 \mu V$, in the voltage range where the differential resistance of the device increases, presumably due to the heating of Nb contact. At $V \gtrsim 800 \mu eV$ (which corresponds to ~ 10 K), the dominant energy relaxation mechanism is likely to be electron-phonon scattering, and the sample is going to be shorter than electron-phonon length ($L \ll L_{e-ph}$), so at such high bias voltages non-equilibrium noise is likely to

be due to Johnson-Nyquist noise of phonon-cooled electrons, and not due to shot noise.

Our primary object of interest is shot noise, i.e., non-equilibrium noise in the regime of elastic transport. Therefore, we concentrate on the behavior of non-equilibrium noise at small bias voltages ($\lesssim 200\mu V$) where, according to our estimates, transport is elastic.

The bottom panel of figure 5.4 presents differential noise vs. bias voltage at different mixing chamber temperatures. At $T_{MC} = 70$ mK the increase to of the differential shot noise to the "asymptotic" value of ≈ 4 K/mV occurs on a voltage scale of $\sim 25 \mu V$, which is a few times $k_B T$ at 70 mK. As the mixing chamber temperature is increased, the crossover from Johnson to shot noise occurs over a larger interval of bias voltages, which approximately correspond to a few times $k_B T$. Overall, the differential noise behaves in qualitative agreement with theoretical expectations.

Let us make a more quantitative comparison. In figure 5.5 we present experimentally measured and theoretically predicted dependence of differential noise temperature on bias voltage for device 1. The theory curves are the predictions of a "naive" theory which is valid for $E \ll E_C$ and also for $E \gg E_C$. At these energies, $R_{NS} = R_N$, and, using equation 2.66, the bias voltage dependence of the effective noise temperature can be written as:

$$T_N^{NS}(V) = \frac{2}{3}T + \frac{1}{3} \frac{eV}{k_B} \coth\left(\frac{eV}{k_B T}\right). \quad (5.1)$$

Theory curves in figure 5.5 are obtained by taking a finite difference of equation 5.1:

$$\left(\frac{dT_N^{NS}}{dV}\right)_{theor} = \frac{T_N^{NS}(V + \Delta V) - T_N^{NS}(V - \Delta V)}{2\Delta V} \quad (5.2)$$

with $\Delta V = 2 \mu V$ which corresponds to the ac bias voltage amplitude used in experiment.

We see that at temperatures 70 mK and 200 mK the "asymptotic" value of dT_N/dV is close to the theoretically predicted value $e/(3k_B) = 3.87$ K/mV, but the detailed shape of the crossover from Johnson noise to shot noise is different. Experimentally, the crossover occurs on a wider voltage scale than predicted by theory. Exceptions are the data taken at 70 mK, where the experimentally observed crossover width is in part due to ac voltage drive of $\sim 4 \mu V$ p-p. At higher temperatures the value of dT_N/dV does not reach the expected asymptotic value. This behavior is not understood and is somewhat counterintuitive. At temperatures below ~ 2 K the electron energy relaxation length

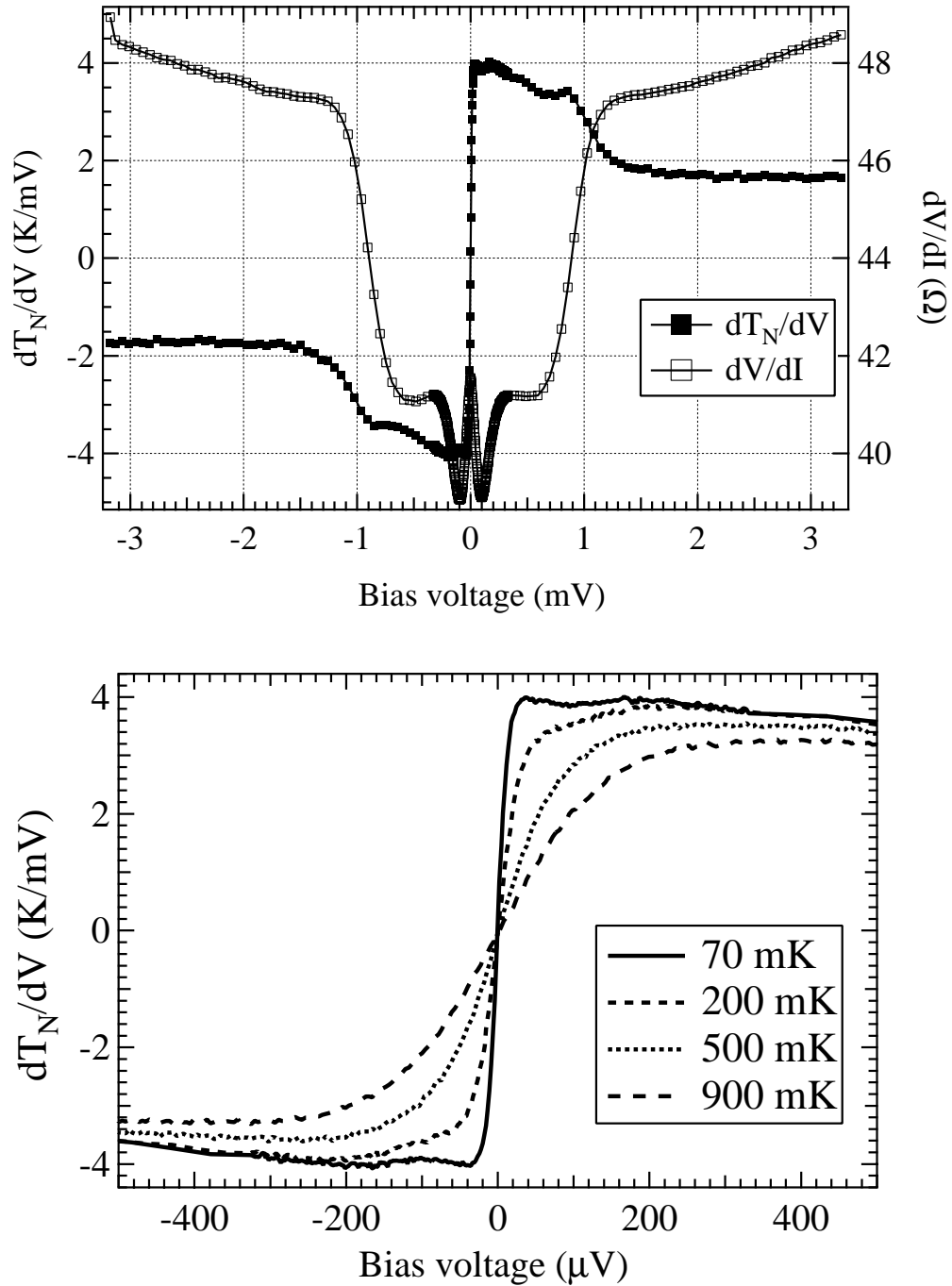


Figure 5.4: Top: dependence of differential non-equilibrium noise dT_N/dV and R_{diff} on bias voltage for device 1 at $T_{M/C} = 70$ mK; bottom: dependence of differential shot noise vs. bias voltage for device 1 at several mixing chamber temperatures.

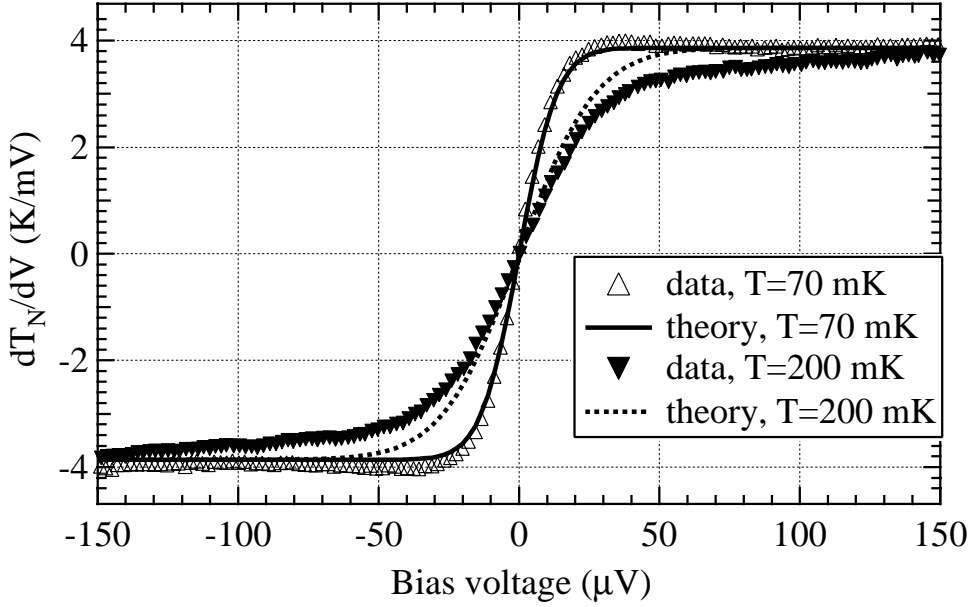


Figure 5.5: Theoretical and experimental dependence of differential shot noise dT_N/dV of device 1 vs. bias voltage at $T_{MC} = 70$ mK and 200 mK.

is expected to be dominated by electron-electron scattering: $L_e \approx L_{ee}$. Therefore, one may expect that the increase of the mixing chamber temperature will tend to *increase* differential noise dT_N/dV (make dT_N/dV closer to hot-electron noise which has a larger slope than shot noise).

5.3.2 Correction for the change of the differential resistance of the device

As discussed in chapter 4, the differential output noise temperature of the rf chain (a quantity that is measured with a lock-in amplifier) is related to the differential noise temperature of the device (equation 4.13):

$$\frac{dT_N^{out}}{dV} = G \left(\frac{dT_N}{dV} C(V) + (T_N - T_{iso}) \frac{dC}{dV}(V) \right), \quad (5.3)$$

where $C(V)$ is the rf coupling between the device and the amplifier:

$$C(V) = \frac{4R_{diff}(V)R_A}{(R_{diff}(V) + R_A)^2}, \quad (5.4)$$

T_{iso} is the physical temperature of the termination on the circulator. Let us estimate the relative magnitude of the 2 terms in brackets in equation 5.3. Since $C(V) \approx 1$, the first term is: $(dT_N/dV)C(V) \approx 4 \text{ K/mV}$. If the resistance of the device is close to 50Ω , i.e., $|R_{diff} - R_A| \ll R_A$, then

$$\left| \frac{dC}{dV} \right| \approx \frac{2(R_{diff}(V) - R_A)}{(R_{diff}(V) + R_A)^2} \frac{dR_{diff}}{dV}. \quad (5.5)$$

From figures 5.2 and 5.3, we can estimate maximal values of dR_{diff}/dV , for example, for device 1: $(dR_{diff}/dV)_{max} \sim 4 \times 10^4 \Omega/V$. The difference $R_{diff} - R_A \sim 10 \Omega$, and the second term in equation 5.3 is:

$$(T_N - T_{iso}) \frac{dC}{dV} \sim 4K \frac{20 \Omega}{10^4 \Omega^2} 4 \times 10^4 \frac{\Omega}{V} \sim 300V/K \quad (5.6)$$

We see that the change in output noise due to the change in rf power, reflected off the device, can be about 5-10% of the "true" change of the noise temperature of the device. Knowing dC/dV , T_{iso} , and $T_N(V)$, we can correct for the change in rf power, reflected from the device, and calculate differential noise due to change in the effective noise temperature of the device alone:

$$\frac{dT_N}{dV} = \frac{1}{G} \frac{dT_N^{out}}{dV} + (T_{iso} - T_N) \frac{dC}{dV}(V) \quad (5.7)$$

Let us make a couple of remarks regarding equation 5.7. First, for our devices, $C(V)$ can be replaced by 1 when deriving equation 5.7 from 5.3, because for R_{diff} between 40 and 60 Ω , $C(V) \gtrsim 0.99$, so the possible error does not exceed 1%. Second, if we are interested in $dT_N(V)/dV$ at small bias voltages ($\lesssim 200 \mu\text{V}$ or so), $T_N(V)$ has to be known only approximately, because at these bias voltages $T_N(V) \lesssim 0.8 \text{ K}$, and its contribution is small compared to $T_{iso} \sim 4 \text{ K}$.

All the differential noise data presented above both for device 1 and device 2 have been corrected according to the procedure described here. The differential resistance $R_{diff}(V)$ was numerically differentiated with respect to the bias voltage, and $dC/dV(V)$ was calculated from equation 5.5 with $R_A = 50 \Omega$. The dependence $T_N(V)$ was calculated from the total output power of the rf chain (the amplifier noise was subtracted, the gain G was obtained in a Johnson noise calibration as described in chapter 4). Then the differential noise of the device dT_N/dV was calculated using equation 5.7.

Figures 5.6 and 5.7 show the uncorrected differential noise $(dT_N^{out}/dV)/G$ and dT_N/dV obtained

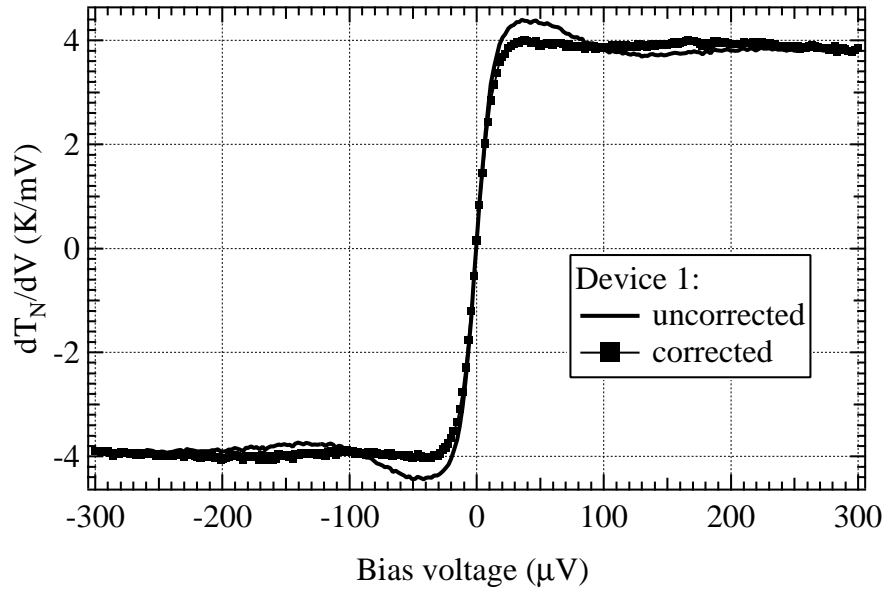


Figure 5.6: Uncorrected differential noise $(dT_N^{out}/dV)/G$ and corrected differential noise dT_N/dV of device 1 at 70 mK.

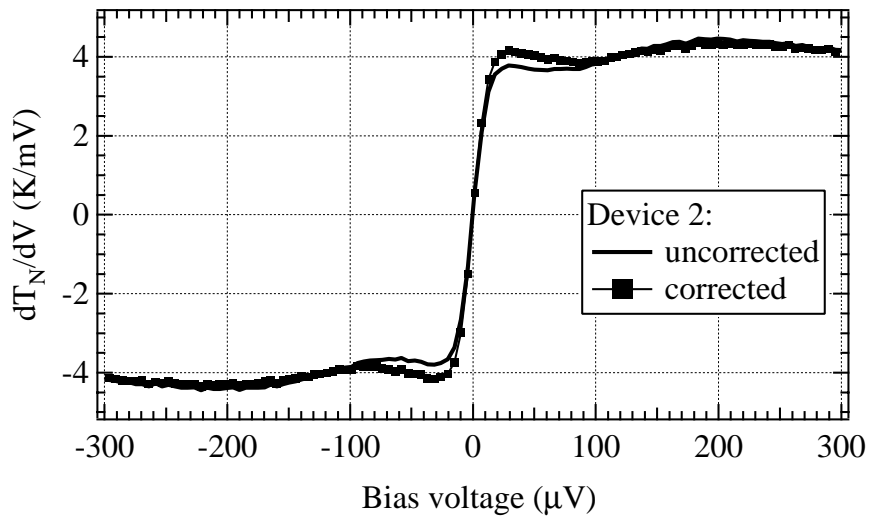


Figure 5.7: Uncorrected differential noise $(dT_N^{out}/dV)/G$ and corrected differential noise dT_N/dV of device 2 at 50 mK.

by the procedure described above for device 1 and device 2. We see that for both devices the correction term contributes up to $\sim 5\text{-}10\%$ of measured differential noise. We also see that for device 1 at bias voltages of about $50\ \mu\text{V}$ the uncorrected noise "overshoots" the corrected differential noise, whereas for device 2 uncorrected noise "undershoots" corrected dT_N/dV . This is to be expected, because the differential resistance of device 1 is *smaller* than $50\ \Omega$, whereas the differential resistance of device 2 is *larger* than $50\ \Omega$. When R_{diff} decreases for device 1, the rf power reflected from the device *increases*, which makes dT_{out}/dV increase. For device 2 it works the other way - when R_{diff} decreases, the rf power reflected from the device *decreases* as well, which leads to decrease of dT_{out}/dV .

5.3.3 Estimate of the errors of correction for reflected rf power

In this section, we make an estimate of systematic errors of the correction procedure. From equation 5.7, we can see, that there are three main potential sources of systematic error: the error in calibrating the gain of the rf chain G , the uncertainty in the temperature of the $50\ \Omega$ termination on the circulator T_{iso} , and the uncertainty of the coupling between the device and the amplifier $C(V)$ due to the fact, that the impedance of the amplifier as seen by the device through the circulator may not be exactly equal to $50\ \Omega$. The uncertainty in gain G is determined by the error of the Johnson noise calibration and is about 3%. When the He level in the cryostat is above the circulator, the physical temperature of the $50\ \Omega$ termination on the circulator is 4.2 K. The Johnson noise of the termination is somewhat attenuated while passing the circulator, but the loss of the circulator should behave like a matched attenuation, so the power radiated toward the device should correspond to temperature close to 4.2 K.

In order to estimate how the power reflected from the device varies as a function of the differential resistance of the device, we performed a test of the circulator at room temperature. The block diagram of the experiment is shown in figure 5.8. Both the source and the ac voltmeter in figure 5.8 are incorporated in the network analyzer HP8722D and have impedances very close to $50\ \Omega$. The network analyzer measures the transmission from port 3 to port 2, and the resistance R is varied. Varying R mimics the effects of the device impedance change on the change of Johnson noise of the termination at port 3 reflected off the device. In figure 5.9 we show the average ratio of power

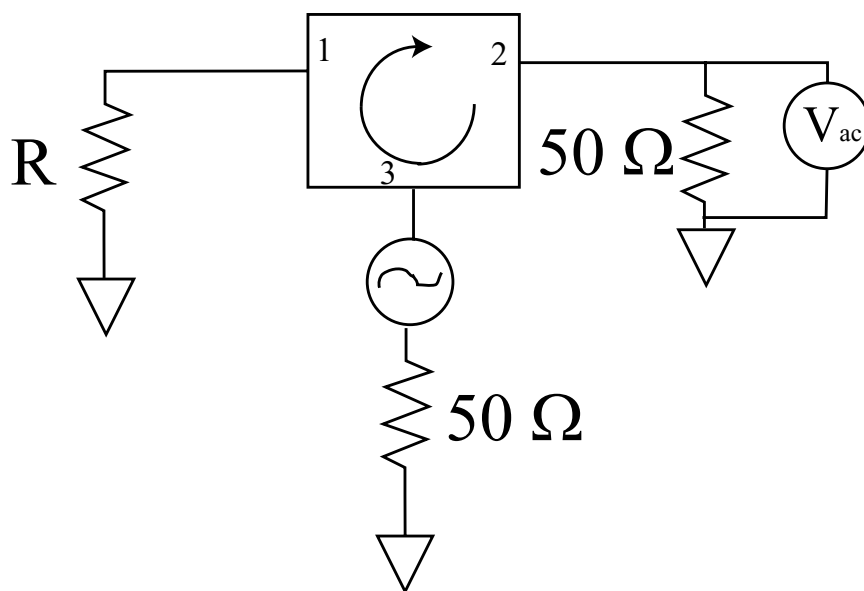


Figure 5.8: Block diagram of the experiment testing the circulator.

transmitted from port 3 to port 2 to the power incident on port 2: P_2/P_3 between 1.25 and 1.75 GHz vs. the value of resistance R . The power displays a minimum near $R = 50 \Omega$. The dependence of power on load resistance is fitted by the dependence

$$\frac{P_2}{P_3} = A^2 + \frac{(R - R_A)^2}{(R + R_A)^2}, \quad (5.8)$$

where A^2 describes leakage of incident power from port 3 to port 2 directly, and the second term describes the power, which is incident on port 3, then is coupled to port 1, is reflected off the resistance R and then gets coupled to port 2. The fit on the graph is for $A = 0.19$ and $R_A = 51.5 \Omega$ - these values give the best agreement with experimental data. The agreement is not perfect, and is better at lower load resistances. This may be in part due to the fact that the chip resistors of larger value have larger physical dimensions and, therefore, have larger parasitic reactances. We infer, that the R_A is different from the "ideal" value of 50Ω by not more than about 2Ω .

In figure 5.10, we re-plot differential noise dT_N/dV vs. bias voltage of device 1 at 70 mK and show our estimated error bars due to uncertainties of R_A and T_{iso} . The uncertainty of the gain results in uncertainty of the overall scale of dT_N/dV , but it will not change the shape of the curve.

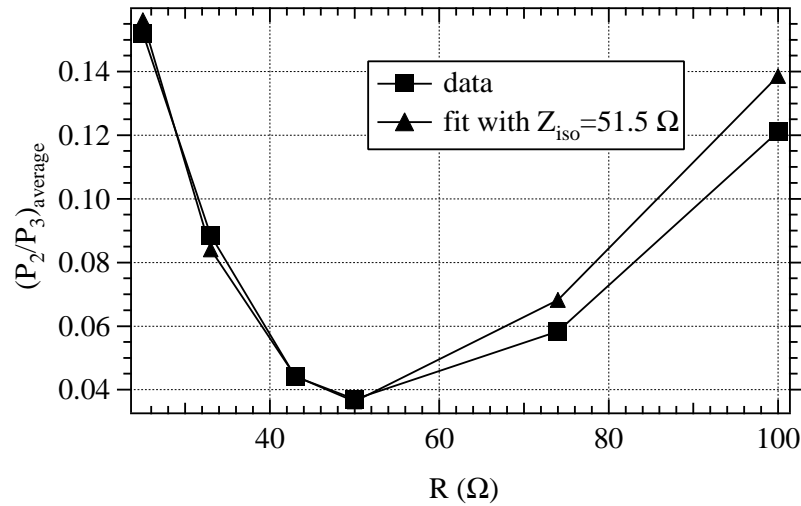


Figure 5.9: Dependence on the ratio P_3/P_2 on the "load" resistance R .

The $\sim 3\%$ error bars due to uncertainty of gain are not shown. The error bars shown are due to "worst" combinations (i.e., combinations giving largest deviations from "ideal" case of $R_A = 50 \Omega$ and $T_{iso} = 4 \text{ K}$) of $\pm 2 \Omega$ error in R_A and $\pm 1 \text{ K}$ error in T_N . At bias voltages where the differential resistance of the device does not change much, the error is dominated by the error in the gain of rf chain. At bias voltages where the resistance of the device changes most steeply with bias voltage, the error is larger than the gain error due to contributions of the uncertainties of R_A and T_N . Overall, the relative error in dT_N/dV due to uncertainties of R_A and T_{iso} does not exceed about 5% for device 1. Added in quadratures with an uncertainty of 3% of the rf chain gain, the overall error in determining differential noise temperature of the device dT_N/dV should not exceed 6%. The corrected differential noise with estimated error bars due to uncertainty of T_{iso} and R_A for device 2 is shown in figure 5.11. The differential resistance change for device 2 is larger, than for device 1, and the errors bars are somewhat larger, than for device 1.

Let us make a few remarks regarding our error estimates for dT_N/dV . The error is proportional to the change in rf coupling dC/dV , which, in turn, is proportional to the change of differential resistance of the device dV/dI . In general, we expect the error to be larger for devices with larger change of differential resistance. For a diffusive N-S device the error is going to be larger at lower temperatures, where the change in resistance is larger. In the next chapter, we will discuss possible

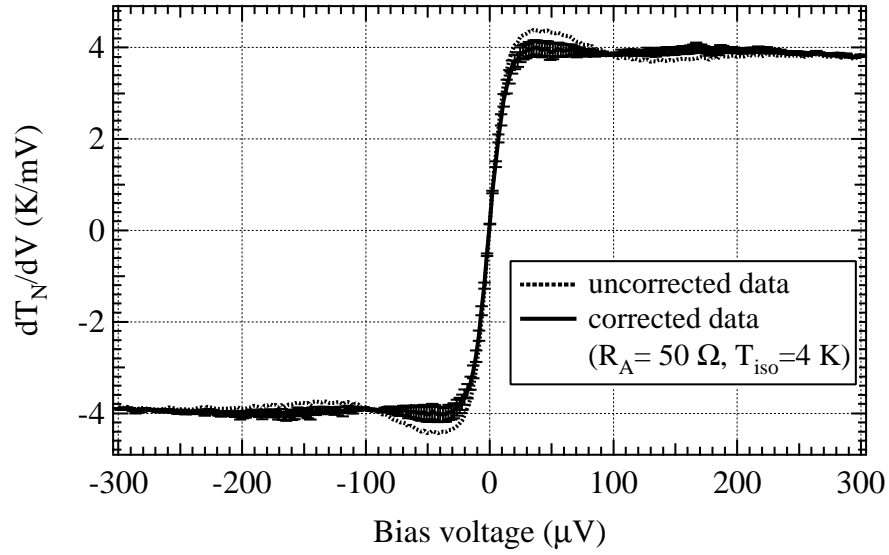


Figure 5.10: Uncorrected differential noise and corrected dT_N/dV for device 1 with error bars due to uncertainties in R_A and T_{iso} . The error bars are shown for "worst" combinations of $\pm 2 \Omega$ error in R_A and ± 1 K error in T_{iso} .

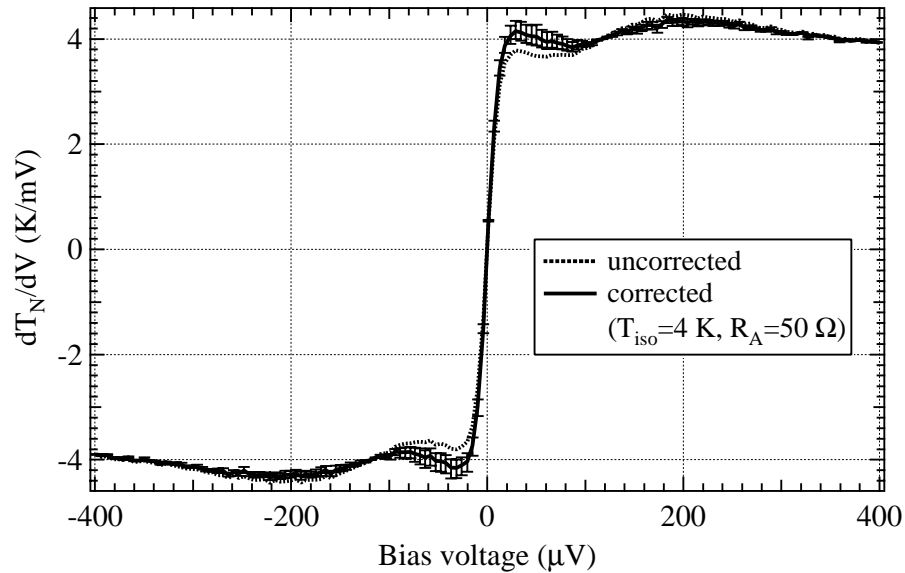


Figure 5.11: Uncorrected differential noise and corrected dT_N/dV for device 2 with error bars due to uncertainties in R_A and T_{iso} . The error bars are shown for "worst" combinations of $\pm 2 \Omega$ error in R_A and ± 1 K error in T_{iso} .

improvements of the setup, which should make the correction procedure easier and more accurate.

5.3.4 Comparison of shot noise between different N-S devices

As seen in figures 5.10 and 5.11, the dependences of differential noise temperatures are quite similar for both N-S devices that we measured. At bias voltages below $\sim 100 \mu\text{V}$, the difference between dT_N/dV for device 1 and device 2 is smaller than the size of error bars. At bias voltages between $100 \mu\text{V}$ and $300 \mu\text{V}$, device 2 displays somewhat higher (by up to $\sim 10\%$) differential noise than device 1. A 10% difference is larger than the errors due to uncertainty of T_{iso} , R_A and gain of the rf chain. At bias voltages between 100 and $300 \mu\text{V}$ non-equilibrium noise exhibited by device 1 and device 2 is different. This difference may occur due to different ratios of interface resistance to the normal wire resistance for device 1 and device 2. It may also be due to difference in the amount of heating in the leads.

Theoretical predictions have been made for shot noise of diffusive N-S junctions at arbitrary energies (Belzig and Nazarov 2001). The prediction is that the quantity dS_I/dV exhibits a broad peak at bias voltage corresponding to a few E_C . In order to compare our data with theoretical predictions at $E \sim E_C$, we convert dT_N/dV into dS_I/dV :

$$\frac{dS_I}{dV} = \frac{4k_B}{R_{diff}} \frac{dT_N}{dV} - \frac{4k_B T_N}{R_{diff}^2} \frac{dR_{diff}}{dV} \quad (5.9)$$

In figure 5.12(a) we present the bias voltage dependence of normalized differential resistance R_{diff}/R_N for both devices. We assume a zero-bias differential resistance equal to R_N . In figure 5.12(b) we present the bias voltage dependence of the dimensionless quantity $(R_N/e)(dS_I/dV)$ for device 1 and device 2.

We see, that both devices 1 and 2 have similar qualitative behavior, both as far as differential resistance and non-equilibrium noise is concerned. At a quantitative level, the transport and noise behavior of devices 1 and 2 are different. Device 2 has larger correction to the resistance, and the quantity $(R_N/e)(dS_I/dV)$ is larger at bias voltages larger than $\sim 70 \mu\text{V}$. For both devices the dependence of $(R_N/e)(dS_I/dV)$ has a broad peak at finite bias voltages, in qualitative agreement with theory (Belzig and Nazarov 2001). Note, however, that the overall scale of the quantity

$(R_N/e)(dS_I/dV)$ is affected by the choice of R_N , an increase of R_N by 10% for device 1 will make $(R_N/e)(dS_I/dV)$ equal for both devices at bias voltages larger than 150 μV .

5.3.5 Non-equilibrium noise of an N-S device driven normal

The superconductivity of Nb contact can be suppressed by applying a magnetic field. We applied a magnetic field of 6 T. Thin Nb film is a type II superconductor, so even at 6 T the superconductivity of Nb is not completely suppressed. The effects of superconductivity are visible in the differential resistance of the device near zero bias voltage. These effects are small - the relative decrease of differential resistance at zero bias voltage is less than 0.5%, and the resistance becomes independent of bias voltage at bias voltages $|V| > 40 \mu\text{V}$. Application of higher magnetic fields led to the heating of the mixing chamber temperature above 100 mK. Measurements of shot noise vs. bias voltage were performed at $B = 6 \text{ T}$ at different mixing chamber temperatures. The dependence of shot noise on bias voltage for device 1 at several different mixing chamber temperatures is presented in figure 5.13. The bottom panel of figure 5.13 presents shot noise data and theoretical predictions for mixing chamber temperatures of 50 and 800 mK. We see that the "asymptotic" value dT_N/dV is close to the expected value of $e/(6k_B)$. At 70 mK the shot noise is larger than expected for the normal conductor. It is possible, that this is due to not completely suppressed superconductivity of Nb contact. Another possible mechanism for this increased non-equilibrium noise is heating of the reservoirs. The shape of dT_N/dV vs. bias voltage at 50 mK on the top panel of figure 5.13 resembles theoretical predictions for a device with reservoirs having finite thermal conductance in figure 2.3. At bias voltages larger than $\sim 1 \text{ mV}$, differential noise decreases, possibly due to electron-phonon scattering.

Finally, figure 5.14 shows, on the same graph, shot noise of a diffusive N-S junction and of the same device driven normal by the application of magnetic field, along with theoretical predictions for both cases. The theoretical curves shown have no adjustable parameters. For comparison, fig. 5.14 also shows the expected hot-electron noise for a diffusive N-S junction (dashed line), which is given by equation 2.67. Our experimental data are a lot closer to "true shot noise" theory than to hot-electron noise.

In summary, shot noise measurements in a diffusive N-S junction driven normal are in semiquan-

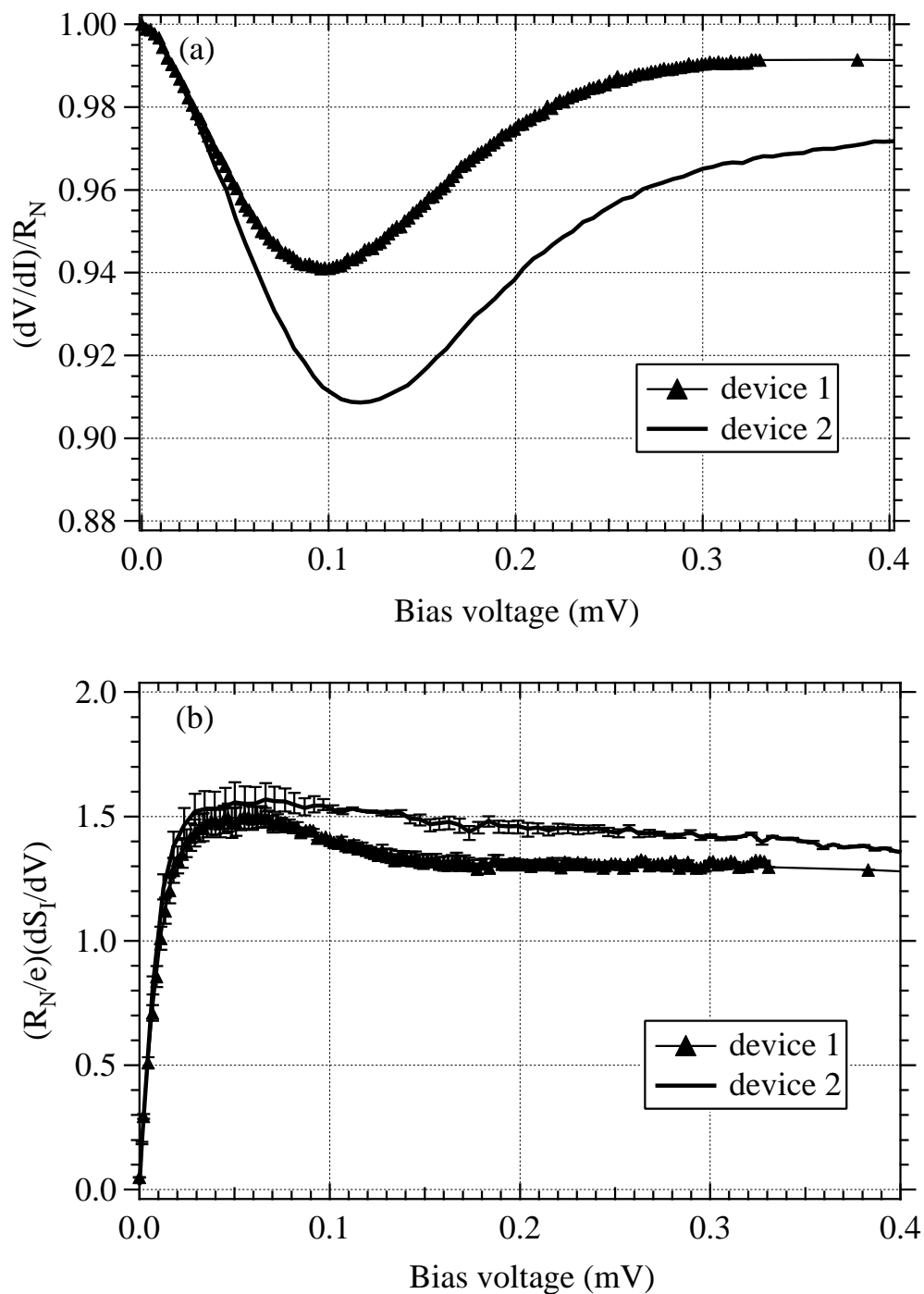


Figure 5.12: Comparison of bias voltage dependence of: (a) differential resistance, and (b) non-equilibrium noise $(R_N/e)(dS_I/dV)$ for devices 1 and 2.

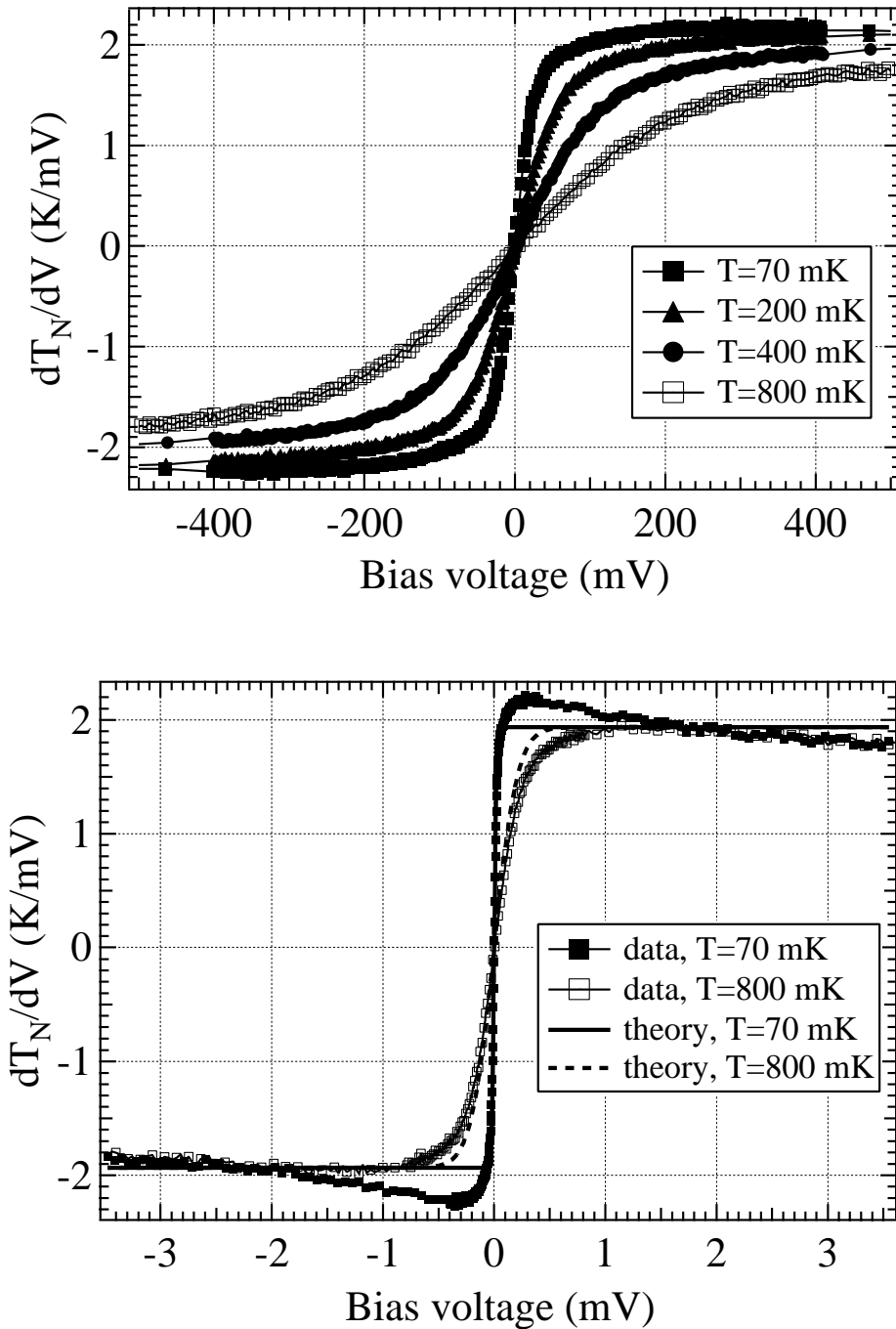


Figure 5.13: Dependence of shot noise vs. bias voltage in device 1 driven normal by a magnetic field of 6T at several mixing chamber temperatures. Bottom panel presents data and theoretical predictions at $T = 70$ mK and 800 mK.

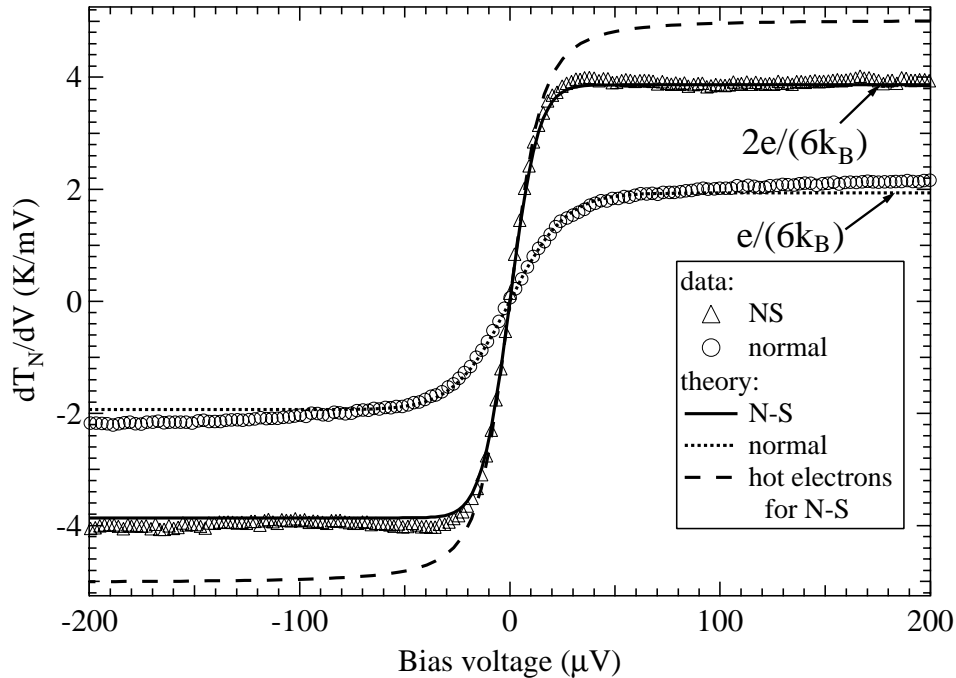


Figure 5.14: Comparison of measured shot noise with theoretical predictions for a diffusive N-S junction (device 1) and for the same device driven normal. Dashed line shows theoretical predictions for hot-electron noise - non-equilibrium noise in the regime $L_{ee} \ll L \ll L_{e-ph}$.

titative agreement with theoretical expectations. The discrepancy between the measured shot noise and theory may be due to not completely suppressed superconductivity of Nb contact pad and due to heating of reservoirs. At bias voltages larger than ~ 1 mV differential noise of an N-S junction driven normal decreases, possibly due to electron-phonon interactions.

5.4 Photon-assisted noise in diffusive N-S junctions

In order to unambiguously demonstrate that the observed increased shot noise is due to effective charge $2e$ of Andreev pairs, we performed measurements of shot noise in the presence of high-frequency irradiation. We irradiated device with microwaves in the frequency range 10-38 GHz and performed measurements of shot noise vs. bias voltage. If the passage of electrons across the device is elastic, we expect to see the photon-assisted features in the noise at bias voltages corresponding

to multiples of photon energy: $V = nh\nu/(2e)$. The location of these photon-assisted features should depend only on frequency of rf irradiation and not depend on the level of rf power.

Figure 5.15 shows theoretical and experimental shot noise vs. bias voltage under high-frequency irradiation at $f = 33.6$ GHz for device 1. Figure 5.15(a) shows theoretical predictions for $T = 100$ mK and rf powers, corresponding to $\alpha = eV_{ac}/(h\nu) = 1.1, 1.4, 1.7, 2.2, 2.8$. Figure 5.15(b) shows experimental data, obtained without rf irradiation and in the presence of 33.6 GHz irradiation with power levels corresponding to the above values of α . Figure 5.15(c) shows the second derivative of noise temperature d^2T_N/dV^2 , obtained by numerical differentiation of experimental data.

It is clearly seen, that in the presence of rf irradiation, shot noise develops features (steps in dT_N/dV , peaks in d^2T_N/dV^2) at bias voltages, corresponding to $h\nu/(2e)$. Ideally, the location of the feature should be completely independent of rf power. It is seen in figure 5.15 that the location of the features changes very little with rf power supplied to the device. The slight change in the location of features probably occurs due to the contributions of other peaks. For $\alpha = 1.1$, it is likely due to the contribution of the peak in d^2T_N/dV^2 at $V = 0$, and for $\alpha = 2.8$ - due to the contributions of peaks corresponding to $n > 1$. In figure 5.15 the minimum and maximum applied rf powers differ by a factor of 10. At higher powers of rf irradiation, the peaks become broader, probably due to heating of the electrons by rf irradiation. The condition for the peaks to be present is $h\nu \gg k_B T_e$, where T_e is electron temperature. If rf power is further increased, the peaks become no longer discernible due to too much heating of electrons.

The theory of photon-assisted noise predicts oscillatory (roughly $\sim J_0^2(\alpha)$) dependence of second derivative d^2T_N/dV^2 at zero bias voltage vs. rf power. This behavior is expected to be present in the regime $h\nu \gg k_B T$, otherwise, d^2T_N/dV^2 decreases monotonically as rf power is increased (this is qualitatively similar to what would be observed if temperature is increased: $d^2T_N/dV^2 \sim 1/T_e$).

Instead of measuring the second derivative of noise temperature at zero bias voltage $d^2T_N/dV^2(V_{bias} = 0)$, we measured the first derivative at a bias voltage of $\sim 20\mu V$, which is proportional to the second derivative d^2T_N/dV^2 at zero bias voltage:

$$\left(\frac{dT_N}{dV}\right)(V_{bias} = 20\mu V) \approx \left(\frac{d^2T_N}{dV^2}\right)(V_{bias} = 0) \times (20\mu V). \quad (5.10)$$

We chose to measure the first derivative because it was much easier to get good signal-to-noise

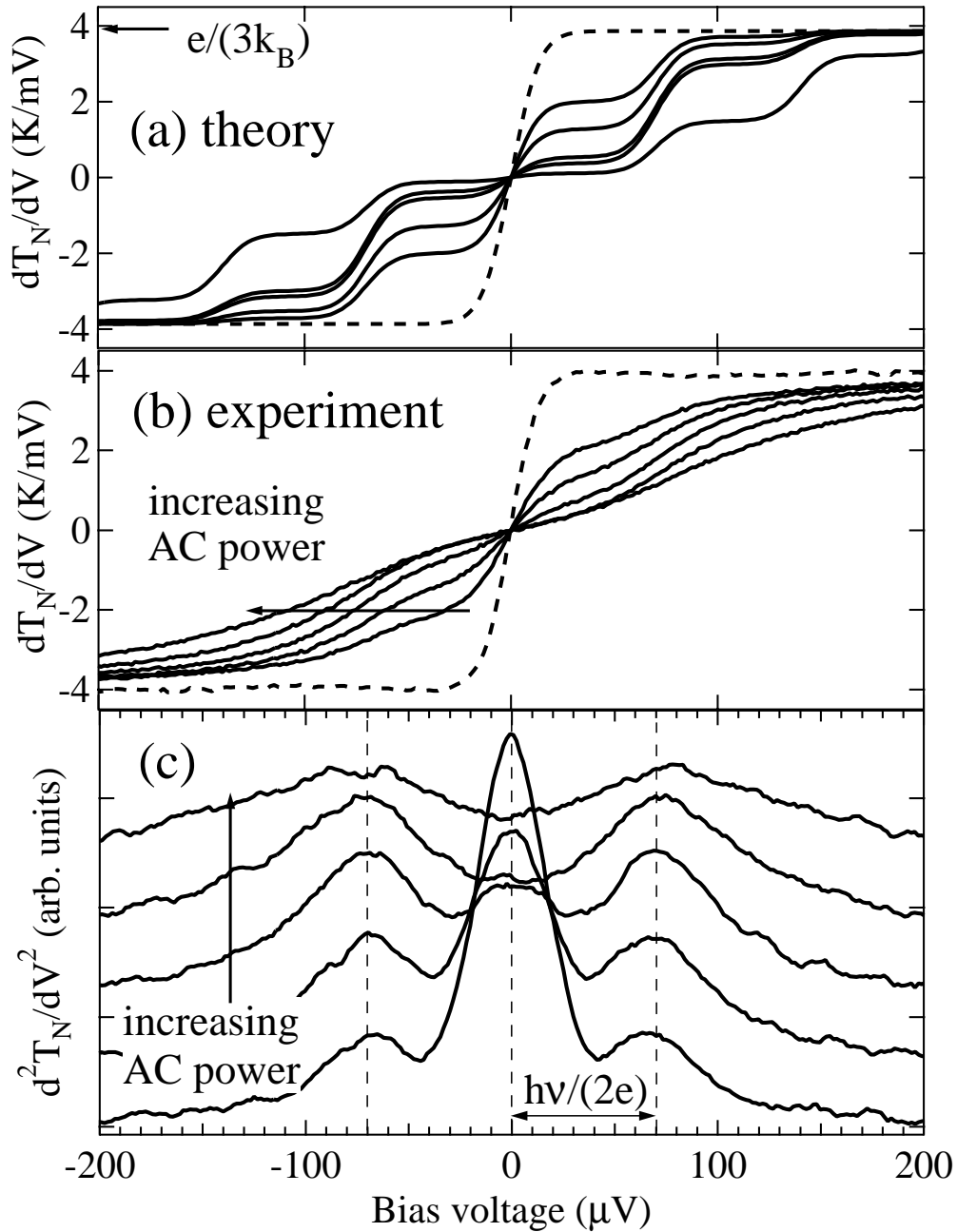


Figure 5.15: Photon-assisted noise features for a diffusive N-S junction (device 1) under rf irradiation at $f = 33.6$ GHz: (a) theory for dT_N/dV at $T=100$ mK without rf (dashed line) and for rf powers, corresponding to $\alpha = 1.1, 1.4, 1.7, 2.2, 2.8$ (solid lines); (b) experimentally measured dT_N/dV with no rf (dashed line) and with rf powers differing by 2 dB and corresponding to the above values of α ; (c) second derivative d^2T_N/dV^2 , obtained by numerical differentiation of experimental data, shows peaks at $V = h\nu/(2e)$.

on dT_N/dV than on d^2T_N/dV^2 . Figure 5.16(a) shows the dependence of dT_N/dV at $V_{bias} = 20\mu V$ vs. rf power for $f = 26.6$ GHz ($h\nu \gg k_B T$) and for $f = 3$ GHz ($h\nu \sim k_B T$). As expected, under rf irradiation at 26.6 GHz differential noise dT_N/dV displays oscillatory behavior vs. rf power, whereas at 3 GHz, dT_N/dV decreases monotonically as rf power is increased. Theoretical predictions for 26.6 GHz and 3 GHz are also presented in figure 5.16. The experimental data at 26.6 GHz display only one oscillation, at higher rf powers the decrease is monotonic. The probable cause of that is heating of electrons by rf excitation: at high rf powers the condition $h\nu \gg k_B T_e$ is not satisfied any more. The minimum of dT_N/dV corresponds to $J_0(\alpha) \approx 0$. The scale of rf powers is arbitrary, because the attenuation from the top of the cryostat to the device and the mismatch between the coaxial cable and the device at 26 GHz are not known to better than ± 10 dB.

Another manifestation of effective charge $2e$ is expected to be visible in the dependence of dT_N/dV vs. rf power. The first minimum of dT_N/dV for a diffusive N-S junction is expected to occur when $J_0(2eV_{ac}/(h\nu)) = 0$. For the normal diffusive conductor the minimum occurs when $J_0(eV_{ac}/(h\nu)) = 0$, so the ac voltages differ by a factor of 2, which corresponds to 6 dB of difference of rf power.

Figure 5.16(b) shows the dependence of dT_N/dV on rf power for device 1 at zero magnetic field (a diffusive N-S junction) and for the same device driven normal by a magnetic field of 5 T. Although the coupling from the rf source to the device is not precisely known, it doesn't appreciably change for the same device in the same mount. The data are in qualitative agreement with predictions - the minima in dT_N/dV for a diffusive N-S junction and for a normal diffusive conductor occur at rf powers which differ by ~ 6 dB. The dominating error factor is electron heating, which makes a minimum for the normal conductor weakly pronounced and may shift the location of the minimum.

The photon-assisted noise features corresponding to 2-photon processes ($n = 2$) and occurring at bias voltages $V = nh\nu/(2e)$ have been observed under rf excitation at $f = 10$ GHz. Figure 5.17 presents the dependence of d^2T_N/dV^2 on bias voltage for device 1 at 2 different power levels of 10 GHz rf irradiation. At lower power level, photon-assisted noise features at $V = h\nu/(2e)$ are visible. If the power is increased by 3 dB, features at $V = 2h\nu/(2e)$ appear whereas features, corresponding to $n = 1$, disappear.

Features, corresponding to more than one-photon process ($n > 1$) have not been observed at

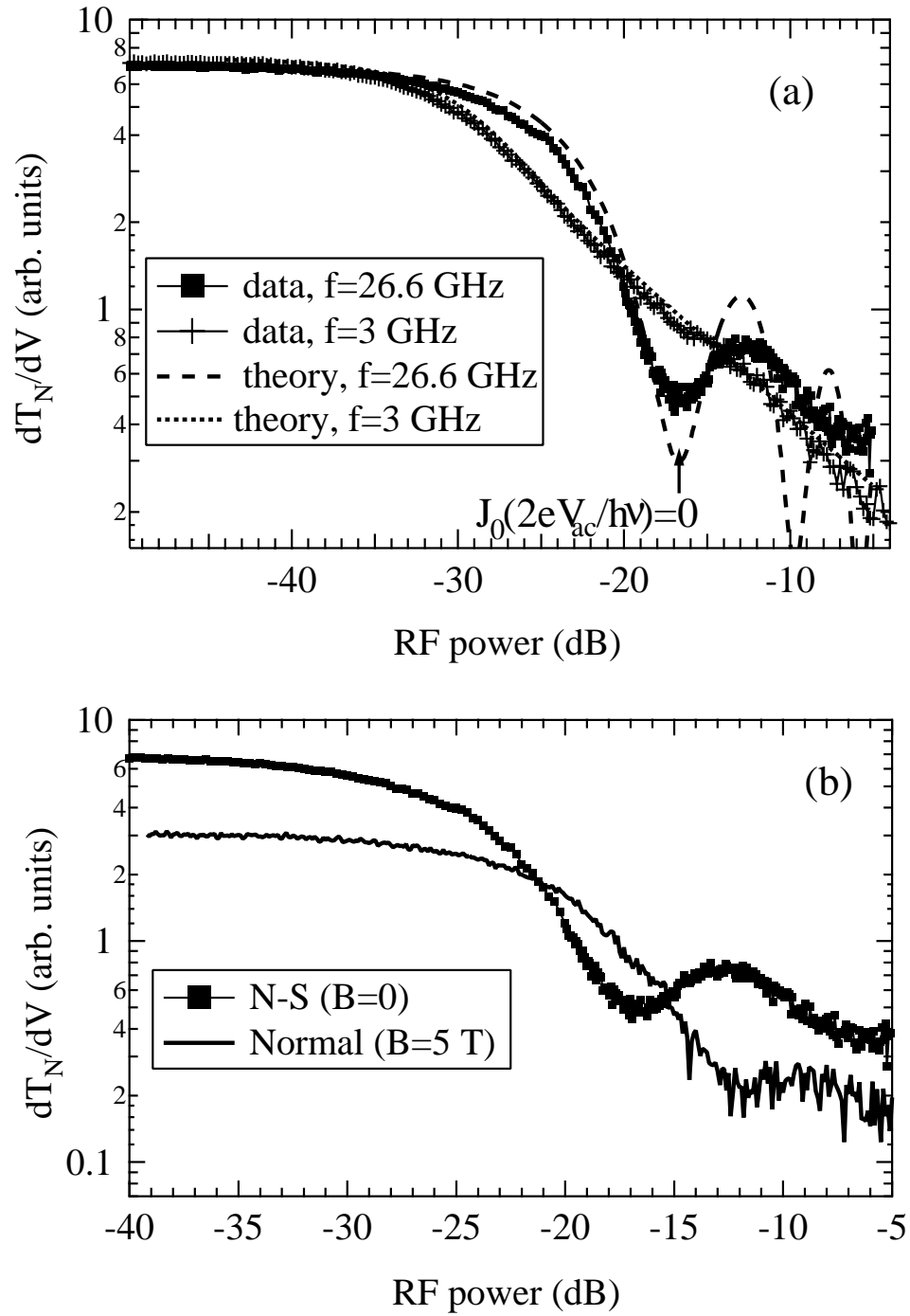


Figure 5.16: Dependence of dT_N/dV on rf power for device 1 at bias voltage $V = 20 \mu\text{V}$.

excitation frequencies above 10 GHz. The probable cause is electron heating by both dc bias and rf excitation. To observe photon-assisted features one needs to apply rf power to the device, corresponding to $\alpha = 2eV_{ac}/(h\nu) \sim 1$. So the larger the rf frequency, the larger the rf power which has to be applied to the device (rf power scales quadratically with frequency.) Also, for higher frequencies the photon-assisted features occur at higher bias voltages $V = nh\nu/(2e)$, so the dc heating will be stronger, too.

Let us qualitatively discuss the possible role of electron heating. Suppose, due to the combination of dc bias and rf excitation the device is in a strong heating regime. Then, assuming that equal powers due to dc and ac voltages would cause equal electron heating, we can write using equation 2.30:

$$T_e(V_{dc}, V_{ac}) = \beta(V_{dc} + \frac{V_{ac}}{\sqrt{2}}). \quad (5.11)$$

In order to see the photon-assisted noise feature corresponding to $n = 1$, we need to have $V_{dc} = h\nu/(2e)$, $V_{ac} \sim h\nu/(2e)$ and $T_e(V_{ac}, V_{dc}) \ll h\nu/k_B$. These conditions can be satisfied if

$$\beta \ll \frac{e}{k_B} = 1.16 \times 10^4 K/V. \quad (5.12)$$

In chapter 2 we made an estimate of $\beta \sim 400$ K/V for our diffusive Au wires. This estimate of β assumed that heat diffuses out of 2 reservoirs. For an N-S device heat can diffuse out of only 1 reservoir, so the value of β is $\sqrt{2}$ times larger, than for a normal diffusive conductor: $\beta_{NS} = \sqrt{2}\beta_N \sim 600$ K/V. This value is a lot smaller than e/k_B and condition 5.12 is going to be satisfied very well for our N-S devices.

In order to observe photon-assisted feature corresponding to $n > 1$, the dc and ac voltages and electron temperature have to satisfy the following conditions: $V_{dc} = nh\nu/(2e)$, $V_{ac} = B_n h\nu/(2e)$, $T_e \ll h\nu/k_B$ (B_n is related to the behavior of Bessel function $J_n(\alpha)$ and grows with n). These conditions will be satisfied if:

$$\beta \ll \frac{e}{k_B} \frac{1}{n + B_n/\sqrt{2}} = \frac{1.16 \times 10^4 K/V}{n + B_n/\sqrt{2}}. \quad (5.13)$$

We see that starting from a certain value of n , the condition 5.13 will not be satisfied any more, so

the higher n is, the more difficult it is to observe the peaks. On the other hand, the frequency of rf excitation does not enter equations 5.12 and 5.13, so in the strong heating regime it should be possible to observe equal number of peaks for all frequencies.

Consider a weak heating regime. In this case, from equation 2.30:

$$T_e(V_{ac}, V_{dc}) = T_{bath} + \frac{\beta^2(V_{dc}^2 + V_{ac}^2/2)}{2T_{bath}^2}. \quad (5.14)$$

For the photon-assisted noise features to be observed, the electron temperature has to be much smaller than $h\nu/k_B$. This condition, after substituting $V_{dc} = nh\nu/(2e)$ and $V_{ac} = B_n h\nu/(2e)$ in equation 2.30, becomes:

$$T_{bath} + \left(\frac{\beta h\nu}{2e}\right)^2 \frac{n^2 + B_n^2/2}{2T_{bath}^2} \ll h\nu. \quad (5.15)$$

From equation 5.15 we see, that in the regime of weak heating the number of peaks which can be observed decreases with the increase of high-frequency excitation ν .

For the estimated value of $\beta = 600$ K/V, the strong heating regime will be realized for $V_{dc} + V_{ac}/\sqrt{2} \gtrsim 300$ - 400 μ V. At $V_{dc} + V_{ac}/\sqrt{2} \lesssim 100$ μ V, the device will be in a weak heating regime. For the excitation frequency $\nu = 30$ GHz and $n = 2$, the magnitude of the second peak is expected to be maximum when $V_{ac} \approx 3h\nu/(2e) = 190$ μ V. The dc voltage is $V_{dc} = h\nu/(2e) = 125$ μ V. Hence $V_{dc} + V_{ac}/\sqrt{2} = 260$ μ V, which is the regime, intermediate between weak and strong heating, and closer to strong heating. The weak heating regime will be realized for $n = 2$ and $f \lesssim 15$ GHz. It is possible, that for our devices photon-assisted noise features corresponding to $n > 1$ can be observed only in the weak heating regime.

Another possibility is the gradual weakening of photon-assisted features for frequencies comparable to or higher than the inverse diffusive transit time $\tau_{diff} = L^2/D$. For example, for device 1: $\tau_{diff}^{-1} \approx 30$ GHz, so for all frequencies between 10 and 38 GHz the frequency of ac excitation is comparable to inverse diffusive transit time. The theoretical prediction (equation 2.41) is derived assuming $\nu \gg \tau_{diff}^{-1}$, no theory has been developed for the case $\nu \sim \tau_{diff}^{-1}$ yet.

The most convincing hallmark of a photon-assisted process is dependence of the location of features on the frequency of rf excitation. For a diffusive N-S junction, we expect photon-assisted noise features to occur at bias voltages $V_{dc}^{NS} = h\nu/(2e)$. We have performed the noise measurements

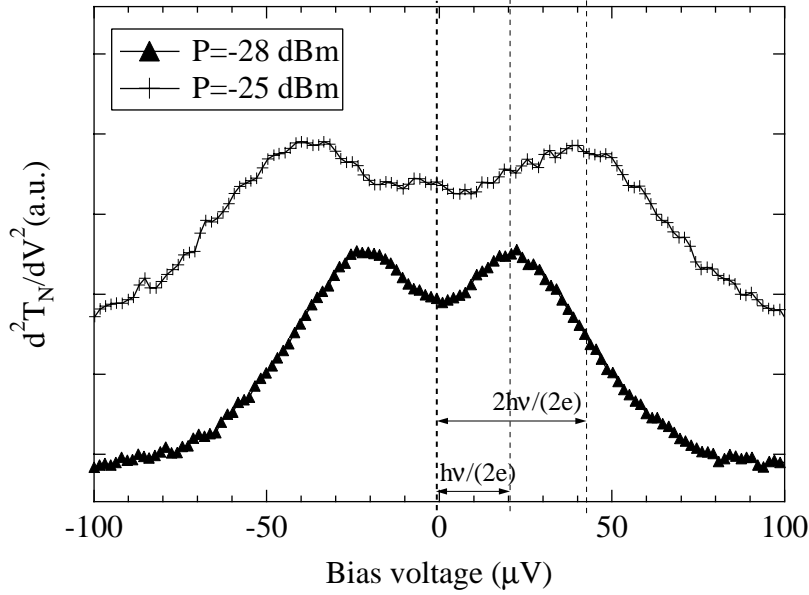


Figure 5.17: Dependence of d^2T_N/dV^2 on bias voltage for a diffusive N-S junction (device 1 at zero magnetic field) under 10 GHz irradiation.

applying rf excitation of several different frequencies. We also repeated the experiment in a magnetic field of 5 T. At this field the Nb contact is driven normal, and our device is effectively a normal diffusive conductor. At $B = 5$ T, we expect photon-assisted noise features to occur at bias voltages $V_{dc}^N = h\nu/e$.

Figure 5.18(a) presents the second derivative of noise temperature d^2T_N/dV^2 vs bias voltage for the N-S device (device 1, solid curves) and for the device driven normal (same device, dotted curves). The curves are scaled to have the same peak height and are offset in the vertical direction by an amount proportional to frequency. The straight dotted and solid lines are theoretical expectations of the peak locations for an N-S device (solid straight lines) and for a normal mesoscopic conductor (dotted straight lines). The peaks occur at theoretically expected peak locations. Figure 5.18(b) presents the peak locations (the dc voltage at which a peak of d^2T_N/dV^2 occurs) vs. frequency of rf excitation. The squares are the data points for an N-S device (device 1 at zero magnetic field), the circles are the data points for the same device driven normal. The solid line is the theoretical expectation for an N-S device with no adjustable parameters: $V_{dc}^{NS} = h\nu/(2e)$; the dotted line is the theoretical expectation for a normal mesoscopic conductor: $V_{dc}^N = h\nu/e$. We see that our data

are in good agreement with theoretical predictions. As expected, our device displays a signature of an effective charge $2e$ at zero magnetic field, whereas at high magnetic field it displays a signature of effective charge e .

For a diffusive N-S junction, the voltage location of the photon-assisted noise features satisfies the Josephson relation $2eV = h\nu$. The photon-assisted noise features, however, are not a manifestation of an ac Josephson effect, because the device has only one superconducting reservoir, and a true Josephson effect cannot take place in this device. Our experimental results constitute the first observation of features obeying the Josephson relation in a system having only one superconducting reservoir, where no true Josephson effect can take place.

It has been noted (Strunk 2000), that similar effects might be a manifestation of Josephson effect in case superconductivity "leaks" across the tunnel barrier and there is Josephson coupling between superconducting contact and the region of induced superconductivity in normal metal. It is not clear whether such situation can take place, i.e., whether the junction can be opaque enough for Josephson coupling to occur and at the same time transparent enough to proximitize normal metal. Even if, hypothetically, such a situation would occur, the features would occur at different dc voltages - Josephson coupling across tunnel junction may result in features at bias voltages, satisfying the relation $2eV_{TJ} = h\nu$, where V_{TJ} is voltage drop across the tunnel junction only, and not across the whole device. For our device, the tunnel junction resistance is much smaller than the resistance of a diffusive wire, so $V_{TJ} \ll V_{dc}$, and Josephson effect features might occur at much smaller bias voltages. We observe features at $V_{dc} = h\nu/(2e)$ and conclude, that the observed photon-assisted noise features are not a manifestation of possible Josephson coupling across the tunnel junction between the normal metal and the superconductor.

In chapter 2, we noted that photon-assisted noise features are similar to the photon-assisted tunneling (PAT) features in the conductance. For an N-S device, the conductance changes as a function of bias voltage, so one may expect PAT features in the conductance to occur along with features in shot noise. For example, the sidebands of the conductance minimum at $V = 0$ would appear at bias voltages $|V| = h\nu/(2e)$. The differential conductance of the device under rf excitation was measured simultaneously with noise, but no PAT-like features was observed in the conductance. A possible explanation for the absence of PAT features in the conductance is a combination of weak

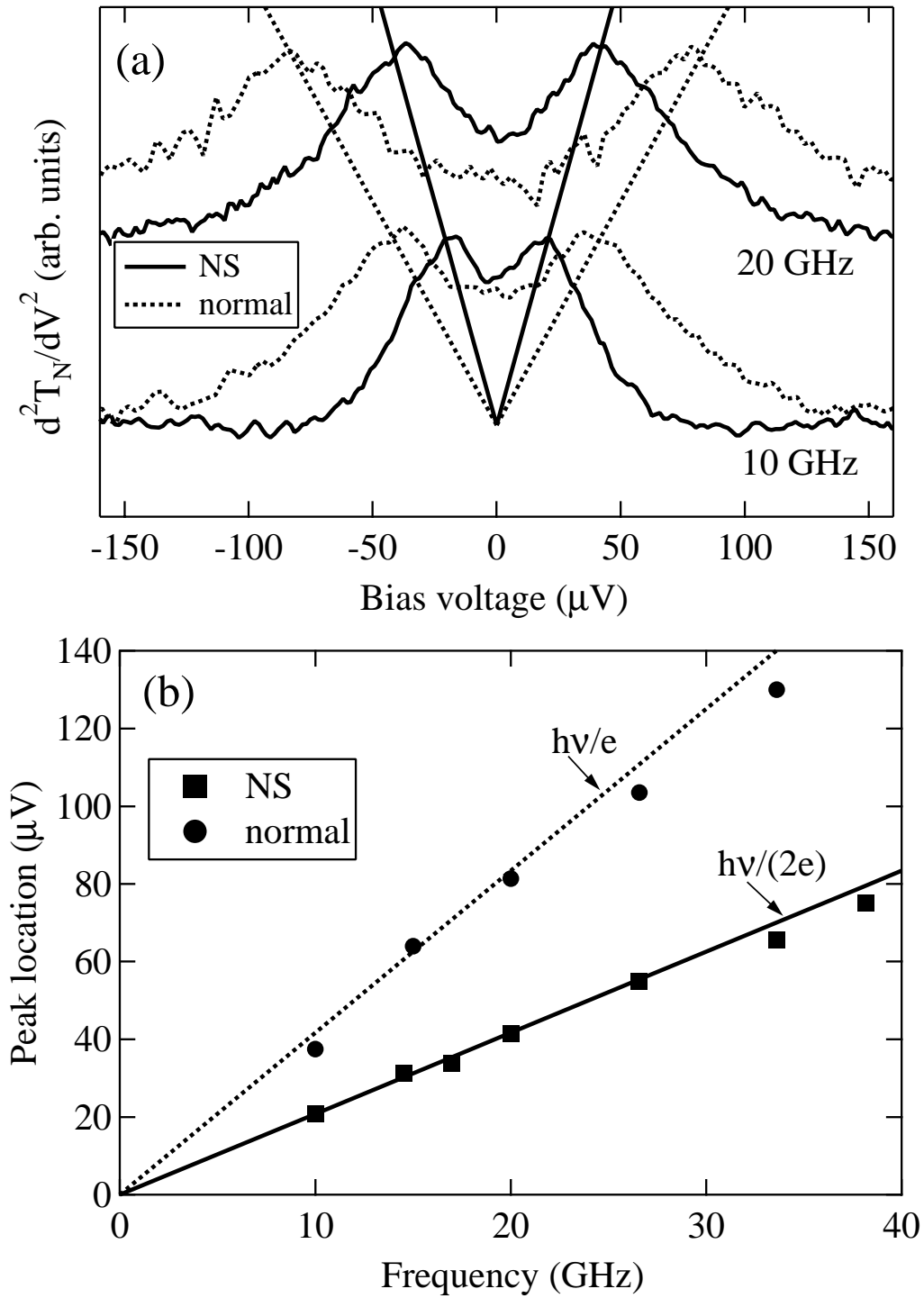


Figure 5.18: Photon-assisted noise peaks location vs. frequency of rf excitation for device 1 (see explanations in text).

non-linearity in the I-V curve and heating. The increase of electron temperature due to applied dc bias and rf excitation may be sufficient to suppress PAT features in the conductance due to weak dependence of conductance on bias voltage. The noise, on the other hand, has a much more pronounced "corner-like" non-linearity, which survives this electron temperature increase.

5.5 Summary of experimental results for diffusive N-S junctions

To summarize our results for diffusive N-S junctions, we performed measurements of non-equilibrium noise in 2 diffusive N-S junctions. We observed shot noise which is approximately doubled compared to a normal mesoscopic conductor, and is in good agreement with theoretical predictions. This constitutes experimental demonstration of effective charge $2e$ in a mesoscopic diffusive N-S junction.

We also performed measurements of shot noise in a diffusive N-S junction in the presence of high-frequency excitation. Under such an excitation of frequency ν , shot noise develops photon-assisted features which occur at characteristic voltages $V_n = nh\nu/(2e)$. The location of the photon-assisted features constitutes another signature of effective charge $q_{eff} = 2e$ due to Andreev reflection. This signature is more uniquely indicative of effective charge $2e$ than doubling of shot noise alone. In the measurement of noise with ac excitation it is straightforward to calculate the effective charge $q_{eff} = nh\nu/V_n$ from known frequency of ac excitation ν and measured dc voltage V_n at which the photon-assisted features occur. In the measurement of shot noise without ac excitation, it is much more difficult to infer the value of effective charge. The inferred magnitude of effective charge is affected by systematic errors of the gain of rf chain and the effects of the device impedance change.

5.6 Transport and noise measurements in Andreev interferometers

We have fabricated Andreev interferometers of two different geometries and performed transport and non-equilibrium noise measurements on these devices. The geometry of the first type of devices - we call it "cross", is presented in figure 5.19. The geometry of the second type of device - which

we call device "Y", is presented in figure 5.28.

Devices of both geometries displayed periodic modulation of the conductance when magnetic field through the superconducting ring was changed, i.e. devices of both geometries behave like Andreev interferometers. The "cross" and "Y" devices displayed significantly different transport and noise properties. In the following subsections we discuss these two types of devices separately.

5.6.1 Transport and noise properties of a device of "cross" geometry

The "cross" structure is a cross-shaped normal wire with 2 ends of the cross attached to normal metal reservoirs, and two other ends attached to the ends of superconducting loop. The SEM picture and schematic of the device is presented in figure 5.19. Only part of the superconducting loop is shown in the SEM picture. The rest of the loop is indicated on the schematic by dashed lines. The area of the loop is about $2.7 \mu\text{m}^2$, taking the average perimeter between the inner and outer boundary of the superconducting loop. The bright regions on the SEM picture along the edges of normal contacts are standing "flags" of gold which remained due to imperfect liftoff. They do not change the topology of the device and are not important.

Transport measurements in "cross" device

By tuning magnetic flux through the superconducting loop, the phase difference between points A and B is continuously changed. When $\Delta\varphi_{AB} = 2\pi n$, point O is maximally proximitized, and the conductance of the wire measured between normal reservoirs is expected to exhibit maximum. When $\Delta\varphi_{AB} = (2n + 1)\pi$, point O is expected to be normal, and the conductance of the normal wire is expected to be equal to the normal-state conductance. Transport and non-equilibrium noise measurements were performed in one device of "cross" geometry. The dependence of differential resistance vs. bias voltage of a "cross" device for several values of magnetic flux is presented in figure 5.20. Contrary to our expectations, differential resistance of the device displays sharp dip in a very narrow (a few μV or less) region of bias voltages close to zero. The magnitude of the dip is strongly modulated by the flux through the superconducting loop. Data in figure 5.20 were measured with a lock-in amplifier applying ac voltage of about $8 \mu\text{V}$ p-p across the device, at smaller ac voltages the decrease of resistance near zero bias voltage is even larger, i.e., this sharp decrease of

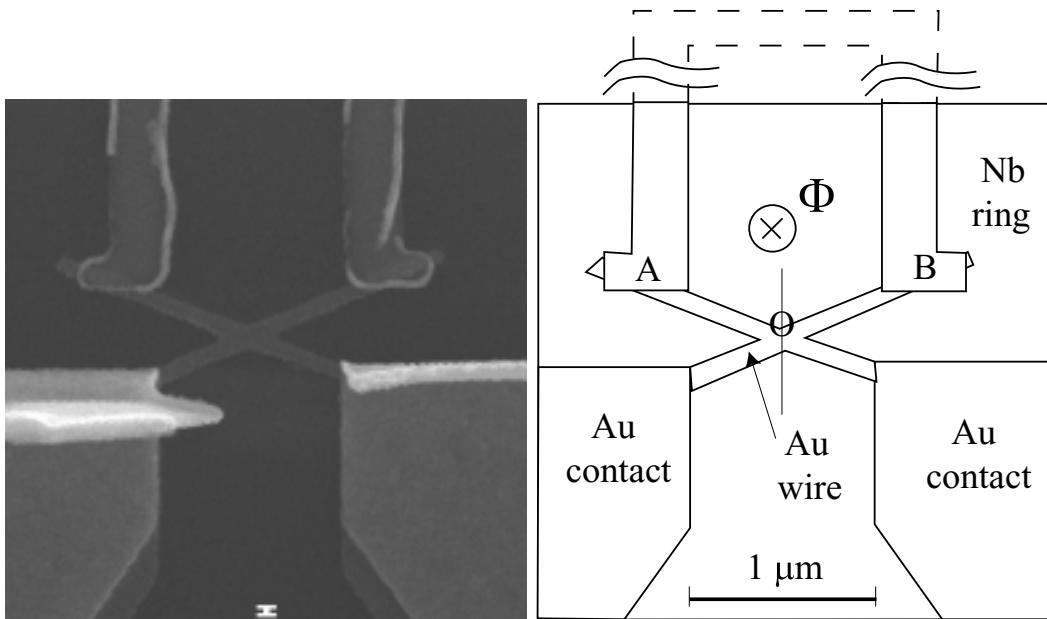


Figure 5.19: SEM picture and schematic of device of "cross" geometry. Nb loop extends beyond the area of the SEM picture.

resistance occurs on a voltage scale of $\lesssim 1 \mu\text{V}$ and behaves similarly to a supercurrent. Modulation of the differential conductance with the same periodicity in magnetic field is also observed at bias voltages up to $\sim 100 \mu\text{V}$, but the magnitude of the modulation at bias voltages $V \gtrsim 15 \mu\text{V}$ is much smaller than near zero bias.

Figure 5.21 presents the dependence of zero-bias differential resistance on magnetic field at mixing chamber temperature $T_{M/C} = 50 \text{ mK}$. The period of differential resistance oscillations is about $\Delta B = 0.76 \text{ mT}$, which is consistent with the estimate based on the average between inner and outer areas of the superconducting loop: $\Delta B_{theor} \approx 0.77 \text{ mT}$. The data in figure 5.21 were taken with an ac bias modulation corresponding to an ac voltage of about $4 \mu\text{V}$ p-p, smaller than ac voltage across the device for data in figure 5.20. This is why the measured zero-bias differential resistance at $\Phi = n\Phi_0$ in figure 5.21 is smaller than in figure 5.20. If the ac voltage drive is further decreased, the measured differential resistance drops even more. The dip in dV/dI near zero bias behaves similarly to a supercurrent shunting a fraction of the normal wire.

The magnitude of the resistance decrease near $V = 0$ displays strong temperature dependence.

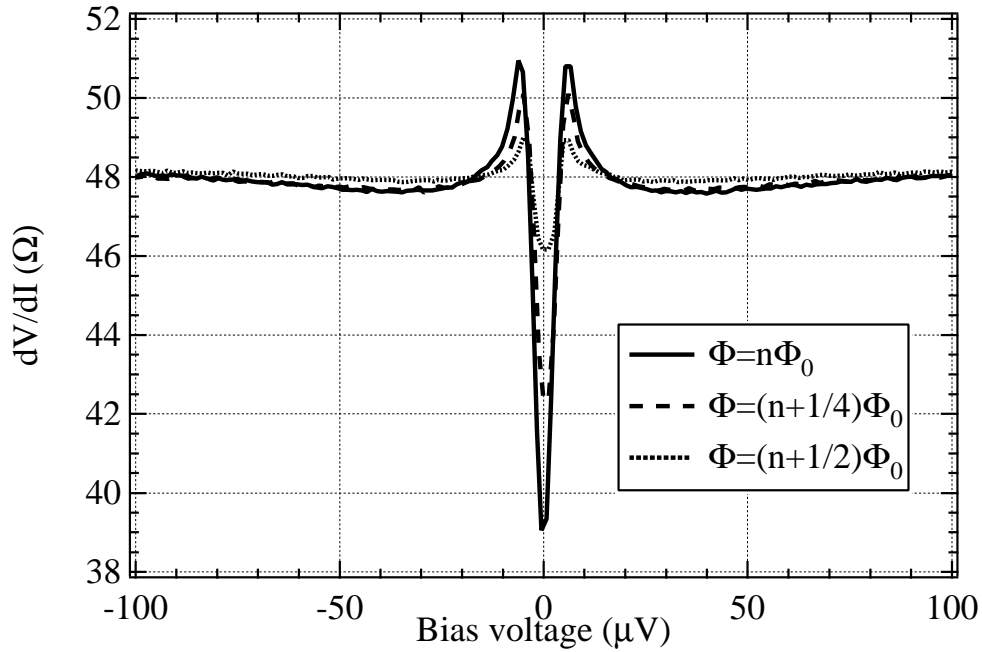


Figure 5.20: Differential resistance vs. bias voltage for "cross" device for several values of magnetic flux at mixing chamber temperature $T_{M/C} = 50$ mK. AC voltage drive ~ 8 μ V p-p.

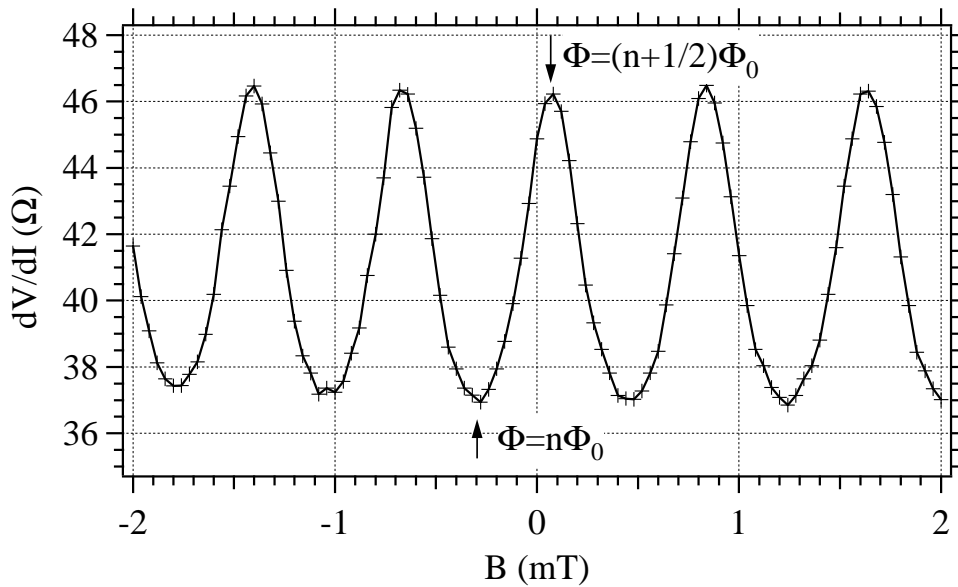


Figure 5.21: Zero bias differential resistance vs. magnetic field for "cross" device. AC bias voltage drive ~ 4 μ V p-p.

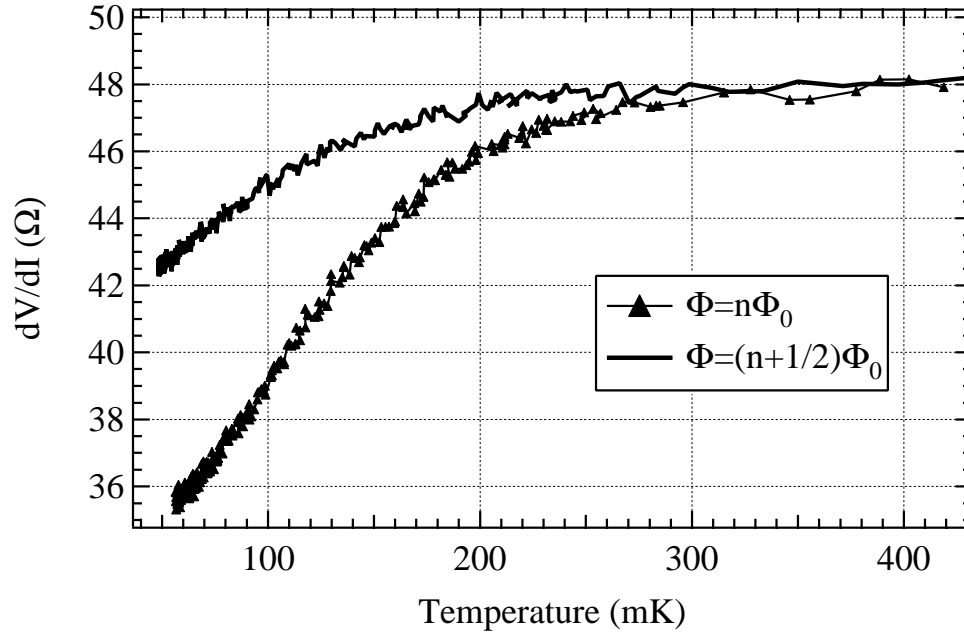


Figure 5.22: Zero bias differential resistance vs. temperature for integer and semi-integer magnetic flux. Bias voltage ac drive $\sim 2 \mu\text{V}$ p-p.

In figure 5.22 we show temperature dependence of zero-bias resistance of "cross" device at integer and semi-integer magnetic flux. The modulation of zero-bias differential resistance "turns on" below the temperature of about 250 mK, and the magnitude of the effect displays strong temperature dependence, especially at low temperatures. Such a strong temperature dependence is qualitatively similar to exponential temperature dependence of supercurrent in diffusive S-N-S junctions which was predicted theoretically (Kulik and Omel'yanchuk 1975) and demonstrated experimentally (Courtois et al. 1995), (Dubos et al. 2001). The modulation of differential resistance at high ($\sim 50 \mu\text{V}$) bias voltages has a much smaller magnitude than the zero-bias decrease in dV/dI . It also has a much weaker temperature dependence. Figure 5.23 shows temperature dependence of the differential resistance of the device at bias voltage $V = 37 \mu\text{V}$. The magnitude of the modulation decreases by a factor of ~ 2 as the temperature is increased from 50 mK to 300 mK and is present at even higher temperatures. This temperature dependence is very different from a steep decrease of modulation of resistance dip near zero bias voltage.

We speculate that the zero-bias decrease of differential resistance of the device is due to "shorting"

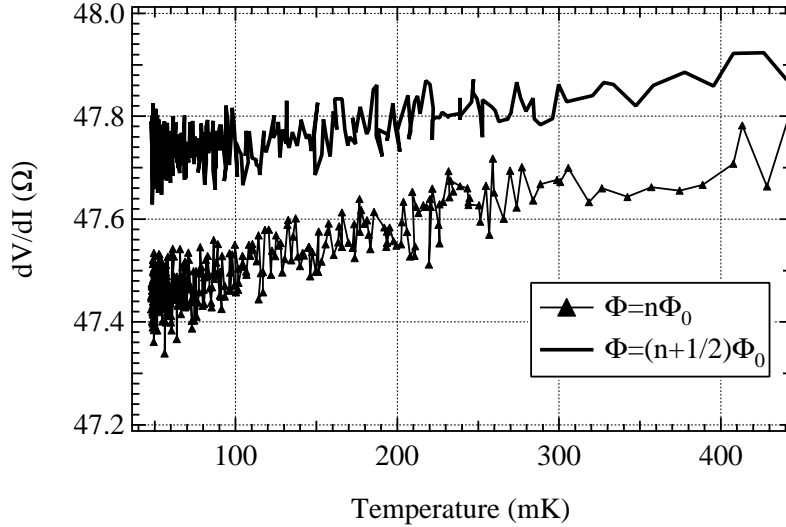


Figure 5.23: Differential resistance at bias voltage $V = 37 \mu\text{V}$ vs. temperature for integer and semi-integer magnetic flux.

of the central part of normal metal wire by a supercurrent flowing through superconducting loop and a diffusive normal wire. The observed effect may be similar to the predicted (Gueron 1997) and recently observed (Shaikhaidarov et al. 2000) effect of a dangling superconductor which we briefly describe below. Consider a structure shown in figure 5.24(a). The dangling superconducting reservoir S_1 is not in the current path, but it can convert a quasiparticle current I_{qp3} into a supercurrent I_{sc} . The net current through the dangling arm is zero: $I_{qp3} = I_{sc}$, but both superconductors are at the same potential as long as the supercurrent does not exceed the critical current $I_C \sim E_C / (e(R_2 + R_3))$. This means that the dangling arm of the normal wire having a resistance R_3 is effectively in parallel with the arm having a resistance R_2 due to the shunting of supercurrent between S_1 and S_2 . The total resistance of the structure measured between N and S_2 is $R_{eff} = R_1 + R_2 R_3 / (R_2 + R_3)$. However, when the current I_{dc} exceeds the critical current I_C , supercurrent can no longer maintain zero potential difference between S_1 and S_2 , and the resistance of the structure increases to $R_1 + R_2$. The maximum supercurrent which can flow through a diffusive mesoscopic wire is proportional to Thouless energy (Fink 1997). In the regime when the length of the wire is much larger than coherence length in normal metal, i.e., when $L \gg \xi = \sqrt{\hbar D / (2\pi k_B T)}$, the maximum supercurrent decreases

exponentially with temperature (Wilhelm et al. 1997), (Fink 1997):

$$I_C \sim \frac{E_C}{eR_N} T^{3/2} \exp(-L/\xi). \quad (5.16)$$

This steep temperature dependence is characteristic of supercurrent between 2 superconducting reservoirs and is usually not seen in the proximity-induced change of the resistance of the normal wires.

A related effect may be present in a structure in figure 5.24(b). On the left we present the schematic of the "cross" device. The central part of the normal metal "cross" is wider than the rest of the normal wires (see figure 5.19 - this occurred unintentionally, probably because of imperfect focus or dose during e-beam lithography) and can be modeled as a resistor R_1 in the circuit on the right of figure 5.24(b). A supercurrent may flow between the terminals of a superconducting loop through normal diffusive wires. This supercurrent will effectively short out resistor R_1 and, at small bias currents, the resistance of the stricture will be equal to $2R$. When the current flowing through resistor R_1 will exceed the supercurrent which can be sustained in a normal diffusive wire between the terminals of the superconducting loop, the resistance will sharply increase to $2R + 2RR_1/(2R + R_1)$. If we make an estimate of relative magnitude of R and R_1 from the SEM picture of the device, we get $R_1/R \sim 0.3-0.4$. Using the ratio of R_1/R , we can estimate the expected magnitude of resistance dip near zero bias:

$$\frac{R(V=0)}{R_N} = \frac{1}{1 + R_1/R/(2 + R_1/R)} \sim 0.85 - 0.9. \quad (5.17)$$

The observed ratio of zero-bias resistance to the normal state resistance is $R(V=0)/R_N \approx 0.75$, so the magnitude of the effect is larger than expected from a simple model. The magnitude of the effect is expected to be strongly temperature dependent, because for our device $\xi \approx 6 \times 10^{-8} \text{ m K}^{1/2}/\sqrt{T} \ll L$ at $T \gtrsim 0.1 \text{ K}$.

At high bias voltages, the magnitude of the conductance is much smaller than at zero bias, and the temperature dependence of the conductance modulation is different from that of a zero-bias resistance decrease. We attribute the phase modulation of the resistance at high bias voltages to proximity effect correction to the resistance. This is consistent with weak temperature dependence of the resistance modulation. Theoretically, for a "cross" geometry, the maximal magnitude of the

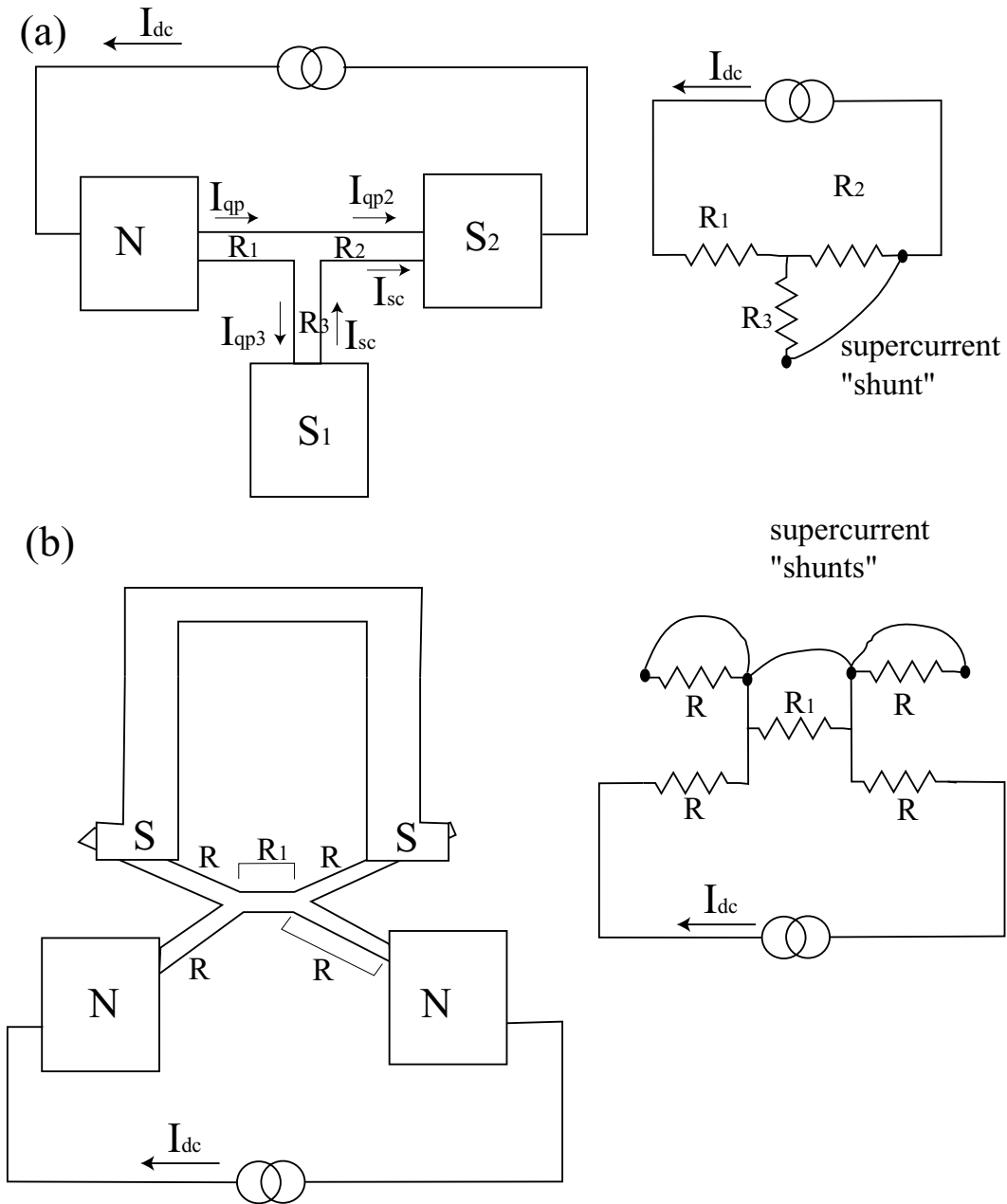


Figure 5.24: a. Schematic of an N-S device with a dangling superconductor and equivalent circuit. Because of conversion of the quasiparticle current into the supercurrent the superconducting reservoirs are shorted together at small currents (adapted from (Gueron 1997)). b. Schematic of the "cross" device and the equivalent circuit.

modulation in resistance at finite bias voltages is expected to be about 6% and occur at bias voltages corresponding to about $E_C = \hbar D/L^2$ where L is the length of one of the normal arms of the device. Qualitatively, this can be understood in the following way. For $\Phi = n\Phi_0$, the phase $\varphi(x, E)$ is constant and can be taken equal to zero. The solution for the pairing angle in the device (moving from the normal reservoir toward the superconductor) will be similar to the solution in a diffusive N-S junction having a normal metal wire of length $2L$. For a diffusive N-S junction, the differential resistance minimum occurs at $E \approx 5E_{CNS} = 5\hbar D/(2L)^2 = 1.25\hbar D/L^2$, which is close to the Thouless energy defined for the "cross" device $E_C = \hbar D/L^2$.

For the "cross" device $E_C \sim 8 \mu\text{V}$, at this bias voltage differential resistance displays a maximum, probably due to disappearance of the supercurrent. Experimentally, the magnitude of differential resistance modulation is smaller than expected (only about 1%). The reduction of the proximity-induced resistance correction could be due to inelastic scattering, because the length of the normal wire is about $1 \mu\text{m}$, which is comparable to electron-electron energy relaxation length $L_{ee} \sim 2 \mu\text{m}$.

In summary, we observed phase-periodic modulation of differential resistance of Andreev interferometer having a "cross" geometry with an $h/(2e)$ periodicity. Based on different temperature dependence of the resistance modulation near zero bias voltage (at $|V| \lesssim 5 \mu\text{V}$) and at high bias voltages ($10\text{-}80 \mu\text{eV}$), we argue that different physical mechanisms are responsible for the modulation of differential resistance at zero bias voltage and at high bias voltages. Steep (close to exponential) temperature dependence of resistance modulation near zero bias voltage suggests that the effect is due to shunting of the central part of the "cross" structure by a supercurrent in a diffusive normal wire between superconducting reservoirs. Relatively weak temperature dependence of conductance modulation at high bias voltages suggests that the effect is due to proximity-induced correction to the resistance, although the magnitude of the effect is smaller than expected theoretically. The device having a "cross" geometry is not well suited for shot noise measurements because of Josephson coupling between the superconducting terminals.

Transport in the presence of high-frequency radiation

We performed transport measurements of the "cross" device under high-frequency rf excitation. In contrast to diffusive N-S junctions, the "cross" device has a sharp non-linearity in differential

resistance near $V = 0$, so PAT features may be observable in the resistance the structure. We have observed photon-assisted features in the frequency range 2.5 - 11 GHz. Surprisingly, the photon-assisted features in the conductance occurred at bias voltages $V = nh\nu/e$, not $nh\nu/(2e)$, as might be expected. The magnitude of the features displayed characteristic oscillatory behavior vs. rf power. In figure 5.25(a) we present the rf power dependence of the differential conductance of the device at bias voltages $V = nh\nu/e$ for $n = 0, 1, 2, 3$. Let us assume that the device has a narrow peak in differential conductance near $V = 0$ and, except for this peak, the differential conductance is constant. Then, from equation 2.36, we expect the following dependence on rf power of the differential conductance in the presence of rf excitation \tilde{G}_{diff} at bias voltages $V = nh\nu/e$:

$$\tilde{G}_{diff}(V = nh\nu/e) = G_{diff N} + [G(V = 0) - G_{diff N}] J_n^2(\alpha), \quad (5.18)$$

where $G_{diff}(V = 0)$ is zero-bias differential conductance, G_N is a normal-state conductance, and $\alpha = eV_{ac}/h\nu$. We used equation 2.36 for non-superconducting devices. This will be explained below.

The features exhibit oscillatory behavior, qualitatively consistent with theoretical predictions. Three oscillations of zero-bias conductance are visible. The damping of the oscillations at high rf powers is likely due to heating by the rf excitation. We propose the following explanation for the observation of photon-assisted features at bias voltages $V = nh\nu/e$. The central part of the device is proximitized by superconducting reservoirs. If one measures the conductance of the structure between the normal reservoirs, the device can be regarded as a series combination of two N-S' junctions, where "S'" means proximitized normal metal. Figure 5.26 shows the schematic of the device and an equivalent circuit of two N-S' junctions in series. The photon-assisted features in the conductance of N-S' junctions occur at dc bias voltages $V_{dc}^{NS} = V_{dc}/2 = nh\nu/(2e)$, so the dc voltage across the structure when the PAT features occur will be equal to $V_{dc} = nh\nu/e$.

Non-equilibrium noise measurements in a "cross" device

We have performed measurements of non-equilibrium noise in a "cross" device. The main results are presented in figure 5.27. Figure 5.27(a) presents bias voltage dependence of effective noise temperature of the "cross" device at integer and semi-integer magnetic flux. The slope of the curves was determined by performing Johnson calibration as discussed in chapter 4. The curves in figure 5.27

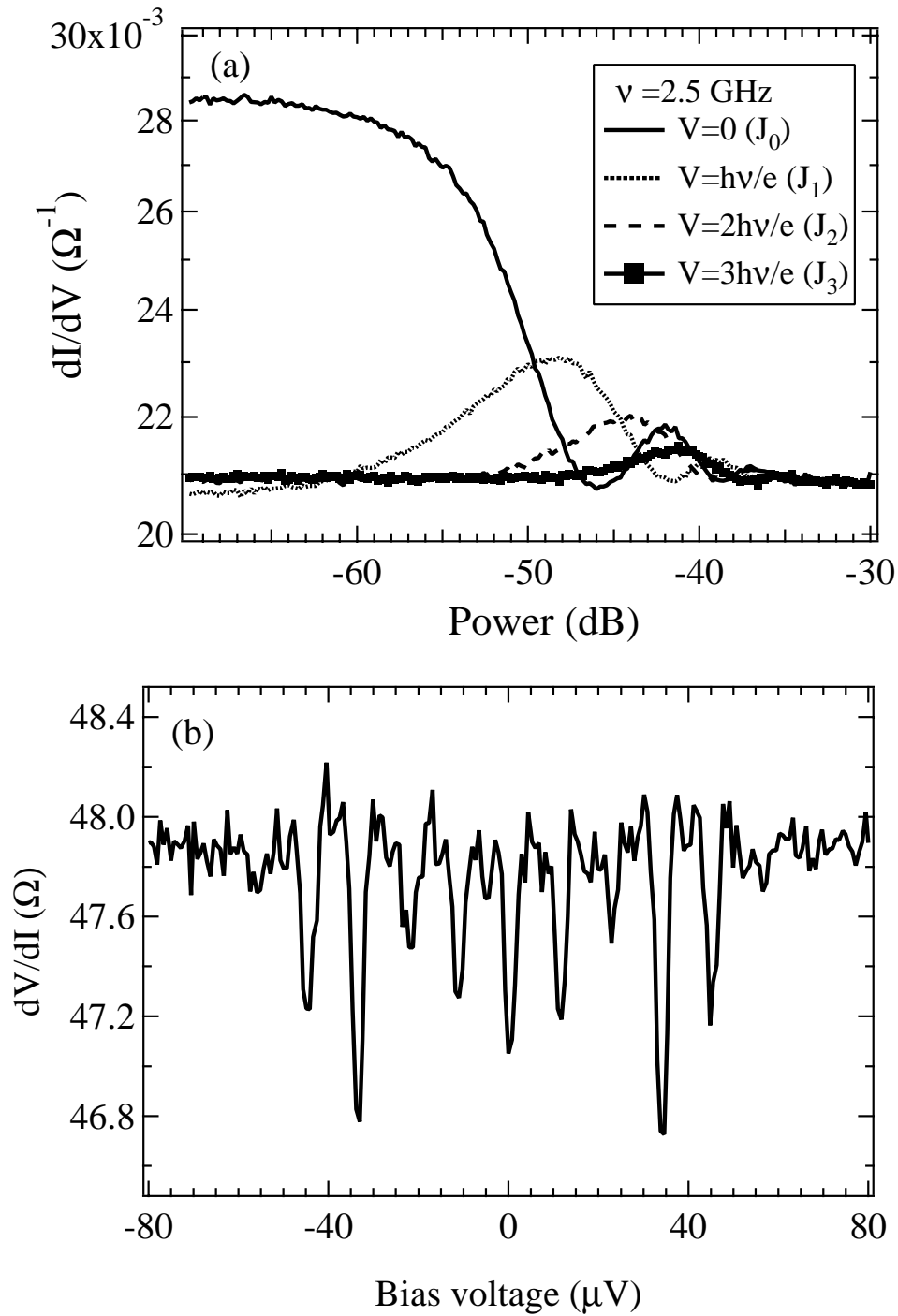


Figure 5.25: (a) Oscillatory dependence of dI/dV on applied rf power at $\nu = 2.5$ GHz at bias voltages, corresponding to $nh\nu/e$, for $n = 0, 1, 2, 3$; (b) Bias voltage dependence of the differential conductance dV/dI under RF excitation at 2.5 GHz showing PAT features at bias voltages $V = nh\nu/e$.

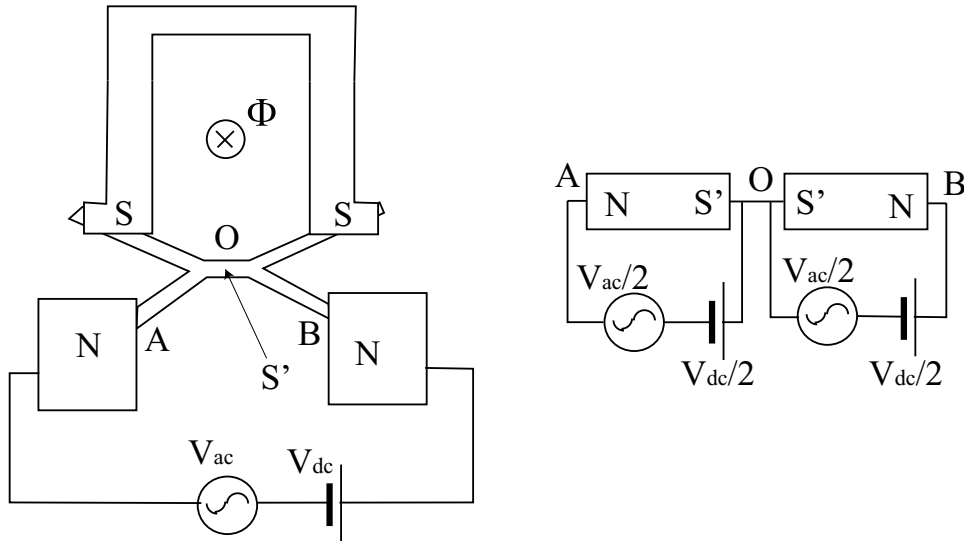


Figure 5.26: Schematic of the device with dc bias V_{dc} and rf excitation V_{ac} and equivalent circuit

have been shifted in vertical direction, so that the linear parts of the $T_N(V)$ dependence extrapolate to $2T_{M/C}/3$ at zero bias voltage. This is because the amplifier noise temperature when the long data set is taken may be different from the amplifier noise temperature during the calibration. We see, that noise temperature $T_N(V)$ displays features at small bias voltages. The measured noise temperature at zero bias voltage is higher, than the physical temperature of the device. This may be due to device impedance change at zero bias, which causes change in the rf power, reflected off the device. These features are phase-sensitive and change with $h/(2e)$ periodicity in magnetic flux. The features in noise occur at a bias voltage range as the zero-bias dip in differential resistance and the increase of differential resistance at $V \approx 10 \mu\text{V}$.

We are unable to make a conclusive explanation of the physical origin of these features. There are several possibilities. The features in noise occur in the bias voltage range where the differential resistance of the device exhibits maximum, presumably due to disappearance of the supercurrent in the normal diffusive wire between superconducting terminals. The observed noise may be due to switching of the supercurrent on and off. Another possibility is that the observed noise is due to the ac Josephson coupling between the terminals of the superconducting loop. Josephson coupling between superconducting reservoirs may cause downconversion of noise from high ($\sim eV/h$) frequencies which will result in excess noise of the device (Schoelkopf 1995). Large excess noise at small (a few μV)

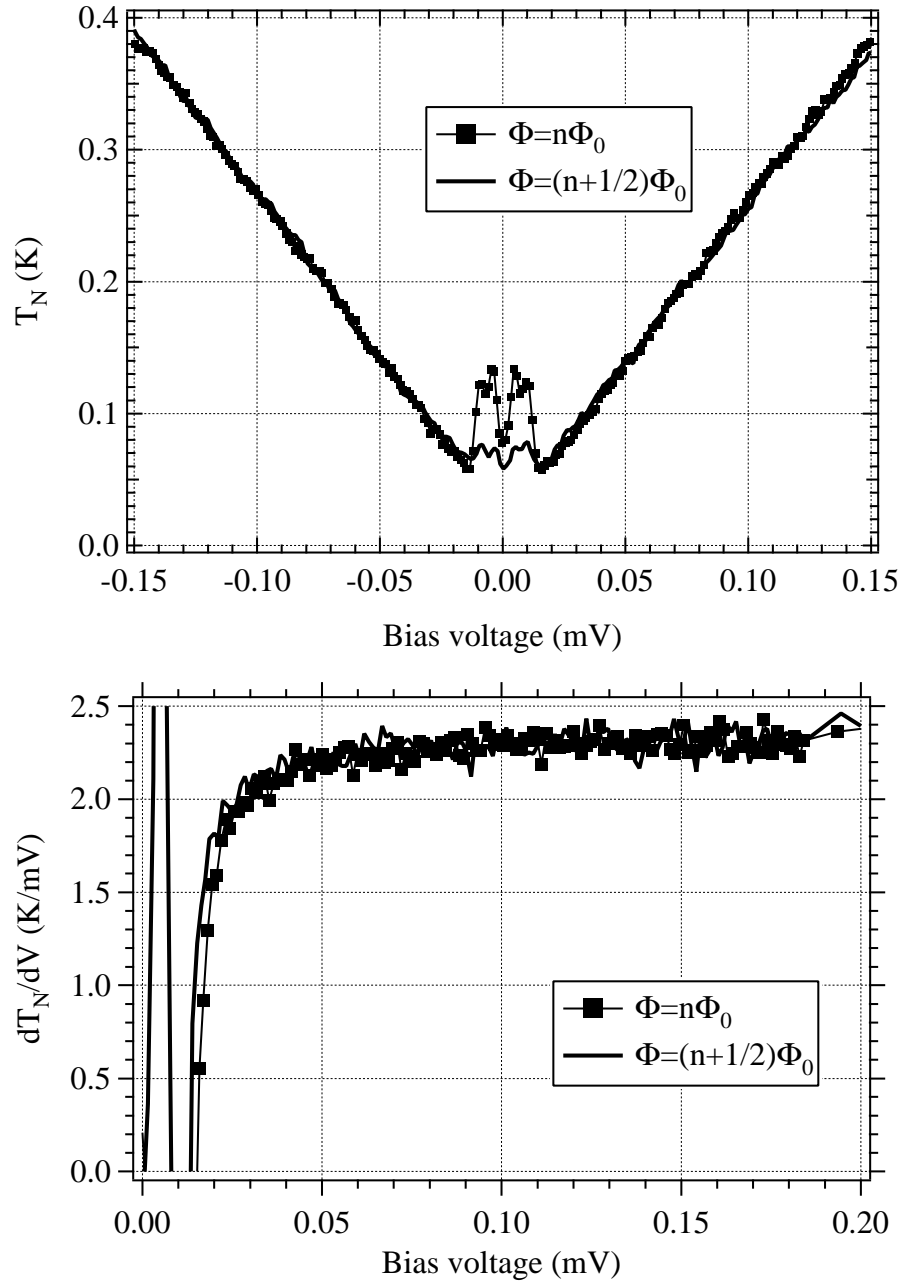


Figure 5.27: Bias voltage dependence of differential noise temperature dT_N/dV for the "cross" device for an integer and semi-integer magnetic flux. Behavior at bias voltages $V \lesssim 20 \mu\text{V}$ is likely due to onset of Josephson coupling between superconducting terminals.

bias voltages has been experimentally observed in long diffusive S-N-S junctions (Hoss et al. 2000). It was proposed (Hoss et al. 2000) that this excess noise is due to the onset of Josephson coupling between the superconducting reservoirs. At bias voltages $V \gtrsim 15 \mu\text{V}$ differential noise $dT_N/dV \sim 2.3 \text{ K/mV}$, which is close to the prediction for the hot-electron noise for $q_{eff} = e$. Figure 5.27(b) shows differential noise dependence on bias voltage at integer and semi-integer magnetic flux. Features at $V \lesssim 15 \mu\text{V}$ are due to the peaks in noise near $V=0$ and also, possibly, due to steep change of device impedance vs. bias voltage. At above $20 \mu\text{V}$, the curves in figure 5.27(b) show no phase-sensitivity of non-equilibrium noise at bias voltages higher than $\sim 15 \mu\text{V}$. We did not apply the correction to the change in rf power reflected off the device to the data in figure 5.27(b). At bias voltages $V \gtrsim 20 \mu\text{V}$ the dependence of differential resistance vs. bias voltage is very weak, and the change in reflected power off the device is going to be negligible. At $|V| \lesssim 15 \mu\text{V}$, the change in device resistance is very steep, and in that bias voltage range we cannot make any reliable estimate of the differential noise of the device dT_N/dV . Additionally, the inverse Thouless time for the "cross" device corresponds to frequency of $\tau_D^{-1} \sim 2 \text{ GHz}$, so the impedance of the device $\nu \sim 1.5 \text{ GHz}$ may be different from the dc differential resistance $R_{diff} = dV/dI$ (Büttiker et al. 1993).

The noise measurements on the "cross" device were unusually "noisy" for unknown reasons - despite long averaging times, we did not manage to obtain as good "signal-to-noise" on the noise of the "cross" device as we got for N-S junctions and for the "Y" device, discussed below. It seems that the "cross" device is more susceptible to electromagnetic interference than N-S junctions and a "Y" device.

In summary, the non-equilibrium noise measurements in a "cross" device exhibits features at bias voltages smaller than $\sim 15 \mu\text{V}$, which exhibit phase-sensitive behavior and are likely due to the onset of Josephson coupling between the terminals of a superconducting loop. At bias voltages $\gtrsim 20 \mu\text{V}$, the effective noise temperature of the device increases linearly with bias voltage with a slope $dT_N/dV \approx 2.3 \text{ K/mV}$, which is close to the expected slope for hot-electron noise in a normal diffusive conductor. This could be due to electron thermalization or due to the heating of reservoirs. The non-equilibrium noise at bias voltages $\gtrsim 20 \mu\text{V}$ exhibits no phase-sensitive behavior.

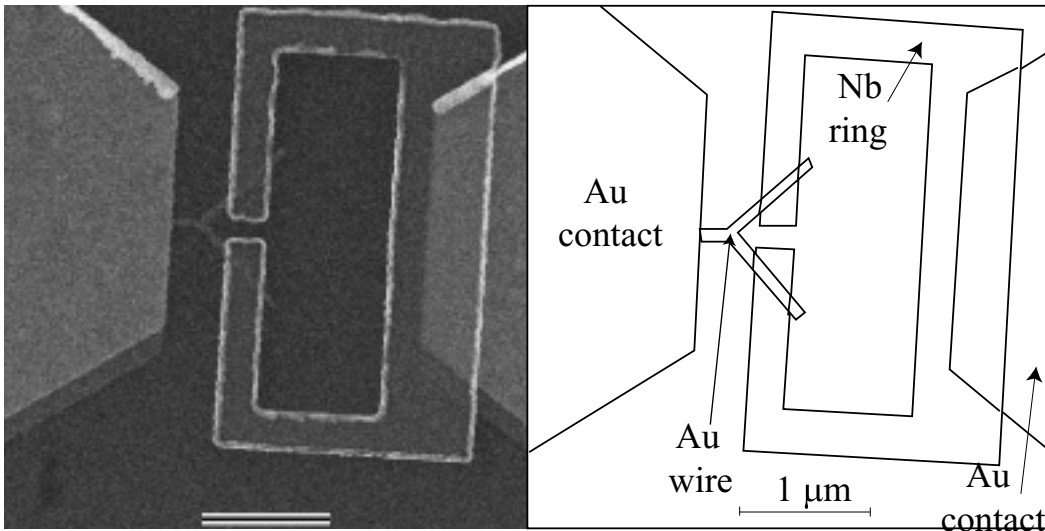


Figure 5.28: SEM picture and schematic of device of "Y" geometry.

5.6.2 Transport and noise properties in device of "Y" geometry

A "Y" device is a fork-shaped normal wire in contact with one normal reservoir and two ends of a superconducting loop. By tuning magnetic flux through the ring the phase difference between the branches of "Y" structure can be continuously tuned. The geometry and schematic of "Y" device is presented in figure 5.28. We performed cryogenic measurements of transport and non-equilibrium noise properties of one "Y" device. We also performed numeric modeling of a device of "Y" geometry and compared results of the transport measurements with theoretical predictions. First, we discuss the results of transport measurements and comparison with theoretical expectation, and later we present the results of non-equilibrium noise measurements in a "Y" structure.

Transport properties of "Y" structure

Device of "Y" geometry displayed modulation of conductance with magnetic field. From the SEM picture of the device, we determine the inner area of the superconducting ring is about $2.9 \mu\text{m}^2$. If the ring was thin, the expected period of conductance modulation would be about $\Delta B = \Phi_0/A_{inner} = 0.7$

mT. Because of the finite thickness of the ring, the effective area may be larger than the inner area of the ring, that will result in decrease of ΔB . Figure 5.29(a) shows the bias voltage dependence of differential resistance of "Y" structure at several values of magnetic flux. The mixing chamber temperature is 50 mK. We see that the conductance of the device changes systematically with the change of magnetic field. At integer flux the reentrant behavior is well-pronounced, at semi-integer flux the reentrant behavior is present, but the amplitude of the resistance change is much smaller. Note that at bias voltages larger than about $130 \mu\text{V}$ the resistance decreases when magnetic flux goes from integer to semi-integer value, as opposed to the range of bias voltages smaller than $130 \mu\text{V}$, where the resistance increases as flux goes from integer to semi-integer value. Figure 5.29(b) shows the magnetic field dependence of zero-bias differential resistance of the "Y" structure. Modulation with a period of about 0.64 mT is clearly seen. This is a little smaller period than expected from the inner area of the superconducting ring. This discrepancy is due to finite width of the niobium ring. Note that calculation of magnetic field was done from measuring the current through the magnet and converting the current in magnetic field knowing the parameters of the magnet: $B = 0.1 (\text{T/A}) I$. Superconducting magnets may have magnetic flux trapped in them, so zero current in the magnet does not necessarily correspond to zero magnetic field. In figure 5.29(b) zero current through the magnet corresponds to approximately semi-integer number of flux quanta through the device (we make this conclusion based on the observation that the resistance of the device has a maximum near $B - B_0 = 0$). Although the horizontal axis of figure 5.29(b) has an unknown offset B_0 , this doesn't affect the conclusions regarding periodic modulation of the conductance of the device.

Comparison of theory and experiment

The transport in the "Y" structure shows no signs of supercurrent or Josephson coupling, so we were able to perform comparison between the observed behavior and theoretical predictions. When the external magnetic flux satisfies the condition $\Phi = n\Phi_0$, the "Y" device is expected to behave similarly to a diffusive N-S junction. In this case, there is no superconducting phase gradients, and the two arms of Andreev interferometer can be "compressed" in one wire, so device "Y" looks like a diffusive N-S junction with non-uniform cross-section of the normal wire - see figure 5.30(a). Because the normal wire is non-uniform, the correction to the resistance may be different, but qualitative

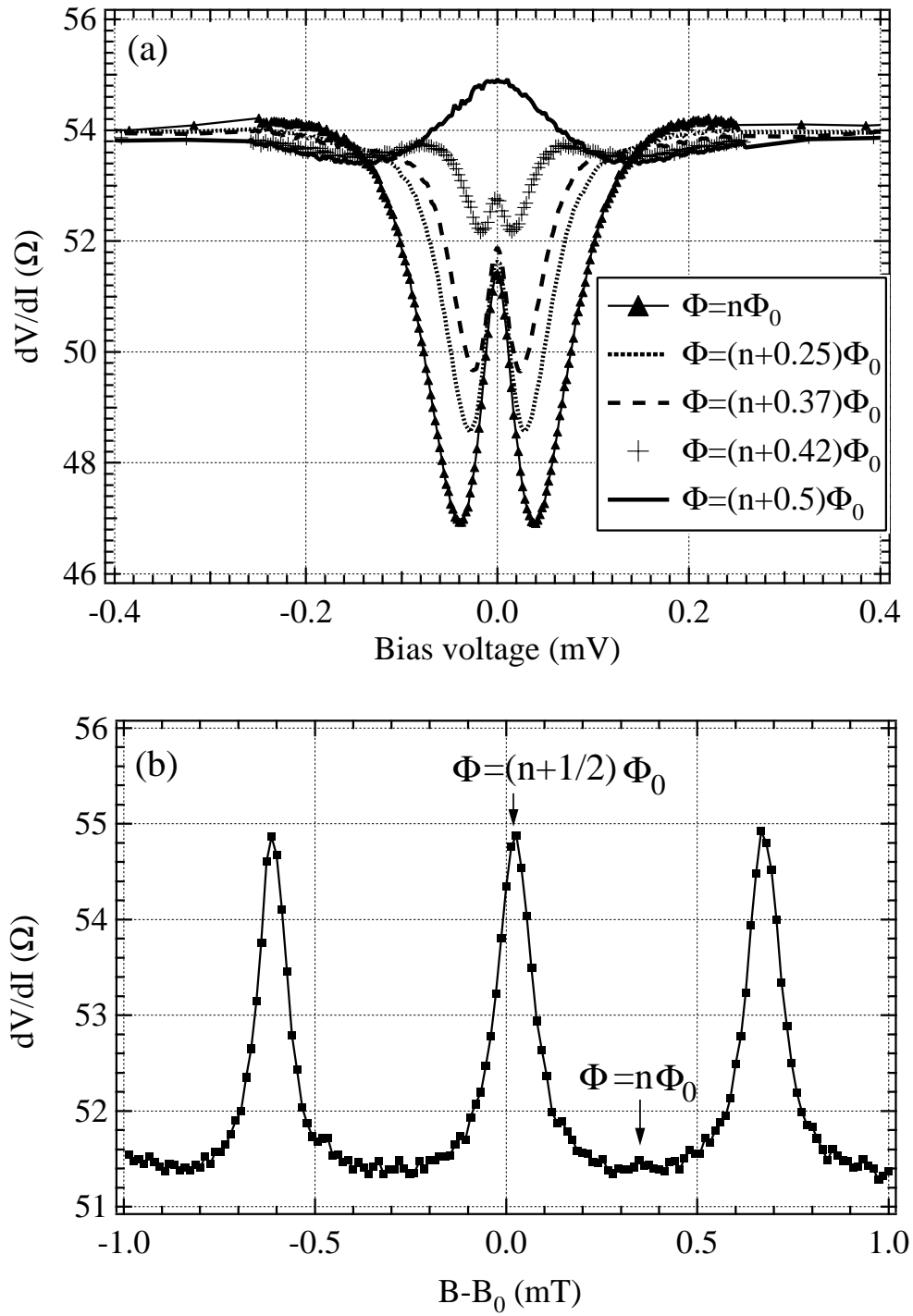


Figure 5.29: Differential resistance vs. bias voltage at different values of magnetic flux and zero-bias differential resistance vs. magnetic field of a "Y" structure.

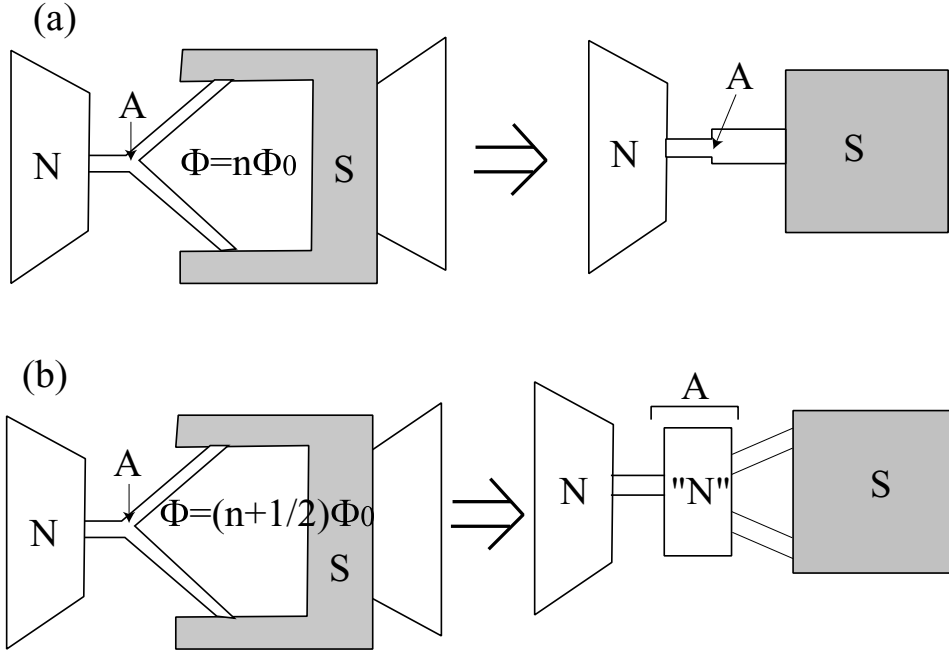


Figure 5.30: Model for calculation of conductance of "Y" structure.

features (e.g. reentrant behavior) should be the same as for a diffusive N-S junction.

When the flux threading the superconducting loop is equal to semi-integer number of flux quanta, i.e. $\Phi = (n + 1/2)\Phi_0$, point A is normal, and the device looks like a normal wire in series with 2 diffusive N-S junctions in parallel - see figure 5.30(b). In this case the correction to the conductance is expected to be smaller, because the conductance of part of the normal wire between normal reservoir and point A is not changed by proximity effect.

To theoretically predict the conductance of the "Y" device in case $\Phi = (n + 1/2)\Phi_0$, we need only the dependence of the conductance of a diffusive N-S junction on energy. From figure 5.30(b) we see that:

$$R_{diff}(V)_{\Phi=(n+1/2)\Phi_0} = R_N + \frac{1}{2}R_{diff}^{NS}(V), \quad (5.19)$$

where $R_{diff}^{NS}(V)$ is the energy dependence of differential resistance of a diffusive N-S junction. Although the "normal" part and 2 N-S junctions are connected in series, electrons do not relax energy in the normal wire (to the left of point A), so the differential resistance both for a diffusive N-S junction and for "Y" structure is determined by the pairing angle $\theta(x, E)$ at the same energy

$E = eV$. Taking the dependence $R_{diff}^{NS}(E)$ for a diffusive N-S junction, we calculate the dependence $R_{diff}(V)_{\Phi=(n+1/2)\Phi_0}$. The result of calculation is presented in figure 5.31(a), Thouless energy is taken to be $E_C = 25\mu\text{eV}$ - this is our estimate for the Thouless energy of the "Y" structure that was studied experimentally. Note, that for "Y" structure we define Thouless energy as $E_C = \hbar D/L^2$, where L is the length of one of the 2 sections of the structure which make contact to the superconducting ring.

For $\Phi = n\Phi_0$ Usadel equation can be solved numerically for both thin and thick section of a model N-S junction in figure 5.30(a); the solutions have to be matched at point A. An alternative approach is to use the effective action functional $U[\theta(x, E)]$ and find the solution of Usadel equation by minimizing the effective action functional (more precisely, by finding $\theta(x, E)$ which yields zero first variation $\delta_E U[\theta(x, E)]$, because the effective action is complex). We obtained numerical solution by direct "minimization" of $U[\theta(x, E)]$ by a gradient descent method. The result is presented in figure 5.31(a).

Figure 5.31(a) also presents experimentally measured normalized differential resistance of "Y" structure at integer and semi-integer values of external flux. To normalize the measured differential resistance, we assumed zero-bias differential resistance at semi-integer flux to be equal to the normal state resistance, i.e. $R_N \equiv dV/dI(V=0)_{\Phi=(n+1/2)\Phi_0}$. We see, that our data are in qualitative agreement with theory. Experimentally, the differential resistance of "Y" device displays reentrant behavior vs. bias voltage. The maximal amplitude of the resistance change at integer flux is about $0.1R_N$; it is much smaller ($\sim 0.03R_N$) at semi-integer flux. The minimum of R_{diff} occurs at $\sim 1.4E_C/e$ for $\Phi = n\Phi_0$ and at substantially higher bias voltage ($\sim 5E_C/e$) for semi-integer flux. These features of the experimental data are consistent with the model, although the magnitude of the resistance change is smaller than expected theoretically, by about a factor of 2 in case of integer flux. The locations of the minima of $R_{diff}(V)$ are in good agreement with theory, the value $E_C \approx 25\mu\text{eV}$ is inferred from the geometry of the sample and the resistivity of normal metal film and is not a fitting parameter.

The theory curves presented in figure 5.31(a) are zero-temperature predictions. At finite temperatures, the features in the curves will be "averaged" over a voltage scale of a few $k_B T/e$, this will lead to decrease of the maximal change of the resistance. For our device the minimum of the resistance

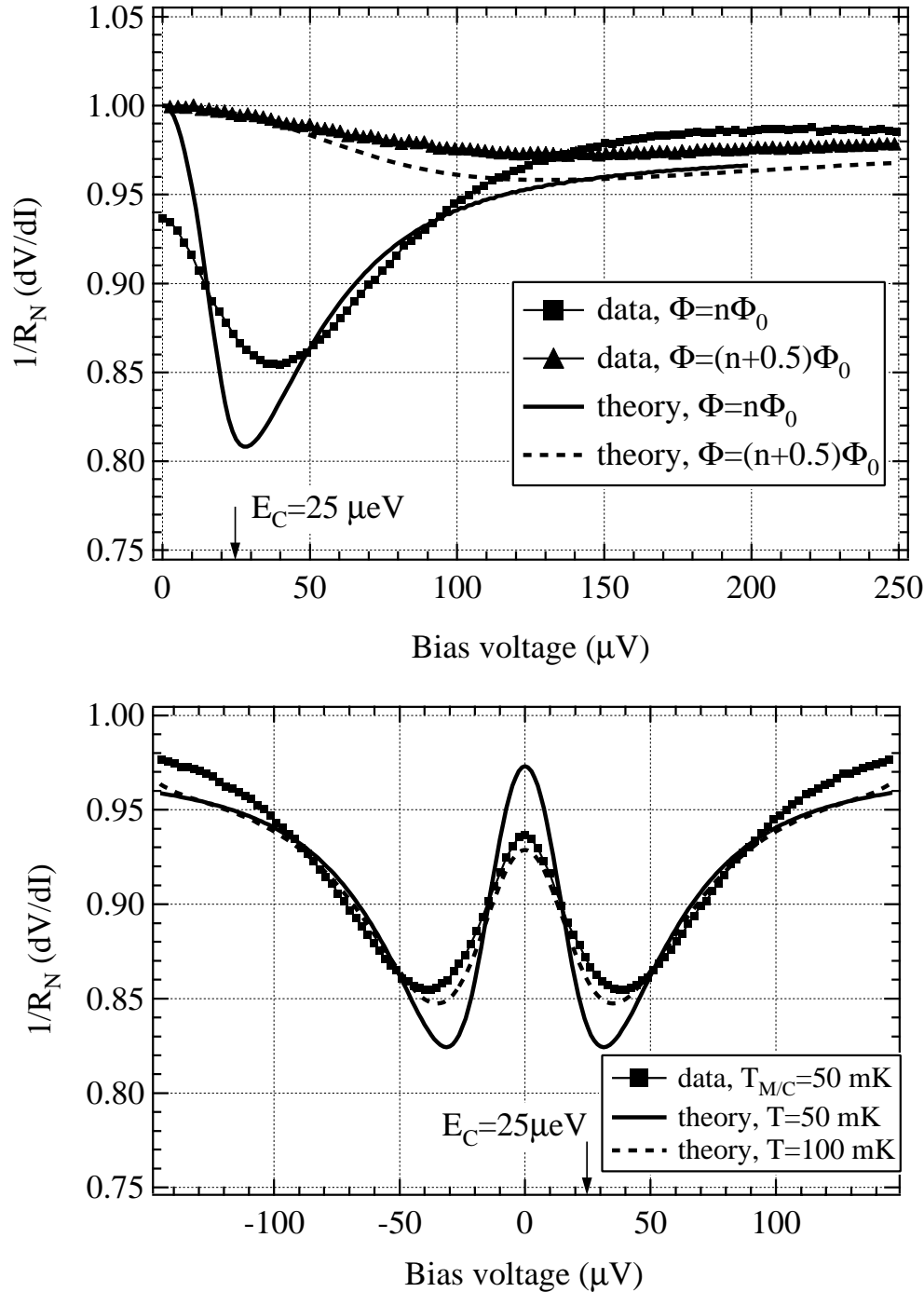


Figure 5.31: Theoretical and experimental dependence of differential resistance of "Y" structure vs. bias voltage. Top panel: experimental data at integer and semi-integer flux and theoretical predictions at $T=0$. Bottom panel: experimental data and theory for finite temperatures. The fit assuming $T = 100 \text{ mK}$ is in better agreement with experiment than the fit assuming $T = T_{M/C} = 50 \text{ mK}$.

occurs at bias voltage $eV \sim E_C \approx 25 \mu\text{V}$. For such a voltage scale the influence of finite temperatures is going to be appreciable even at 50 mK ($k_B T \approx 4 \mu\text{eV}$ at 50 mK, which is similar to the voltage range over which R_{diff} changes in case of integer flux). To make a fair comparison of theory with experimental data, we need to take into account finite temperature in our calculation. Differential conductance dI/dV at finite temperature can be calculated from zero-temperature conductance by convolving the latter with a thermal kernel (equation 2.49):

$$\frac{dI}{dV}(eV, T) = \int_{-\infty}^{+\infty} \frac{dI}{dV}(eV + E, T = 0) \frac{1}{4k_B T \cosh^2\left(\frac{E}{2k_B T}\right)} dE \quad (5.20)$$

Figure 5.31 presents experimental data for $\Phi = n\Phi_0$, along with theoretical predictions for $T = 50$ mK (solid line) and 100 mK (dashed line). Differential conductance of the device at $\Phi = (n + 1/2)\Phi_0$ does not change appreciably on voltage scales of a few $k_B T/e$, and taking finite temperature into account doesn't visibly modify theoretical predictions for $\Phi = (n + 1/2)\Phi_0$. Although the mixing chamber temperature was 50 mK, the data for $\Phi = n\Phi_0$ are much closer to the predictions at 100 mK. It is possible, that this effect is at least in part due to the heating of the reservoirs by dc voltage applied to the device. It is extremely difficult to build a quantitative model describing heating of the reservoirs; we did not do that. Other possible sources, which can modify the conductance are inelastic scattering of electrons in the normal wire and imperfect interface between normal metal and superconductor - both these effects are expected to decrease the change of resistance. Our simplified model did not take the effects of inelastic scattering, imperfect interface and imperfect reservoirs into account. In spite of these simplifying assumptions, the measured differential resistance of the "Y" structure is in fair agreement with the theoretical predictions. The numerical modeling was performed only for cases of integer and semi-integer magnetic flux. The case of arbitrary flux is more difficult to handle theoretically - in this case one needs to solve for both $\theta(x, E)$ and $\varphi(x, E)$, moreover, it seems that in this case the application of an effective action concept at finite energies is not straightforward.

Non-equilibrium noise in "Y" structure

We also performed non-equilibrium noise measurements for "Y" structure. The resistance of the device is close to 50Ω , so the device should be well-matched to the amplifier. The measurements were performed using an ac bias modulation and lock-in detection technique. As described in chapter 4, Johnson noise calibration was used to determine the gain and noise temperature of the measurement setup. This allowed converting noise data into absolute temperature units.

Figure 5.32 presents the bias voltage dependence of the differential noise temperature of the rf chain referred to the input dT_{in}/dV :

$$\frac{dT_N^{in}}{dV} = \frac{1}{G} \frac{dT_N^{out}}{dV}. \quad (5.21)$$

As discussed in the section about the effects of the circulator, the quantity dT_N^{in}/dV has contributions from differential noise temperature of the device dT_N/dV and from the change of Johnson noise of the termination on the circulator reflected off the device. Combining equations 5.20 and 5.7, we obtain:

$$\frac{dT_N}{dV} = \frac{dT_N^{in}}{dV} + (T_{iso} - T_N) \frac{dC}{dV}(V) \quad (5.22)$$

We see that, overall, the differential noise is close to the expectation for a diffusive N-S junction - the value of dT_N^{in}/dV is close to 4 K/mV. There is a systematic dependence of measured differential noise dT_N^{in}/dV . At bias voltages between ~ 50 and $\sim 150 \mu\text{V}$ differential noise is the largest for integer flux $\Phi = n\Phi_0$ and the smallest for the semi-integer flux $\Phi = (n + 1/2)\Phi_0$. The maximum magnitude of the flux modulation occurs at a bias voltage of about $100 \mu\text{V}$ and is about 10%. As with diffusive N-S junctions, we need to subtract the term $(T_{iso} - T_N) \frac{dC}{dV}(V)$ to obtain the differential noise of the device dT_N/dV .

In order to check, whether it is a fair assumption to replace rf impedance of the device by dc differential resistance, we measured the bias voltage dependence of external rf power reflected from the device simultaneously with dc differential resistance R_{diff} . Figure 5.33 presents bias voltage dependence of R_{diff} and reflected power P_{refl} on bias voltage of the device at integer flux and at $\Phi \approx (n + 0.45)\Phi_0$. Dashed lines are dc resistance curves, solid lines are rf power curves. DC differential resistance and rf power were measured simultaneously. We see that, qualitatively, P_{refl}

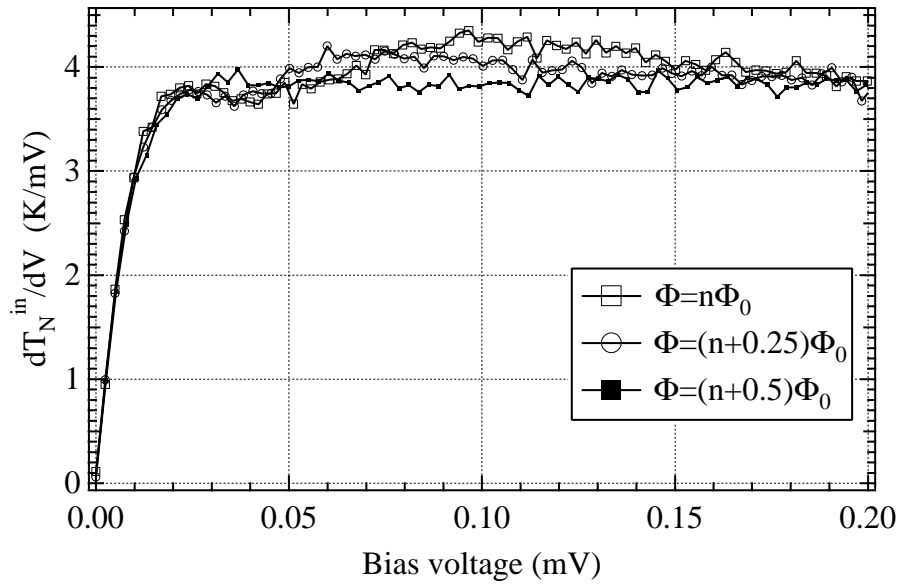


Figure 5.32: Differential noise of the rf chain referred to the input vs. bias voltage of the device at several values of magnetic flux.

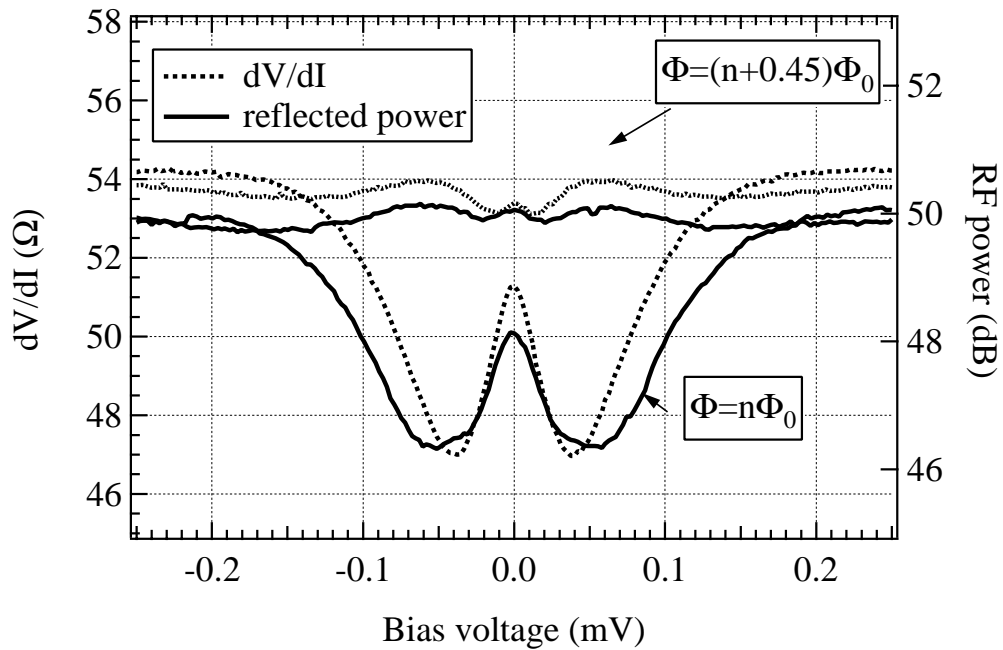


Figure 5.33: Bias voltage dependence of dc differential resistance and reflected rf power at 1.5 GHz at integer and half-integer flux.

exhibits similar behavior to R_{diff} . However, the detailed shape of the dc resistance and rf power vs. bias voltage is different. The minima in P_{refl} occur at bias voltage different from bias voltages at which minima in R_{diff} occur. That means that for this device we cannot take the rf impedance of the device to be equal to differential resistance dV/dI . The situation is a lot better for the case of semi-integer flux, because in this case there is very little change of both differential resistance and reflected power vs. bias voltage, so the uncertainties of the correction procedure are going to be less important. For the case of integer flux the correction may have larger errors due to large ($\sim 15\%$) change of differential resistance occurring over a relatively narrow bias voltage interval (due to a larger length of device and, hence, a smaller Thouless energy) and also due to the presence of finite-frequency effects in the impedance of the device. In our experiments, we cannot perform the calibration necessary to measure the rf impedance of the device. To perform the correction for the Johnson noise of the circulator, we use the dc value of differential resistance; it is understood, that there will be some additional systematic error due to the difference between impedance of the device at 1.5 GHz $Z(\nu)$ and $R_{diff} = dV/dI$.

Figure 5.34 presents differential noise temperature dT_N/dV vs. bias voltage for the "Y" device at 3 different values of magnetic flux. Data presented in figure 5.34 are corrected for the change in the circulator's noise. The data were corrected assuming $R_A = 50 \Omega$ and $T_{iso} = 4$ K. The error bars are the "worst" combinations of $\pm 2 \Omega$ uncertainty in amplifier's impedance R_A and due to ± 1 K uncertainty of the physical temperature of the circulator T_{iso} . The error bars due to $\sim 3\%$ uncertainty of the gain of the rf system are not shown.

We see, that the correction does not introduce any visible error bars for the case of semi-integer flux $\Phi = (n + 1/2)\Phi_0$. This is because of very weak dependence of $R_{diff}(V)$. Measurements of reflected rf power at 1.5 GHz confirm very weak dependence of reflected rf power when the flux is close to semi-integer value. The slope of $T_N(V)$ at semi-integer flux is about 3.9-4 K/mV, which corresponds to current spectral density of $4/3eI$, i.e., to an effective charge $q_{eff} = 2e$, as in case of a diffusive N-S junction.

For $\Phi = n\Phi_0$ and $\Phi = (n + 1/4)\Phi_0$, because of steep dependence of $R_{diff}(V)$, the error bars exceed the gain uncertainty and, for the case of integer flux, are up to $\sim 15\%$ of the inferred value of dT_N/dV . Based on the estimated error bars, at most bias voltages we cannot convincingly claim that

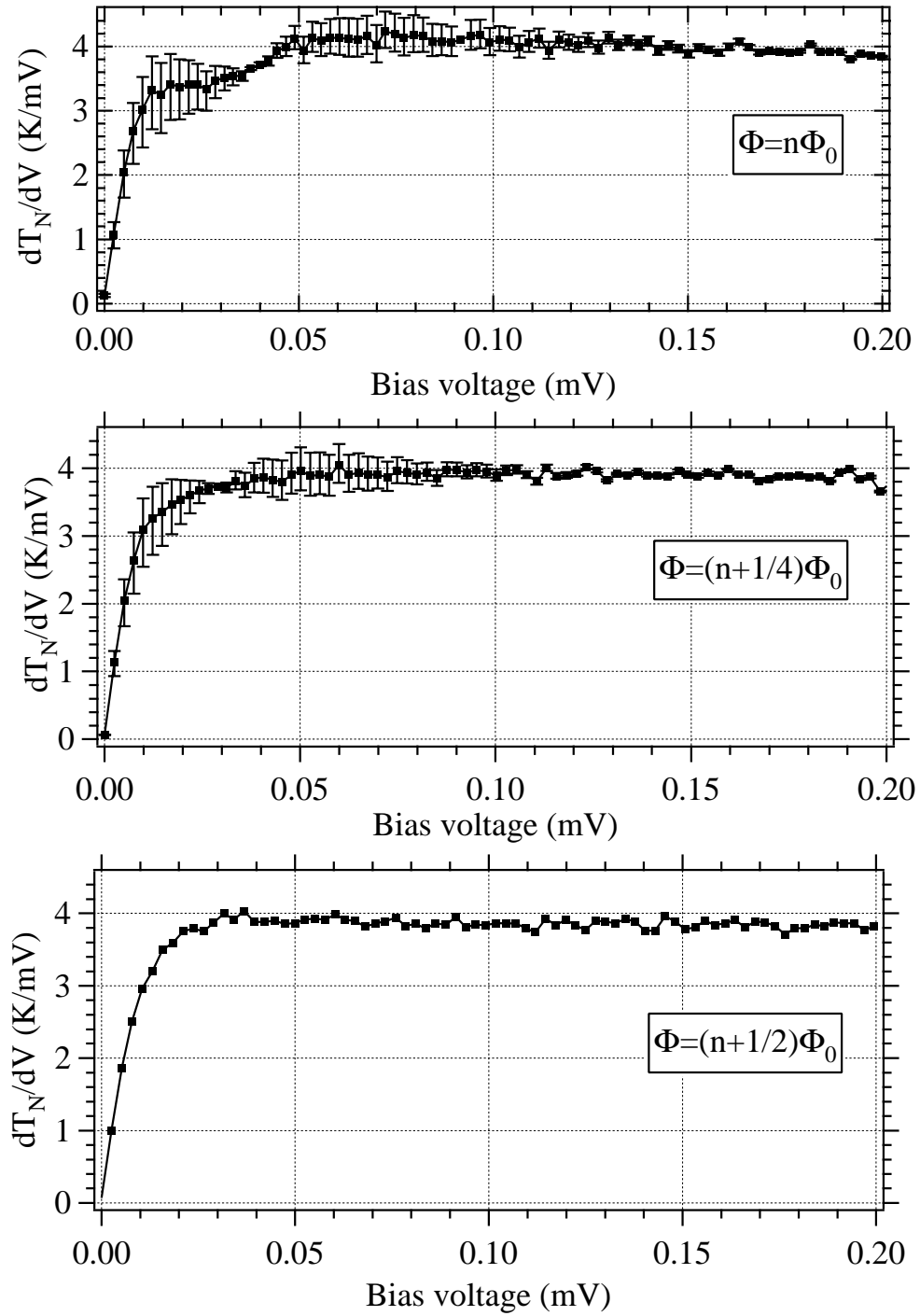


Figure 5.34: Corrected dT_N/dV for device "Y" at several different values of magnetic flux ($T_{M/C} = 50$ mK). Error bars are the worst error estimates due to $\pm 2 \Omega$ uncertainty for R_A and ± 1 K uncertainty for T_{iso} .

we see the phase-dependence of shot noise of Andreev interferometer. There is a narrow range of bias voltages around 30-40 μV , where, because of the minimum of differential resistance, the derivative of reflected power with respect to bias voltage should vanish. However, as seen in figure 5.33, minimum of a dc differential resistance does not exactly correspond to the minimum of reflected rf power, so it is difficult to argue quantitatively that the observed difference between calculated dT_N/dV at integer and semi-integer flux around $V = 40\mu\text{V}$ is not due to the change of high-frequency impedance at 1.5 GHz vs. bias voltage. At large bias voltages ($\gtrsim 100 \mu\text{V}$), there is no phase modulation of dT_N/dV within the error of our measurement.

In a situation where the errors in dS_I/dI are dominated by the uncertainties due to device impedance change, it is more convenient to measure the magnetic field dependence of T_N or S_I at a constant dc current through the device. Figure 5.35(a) shows the magnetic field dependence of T_N at dc current $I = 1.06 \mu\text{A}$. The drift of the amplifier noise temperature was linear in time and was subtracted. The magnitude of the drift was ~ 20 mK over the time of the magnetic field sweep. The effective noise temperature T_N clearly changes in phase with the differential resistance of the device. The maximum change of T_N is about 15%. The modulation of T_N is observed in the range of bias voltages where the differential resistance R_{diff} is phase-sensitive (at bias voltages $V \lesssim 100 \mu\text{V}$).

The phase modulation of T_N may be due to a "trivial" effect of changing of Z_{diff} . Since $T_N = S_I Z_{diff} / (4k_B)$, change of Z_{diff} will cause change in T_N even if S_I is constant. The "non-trivial" phase modulation of shot noise would be the change of S_I with magnetic flux at constant I . From the measured T_N we can calculate S_I , again, assuming $Z_{diff} = dV/dI$. Fig. 5.35(b) shows the magnetic field dependence of "effective charge" $q_{eff} = 3k_B(T_N - 2T_{bath}/3) / (2eR_{diff})$ vs. magnetic field at constant current. We see, that whereas T_N exhibits pronounced modulation with magnetic flux, S_I does not exhibit periodic modulation with magnetic flux within the uncertainty of this measurement.

In summary, we performed non-equilibrium noise measurements in an Andreev interferometer. At semi-integer flux we measured shot noise close to the shot noise of a diffusive N-S junctions and corresponding to an effective charge $q_{eff} = 2e$. At magnetic flux values $\Phi = n\Phi_0$ and $\Phi = (n+1/4)\Phi_0$ we measured shot noise within the error bars (10-15%) from shot noise, corresponding to the effective charge $2e$. Large magnitude of error bars was due to a steep bias voltage dependence of the differential

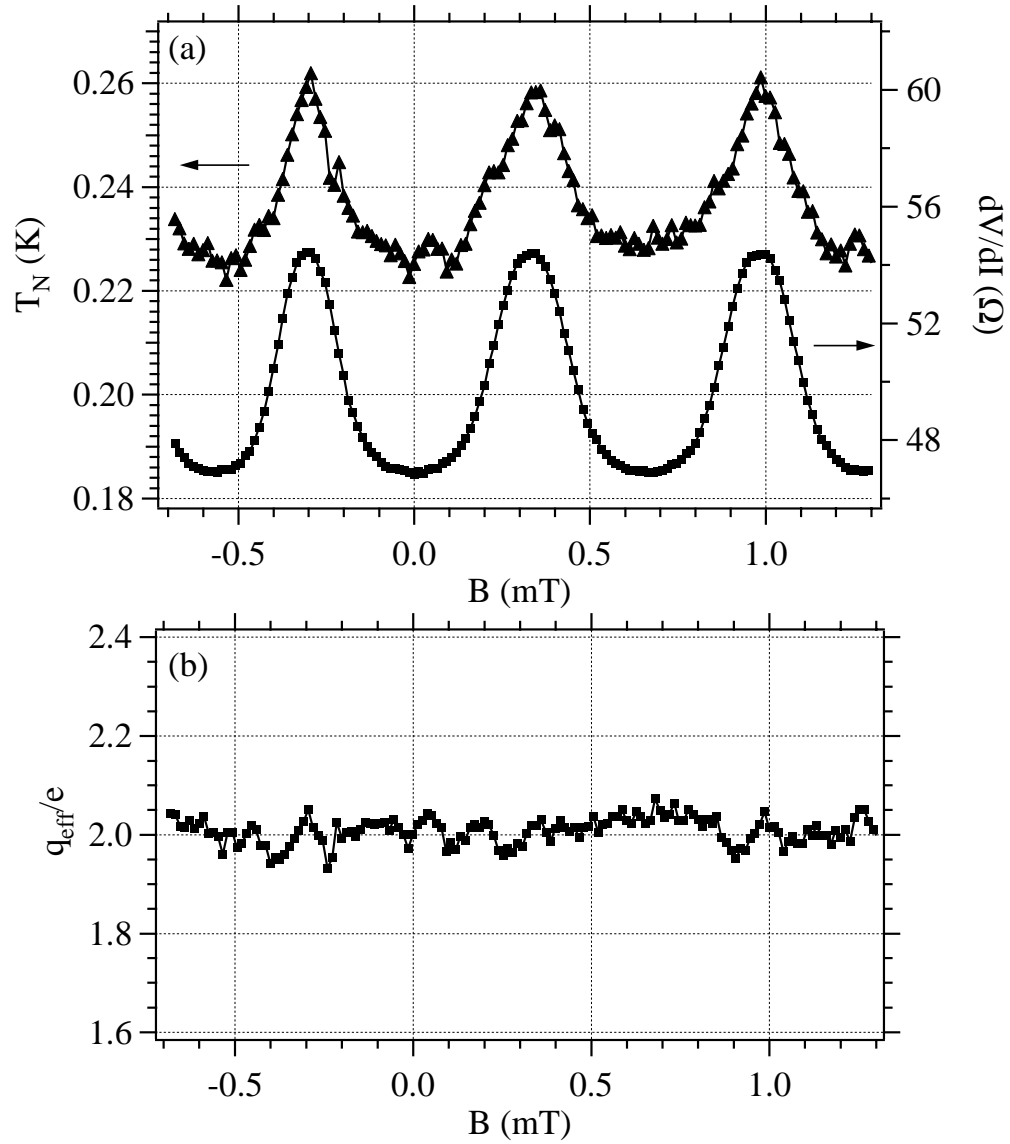


Figure 5.35: (a) Noise temperature of the device at $I = 1.06 \mu\text{A}$ vs. magnetic field; (b) Effective charge calculated from data in (a).

resistance of the device and due to finite-frequency effects on the impedance of the device. The effective noise temperature T_N displayed a pronounced modulation vs. magnetic field in phase with the differential resistance of the device. Within the uncertainty of our experiments, this modulation is due to the change of the differential resistance of the device, and not due to the modulation of the current spectral density S_I .

Chapter 6

Discussion

6.1 Summary of results presented in this thesis

In summary, we experimentally investigated transport and non-equilibrium noise properties of mesoscopic hybrid normal metal - superconductor devices. Non-equilibrium noise in hybrid N-S devices was used as a sensitive probe of correlations revealing the nature of current carriers.

We developed a fabrication process at Yale which allowed fabrication of sub- μm mesoscopic N-S structures. During the course of the project, an e-beam lithography system was installed on JEOL6400 scanning electron microscope which made it possible to write narrow (~ 50 nm) wires and perform alignment between layers to ~ 100 - 150 nm.

A high-sensitivity cryogenic setup was developed and used for noise measurements. Performing measurements at GHz frequencies allowed using large bandwidth and achieving high signal-to-noise ratio in our noise measurements. Because the impedance of the device is changing as a function of bias voltage, a mathematical model taking into account the effects of the device impedance change was developed. The model allowed calculation of non-equilibrium noise of the device from measured output noise of the measurement setup in case where the impedance of the device is not constant.

In the work described in this thesis, several novel results in the field of mesoscopic shot noise were found. Shot noise power in a diffusive device was measured to be doubled compared to the shot noise in normal diffusive conductor. This doubling of shot noise occurs due to the process of

Andreev reflections and is a signature of the effective charge $q_{eff} = 2e$ in a diffusive N-S junction. We performed measurements of shot noise in diffusive N-S junctions in the presence of high-frequency rf excitation. Under such an excitation, shot noise in a diffusive N-S junction develops photon-assisted features at bias voltages $V = nh\nu/q_{eff} = nh\nu/(2e)$. Observation of this effect provides an even clearer signature of effective charge $2e$, because the locations of the photon-assisted noise features are not sensitive to heating of reservoirs due to dc and ac bias applied. The location of the photon-assisted features in a diffusive N-S junction satisfy Josephson relation $2eV - h\nu$. This is the first experimental observation, where the Josephson frequency manifests itself in a system with only one superconducting reservoir and no weak links, where a true Josephson effect cannot take place.

We also fabricated diffusive Andreev interferometers and experimentally studied mesoscopic transport and non-equilibrium noise in these devices. Transport in these devices is phase-sensitive and displays periodic behavior in magnetic field with the period corresponding to magnetic flux quantum $h/(2e)$. We performed the first measurements of non-equilibrium noise in Andreev interferometers. We experimentally studied non-equilibrium noise in interferometers of 2 different geometries. When non-equilibrium noise is measured between 2 normal reservoirs of an Andreev interferometer, the measured noise is close to the expected hot-electron noise for a normal mesoscopic conductor. On the other hand, in a geometry where noise is measured between a normal and a superconducting reservoir, the observed noise is close to the shot noise of a diffusive N-S junction, bearing signatures of an effective charge $2e$.

6.2 Suggestions for future experiments

An interesting and challenging experiment is to observe phase sensitivity of shot noise in Andreev interferometer. It may be possible to engineer the geometry of the device so that the phase sensitivity of the noise will be more pronounced. Recently theoretical progress with calculating the shot noise in diffusive N-S junctions at arbitrary energies (Belzig and Nazarov 2001) gives some hope that shot noise in Andreev interferometers at arbitrary energies may be understood theoretically in the near future.

From a technical point of view, the systematic errors of our noise measurements were dominated by the difficulty of precisely estimating the fraction of the Johnson noise of a circulator, which is

reflected off of the device and coupled into the amplifier. In our experiments, the circulator is in He bath at a temperature of 4 K. If the circulator was cooled down to the mixing chamber temperature, the contribution of the circulator's noise would be almost 2 orders of magnitude smaller. That would reduce the error associated with the Johnson noise of the circulator and allow much more precise measurements of non-equilibrium noise.

Cooling of the circulator down to the mixing chamber temperature would allow one to perform detailed tests of shot noise theory in N-S junctions at arbitrary energies ($E \sim E_C$). It will also allow higher-quality shot noise measurements in Andreev interferometers, targeted at demonstrating phase-sensitive behavior of shot noise. An interesting set of experiments would be studying finite-frequency transport in diffusive N-S devices. As demonstrated in this thesis, the devices with lengths of 0.5-1 μm display signatures of phase-coherent transport. For such devices, diffusive time can correspond to a frequency below ~ 1 GHz. Measuring the rf reflection from an Andreev interferometer at 1.5 GHz showed, that at that frequency the impedance of the device is different from dc resistance. Detailed measurements of transport in these devices at GHz frequencies may shed light on electron dynamics in mesoscopic N-S systems at frequencies $\nu > \tau_{diff}^{-1}$.

Bibliography

- Abrahams, E., P. W. Anderson, P. A. Lee, and T. V. Ramakrishnan (1981). Quasiparticle lifetime in disordered two-dimensional metals. *Physical Review B* *24*(12), 6783–6789.
- Altshuler, B. L., A. G. Aronov, and D. E. Khmelnitsky (1982). Effects of electron-electron collisions with small energy transfers on quantum localisation. *Journal of Physics C* *15*(36), 7367–7386.
- Anantram, M. P. and S. Datta (1996). Current fluctuations in mesoscopic systems with Andreev scattering. *Physical Review B* *53*(24), 16390–16402.
- Andreev, A. F. (1964). The thermal conductivity of the intermediate state in superconductors. *Sov. Phys. JETP* *19*, 1228.
- Büttiker, M. (1992). Scattering theory of current and intensity noise correlations in conductors and wave guides. *Physical Review B* *46*(19), 12485–12507.
- Büttiker, M., A. Prêtre, and H. Thomas (1993). Dynamic conductance and the scattering matrix of small conductors. *Physical Review Letters* *40*(26), 4114–4117.
- Beenakker, C. W. J. (1992). Quantum transport in semiconductor-superconductor microjunctions. *Physical Review B* *46*(19), 12841–12844.
- Beenakker, C. W. J. and M. Buttiker (1992). Suppression of shot noise in metallic diffusive conductors. *Physical Review B* *46*(3), 1889–1892.
- Belevtsev, B. I., Y. F. Komnik, and E. Y. Beliaev (1998). Electron relaxation in disordered gold films. *Physical Review B* *58*(12), 8079–8086.
- Belzig, W. and C. Bruder (1996). Local density of states in a dirty normal metal connected to a superconductor. *Physical Review B* *54*(13), 9443–9448.

- Belzig, W. and Y. V. Nazarov (2001). Full current statistics in diffusive normal-superconductor structures. *cond-mat/0103235*.
- Blanter, Y. M. and M. Büttiker (2000). Shot noise in mesoscopic conductors. *Physics Reports* 336, 1–166.
- Blonder, G. E., M. Tinkham, and T. M. Klapwijk (1982). Transition from metallic to tunneling regimes in superconducting microconstrictions: Excess current, charge imbalance, and super-current conversion. *Physical Review B* 27(7), 4515–4532.
- Callen, H. B. and T. A. Welton (1951). Irreversibility and generalized noise. *Physical Review* 83(1), 34–40.
- Charlat, P., H. Courtois, P. Gandit, D. Mailly, A. F. Volkov, and B. Pannetier (1996). Reentrance of the metallic conductance in a mesoscopic proximity superconductor. *Physical Review Letters* 77(24), 4950–4953.
- Chouvaev, D., L. Kuzmin, and M. Tarasov (1999). Normal-metal hot-electron microbolometer with on-chip protection by tunnel junctions. *Superconductor Science and Technology* 12(11), 985–988.
- Courtois, H., P. Charlat, P. Gandit, D. Mailly, and B. Pannetier (1999). The spectral conductance of a proximity superconductor and the reentrance effect. *Journal of Low-Temperature Physics* 116(3-4), 187–213.
- Courtois, H., P. Gandit, and B. Pannetier (1995). Proximity-induced superconductivity in a narrow metallic wire. *Physical Review B* 52(2), 1162–1166.
- Cron, R., M. F. Goffman, D. Esteve, and C. Urbina (2001). Multiple-charge-quanta shot noise in superconducting atomic contacts. *Physical Review Letters* 86(18), 4104–4107.
- de Gennes, P. G. (1966). *Superconductivity in Metals and Alloys*. New York: W.A. Benjamin, Inc.
- de Jong, M. J. M. (1995). *Shot Noise and Electrical Conduction in Mesoscopic Systems*. Ph. D. thesis, Leiden University.
- de Jong, M. J. M. and C. W. J. Beenakker (1994). Doubled shot noise in disordered normal metal superconductor junctions. *Physical Review B* 49(22), 16070–16073.

- de Jong, M. J. M. and C. W. J. Beenakker (1997). *Mesoscopic Electron Transport*, Chapter "Shot Noise in Mesoscopic Systems". Dordrecht, the Netherlands: Kluwer Academic Publishers.
- De-Picciotto, R., M. Reznikov, M. Heiblum, V. Umansky, G. Bunin, and D. Mahalu (1997). Direct observation of a fractional charge. *Nature* 389(6647), 162–164.
- de Vegvar, P. G. N., T. A. Fulton, W. H. Mallison, and R. E. Miller (1994). Mesoscopic transport in tunable Andreev interferometers. *Physical Review Letters* 73(10), 1416–1419.
- den Hartog, S. G., B. J. van Wees, and T. M. Klapwijk (1997). Reentrant behavior in the superconducting phase-dependent resistance of a disordered two-dimensional electron gas. *Physical Review B* 56(21), 13738–13741.
- Deutscher, G. and P. G. de Gennes (1969). *Superconductivity*, pp. 1005.
- Dicke, R. H. (1946). The measurement of thermal radiation at microwave frequencies. *The Review of Scientific Instruments* 17(7), 268–275.
- Dieleman, P., H. G. Bukkems, T. M. Klapwijk, M. Schicke, and K. H. Gundlach (1997). Observation of Andreev reflection enhanced shot noise. *Physical Review Letters* 79(18), 3486–3489.
- Dieleman, P. and T. M. Klapwijk (1998). Shot noise beyond the tucker theory in niobium tunnel junction mixers. *Applied Physics Letters* 72(13), 1653–1655.
- Dimoulas, A., J. P. Heida, B. J. van Wees, T. M. Klapwijk, W. van der Graaf, and G. Borghs (1995). Phase-dependent resistance in a superconductor-two-dimensional-electron-gas quasiparticle interferometer. *Physical Review Letters* 74(4), 602–605.
- Dorokhov, O. N. (1984). On the coexistence of localised and extended electronic states in the metallic phase. *Solid State Communications* 51(6), 381–384.
- Dubash, N. B., G. Pance, and M. J. Wengler (1994). The measurement of thermal radiation at microwave frequencies. *IEEE Transactions on Microwave Theory and Techniques* 42(4), 715–725.
- Dubos, P., H. Courtois, B. Pannetier, F. K. Wilhelm, Zaikin, and G. Schon (2001). Josephson critical current in a long mesoscopic s-n-s junction. *Physical Review B* 63(6), 064502/1–5.
- Echternach, P. M., M. E. Gershenson, and H. M. Bozler (1993). Evidence of interference between

- electron-phonon and electron-impurity scattering on the conductivity of thin metal films. *Physical Review B* 47(20), 13659–13663.
- Eom, J., C. J. Chien, and V. Chandrasekhar (1998). Phase dependent thermopower in Andreev interferometers. *Physical Review Letters* 81(2), 437–440.
- Eom, J., C. J. Chien, and V. Chandrasekhar (1999). Reentrance effect in normal-metal/superconducting hybrid loops. *Physical Review B* 60(22), 15356–15363.
- Esteve, D., H. Pothier, S. Gueron, N. O. Birge, and M. H. Devoret (1997). *Mesoscopic Electron Transport*, Chapter The Proximity Effect in Mesoscopic Diffusive Conductors. Dordrecht, the Netherlands: Kluwer Academic Publishers.
- Fink, H. J. (1997). Supercurrents through SNS proximity-induced junctions. *Physical Review B* 56(5), 27322737.
- Golubov, A. A., F. K. Wilhelm, and A. D. Zaikin (1997). Coherent charge transport in metallic proximity structures. *Physical Review B* 55(2), 1123–1137.
- Gramespacher, T. and M. Büttiker (2000). Distribution functions and current-current correlations in normal-metal/superconductor heterostructures. *Physical Review B* 61(12), 8125–8132.
- Gueron, S. (1997). *Quasiparticles in a Diffusive Conductor: Interaction and Pairing*. Ph. D. thesis, CEA Saclay.
- Gueron, S., H. Pothier, N. O. Birge, D. Esteve, and M. H. Devoret (1996). Superconducting proximity effect probed on a mesoscopic length scale. *Physical Review Letters* 77(14), 3025–3028.
- Henny, M., S. Oberholzer, C. Strunk, T. Heinzel, K. Ensslin, M. Holland, and C. Schönenberger (1999). The fermionic Hanbury Brown and Twiss experiment. *Science* 284(5412), 296–298.
- Henny, M., S. Oberholzer, C. Strunk, and C. Schönenberger (1999). 1/3-shot-noise suppression in diffusive nanowires. *Physical Review B* 59(4), 2871–2880.
- Horowitz, P. and W. Hill (1989). *The Art of Electronics, second edition*. New York: Cambridge University Press.
- Hoss, T., C. Strunk, T. Nussbaumer, R. Huber, U. Staufer, and C. Schönenberger (2000).

- Multiple Andreev reflection and giant excess noise in diffusive superconductor/normal-metal/superconductor junctions. *Physical Review B* 62(6), 4079–4085.
- Hanbury Brown, R. and R. Q. Twiss (1956). Correlation between photons in two coherent beams of light. *Nature* 177(4497), 27–29.
- Ivanov, D. (1998). Private Communications, Unpublished.
- Jehl, X., M. Sanquer, R. Calemczuk, and D. Mailly (2000). Detection of doubled shot noise in short normal-metal/superconductor junctions. *Nature* 405(6782), 50–53.
- Johnson, J. (1928). Thermal agitation of electricity in conductors. *Physical Review* 32, 97–109.
- Kane, C. L. and M. P. A. Fisher (1994). Nonequilibrium noise and fractional charge in the quantum Hall effect. *Physical Review Letters* 72(5), 724–727.
- Karasik, B. S., W. R. McGrath, H. G. LeDuc, and M. E. Gershenson (1999). A hot-electron direct detector for radioastronomy. *Superconductor Science and Technology* 12(11), 745–747.
- Khlus, V. A. (1987). Current and voltage fluctuations in microjunctions between normal metals and superconductors. *Sov. Phys. JETP* 66(6), 1243–1249.
- Koch, R. H., D. J. Van-Harlingen, and J. Clarke (1982). Measurements of quantum noise in resistively shunted Josephson junctions. *Physical Review B* 26(1), 74–87.
- Kogan, S. M. (1996). *Electronic Noise and Fluctuations in Solids*. Cambridge: Cambridge University Press.
- Kozhevnikov, A. A., R. J. Schoelkopf, L. E. Calvet, M. Rooks, and D. Prober (2000a). Measurements of shot noise in diffusive normal metal - superconductor junctions. *Journal of Low-Temperature Physics* 118(5-6), 671–678.
- Kozhevnikov, A. A., R. J. Schoelkopf, L. E. Calvet, M. J. Rooks, and D. E. Prober (2000b). Shot noise measurements in diffusive normal metal-superconductor (n-s) junctions. *Journal of Low-Temperature Physics* 118(5-6), 671–678.
- Kozhevnikov, A. A., R. J. Schoelkopf, and D. E. Prober (2000). Observation of photon-assisted noise in a diffusive normal metal - superconductor junction. *Physical Review Letters* 84(15), 3398–3401.

- Kulik, I. O. and A. N. Omel'yanchuk (1975). Microscopic theory of the Josephson effect in superconducting bridges. *JETP Letters* 21, 96.
- Kumar, A., L. Saminadayar, D. C. Glattli, Y. Jin, and B. Etienne (1996). Experimental test of the quantum shot noise reduction theory. *Physical Review Letters* 76(15), 2778–2881.
- Landau, L. D. and E. M. Lifshitz (1980). *Statistical Physics Part 1*. Oxford: Pergamon.
- Landauer, R. (1957). Spatial variations of currents and fields due to localized scatterers in metallic conduction. *IBM Journal of Research and Development* 1(3), 223.
- Lesovik, G. B. (1989). Excess quantum noise in 2d ballistic point contacts. *JETP Letters* 49(9), 513–515.
- Lesovik, G. B. and L. S. Levitov (1994). Noise in an ac biased junction: nonstationary aharonov-bohm effect. *Physical Review Letters* 72(4), 538 – 541.
- Lesovik, G. B., T. Martin, and J. Torres (1999). Josephson frequency singularity in the noise of normal-metalsuperconductor junctions. *Physical Review B* 60(17), 11935–11938.
- Lesovik, G. B., T. Martin, and J. Torres (2000). Josephson effect in mesoscopic junctions with a single superconductor. In C. Glattli, M. Sanquer, and J. T. T. Van (Eds.), *Quantum Physics at Mesoscopic Scale*, France, pp. 415–421. EDP Sciences.
- Liu, R., B. Odom, Y. Yamamoto, and S. Tarucha (1998). Quantum interference in electron collision. *Nature* 391(6664), 263–265.
- Martin, T. and R. Landauer (1992). Wave-packet approach to noise in multichannel mesoscopic systems. *Physical Review B* 45(4), 1742–1755.
- McCord, M. A. and M. J. Rooks (1989). In *Handbook of Microlithography, Micromachining and Microfabrication*, pp. 128–252.
- Nabity, J. (1998). Nanometer pattern generation system. user's guide, version 7.6, release 7/98.
- Nagaev, K. E. (1992). On the shot noise in dirty metal contacts. *Physical Letters A* 169(1-2), 103–107.
- Nagaev, K. E. (1995). Influence of electron-electron scattering on shot noise in diffusive contacts. *Physical Review B* 52(7), 4740–4743.

- Nagaev, K. E. and M. Büttiker (2001). Semiclassical theory of shot noise in disordered superconductor - normal metal contacts. *Physical Review B* 63(8), 081301(R).
- Nazarov, Y. V. and T. H. Stoof (1996). Diffusive conductance as Andreev interferometers. *Physical Review Letters* 76(5), 823–826.
- Nyquist, H. (1928). Thermal agitation of electric charge in conductors. *Physical Review* 32, 110–113.
- Petrashov, V. T., V. N. Antonov, P. Delsing, and T. Claeson (1993). Phase memory effects in mesoscopic rings with superconducting "mirrors". *Physical Review Letters* 70(3), 347–350.
- Petrashov, V. T., V. N. Antonov, P. Delsing, and T. Claeson (1995). Phase controlled conductance of mesoscopic structures with superconducting "mirrors". *Physical Review Letters* 74(26), 5268–5271.
- Petrashov, V. T., R. S. Shaikhaidarov, P. Delsing, and T. Claeson (1998). Phase-sensitive reentrance into the normal state of mesoscopic SNS structures. *JETP Letters* 67(7), 513–520.
- Pothier, H., S. Gueron, D. Esteve, and M. Devoret (1994). Flux-modulated Andreev current caused by electronic interference. *Physical Review Letters* 73(18), 2488–2491.
- Pozar, D. M. (1993). *Microwave Engineering*. Reading, MA: Addison-Wesley.
- Pucel, R. A. (1961). *Proc. IRE* 49, 1080.
- Reznikov, M., R. De-Picciotto, T. G. Griffiths, M. Heiblum, and V. Umansky (1999). Observation of quasiparticles with one-fifth of an electron's charge. *Nature* 399(6733), 238–241.
- Reznikov, M., M. Heiblum, H. Shtrikman, and D. Mahalu (1995). Temporal correlation of electrons: Suppression of shot noise in a ballistic quantum point contact. *Physical Review Letters* 75(18), 3340–3343.
- Rogovin, D. and D. J. Scalapino (1974). Fluctuation phenomena in tunnel junctions. *Annals of Physics* 86(1), 1–90.
- Saminadayar, L., D. C. Glattli, Y. Jin, and B. Etienne (1997). Observation of the $e/3$ fractionally charged Laughlin quasiparticle. *Physical Review Letters* 79(13), 2526–2529.

- Schoelkopf, R. J. (1995). *Studies of noise in Josephson-effect mixers and their potential for sub-millimeter heterodyne detection*. Ph. D. thesis, California Institute of Technology.
- Schoelkopf, R. J., P. J. Burke, A. Kozhevnikov, D. E. Prober, and M. J. Rooks (1997). Frequency dependence of shot noise in a diffusive mesoscopic conductor. *Physical Review Letters* 78(17), 3370–3373.
- Schoelkopf, R. J., A. Kozhevnikov, D. E. Prober, and M. J. Rooks (1998). Observation of "photon-assisted" shot noise in a phase-coherent conductor. *Physical Review Letters* 80(11), 2437–2440.
- Schottky, W. (1918). Über spontane Stromschwankungen in verschiedenen Elektrizitätsleitern. *Ann. Phys. (Leipzig)* 57, 541.
- Segall, K. and D. Prober (2001). Quantum Partition Noise in a Superconducting Tunnel Junction (preprint, submitted to Phys. Rev. B).
- Shaikhaidarov, R., A. F. Volkov, H. Takayanagi, V. T. Petrashov, and P. Delsing (2000). Long-range phase-coherent effects in the transport properties of mesoscopic superconductor-normal metal structures. *Physical Review B* 62(22), R14649–52.
- Sohn, L. L., L. P. Kouwenhoven, and G. Schön (Eds.) (1997). *Mesoscopic Electron Transport*. Dordrecht, the Netherlands: Kluwer Academic Publishers.
- Soulen, R. J., J. M. Byers, M. S. Osofsky, B. Nadgorny, T. Ambrose, S. F. Cheng, P. R. Broussard, C. T. Tanaka, J. Nowak, J. S. Moodera, A. Barry, and J. M. D. Coey (1999). Measuring the spin polarization of a metal with a superconducting point contact. *Science* 282, 85–88.
- Spiegel, D. R. and R. J. Helmer (1995). Shot-noise measurements of the electron charge: an undergraduate experiment. *American Journal of Physics* 63(6), 554–560.
- Steinbach, A. H., J. M. Martinis, and M. H. Devoret (1996). Observation of hot-electron shot noise in a metallic resistor. *Physical Review Letters* 76(20), 3806–3809.
- Stoof, T. H. and Y. V. Nazarov (1996). Kinetic-equation approach to diffusive superconducting hybrid devices. *Physical Review B* 53(21), 14496–14505.
- Strijkers, G. J., Y. Ji, F. Y. Yang, C. L. Chien, and J. M. Byers (2001). Andreev reflections at metal/superconductor point contacts: Measurement and analysis. *Physical Review B* 63, 104510.

- Strunk, C. (2000). personal communication.
- Tien, P. K. and J. P. Gordon (1963). Multiphoton process observed in the interaction of microwave fields with the tunneling between superconductor films. *Physical Review* *129*(2), 647–651.
- Tinkham, M. (1995). *Introduction to Superconductivity*. New York: McGraw Hill.
- Torres, J. and T. Martin (1999). Positive and negative Hanbury-Brown and Twiss correlations in normal metal - superconducting devices. *European Physical Journal B* *12*(3), 319–322.
- Upadhyay, S. K., A. Palanisami, R. N. Louie, and R. A. Buhrman (1998). Probing ferromagnets with Andreev reflection. *Physical Review Letters* *81*(15), 3247–3250.
- Usadel, K. D. (1970). Generalized diffusion equation for superconducting alloys. *Physical Review Letters* *25*(8), 507–509.
- Volkov, A. F., A. V. Zaitsev, and T. M. Klapwijk (1993). Proximity effect under nonequilibrium conditions in double-barrier superconducting junctions. *Physica C* *210*(1-2), 21–34.
- Wahlgren, P. (1998). *The Radio Frequency Single-Electron Transistor and the Horizon Picture for Tunneling*. Ph. D. thesis, Chalmers University of Technology.
- Wilhelm, F. K., A. D. Zaikin, and G. Schön (1997). Supercurrent in a mesoscopic proximity wire. *Journal of Low-Temperature Physics* *106*(3-4), 305–310.
- Wilson, C. M., L. Frunzio, and D. E. Prober (2001). Time-Resolved Measurements of Thermodynamic Fluctuations of the Particle Number in a Dilute Fermi Gas (preprint, submitted to *Phys. Rev. Lett.*).
- Wind, S., M. J. Rooks, V. Chandrasekhar, and D. E. Prober (1986). One-dimensional electron-electron scattering with small energy transfers. *Physical Review Letters* *57*(5), 633–636.
- Yip, S. (1995). Conductance anomalies for normal-metal - insulator - superconductor junctions. *Physical Review B* *52*(21), 15504–15508.